A Study Of The X-ray Transient A0620-00

Sushan Yow

Mullard Space Science Laboratory
Department of Space and Climate Physics
University College London

A thesis submitted to the University of London

for the degree of Master of Philosophy

October 12, 2006

Abstract

This thesis is a study of the X-ray transient A0620-00. A0620-00 is a binary system consisting of a black hole candidate and a late-type main sequence star. Its last recorded outbursts were in 1917 and 1975. This black hole candidate binary system is chosen for this study as it is the brightest optical source in quiescence among black hole candidates. Furthermore its long quiescence period ($\sim$60 years) allows ample opportunities to study the properties of the black hole candidate, the mass donor star and the accretion disk.

This investigation involves the analysis of a series of optical spectra of A0620-00 collected at the 2.3m ANU telescope at Siding Spring Observatory (SSO), over the span of 5 years (with observing campaigns in 2000, 2003, and 2004).

The most prominent spectral feature in these spectra of A0620-00 is a double peaked Hα emission line centred at 6562.8 Å. The double peaked line indicates the presence of an accretion disk. The physical conditions and dynamics of an X-ray transient that lead to the formation of this optical Balmer line can be inferred from the data. It is unclear if the mechanisms which produce the Balmer line during quiescence and during outbursts are similar.

The objective of this thesis is to look for variations in the optical spectra of A0620-00 during quiescence, and in particular, for changes in the profile and the strength of the normalised flux of the double peaked Hα emission line. Scrutiny of the Hα profile over time provides an insight into the possible changes in the physical conditions of the flow in the disk, hence the resulting radiation.

The analysis of the spectra found the Hα line profile to be varying. The asymmetry in the shape of the double peaked line profile and periodic variation of the equivalent widths support the presence of a hotspot, as well as a weak wind on the accretion disc. The line width of Hα varies over time which could be the result of an expanding of the inner edge of the accretion disc, resulting in the emission region being much closer to the compact object. There are also changes in the equivalent width that indicate a possible increase in the mass accretion rate, hence a higher luminosity. However this increase in accretion rate is not enough to induce a mini outburst in the system, nor to produce a strong wind in the disc. The diagnosis suggests that the accretion disc could be in a state of instability, where the inner edge is expanding and contracting.

Contents

List of Figures

List of Tables

Chapter 1

Introduction

1.1 Objective

This is a study of the X-ray transient A0620-00. An X-ray transient (XT) is a binary system, whose X-ray source suddenly increases in X-ray brightness and then returns to the initial brightness after a period of usually weeks or more. A0620-00 is made up of a stellar sized black hole candidate, surrounded by a fully developed accretion disc (Haswell & Shafter, 1990), and a cool, less massive main sequence star. This XT has a quiescence period of about 60 years. The last recorded outburst from A0620-00 was in 1975, and it is now past half of its "quiet" period. Please refer to Section 1.4 for more details on this system.

A0620-00 was chosen as a target of study because it is the brightest optical source in quiescence among black hole candidates (Leibowitz *et al.*, 1998). Its long quiescence period allows ample opportunities to study the properties of the black hole candidate, its companion dwarf star, the accretion disc surrounding the black hole candidate, as well as the interaction between the accreting compact object and its donor companion.

An analysis was performed on a series of optical spectra of A0620-00 in quiescence, collected over 5 years (in 2000, 2003 and 2004). The most prominent feature in all of the spectra is a double peaked Balmer emission line, Hα (6563 Å). The double peaked line is an indication of the presence of an accretion disc. The physical conditions and dynamics of an X-ray transient that lead to the formation of this optical Balmer line can be inferred from the data. It is unclear if the mechanisms which produce the Balmer line during quiescence and during outbursts are similar.

The objective is to look for variations in the optical spectra of A0620-00 during quiescence, and in particular, for changes in the profile and the intensity of the normalised flux of the double peaked Hα emission line. Scrutiny of the Hα profile over time may provide an insight into the possible changes in the physical properties of the disc, which may reveal the line formation process involved and the possible changes in the line formation region.

The expected variations which may be uncovered include a change in the shape of the wings of the emission line. This would indicate a change in the distance between the outer edge of the disc and the main emission region. A steeper slope indicates the line originates from an emission region of a radius closer to the outer edge of the accretion disc, hence a lower velocity.

A change in the intensity of the emission line, on the other hand, points to absorption and scattering. Absorption and scattering are affected by the density of the disc and its surrounding. A possible source of absorption and scattering is stellar wind from accretion. Although a strong stellar wind is not expected from this system, a black hole candidate that is slowly accreting its small companion may still give rise to a small degree of stellar wind.

1.2 Overview of X-ray Binaries

X-ray transients are a subclass of X-ray binaries. An X-ray binary is made up of a normal star and a compact object such as a white dwarf, a neutron star, or a black hole. The compact object is usually encircled by an accretion disc, which is formed by the infalling flow of matter. The compact object and companion star revolve around a common centre of gravity. Each object has an elliptical orbit such that at any instant, the two objects are on opposite sides of the centre of mass. A schematic diagram of an X-ray binary system is depicted in Figure 1.1. X-rays are thought to be produced in a region close to the compact object, usually in the accretion disc.

Matter within the accretion disc moves in approximately Keplerian orbits. The viscosity within concentric regions of the disc generates heat and depletes the angular momentum. The drop in angular momentum results in matter spiralling inward towards the compact star. However, in the case of a black hole, the matter is drawn toward the event horizon.

There are many subclasses of X-ray binaries, namely low mass X-ray binaries

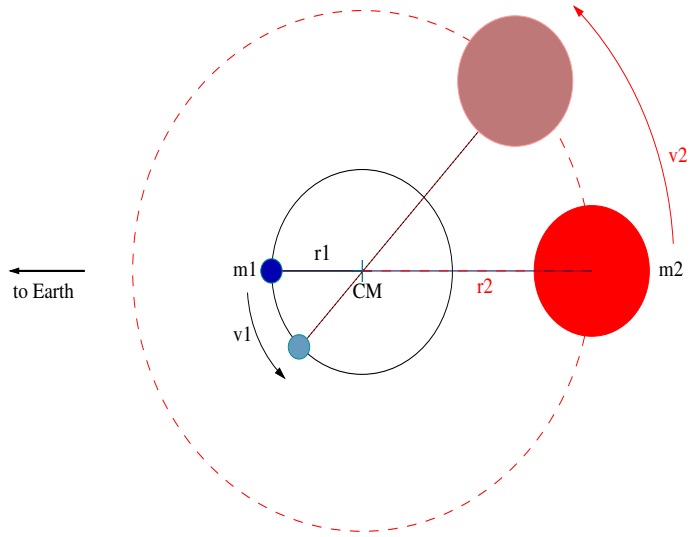

Figure 1.1: Schematic of an X-ray binary system. m1 and m2 are the masses of the compact object and the companion star, respectively. m1 is surrounded by an accretion disc (not drawn). Both m1 and m2 orbit about a centre of mass, denoted by CM, at the corresponding distance r1 and r2 from CM. Both m1 and m2 revolve around CM at the subsequently radial velocity v1 and v2.

(LMXB), high-mass X-ray binaries (HMXB), Be X-ray binaries, X-ray bursters, X-ray pulsars, X-ray transients (XT), and microquasars.

The mechanism that brought about the transient behaviour differs for subclasses, especially those of much higher outburst luminosity such as bursters. The outburst in an X-ray burster, similar to that of a classical nova, is due to thermonuclear flashes.

Classical novae are commonly found in close binary systems, usually with a main sequence star, and a hot, but less massive white dwarf. A classical nova undergoes a sudden surge in its brightness by several orders of magnitudes (commonly known as outbursts), and then fades slowly back to normal.

An X-ray burster is a source of very short and intense outburst of X-ray (usually of the order of 1-30 keV. The outburst of an X-ray burster is due to the build up of a shell of accreted matter on to the surface of the central object. The build-up of these degenerate matter rises the temperature pass a critical temperature at which it ignites fusion of the material. In a degenerate medium, fusion is a runaway process, hence the powerful X-ray bursts.

The outburst of X-ray transients are less powerful. An X-ray Transient (XT)

contains a compact object that is more massive than 1.4 $M_{\odot}$, and a normal star. The compact object can either be a neutron star or a black hole candidate. The system has periods of enhanced X-ray emission, which are commonly known as outbursts. The outbursts typically last longer than a week, and their occurrence may or may not be periodic.

X-ray transients are further divided into two classes, which are analogous to High Mass X-ray Binaries (HMXB), and Low Mass X-ray Binaries (LMXB).

HMXBs consist of a neutron star or black hole candidate with an early-type massive stellar companion (usually more than 5 $M_{\odot}$). The companion loses mass through a stellar wind which flows out isotropically from the companion. Due to the orbital motion of the companion, materials from the wind will inevitably "collide" with the compact object. Hence, in this case, the accretion of matter onto the compact object occurs via the stellar wind from the companion star (see Figure 1.2). The impact of the interaction between the stellar wind and the compact object is strong enough to produce X-ray emission. HMXBs are characterised by having more higher energy X-rays ($\geq$ 6 keV) in the spectrum in transient than in quiescence.

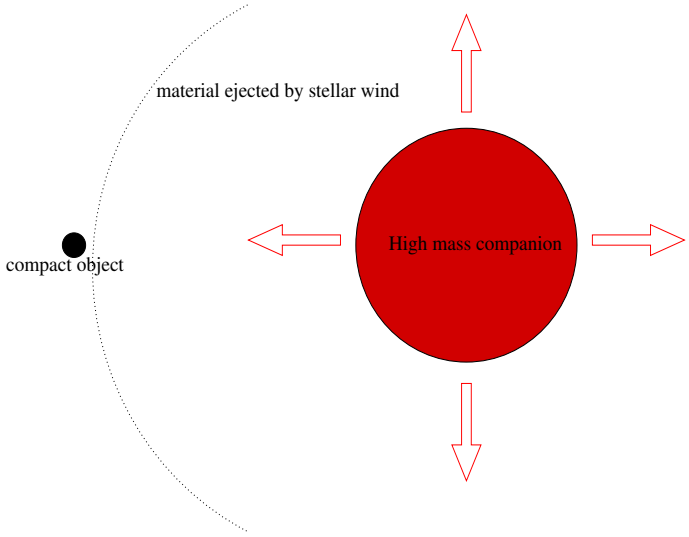

Figure 1.2: Schematic of an High Mass X-ray Binary. The compact object is either a neutron star or black hole candidate, with a massive companion. Accretion of material from the companion is facilitated by its stellar wind.

LMXBs contain a neutron star or a black hole candidate and a late-type, low-mass K-M type main sequence star (less massive than the compact object)

revolving around each other. In some cases the companion can either be a degenerate or evolved, subgiant or red giant star.

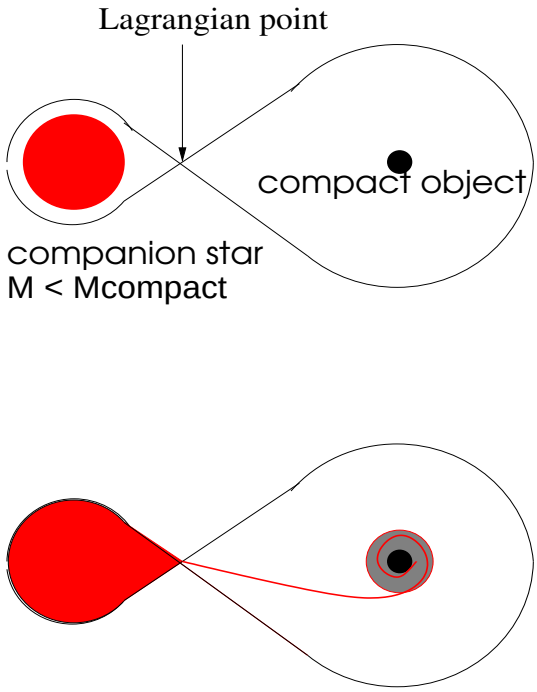

Figure 1.3: Schematic of an Low Mass X-ray binary. The top figure shows the Robe lobes of the components of a low mass X-ray binary. The lower figure depicts what happens during Roche lobe overflow. The shaded area around the compact object represents the accretion disc.

Mass transfer from the companion to the compact object takes place via Roche lobe overflow (see Figure 1.3). The material transferred tends not to be accreted by the compact object immediately due to its angular momentum. An accretion disc is formed by the orbiting material which loses its angular momentum as it spirals onto the compact object. As the material spirals in, it heats up over $1{\times}10^6$ K, resulting in X-ray emission. These transient events often generate more lower energy (typically < 6 keV) X-rays than in quiescence.

The Roche lobe of an object outlines the volume around the object within which matter is gravitationally bound to it. In a binary system, the Roche lobe of each component is drawn to points where the gravity from the companion is equal to the gravity from the compact object. These are known as the Lagrangian points. When the companion fills its Roche lobe, material from the companion will flow through the first Lagrangian point (L1, see Figure 1.4) towards the com-

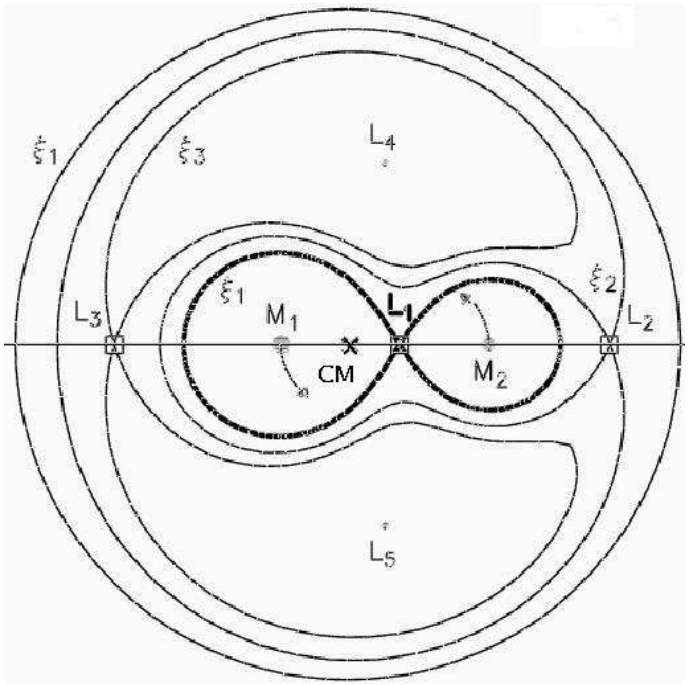

Figure 1.4: This is a depiction of the Roche lobe geometry of a binary system. M1 and M2 are the masses of the compact object and companion respectively. L1 denotes the first Lagrangian point, and L2, L3, L4, L5 are the subsequent Lagrangian points. Excerpt from Frank *et al.* (2002).

pact object. The Roche lobe can be filled by either expansion of the companion star or shrinking of the Roche lobe itself. The Roche lobe will shrink due to the decrease in the separation of the two components, resulting from the loss of angular momentum (Frank *et al.*, 2002). Figure 1.4 illustrate the Roche lobe geometry of a binary system.

In particular, the LMXB transients are believed to be powered by thermal and viscous instability in the accretion disc. It is believed that thermal stability of the disc can be achieved if the rate of change of radiative cooling as function of temperature is greater than that of viscous heating (Frank *et al.*, 2002). However, the thermally stability of the disc is affected by different heating mechanisms of the disc, such as local turbulence, irradiation, tidal dissipation and/or the impact of the accretion stream.

The accretion disc can be irradiated by the X-rays produced by the accretion flow, and X-ray reprocessing. Irradiation has a role in changing the relation between the midplane and surface temperature of the disc, altering the critical

surface densities and affecting convection. As the surface temperature of the disc exceeds the ionisation temperature, the disc becomes ionised, hence causing instability in the disc. Furthermore, it also lowers the minimum critical surface density of the disc required and the critical mass-transfer rate which dictate the instability of hot discs. Disc instability is also caused by heating via tidal dissipation and/or the impact of the accretion stream. These processes lower both the minimum and maximum critical surface densities, hence narrowing the density criterion for disc stability (Lasota, 2001).

1.3 Orbital Parameters

It is possible to derive parameters that describe the binary system from observations. Among them are the orbital period of the components and their radial velocities, from which a mass function can be calculated.

1.3.1 The Orbital Period and Radial Velocities

The orbital period is the time taken for one component to revolve around a common centre of gravity. By studying the light curve of the target over time, it is possible to search for a periodic change in the flux. If a periodic change is found, the time taken for the pattern to repeat is the orbital period. Alternatively, it can be measured from the radial velocity shifts of the line centre of a spectral line.

Lines in spectra of spectroscopic binaries are shifted by Doppler shifts due to the orbital motion of the components. This Doppler shift velocity, also known as radial velocity, can be calculated from line measurements by Equation 1.1.

$$V_{rad} = \frac{\lambda_{obs} - \lambda_{emit}}{\lambda_{emit}} \times c \tag{1.1}$$

where λ_{obs} is the observed wavelength of the line, and λ_{emit} is the rest wavelength of the line. The wavelengths are expressed in Angstroms (Å), and c is the speed of light (3×10^5 km s^{-1}).

The radial velocities of the components are then plotted against the orbital phase as in Figure 1.5 to show the orbital motion of the components.

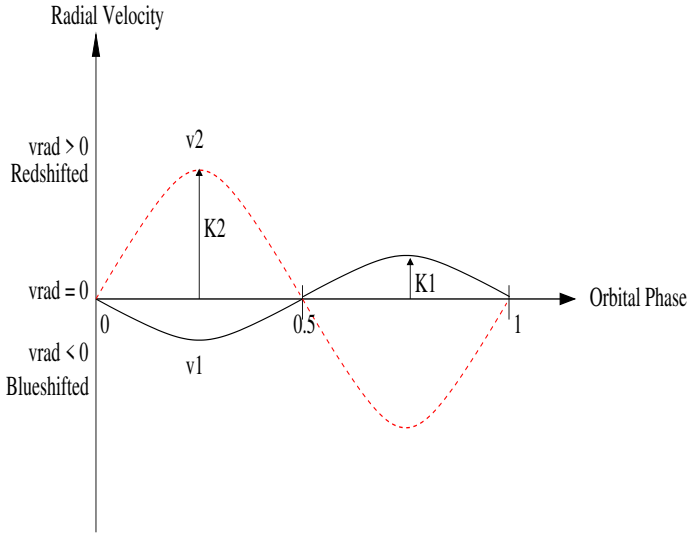

Figure 1.5: This is a plot of radial velocities of the components of a binary system. The radial velocity of the compact object is denoted by $v1$, with a semi-amplitude $K1$. $v2$ and $K2$ refers to the radial velocity and the velocity semi-amplitude of the companion object.

1.3.2 The Mass Function

From the radial velocity curve, the semi-amplitude of the radial velocity is measured and is used to calculated the mass function of the system (see Equation 1.3). The mass function uses Kepler's laws to define the relationship between the masses of the two components of a spectroscopic binary. It assumes that the orbit has a low ellipticity.

$$f(M_1, M_2) = \frac{M_1^3 \sin^3 i}{(M_1 + M_2)^2} \tag{1.2}$$

$$= \frac{P v_2^3}{2\pi G} \tag{1.3}$$

where M_1 and M_2 are the masses of the primary object and secondary object respectively, and i is the orbital inclination angle in degrees. P is the orbital period in seconds, v_2 is the radial component of the velocity of the secondary star, and G is the gravitational constant (6.67×10^{-11} Nm^2 kg^{-2}). All of the parameters above are expressed in mks units. The mass function is usually expressed in terms

of solar masses, $M_\odot$ ($\sim 2 \times 10^{30}$ kg).

1.4 A0620-00

1.4.1 The Nature of A0620-00

A0620-00 is a binary star system. It is located at Right Ascension, $\alpha = 06^h\ 22^m\ 44^s.5$, Declination, $\delta = -00^\circ\ 20'\ 44.9''$ (epoch 2000), at a distance of 1.05 kpc (Shahbaz *et al.*, 1994). It was initially thought to be an X-ray nova, and it was the first X-ray nova to be identified with an optical object (Johnston & Kulkarini, 1990).

However, A0620-00 was later confirmed to be an X-ray transient (Whelan *et al.*, 1977; Murdin *et al.*, 1980), composing of a stellar-size black hole candidate and a spectral class K dwarf star (McClintock & Remillard, 1986; Oke, 1977).

The X-ray 1975 outburst of A0620-00 was first detected in the hard X-ray energy band above 10 keV. The rise to its peak luminosity was found to be due to the underlying soft X-ray between 1-6 keV (Elvis *et al.*, 1975). The X-ray luminosity faded beyond detection within 7 months of the outburst (McClintock & Remillard, 1990), and it is believed that A0620-00 has been in quiescence since.

1.4.2 Findings From Past Observations

A0620-00 was first discovered as an X-ray source on 3 August 1975 using the Ariel V Sky Survey Experiment (Elvis *et al.*, 1975). This source was first thought to be a nova (Nova Monocerotis 1975), hence the name (Wheeler *et al.*, 1989). It was later discovered that Harvard photographic plates had been taken of a previous outburst, more than 60 years prior to the outburst in 1975, therefore it was also known as Nova Monocerotis 1917. Besides the latter name, it was also given many names, such as V616 Monocerotis, the optical counterpart of the source (Leibowitz *et al.*, 1998), A0601-00[1], A0621-00[1], Mon X-1[1] ([1] Whelan *et al.* (1977)).

In quiescence, A0620-00 has a visible magnitude, $V \sim 18.3$ (Haswell *et al.*, 1990). During its outburst in 1975, it reached beyond $V \sim 12$, and it was also the brightest X-ray source in the sky (Elvis *et al.*, 1975). The X-ray luminosity peaked at 1.0×10^{38} erg s^{-1} in the 1-10 keV energy band on August 12, 1975 (Elvis *et al.*, 1975). The peak luminosity lasted for several days, before it began

to decline (Kaluzienski *et al.*, 1977). The X-ray decay was interrupted with occasional halts in the decay process, which were accompanied by a temporary increase in flux.

After $\sim$ 29 days from the start of the decay, it was detected to have halted for $\sim$ 10 days, and at the same time increased in its flux, before it continued to fade for another $\sim$ 20 days (Kaluzienski *et al.*, 1977). The decay stopped again for about a month, and the increase in the X-ray flux was detected again for about another month. Finally, approximately 7 months after the outburst, the X-ray luminosity had decline beyond 10^{32} erg s^{-1} (McClintock & Remillard, 1990), in March 1976, the detection limits at that time (see Figure 1.6).

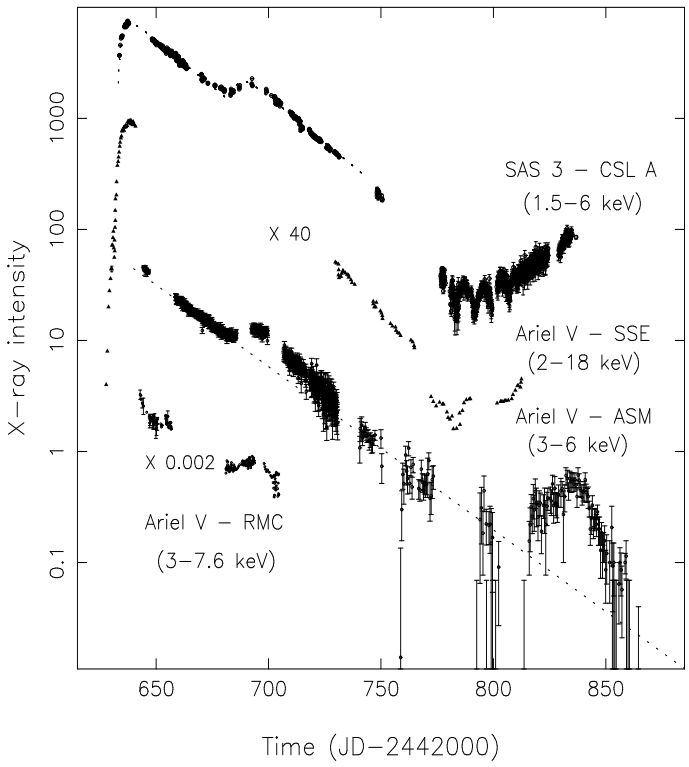

Figure 1.6: X-ray intensity A0620-00 during its outburst(s), taken from different missions. Excerpt from: Kuulkers (1998)

By then, its optical luminosity which peaked at $V \sim 10.4$ (Locher, 1975), began to fade too. Fifteen months after its outburst, A0620-00 returned to its quiescence at visible magnitude (Shahbaz *et al.*, 1994; McClintock *et al.*, 1995). Like its X-ray intensity, the optical magnitude was fading and brightening during the course of the X-ray decay. Figure 1.7 shows a comparison of the optical

outburst light curve to the X-ray outburst light curve of A0620-00. Kuulkers (1998) compiled the optical outburst data from an unpublished report by Webbink (1978) which included photoelectric, photographic and visual observations. The data also incorporate findings from observations and reports by Borisov *et al.* (1977); Chevalier *et al.* (1980); Duerbeck & Walter (1976); Hudec (1977); Liutyi (1976); Lyutyi (1976); Lloyd *et al.* (1977) and Robertson *et al.* (1976).

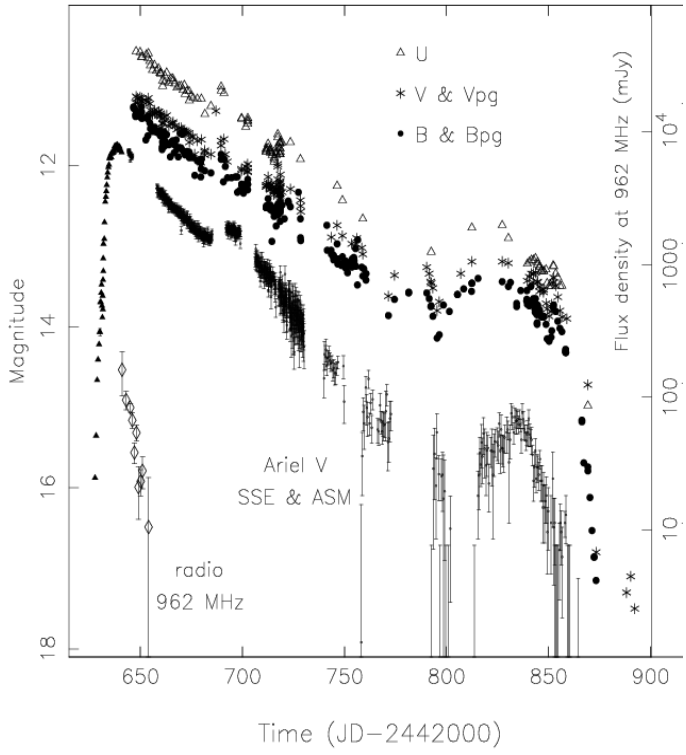

Figure 1.7: Optical (UBV) light curve of A0620-00 during its outburst in 1975. The X-ray data were from Ariel V ASM and SSE. The vertical axis on the right is a measure of the X-ray intensity while the left axis is a measure of the optical magnitude. Optical data were compiled from Webbink (1978); Borisov *et al.* (1977); Chevalier *et al.* (1980); Duerbeck & Walter (1976); Hudec (1977); Liutyi (1976); Lyutyi (1976); Lloyd *et al.* (1977) and Robertson *et al.* (1976) Excerpt from: Kuulkers (1998)

No further outbursts were detected after 1975. It was noted that there was a modest increase ($\sim$ 0.3 mag) in the visual brightness between observations in 1977 by Oke (1977), and in 1992 by McClintock *et al.* (1995). This increase was attributed to the ellipsoidal and secular variability of A0620-00 (McClintock & Remillard, 1990). Such change is most probably caused by the tidal distortion of

the secondary star by the compact object. Taking this into account, an observation in 1998 found the total V magnitude to be about the same since its fade-out in 1976 (McClintock & Remillard, 2000). So far, there has been no significant change in the V magnitude reported.

Years later, its X-ray luminosity was measured at $\sim 6 \times 10^{30}$ erg s^{-1} (0.1-2.4 keV, at 1 kpc) using *ROSAT* in 1992 (McClintock *et al.*, 1995), and 2.8×10^{30} erg s^{-1} (0.3 to 0.7 keV, at 1 kpc) using *Chandra* in 2000 (Garcia *et al.*, 2001). Using *WebPIMMS*, the *ROSAT* luminosity was converted to X-ray flux measured in the 0.3-7 keV band, giving 2.0×10^{-14} erg cm^{-2} s^{-1}, which was comparable to the *Chandra* value of 1.8×10^{-14} erg cm^{-2} s^{-1}.

1.4.3 Orbital Parameters of A0620-00

The optical quiescent spectrum of A0620-00 mainly comprises of a double peaked Balmer emission lines (Hα and Hβ) from the accretion disc (Johnston *et al.*, 1989), and a continuum with absorption features of a K4V - K7V star (Oke, 1977; Haswell *et al.*, 1990) (see Figure 1.8). The following parameters are determined from a series of such spectra taken over a few years.

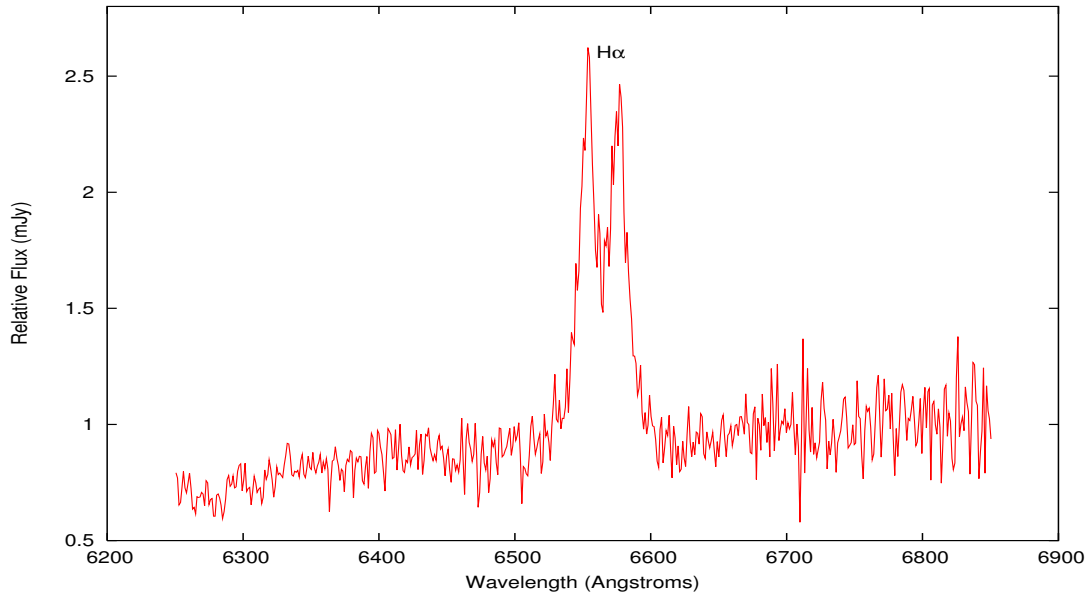

Figure 1.8: Example of a A0620-00 spectrum during quiescence with the labelled Hα($\lambda\lambda$6563) line. This is a spectrum taken on 29 January 2000 (JD +1572.99) at the 2.3m DBS telescope at ANU.

1.4.3.1 Orbital Period

McClintock & Remillard (1986) found from their photometric observations between 1981-1985, that the orbital period of the system is 7.75234 ± 0.0001 hr or ∼ 0.323 days. The ephemeris from McClintock & Remillard (1986) is used by other authors mentioned in this thesis, as well as for the data analysis in this thesis (see Table 1.1). Contrary to convention, McClintock & Remillard (1986) had defined the orbital phase zero to be inferior conjunction of the companion star, the position where the companion star is behind the compact object. Therefore this orbital phase definition is 180° out of phase with the conventional definition.

Table 1.1: Ephemeris of A0620-00 (McClintock & Remillard, 1986)

Parameter	Value (Circular Orbit Solution)	
T_0 (spectroscopic)	HJD 2,446,082.7481 ± 0^d.0008	(at maximum velocity)
T_0 (photometric)	HJD 2,445,477.827 ± 0^d.005	(at primary minimum)
$Period_{photometric}$	7.75234 ± 0.00010 (hr)	
	0.323014 ± 0.000004 (days)	

HJD refers to Heliocentric Julian Date

1.4.3.2 Radial Velocity of Companion Star

From the ephemeris, McClintock & Remillard (1986) obtained a radial velocity curve for the companion K dwarf. They determined the semi-amplitude of the radial velocity to be 457 ± 8 km s^{-1}. Similarly, Johnston *et al.* (1989) used the photometric period by McClintock & Remillard (1986) and cross-correlated their A0620-00 spectra with that of a K5V star to obtain their own radial velocity. Their semi-amplitude for the K dwarf was $K_2 = 460 \pm 40$ km s^{-1} for their low-resolution observations (>7.5 Å) , and $K_2 = 453 \pm 11$ km s^{-1} for their high-resolution observations (1.8 Å). Further investigations by Marsh *et al.* (1994) found $K_2 = 433 \pm 3$ km s^{-1} which is also consistent with K_2 found by McClintock & Remillard (1986) and Johnston *et al.* (1989) at 3σ.

Shahbaz *et al.* (2004) independently determined an ephemeris with T_0 at JD 2,452,646.6365 ± 0.0005. They had followed the normal convention in defining the orbital phase zero. Shahbaz *et al.* (2004) obtained $K_2 = 403 \pm 4.5$ km s^{-1}, which is within 3σ of McClintock & Remillard (1986).

1.4.3.3 The Mass Function

With $K_2 = 457 \pm 8$ km s^{-1}, McClintock & Remillard (1986) calculated the corresponding mass function of the compact object to be $f(M) = 3.18 \pm 0.16$ M$_\odot$. This value is above the mass of a neutron star for the stiffest possible nuclear equation (2.7 M$_\odot$). The 3σ lower limit on the mass of the compact object is 3.2 M$_\odot$. As a result, A0620-00 became a prime black hole candidate. Their observations strongly suggest the companion star to be a K dwarf star, possibly of spectral class K3V to K5V, consistent with the prediction by Oke (1977).

Using the results of McClintock & Remillard (1986), together with further observations, Haswell & Shafter (1990) found a mass function, $f(M) = 3.82 \pm 0.24$ M$_\odot$. By assuming a mass ratio, $0.2 \leq q \leq 0.5$, and an inclination, $59^\circ \leq i \leq 85^\circ$, they calculated the mass of the compact object to be in the range of 3.1 M$_\odot \leq$ M$_{compact} \leq$ 7.6 M$_\odot$, and found the corresponding companion mass to be in the range of 0.03 M$_\odot \leq$ M$_{secondary} \leq$ 1.5 M$_\odot$ (Haswell *et al.*, 1990).

The later study by Johnston & Kulkarini (1990) yielded a mass function of $f(M)_{low} = 3.30 \pm 0.95$ M$_\odot$ for the low resolution data, and a mass function of $f(M)_{high} = 3.1 \pm 0.2$ M$_\odot$ for the high resolution data.

Shahbaz *et al.* (2004) determined the masses of the compact object $M_1 = \frac{3.09 \pm 0.09}{\sin^3 i}M_\odot$ and its companion $M_2 = \frac{0.21 \pm 0.04}{\sin^3 i}M_\odot$ as a function of the inclination of the system. Shahbaz *et al.* (2004) obtain a lower limit of M_1 which is very close to the lower limit of the range of M_1 calculated by McClintock & Remillard (1986).

Subsequent investigations led to the refinement of K_2. The resulting mass function from the independent studies mentioned above are consistent with one another. All investigations, except that by Shahbaz *et al.* (2004) confirmed that the mass of the compact object is greater than the maximum calculated mass for a neutron star, thus strongly suggesting that the compact object in A0620-00 is a black hole.

1.5 Line Profile of the Double Peaked Emission Line

The spectra of XT in quiescence are characterised by strong Balmer emission lines with a relatively flat continuum. Emission lines are broadened due to the

rotational motion of material in the source, hence often these emission lines appear to be double peaked. The double peaked emission lines of XT originate from an accretion disc around the compact object.

The relationship between the broadened line and the radial velocity of the source is expressed in the Doppler shift equation (see Equation 1.1). The value of λ_{obs} is the observed wavelength of the line's peak. For the case of a double peaked line, it will be the wavelength of the blue peak for radical velocity of the blue shifted line and the wavelength of the red peak for the red shifted line.

The rotational velocity or Doppler shift velocity of a physically thin and near circular disc can be approximated to its Keplerian velocity (see Equation 1.4).

$$\begin{aligned} V_{dop} &\approx V_{Kep} \\ &= \sqrt{\frac{GM}{R}} \end{aligned} \tag{1.4}$$

where V_{dop} is the Doppler shift velocity, V_{Kep} is the Keplerian velocity, G is the gravitational constant, M is the mass of the central object, and R is the distance of a point on the disc to the central object.

However, for a distant observer, the inclination angle, i, between the observer's line-of-sight and the normal to the disc plane with the azimuthal angle relative to the line-of-sight, θ, should be taken into consideration (see Equation 1.5) (Horne & Marsh, 1986).

$$V_{dop} = V_{Kep} \sin i \sin \theta \tag{1.5}$$

Figure 1.9 shows a comparison of an emission line from a non-rotating source to an emission line from a rotating source. The blue shifted peak comes from the region of the disc that is rotating towards the observer, while the red shifted peak comes from the region that is moving away.

To have a better understanding of the formation of the double peaked emission line profile, Horne & Marsh (1986) used the loci of a constant radial velocity of

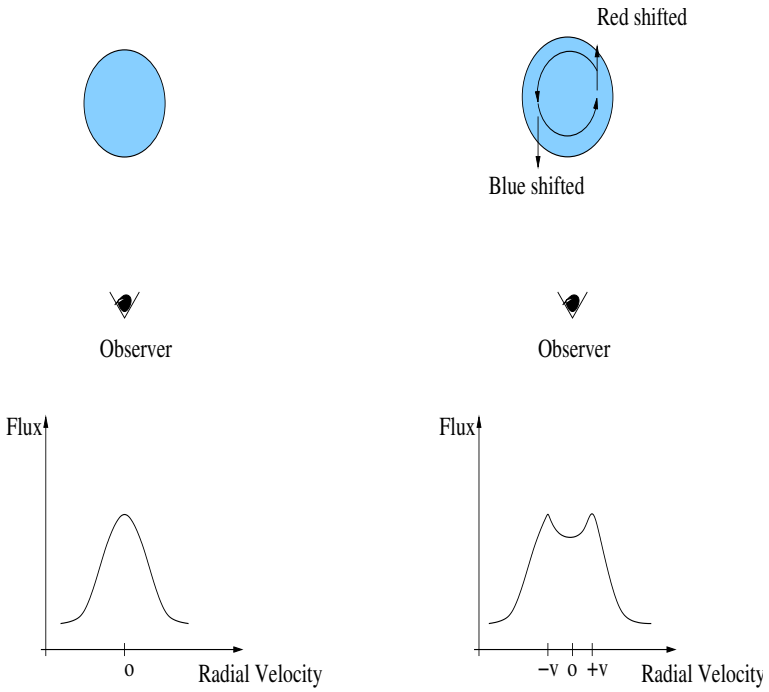

Figure 1.9: The emission line on the left is from a non-rotating source. The emission line on the right shows a double peaked feature, due to the rotation of the source.

a Keplerian disc to trace out a 'dipole field' pattern (as shown in the top of Figure 1.10.) The radial velocity and the distance from the compact object are represented by the vertical axis and the horizontal axis.

The disc emission profile, as shown in the bottom figure of Figure 1.10, is a plot of Doppler shift velocity as a function of flux. The profile is produced by binning flux from various parts of the disc with the same Doppler shift velocities. Each shaded velocity bin in the profile originates from the crescent-shaped section of the disc (shaded in the same way) in the 'dipole field' plot. The height of a shaded bin in the profile corresponds to the area of the similarly shaded crescent region in the 'dipole field' (see Figure 1.10).

The area of the crescents varies inversely with the velocity. Therefore the emission from the bins in the wings of the profile come from regions close to the centre of the disc. The flux of the bins adjacent to $V = 0$ is due to contributions from material moving normal to the line-of-sight, and is limited by the outer radius of the disc. The double peaked feature also reflects the inclination of the system. The sharper the peak, the higher the inclination (Marsh & Horne, 1988).

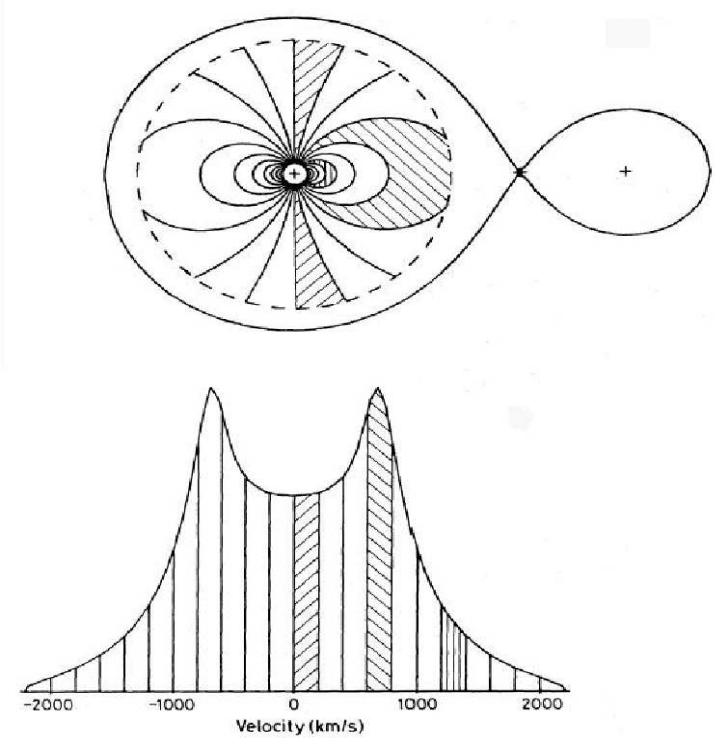

Figure 1.10: Taken from Horne & Marsh (1986), the top figure is the dipole field traced out by a Keplerian accretion disc. The figure below is the velocity profile; the shaded regions correspond to the shaded regions of the disc in the dipole field.

1.5.1 The Process of Double Peaked Line Formation

Emission lines can be produced in regions of the accretion disc which are optically thin to continuum radiation, but optically thick to lines (Lin, 1991). If the entire disc is optically thin, most of the intensity of the emission lines would originate from the outer regions of the disc. However emission lines can also propagate from a temperature-inversion layer on an accretion disc. A temperature-inversion layer is a layer on the accretion disc surface that is hotter than disc beneath it. It is usually formed when the disc is irradiated by UV and X-rays. Its presence will result in the disc being opaque to the continuum.

The observations of A0620-00 used in this assay were collected during its quiescence period. The X-ray flux was measured at 1.8 $\times 10^{-14}$ erg cm^{-2} s^{-1} in 2000 by *Chandra* (Garcia *et al.*, 2001), hence the X-ray flux of A0620-00 is unlikely to be enough to generate a temperature-inversion layer. During this period of quiescence, mass transfer of in A0620-00 is expected to be low. As a consequence,

the accretion disc has a low surface density and is transparent to the optical continuum. Due to the inefficient cooling of the optically thin medium, the accretion disc, though of low density, will heat up and eventually become hotter than a high density disc. Hence, a large portion of the disc is involved in line emission. Using the dipole field model, emission from a larger area on the disc, will therefore produce wider and more intense peaks.

For the double peaked lines (Balmer lines such as Hα and Hβ) to form in A0620-00, its accretion disc should be optically thin and hot, and the emitting region close to the black hole candidate. The emission process is likely to be dominated by collisional-ionisation or collisional-recombination. The line profile from an emission region close to the central object has a larger line width and a wider peak-to-peak separation than a profile of an emission region closer to the outer edge.

1.5.2 Theoretical Line Profiles For Rotating Accretion Discs

Smak (1981) presented a series of theoretical profiles of emission lines for close binary systems with high orbital inclination ($\geq 45°$). The discs in these profiles were assumed to be flat, Keplerian and axial symmetrical. The emissivity function $f(r)$ is a function of the radius of disc and is approximated to be $f(r) \sim r^{-\alpha}$, where $1 \leq \alpha \leq 2$.

The emission line profile is expressed as:

$$F(u) \sim \int_{r_{\rm in}}^{r_z} \frac{r^{3/2}\, f(r)\, \mathrm{d}r}{\left[1 - r(\frac{u}{\sin i})^2\right]^{1/2}}. \tag{1.6}$$

where u is a dimensionless radial velocity, $f(r)$ is the emissivity function, $r_{\rm in}$ is the inner radius of the disc, and $r_z = \min[1, (\frac{u}{\sin i})^{-2}]$ is the outer limit on the disc, i is the inclination angle, and $(\frac{u}{\sin i})^2 < r_{\rm in}^{-1}$ (Soria, 1999).

The Keplerian velocity is related to the radial position on the disc plane by see Equation 1.4. Hence by substituting $f(u) \sim r^{-\alpha}$ and $x = \frac{ur^{1/2}}{\sin i}$, Equation 1.6 becomes:

$$F(u) \sim \left(\frac{u}{\sin i}\right)^{2\alpha-5} \int_{x_{\rm in}}^{x_z} \frac{x^{4-2\alpha}\, \mathrm{d}x}{(1-x^2)^{1/2}} \tag{1.7}$$

where $x_{in} = \frac{u r_{in}^{1/2}}{\sin i}$ and $x_z = \min(\frac{u}{\sin i}, 1)$.

Equation 1.7 can be solved analytically for $\alpha = 1$, 1.5, 2, using solutions given in Gradshteyn & Ryzhik (1994). The solutions are given as Equation 1.8 and 1.9 for $\alpha = 1$, Equation 1.10 and 1.11for α =1.5, and Equation 1.12 and 1.13for α =2. Figure 1.11 is a plot of the solutions to Equation 1.7 for the different α values.

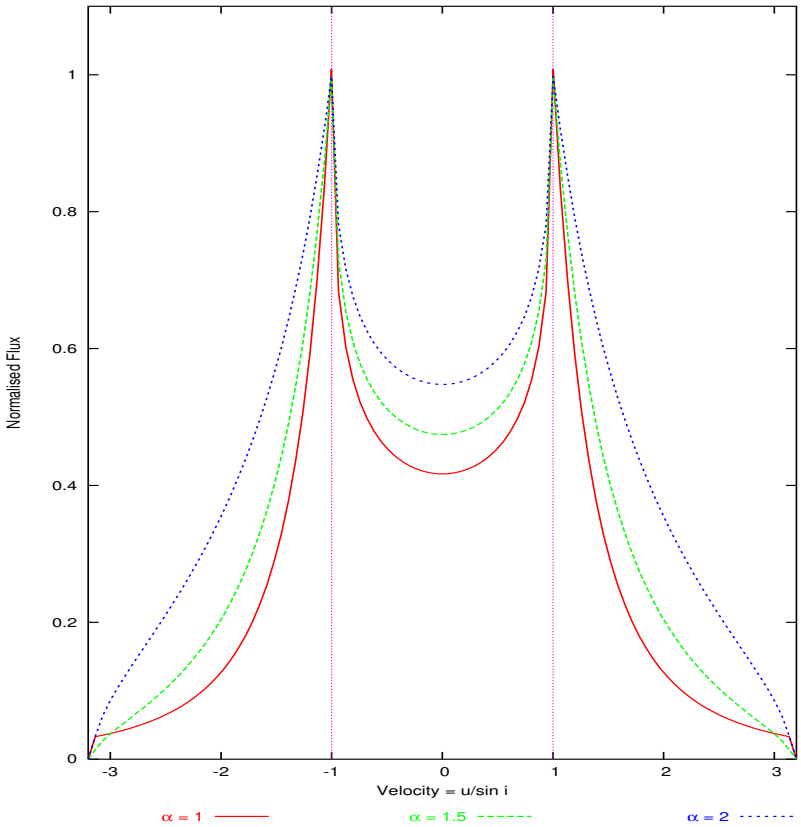

Figure 1.11: These are emission profiles for a flat, geometrically thin Keplerian disc, calculated for α= 1 (red line), 1.5 (green dashes) and 2 (blue short dashes) (using Equations 1.8 to 1.13) and for $r_{in} = 0.1$. The profiles are normalised to the same maximum flux. The vertical lines indicate the maximum lateral positions of the peaks, at velocity $(\frac{u}{\sin i}) = \pm 1$, for a constant disc dimension. The emissivity function defines the shape of the wings, $\alpha = 1$ produces a flatter wing shape than that defined by α =1.5 and 2. The flatter wings indicate a line emitting region that is further from the outer edge of the disc, than the steeper wing shapes. Reproduced from Soria (1999).

For $\alpha = 1$ and $0 \leq \frac{|u|}{\sin i} \leq 1$:

$$F(u)_{\alpha=1} \sim \left(\frac{u}{\sin i}\right)^{-3} \left\{ -\frac{1}{2}\frac{u}{\sin i}\left[1 - \left(\frac{u}{\sin i}\right)^2\right]^{1/2} + \frac{1}{2}\arcsin\left(\frac{u}{\sin i}\right) + \frac{1}{2}\frac{u}{\sin i}\, r_{\rm in}^{1/2}\left[1 - r_{\rm in}\left(\frac{u}{\sin i}\right)^2\right]^{1/2} - \frac{1}{2}\arcsin\left(\frac{u}{\sin i}\, r_{\rm in}^{1/2}\right)\right\} \quad (1.8)$$

For $\alpha = 1$ and $1 \leq \frac{|u|}{\sin i} \leq r_{\rm in}^{-1/2}$:

$$F(u)_{\alpha=1} \sim (\frac{u}{\sin i})^{-3} \left\{ \frac{\pi}{4} + \frac{1}{2}\frac{u}{\sin i}\, r_{\rm in}^{1/2}\left[1 - r_{\rm in}\left(\frac{u}{\sin i}\right)^2\right]^{1/2} - \frac{1}{2}\arcsin\left(\frac{u}{\sin i}\, r_{\rm in}^{1/2}\right)\right\} \quad (1.9)$$

For $\alpha = 1.5$ and $0 \leq \frac{|u|}{\sin i} \leq 1$:

$$F(u)_{\alpha=1.5} \sim \left(\frac{u}{\sin i}\right)^{-2} \left\{ -\left[1 - \left(\frac{u}{\sin i}\right)^2\right]^{1/2} + \left[1 - r_{\rm in}\left(\frac{u}{\sin i}\right)^2\right]^{1/2}\right\} \quad (1.10)$$

For $\alpha = 1.5$ and $1 \leq \frac{|u|}{\sin i} \leq r_{\rm in}^{-1/2}$:

$$F(u)_{\alpha=1.5} \sim \left(\frac{u}{\sin i}\right)^{-2} \left[1 - r_{\rm in}\left(\frac{u}{\sin i}\right)^2\right]^{1/2} \quad (1.11)$$

For $\alpha = 2$ and $0 \leq \frac{|u|}{\sin i} \leq 1$:

$$F(u)_{\alpha=2} \sim \left(\frac{u}{\sin i}\right)^{-1} \left\{\arcsin\left(\frac{u}{\sin i}\right) - \arcsin\left(\frac{u}{\sin i}\, r_{\rm in}^{1/2}\right)\right\} \quad (1.12)$$

For $\alpha = 2$ and $1 \leq \frac{|u|}{\sin i} \leq r_{\rm in}^{-1/2}$:

$$F(u)_{\alpha=2} \sim \left(\frac{u}{\sin i}\right)^{-1} \left\{\arcsin\left(\frac{u}{\sin i}\right) - \arcsin\left(\frac{u}{\sin i}\, r_{\rm in}^{1/2}\right)\right\} \quad (1.13)$$

1.6 Expected Variations in Line Profile

There were no optical spectroscopic data in A0620-00 during its outburst on 3 August 1975. Shortly after the outburst in August 1975, the optical spectrum was reported to be featureless, except for interstellar lines (Whelan *et al.*, 1977). However, the observations with the 5m Hale telescope on 30-31 August 1975 reported very weak Balmer and HeII emission (Searle *et al.*, 1975). Further observations in the following days strongly suggest that the Balmer lines are emission lines superimposed on absorption lines, but they consist of only the Hα emission line (Oke & Greenstein, 1977). The observations conducted by Whelan *et al.* (1977) with the 3.9m Anglo-Australian telescope in September 1975 to May 1976 reported an absence of the Hα emission line in the initial months of the observing period. Hα was later found to be present in the November 1975 and further observations conducted later. In spite of that, Hα was not always a distinctive double peaked line.

Unfortunately, the spectra of these observations are on photographic plate and are not archived for remote access, hence it is not possible to compare the Hα features shortly after the outburst, with those in its present quiescent state.

1.6.1 Peak-to-Peak Separation and Wings of the Double Peaked Line

For a double peaked emission line corrected to the black hole reference frame, the separation of the peaks indicates the velocity of the region where the line is emitted from. The theoretical separation of the peaks is calculated to be twice the projected velocity of the emitting region on the disc.

The lateral positions of the sharp peaks in Figure 1.11 are at the maximum possible values. The wider the separation, the higher the radial velocity of the line, hence the closer the emitting region is to the central object. The peak-to-peak separation in Figure 1.11 portrayed the line emitting region to be closer to the accreting source than the outer edge of the accretion disc. In these accretion disc models (excerpts from Smak (1981)), the inclination of the plane of the system, i (see Equations 1.8 to 1.13), plays a part in defining the sharpness of the peaks. As the inclination of the system is not expected to change over time, any change in the sharpness is attributed to the change in the physical condition

and mechanism of the emitting region on the disc.

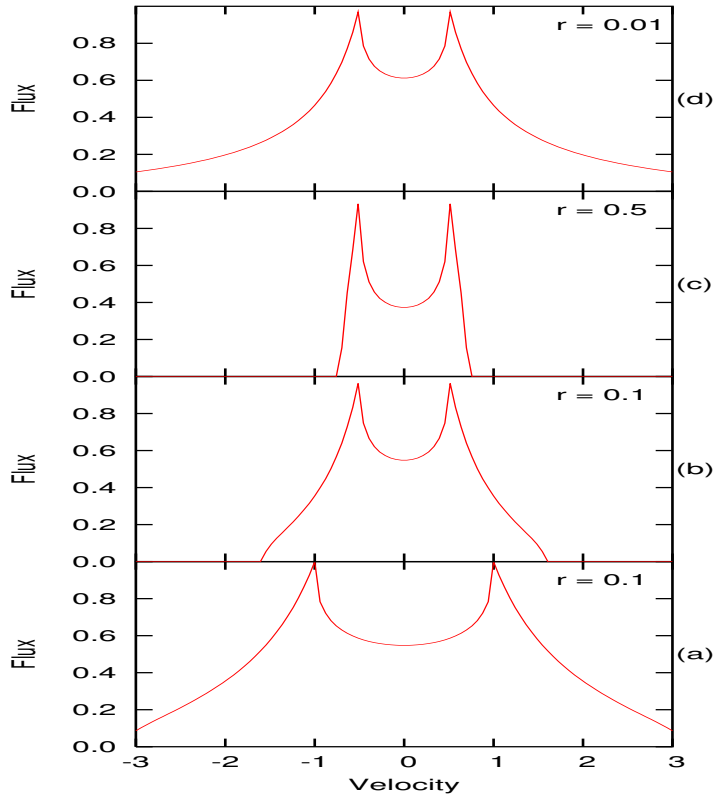

Figure 1.12: The figures above show a series of simulated emission line profile for line emission region of accretion disc of different dimensions. "r" is a ratio of radial position of line emission region on the disc to the radial position of the outer edge of the disc, with respect to the centre of the accretion disc. The profiles are normalised to the same maximum intensity. Figures 1.12a and 1.12b show how the profile changes with the change in the distance of emission region to the inner edge of the disc, for a constant size accretion disc. Figure 1.12c is a profile for an emission region which is closer to the outer edge of the disc. It is a cooler emission due to its lower velocity. In contrast, Figure 1.12d shows a line profile from an emission region closer on the disc to the central accreting object than the emission region in both Figures 1.12a and 1.12c.

Figure 1.12 shows the line profiles for different peak-to-peak separations for accretion discs, having different radial extents but possessing a similar emissivity function. The change in the velocity of the line emission region on an accretion disc is reflected in the emission line profile. Figures 1.12a and 1.12b show how the profile changes with the change in emission region for a constant size accretion

disc. For an emission region closer to the inner edge of the disc, the separation between peak will be wider, due to the higher velocity and accompanied by a flatter slope of the wings, compared to an emission region closer to the outer edge of the disc.

Figures 1.12c and 1.12d are simulated profiles of the emission line from emission regions of the same velocity and different disc dimensions. Figure 1.12c is a profile for an emission region which is closer to the outer edge of the disc. The slope of its wings are steeper than that of Figures 1.12a, 1.12b, and 1.12c, indicating the faster decline in velocity as it approaches the outer edge of the disc. It is a cooler emission due to its lower velocity. In contrast, Figure 1.12d shows a line profile from an emission region closer on the disc to the central accreting object than the emission region in both Figures 1.12a and 1.12c. The slope of its wings are flatter, as the radial extent from the emitting region to the outer edge of the disc is larger.

1.6.2 The Other Component(s) in the Spectrum

Haswell & Shafter (1990); Marsh *et al.* (1994) and Shahbaz *et al.* (2004) discovered a hotspot in the accretion disc of A0620-00, in their investigations. Since the spectrum of A0620-00 could include a hotspot component, the peak-to-peak separation will not be an accurate parameter of the distance of the emitting region from the central object on the accretion disc. A hotspot on the accretion disc is where the stellar material from the donor companion impacts the accretion disc. In cases of accreting binaries like A0620-00, a hotspot is not unexpected. The hotspot may show up as a smaller peak which moves between the double peaks as a function of the orbital phase, possibly smearing out the double peaks.

The possible presence of a hotspot can be confirmed by shifting the spectra to the black hole reference frame and grouping them according to their orbital phase. The hotspot component in the spectra is expected to be consistent in its position in the spectra, corresponding to its physical position on the accretion disc, with respect to the black hole candidate. For instance, at orbital phase 0.8, the hotspot is moving away from the observer, and it is therefore expected to be found in the red region of the double peaked line in the spectrum (see (b) and (c) of Figure 1.13). The motion of the hotspot component in the spectra is expected to be consistent over time for an unchanging accretion disc.

Figure 4.15 shows a series of simulated emission line profiles of a rotating accretion disc with a hotspot component at different orbital phases. All of the simulated profiles except (a), (b), (j) and (k), in Figure 4.15, appeared to be tripled peaked, with the peak in the middle being a component of the hotspot. The hotspot component is moving between the red and the blue peaks of the emission line. The profiles in (a) to (k) show the movement of the hotspot component from the red peak to the blue peak. The hotspot component shown in (k) will, after this stage, starts to move towards the red peak, as shown sequentially in (j), (i), (h) etc, to the stage shown in (a).

The other possible components that could affect the spectra could be the effects of the stellar wind from the accretion disc. These components manifest in the sudden gain or drop in the intensity of the Hα line. For example, if the Hα line passes through a wind propagating towards the observer, both peaks would be more intense than usual, but the blue peak would be more intense than the red peak. However, the peaks would be less intense for a wind travelling away from the observer. Strong winds from the accretion disc are not expected of A6020-00, therefore, the effects are not expected to manifest often.

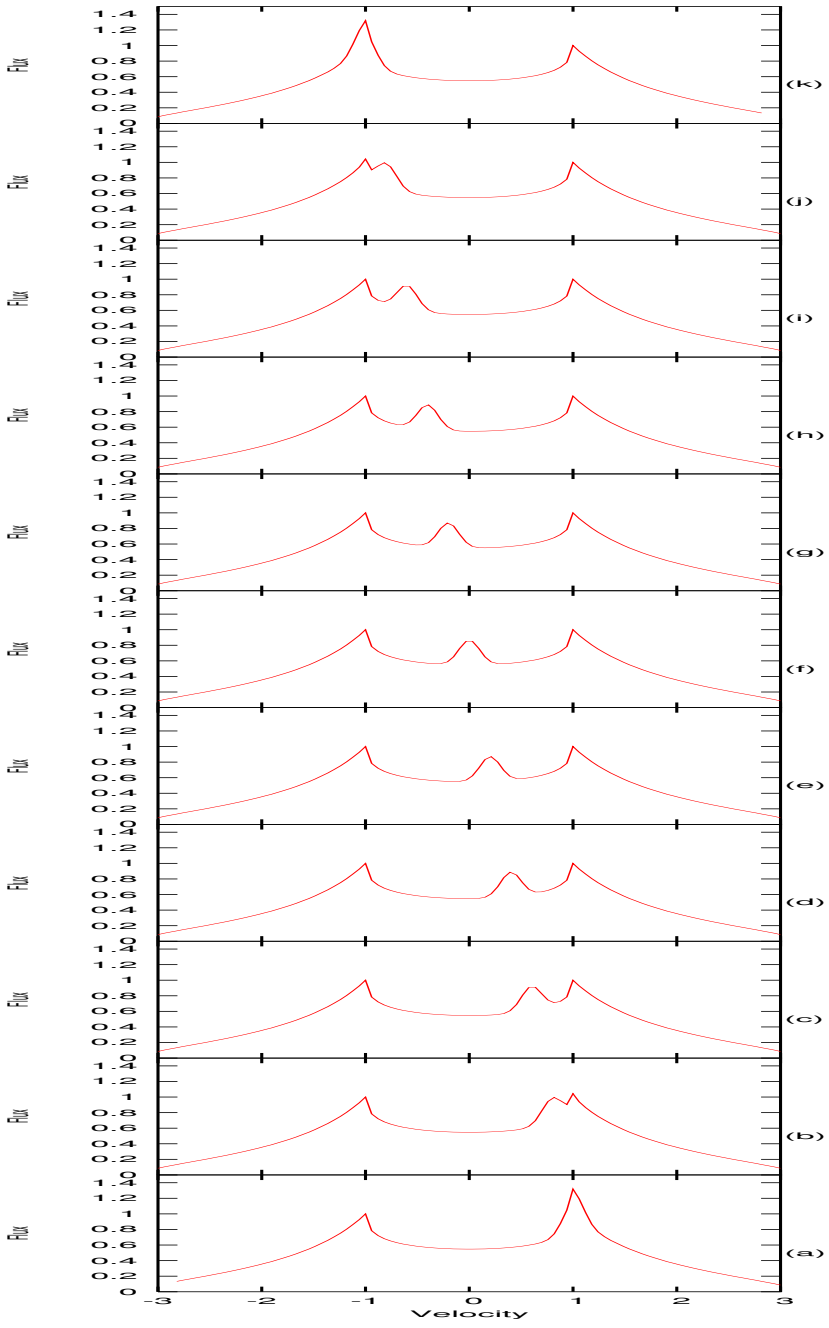

Figure 1.13: The figures above show a series of simulated emission line profile of a rotating accretion disc with a hotspot component at different orbital phases. All the figure, except the top and bottom two figures (a,b,j,k), are clearly tripled peaked, with the peak in middle being a component of the hotspot, which moving between the red and the blue peaks of the emission line. The line profiles in (a) to (k) show the movement of the hotspot component from the red peak to the blue peak. The hotspot component shown in (k) will, after this stage, starts to move towards the red peak, as in shown sequentially in (j), (i), (h) etc to the stage in (a).

Chapter 2

Observations

2.1 The Telescope

Figure 2.1: [1]Siding Spring Observatory

The observations used in this investigation were taken with the Dual Beam Spectrograph (DBS) on the 2.3m telescope at Siding Spring Observatory (SSO). The telescope is part of the Research School of Astronomy and Astrophysics at the Australian National University (ANU). It is also known as the Advanced Technology Telescope (ATT), hereafter ANU 2.3m. The SSO is located in the Warrumbungle Mountains in the central west region of New South Wales, Australia. SSO has several telescopes on the site. To name a few, the 3.9m Anglo-

Australian Telescope (AAT), the 2m Faulkes Telescope, the 1.24m UK Schmidt Telescope, and the 0.6m Uppsala Schmidt Telescope.

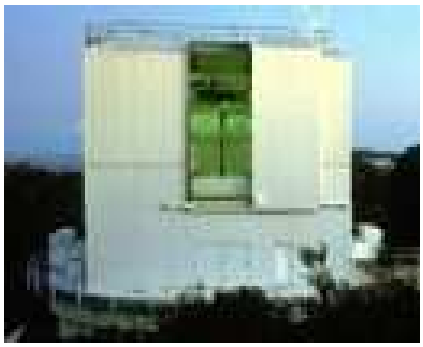

Figure 2.2: [1]The rotating building of the ANU 2.3m Telescope

The ANU 2.3m was built in the early 1980s and incorporates three radical features combined in a single instrument, namely a thin mirror, an altitude-azimuthal mount, and a rotating building.

2.1.1 [2]Technical Specifications of ANU 2.3m

Figure 2.3: [1]The 2.3m Advanced Technology Telescope

[1]Pictures of the telescope are excerpts from http://www.sidingspringexploratory.com.au/index.htm.
[2]Technical specifications of the telescope are summarised from http://www.mso.anu.edu.au/observing/2.3m/DBS/ and Rodgers *et al.* (1988).

The ANU telescope has a 2.3 m, f/2.05 primary mirror with a focal length of 4715 mm, an outside diameter of 2300 mm, a central hole diameter of 500 mm and a 3.973 m^2 collecting area. Its 0.3 m, f/18 secondary mirror, has a focal length of 18 m and a plate scale of 4.964 arcsec/mm. In conjunction with the primary mirror, it provides unvignetted fields of view of 80 mm in diameter or 6.62 arcmin at two Nasmyth foci and a Cassegrain focus. The DBS is permanently mounted at the Nasmyth A focus of the telescope.

The telescope has a spatial resolution of $5.02''$/mm and a f/ratio of 17.9. It operates in the visible band between 3200 - 9000 Å. Light is split by a dichroic at around 6000 Å, and fed into two similar spectrographs: one of them is equipped with a red optimised detector, the other a blue optimised detector.

There are five different dichroics available for the beam-splitter (see Figure 2.4). Each switches from transmission to reflection at around 6000 Å, though this may be varied over about 1000 Å, depending on the dichroic. The transition takes place between 400 Å and 1000 Å for the various dichroics. The plane mirror (D6 on the mounting cell) on the beam splitter is selected to use the blue arm alone. However, all the light will be sent to the red arm if the beam splitter is empty.

There are four gratings available for each arm, and the 600 grooves/mm gratings were used for both red and blue arms for the A0620-00 observations. Table 2.1 gives the details of the gratings used.

Table 2.1: The gratings used for observing A0620-00. All gratings give dispersions of approximately two pixels per resolution element.

Grating grooves/mm	Order	Blaze angle	Resolution (Å)	Resolution (km s^{-1})	Range (Å)
600B	1	6°54'	2.2	166	1900
600R	1	13°00'	2.2	92	1900

Note: 600B and 600 R refers to the grating used for the blue arm and red arm respectively.

A filter wheel located before the slit carries five neutral density filters of 48 mm diameter and a large clear aperture of 120 mm. The clear aperture allows unvignetted use of the full 80 mm field at the slit. The five neutral density filters are Melles Griot metal-on-glass filters which allow approximately 50%, 10%, 1%, 0.1% and 0.01% transmission at 5000 Å. The 48 mm filter diameter restricts the usable slit length to 26 mm or 2.2 arcmin.

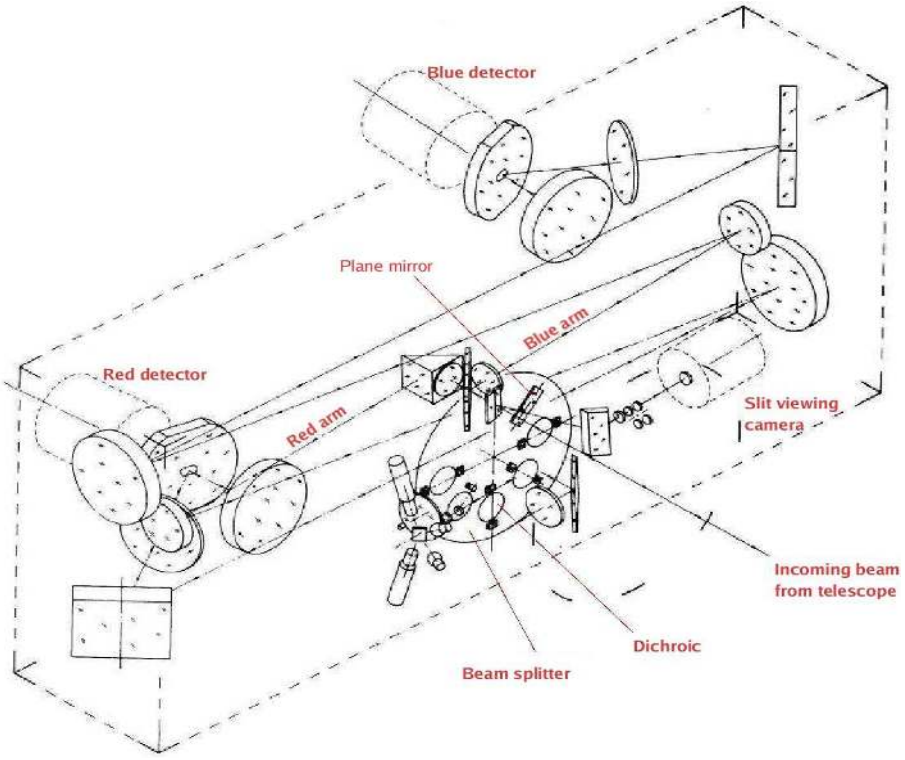

Figure 2.4: Isometric view of the components of the spectrograph. Excerpt from Rodgers *et al.* (1988)

The remotely controlled bi-parting slit opens to 4 mm (20 arcsec) with an accuracy of approximately 20 micron. The entire slit assembly is tilted by 10°, allowing a CCD camera to image the reflective slit jaws and the slit is used for offset guiding.

When a photon strikes the CCD surface, electrons are emitted and are collected in the pixels. The DBS CCDs are SITe 1752×532, 15μ pixel devices, which take about 70 seconds to be read, however, the CCDs are windowed (to provide a readout of 35 seconds or less) for a single object like A0620-00.

2.2 Observational Settings

A0620-00 was observed with the DBS on the 2.3m Advanced Technology Telescope by Helen Johnston and Kinwah Wu. The grating of 600 grooves mm^{-1} was used for both spectrographs, but only the spectra region from the red spectrograph were used in this investigation. The spectra were from the wavelength

interval 6250-6850 Å, centred on the Hα line ($\lambda\lambda$6563).

Table 2.2: Instrument settings of the observations of A0620-00

	Red arm
Gratings	600R
Centre wavelength	6563 Å
Grating angle	11° 50″
Dispersion	1.11 Å/pixel
Resolution	2.23 Å
Wavelength range	5560 - 7530 Å
Slit width	2.1 arcsec
Exposure time	1800 s

The observations obtained at the ANU 2.3m telescope span 5 years, and total 92 spectra. They were taken in January, February and December 2000, January 2003, and January 2004. The orbital phase of each spectrum was calculated by Helen Johnson using the ephemeris determined by McClintock & Remillard (1986) (orbital period, $P = \sim 0.323$ days, and a spectroscopic T_0 = HJD 2,446,082.7481 $\pm$ $0^d.0008$). The uncertainty in the orbital phase implied by extrapolating the orbital ephemeris to the 2000 epoch of observation was determined to be of the order 0.22. This uncertainty increases to 0.26 for the 2003 epoch, and further to 0.28 for the 2004 epoch.

A summary of the observations is listed in Table 2.2, the full details of the spectra and the brief notes on the observing conditions are listed in Appendix A and Appendix B, respectively.

The 2000 and 2003 observations cover one complete orbital period, while the 2004 observations cover orbital phase 0.5 to phase 1. Spectrum of a observation taken on a JD +1000.00 is hereafter referred to by "spectrum JD +1000.00" or "JD +1000.00". Table 2.4 shows the statistics of the number of spectra per year and the orbital phase.

Some of these spectra were taken on nights when there were clouds or when the weather condition were non photometric, resulting in lower signal-to-noise (SNR). The observations from 2000 December 24 (JD +1902.98 to JD +1903.23) and 26 (JD +1904.95 to JD +1905.24) were taken under poor weather conditions. Despite these factors, the slit size was maintained throughout the observations, to maintain a consistent spectral resolution.

Table 2.3: Summary of observations of A0620-00

Date	**No. of spectra**	**Epoch (JD 2450000+)**	**Range of Orbital Phase**	**Wavelength Range (Å)**	**Å per bin**
00Jan29	6	1572.95-1573.06	0.519-0.861	6250-6854.5	1.1092
00Jan30	5	1573.96-1574.06	0.648-0.972	6250-6853.6	1.1074
00Jan31	5	1574.96-1575.05	0.740-0.017	6250-6852.9	1.1062
00Feb01	7	1575.93-1576.06	0.738-0.154	6250-6853.0	1.1064
00Dec24	8	1902.97-1903.23	0.219-0.007	6250-6854.6	1.1093
00Dec26	11	1904.95-1905.24	0.346-0.240	6250-6854.6	1.1093
03Jan10	10	2650.00-2650.20	0.888-0.514	6250-6852.4	1.1054
03Jan11	9	2650.98-2651.21	0.919-0.640	6250-6852.4	1.1054
03Jan12	9	2651.94-2652.15	0.910-0.562	6250-6852.4	1.1054
03Jan13	11	2652.97-2653.19	0.081-0.775	6250-6852.4	1.1054
04Jan28	5	3032.04-3032.13	0.637-0.924	6250-6851.8	1.1042
04Jan29	6	3032.98-3033.11	0.544-0.937	6250-6852.0	1.1046

The Julian Date format – JD 2451000.00 is hereafter JD +1000.00

Table 2.4: Statistics of observations in different years and orbital phase

Orbital Phase	**Year 2000**	**Year 2003**	**Year 2004**	**Total**
0.0-0.1	5	5	0	10
0.1-0.2	3	6	0	9
0.2-0.3	3	6	0	9
0.3-0.4	2	3	0	5
0.4-0.5	2	4	0	6
0.5-0.6	2	5	1	8
0.6-0.7	4	3	2	9
0.7-0.8	6	1	4	11
0.8-0.9	9	1	2	12
0.9-1.0	6	5	2	13
Total number of Spectra	42	39	11	**92**

Chapter 3

Data Analysis

3.1 Standard Data Reduction

The initial data reduction of all the observations was done by Helen Johnston, and is briefly described below. A detailed description of the data reduction procedures can be found in Massey (1997).

1. In each CCD frame, there exist a bias level i.e. the intrinsic noise offset of several hundred counts. The bias level is individually determined for each frame and then subtracted from the image.

2. Next, the pixel-to-pixel sensitivity variations of the chip are corrected by dividing every image by a "flat-field". The flat field is an image of uniform illumination, which in this case is due to a white-light lamp. However, the emission from the lamp is not spectrally uniform, so the flat-field was normalised by a low-order polynomial to remove the colour of the lamp.

3. Then, the effects of cosmic rays, which show up as very bright pixels or pixel clumps, are removed by comparing the adjacent pixels of the same object.

The resultant two-dimensional images are then subjected to wavelength and flux calibrations. These calibrations are crucial to extract the spectra of the intended object. Steps involved in the calibration are briefly described in the following, and are described in detail in Massey *et al.* (1992).

1. To remove the effects of sky lines, the spectrum in each image is located and "sky" regions on either side are defined. The "object" pixels at each location along the detector are summed and the sky background subtracted from them. The resultant spectrum with flux (in counts) is now a function of position along the CCD.

2. The wavelength scale is calibrated by comparing each spectrum with arc lamps spectra with known discrete lines;

3. This scale is then applied to the extracted object spectra, so they are now in counts as a function of wavelength;

The flux of the spectrum is measured in counts, and should be converted to Jansky (Jy) or erg cm^{-2} $s^{-1}Hz^{-1}$ or flux (erg cm^{-2} s^{-1}). Hence further flux calibration is necessary, so the features introduced by the atmosphere can be removed from the calibrated spectrum.

Absolute flux calibration should be done by comparing with the spectrum of a "flux standard" star. The spectrum of this star is known to be featureless at the long wavelength (red) end, where the prominent atmospheric features are. The flux of the standard spectrum is known at every wavelength, thus at any wavelength, it is possible to convert the number of counts to flux for the target.

However, some of the A0620-00 spectra were taken on nights when there were clouds or when the weather conditions were not conducive for a clear observation. Furthermore, if the seeing was poor during certain observations, the target A0620-00 would have appeared fainter than it really was. Despite the non photometric observing conditions, the slit was not widened. Therefore, taking these effects into account, only the shape of each of the spectrum was calibrated, and the values of the calibrated flux were not absolute.

3.2 The Reduced Data

After the initial optical data reduction was performed, the data were then dereddened by $E(B-V) = 0.39$ (Wu *et al.*, 1976). Each A0620-00 spectrum covers a wavelength interval from 6250 Å to $\sim$ 6855 Å.

The orbital period was divided into ten orbital phase bins, and the orbital phase of each spectrum was calculated by Helen Johnston, using the photometric

ephemeris defined in McClintock & Remillard (1986). The photometric ephemeris is the Heliocentric Julian Date (HJD) at the orbital phase zero (the inferior conjunction of the companion star), T_0 (photometric) = HJD 2,445,477.827 $\pm$ $0^d.005$ (see Table 1.1). The spectra were then grouped by their respective orbital phases to produce Figures C.1 to C.10 in Appendix C. Each spectrum is allocated to bins of size 0.1 of an orbital phase period. For example, Figure C.8 (included here as Figure 3.1) shows a group of spectra in the orbital phases 0.7 to 0.8.

The spectrum of the template star, BS753, was added to each figure for comparison of the absorption lines. The template spectrum was scaled down by a constant to match the flux of the A0620-00 spectra. The A0620-00 spectra and the template spectrum were evenly-spaced in flux and plotted in the centre-of-mass (CM) reference frame. Each mark on the vertical axis of the plots denotes the 1 flux unit mark for each spectrum. Each A0620-00 spectrum is identified by the Julian Date (JD) of its observation. The spectra are plotted chronologically for each orbital phase bin. The JD reference of each spectrum e.g. JD 2453033.04, is abbreviated to the form JD +3033.04

The spectra in Figures C.1 to C.10 are plotted in ascending JD (earliest JD at the bottom) at the same vertical interval, hence the differences in the continuum flux level are clearly displayed. This is especially obvious in Figures C.3, C.8, C.9 and C.10. The intensity and shape of the Hα emission line are also perceived to vary. The differences are most evident in Figures C.7, C.8 (Figure 3.1), C.9 and C.10. For instance, in Figure 3.1, the Hα line of the spectrum JD +3033.04 (2004 January 29) has a stronger and more defined double peaked profile, compared to that observed in spectrum JD +1903.16 (2000 December 26).

To illustrate that these effects are phase independent, two sets of two spectra of the same orbital phase are examined. The spectra JD +1575.05 (2000 January 31) and JD +1576.02 (2000 February 01) are at the same 0.017 orbital phase, while the spectra JD +1576.04 (2000 February 01) and JD +2652.97 (2003 January 13) are at the same 0.081 orbital phase (taken from Figure C.1). Figure 3.2 shows that both spectra JD +2652.97 and JD +1576.04 have a similar double peaked Hα profile, whose red peak is stronger. In contrast, spectrum JD +1576.02 has a strong and clear triple peaked Hα profile, and spectrum JD +1575.05 has a weaker and double peaked Hα profile.

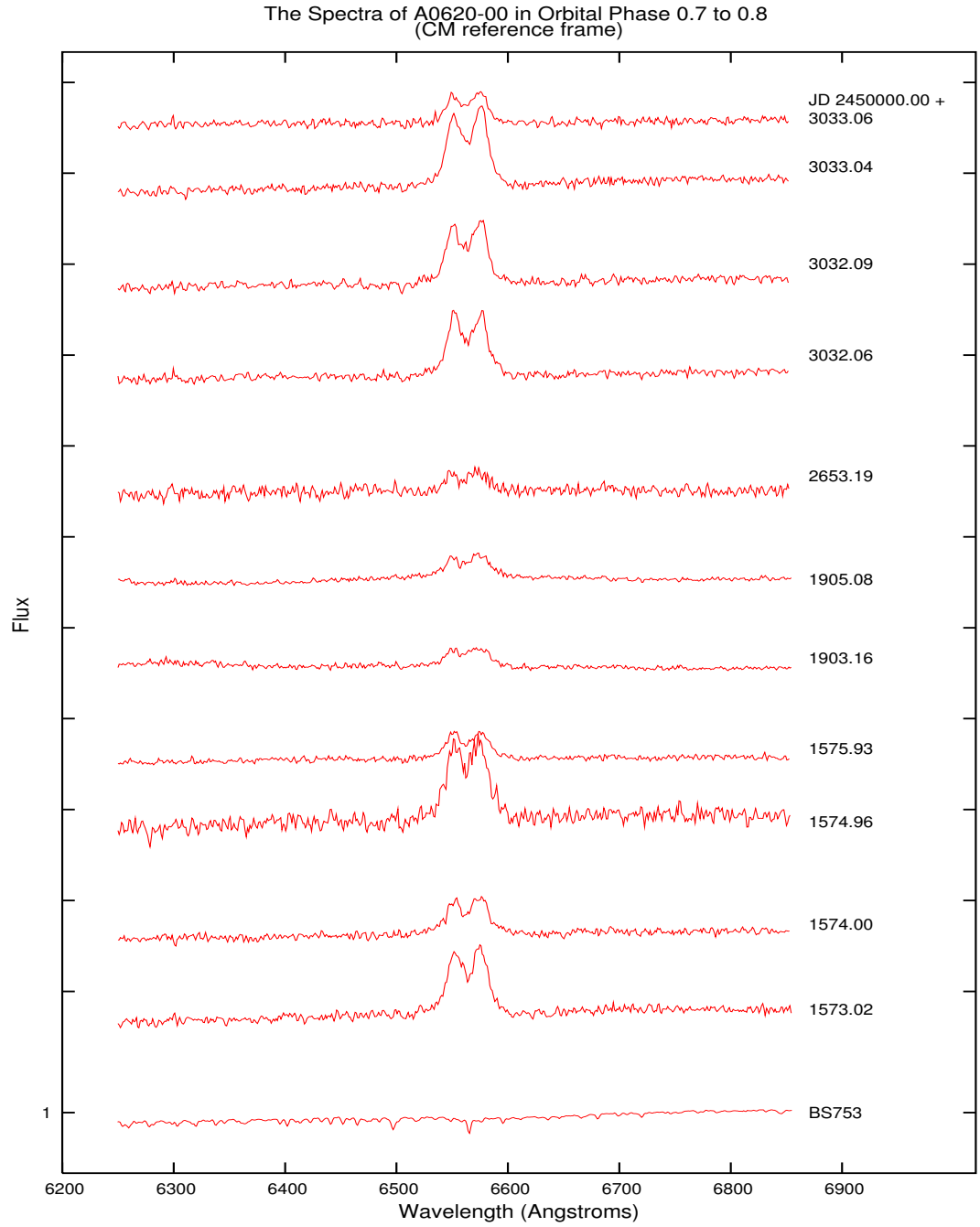

Figure 3.1: The original A0620-00 spectra in the orbital phase bin 0.7-0.8, in the centre-of-mass reference frame. The profile of the Hα of JD +3033.04 is a strong and well-defined double peaked emission line, compared to that of JD +1903.16, which is weaker and less well-defined profile.

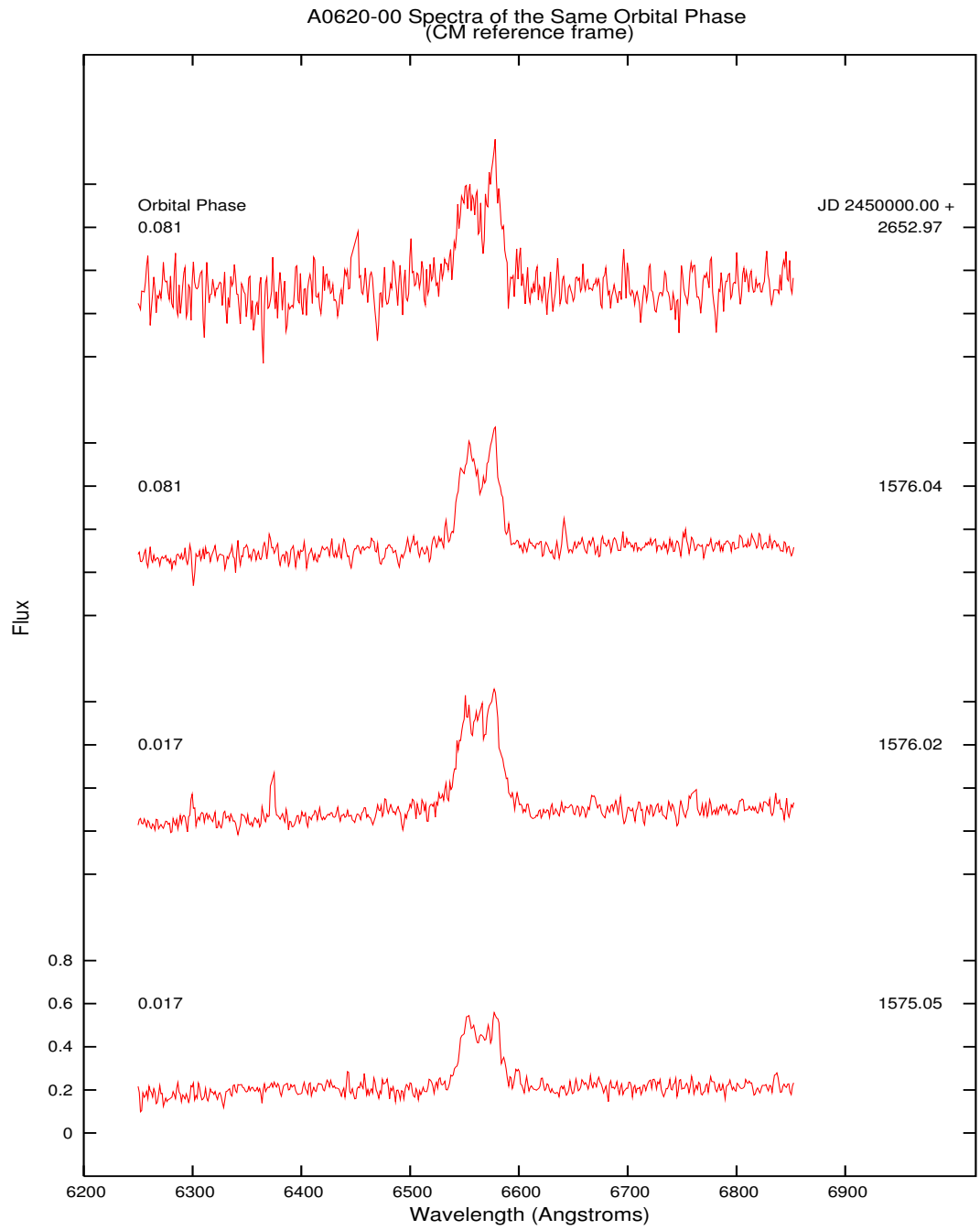

Figure 3.2: These are two sets of A0620-00 spectra in the same orbital phases, in CM reference frame. These spectra were selected from the orbital phase bin 0.9-1.0. The spectra taken on JD +1575.05 and JD +1576.02 are at the same 0.017 orbital phase, while spectra taken on JD +1576.04 and JD +2652.97 are at 0.081. The spectra JD +2652.97 and JD +1576.04 have a similar double peaked Hα, whose red peak is stronger. The Hα line profile seems to be strong, and triple peaked in spectrum JD +1576.02, and appears to be weaker and double peaked in spectrum JD +1575.05.

3.3 Normalisation of Data

Some of the spectra were taken under non photometric conditions, so the flux in each spectrum is not absolute, hence it is difficult to compare spectra from different observation nights. In order to make a comparison of all the spectra, the flux level of the spectra needs to be normalised. The normalisation factor for each whole spectrum is a constant, derived from the average of the flux taken from the same selected regions of the continuum of each spectrum. The continuum regions are selected such that the Hα line, which is taken to be between 6520 Å and 6620 Å, is excluded. The spectra are normalised with this method to preserve the shape of the spectrum, as each spectrum is a combination of emission from both the accretion disk and companion star.

There are two steps in the normalisation procedure. First the average flux for each spectrum at both the short (blue) wavelength end (wavelength $<$ 6520 Å) and the long (red) wavelength end (wavelength $>$ 6620 Å) are determined, to get an overall mean of the continuum flux for each spectrum. Each spectrum is then normalised to its respective mean flux.

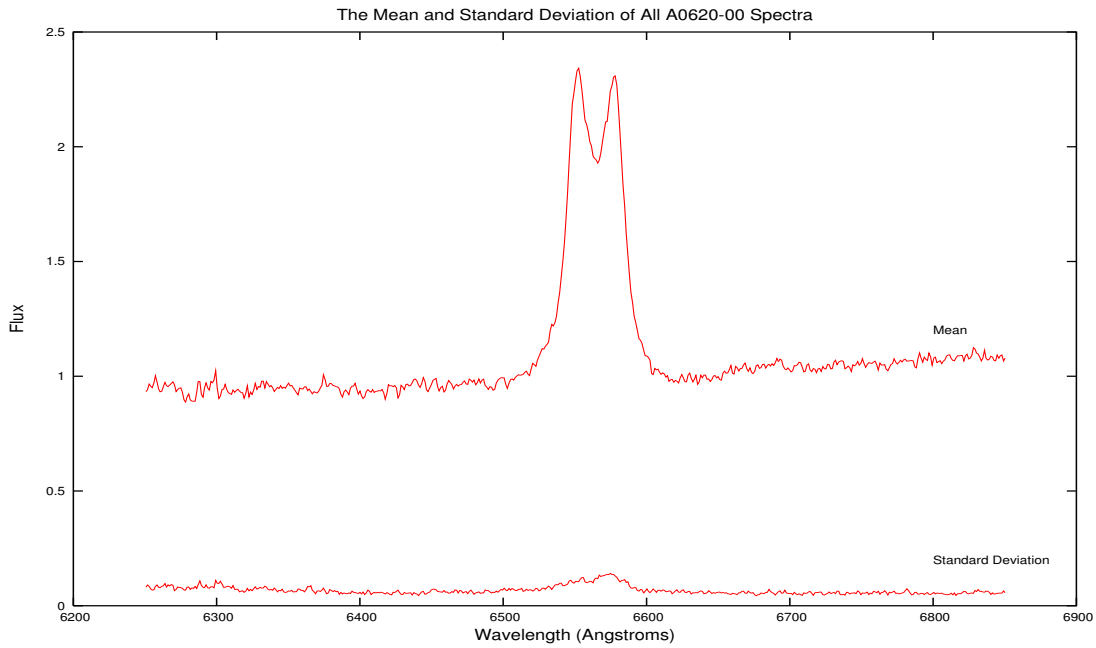

Figure 3.3: The mean normalised spectrum and its associated standard deviation.

The mean of these mean-normalised spectra is derived to calculate the associated standard deviation in order to find the least varying region of all of the

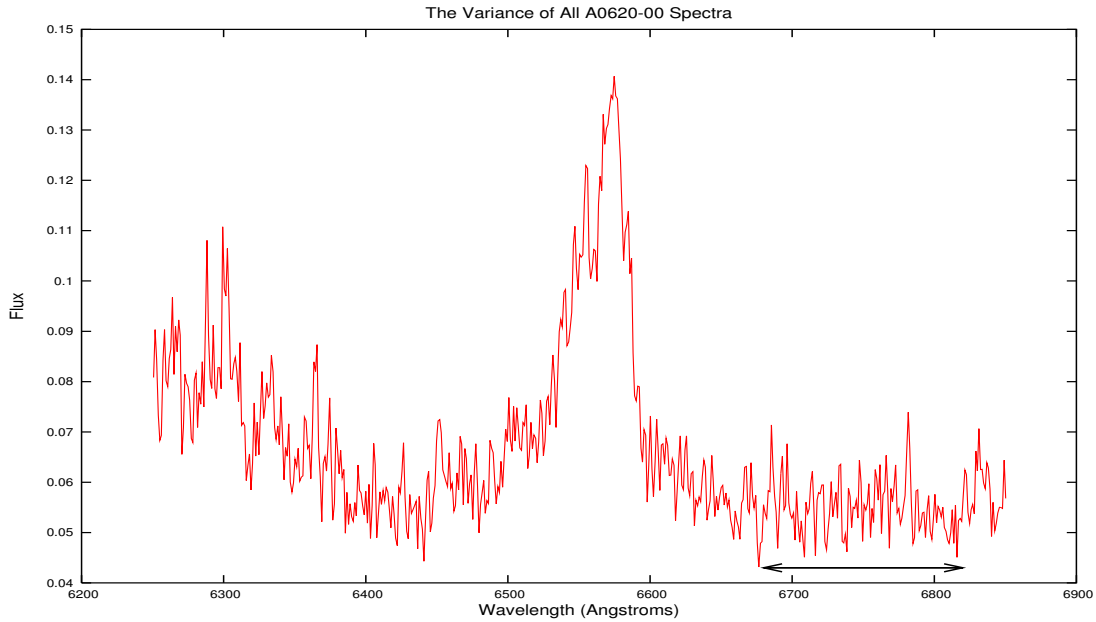

Figure 3.4: The associated standard deviation of the mean normalised spectrum in Figure 3.3 shown on a larger scale. The region defined by the arrow indicates the least varying region of the spectrum. The mean flux of this region is the constant used for normalisation.

spectra. Figure 3.3 shows a plot of the mean and the associated standard deviation of all of the spectra. Assessment of the standard deviation revealed the flattest region to be between $\sim$ 6680 and 6820 Å (shown in Figure 3.4). It is possible that the contribution from the companion is constant at this range. Finally, each original unnormalised spectrum is normalised by its respective average flux between 6680 and 6820 Å. Figure 3.5 shows the effects of normalisation for spectra of the same orbital phases in Figure 3.2.

The spectra in Figure 3.5 are plotted on the same scale, and are evenly spaced. Each set of vertical tic marks is represented by the same vertical scale as the bottom spectrum. These are the normalised spectra of observations taken on JD +1575.05 and JD +1576.02. They now have comparatively the same intensity for the Hα line.

As with the unnormalised spectra, the spectra JD +2652.97 and JD +1576.04 have a similar double peaked Hα profile, whose red peak is more intense. The JD +1576.02 observation shows a strong and distinct triple peaked Hα profile. The JD +1575.05 spectrum has double peaked Hα profile with other smaller spectral components between the two distinctive peaks.

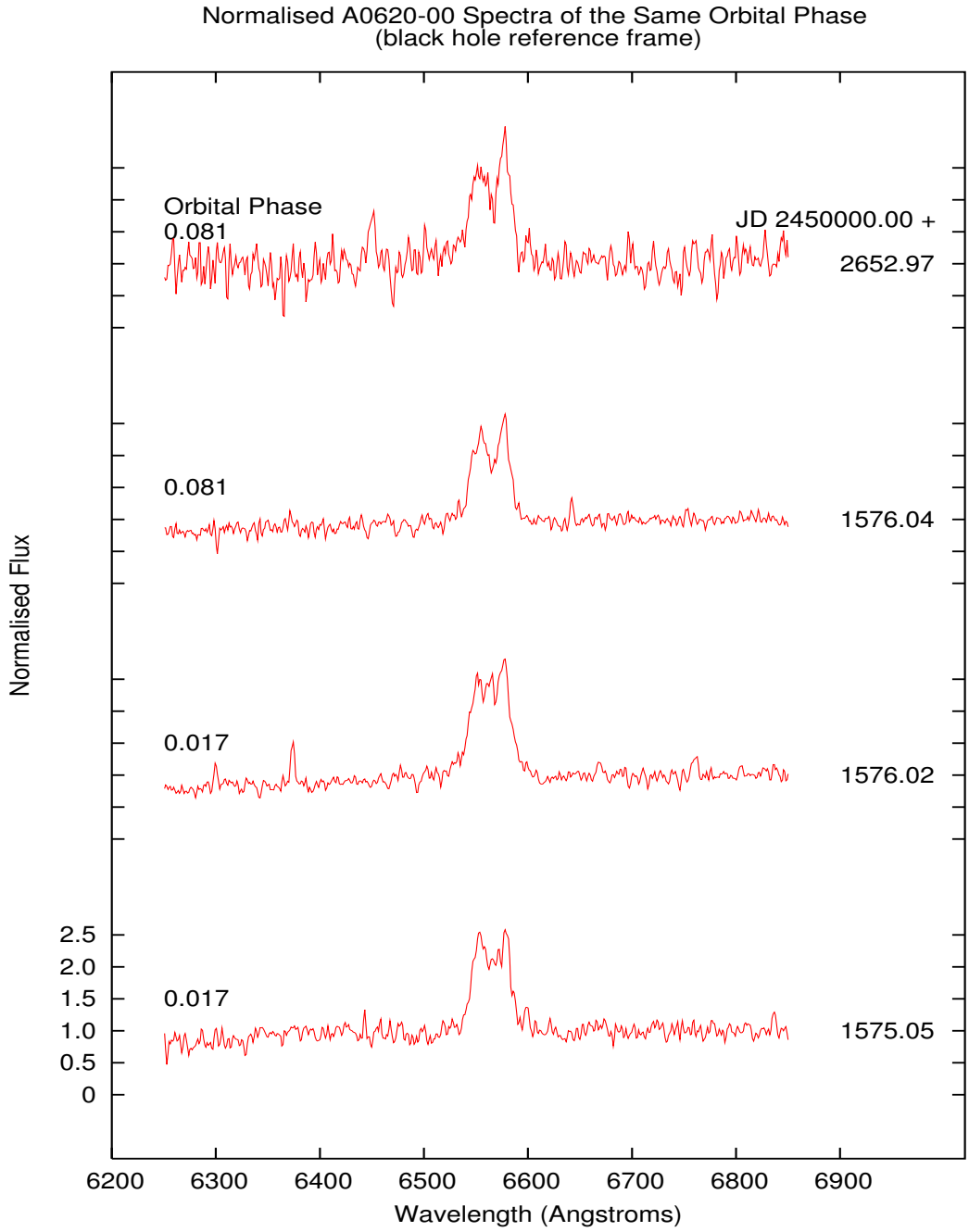

Figure 3.5: The normalised spectra counterparts of the spectra shown Figure 3.2, in the black hole reference frame. Each spectrum is plotted with an error bar on the right. The spectra JD +2652.97 and JD +1576.04, both of orbital phase 0.081, have a similar double peaked Hα, whose red peak is stronger. The JD +1576.02 observation (of orbital phase 0.017) shows a strong and distinct triple peaked Hα. The JD +1575.05 spectrum (of orbital phase 0.017) has double peaked Hα, with other smaller spectral components between the two distinctive peaks.

3.3.1 The Radial Velocity Curve

The mean of all normalised spectra of A0620-00 is shown in Figure 3.6. The distinctive double peaked emission line is generally interpreted as the result of the radial velocity of the accretion disc surrounding the black hole.

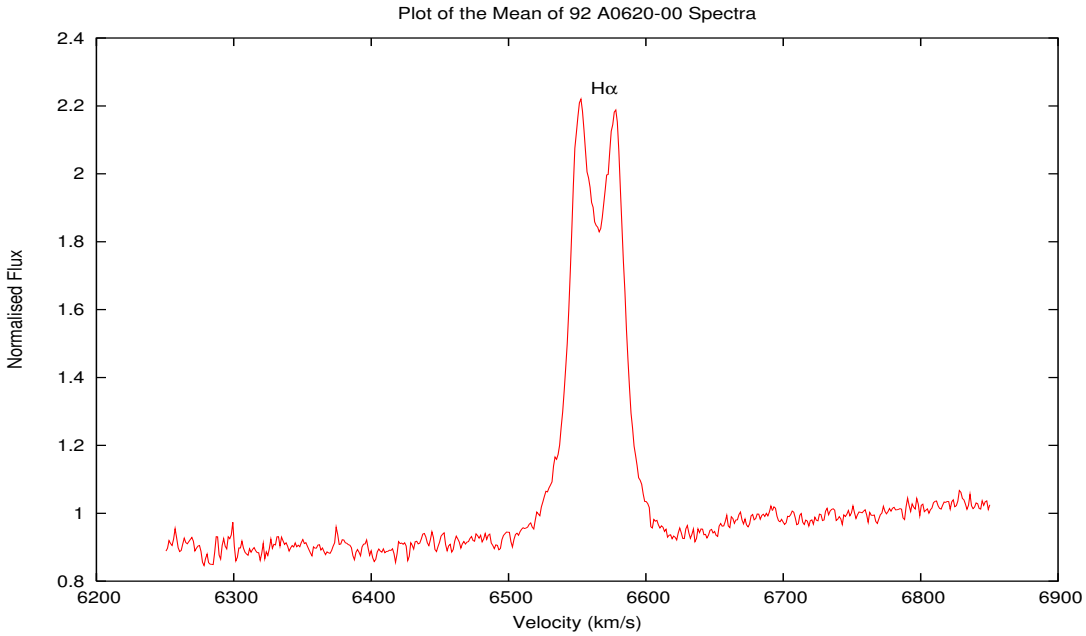

Figure 3.6: The mean spectrum of 92 normalised A0620-00 spectra (black hole reference frame). The double peaked Gaussian is the most prominent feature of the A0620-00 spectra.

In many of the spectra, the companion star's FeI ($\lambda\lambda$6496.5) absorption line is identified (see Figure 3.7). This indicates contamination of the spectrum by the companion K dwarf of A0620-00. The spectrum of BS753 (also known as HD 16160) is a K3V star, and is used as a template star for the companion object in this investigation. The comparison of the A0620-00 spectra with the template star is used to determine the radial velocity of the companion. The spectra of A0620-00 are individually cross-correlated with the BS753 spectrum. The effect of the template star's own radial velocity, $V_{BS753} = 23.4$ km s^{-1} (Wilson, 1953), is removed prior to the cross correlation.

The XCSAO application in the NOAO package in IRAF was used to determine the radial velocity of the companion star. The application matches the deepest absorption line of the template spectrum to that of the A0620-00 spectra to obtain

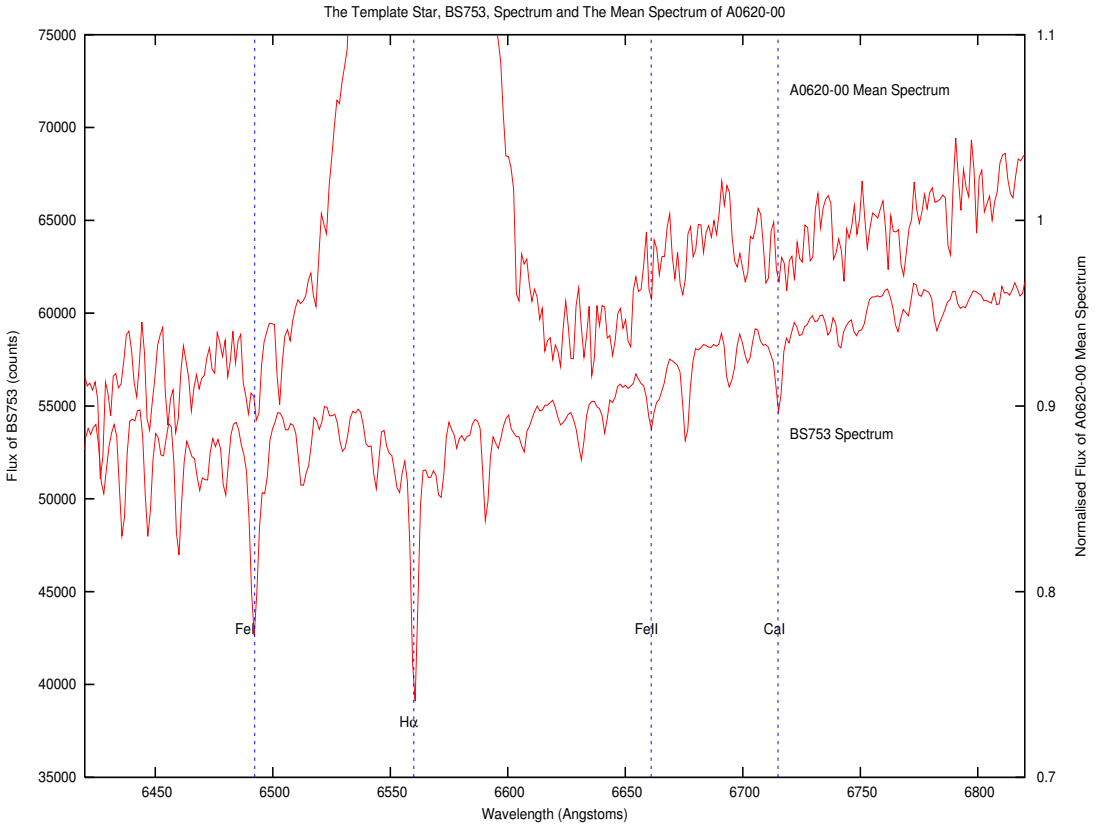

Figure 3.7: The BS753 spectrum has a similar resolution as the A0620-00 spectra. The labelled lines are prominent absorption lines of the template star: FeI($\lambda\lambda$6496.5), Hα($\lambda\lambda$6563), Fe II($\lambda\lambda$6666.45) and CaI($\lambda\lambda$6717.68). The top spectrum is the mean spectrum of the A0620-00 spectra, and the lower spectrum is the spectrum of the template star BS753.

the corresponding Doppler shift. The wavelength range of the cross correlation does not include the region (6520 - 6620 Å) of the double peaked Hα. The radial velocities obtained are in the reference frame of the centre of mass of the binary system.

The cross correlation was performed over the wavelength range of 6250.0 - 6855 Å, ignoring the 6520 - 6620 Å region. To constrain the correlation, the maximum and minimum limits of velocities were set at $\pm$520 km s^{-1}. The $\pm$520 km s^{-1} constraint stems from literature that found the radial velocity to be in the vicinity of $\sim$ 400 - 500 km s^{-1}. A similar range is also found for the majority of data points that form an outline of a sine function. The values of the parameters used in the application are shown in Table 3.1.

Table 3.1: Parameter settings for XCSAO

Lines to eliminate from spectrum	badline.dat 6520-6620 (Å)
Initial velocity source	zero
Initial velocity guess (km/sec) or z	0
Minimum allowable velocity (km/sec)	-520
Maximum allowable velocity (km/sec)	520
Absorption line rejection (in sigma of fit)	100
Emission line rejection (in sigma of fit)	100
Range of wavelength	
Starting wavelength	6250 Å
Ending wavelength	6855 Å

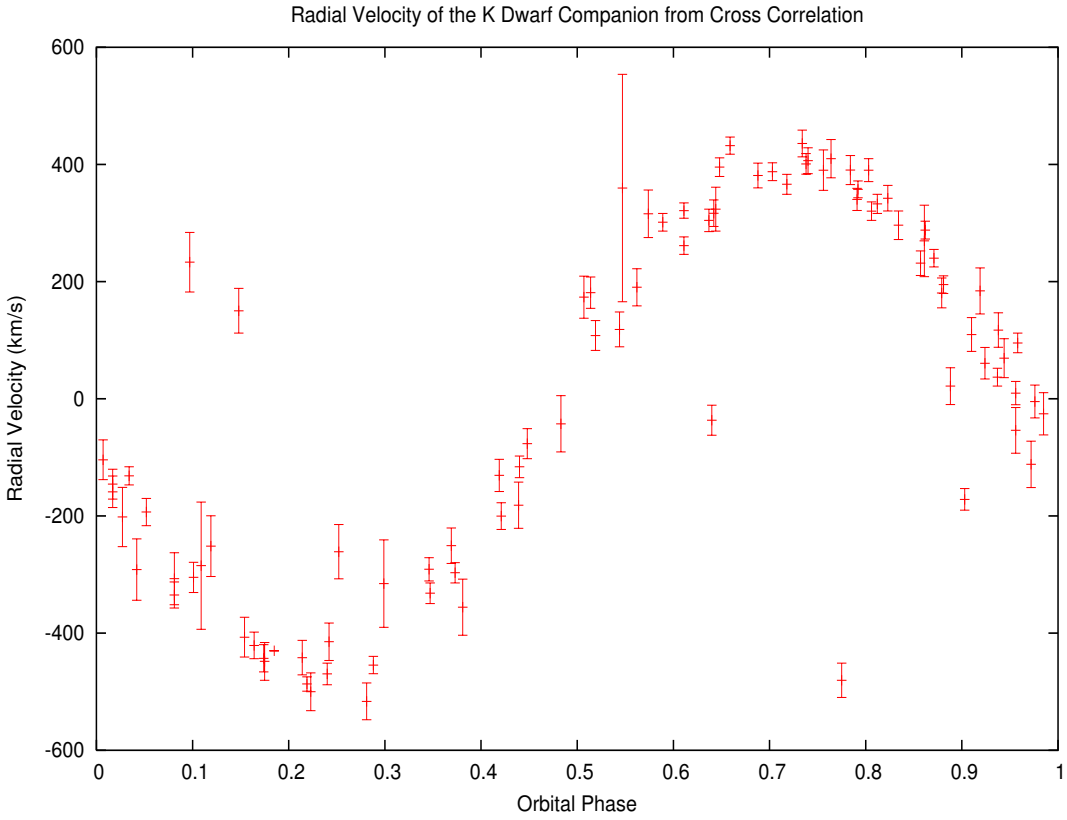

Figure 3.8: Each point is the radial velocity of the companion star at a phase determined from the cross correlation. Most of these velocity values form an outline of a sine function.

The radial velocities derived cover a range of velocities for different orbital phases. Figure 3.8 shows all the radial velocities obtained from the correlation as a function of the orbital phase. Almost all of the velocity points form an outline of a sine function, with the exception of a few points.

Consequently, 5 out of the 92 spectra were not used in the fit routine as these points do not lie within 1σ ($\pm$ 250 km s^{-1}) of the majority of the points in the same and adjacent orbital phase bins. The remaining velocities points were then fitted by a sine function, which defines the relationship between the orbital phase and the radial velocities (see Figure 3.9). The fit is constrained by fitting the most number of points that lie within $\pm$ 250 km s^{-1} of the sine function. Figure 3.9 shows the selected velocity points with errors, and the sine function used to to fit them (Equation 3.1).

Figure 3.10 is a comparison of the fit function obtained in this investigation to that (see Equation 3.3) obtained by Marsh *et al.* (1994). Equations 3.1 and

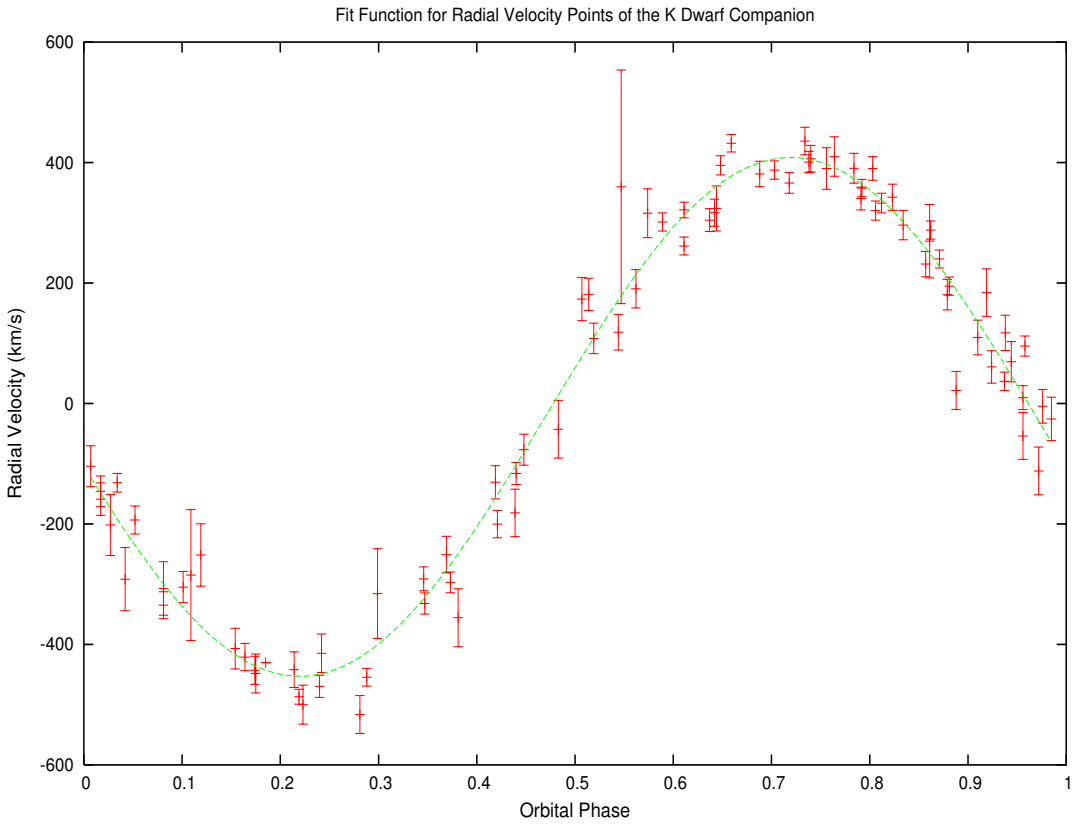

Figure 3.9: The fits of the radial velocities points of the companion star, using Equation 3.1.

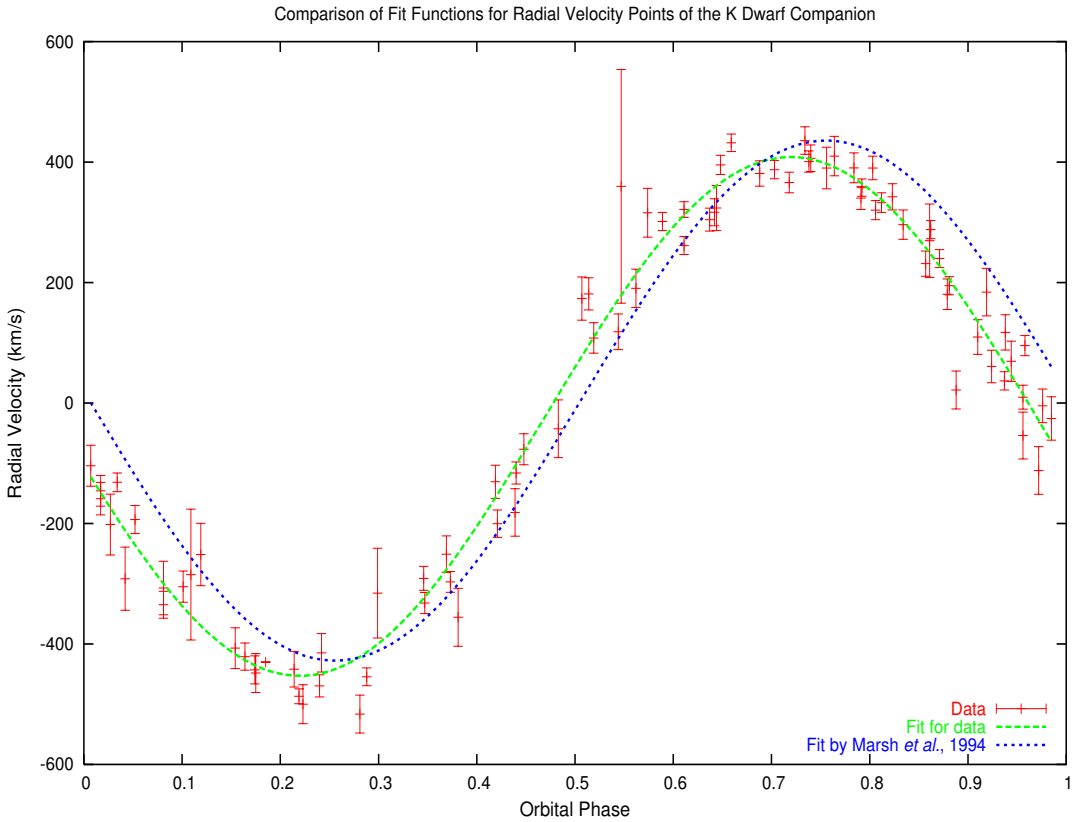

Figure 3.10: Comparison of the fit function obtained (green dashes) to that of Marsh *et al.* (1994) (blue short dashes). The velocity curve calculated by Marsh *et al.* (1994) has been phase corrected for consistency with McClintock & Remillard (1986), by shifting the function by half an orbital phase.

3.3 express the radial velocity as a function of the orbital phase, ϕ:

$$\begin{aligned} V_2 &= -((22 \pm 6) + (431 \pm 8) \sin 2\pi \\ &\quad [\phi + (30 \pm 3) \times 10^{-3}]) \end{aligned} \tag{3.1}$$

where V_2 is the radial velocity of the companion star in this thesis, and ϕ is the orbital phase.

$$\begin{aligned} V_{2(marsh)} &= (4 \pm 2) \\ &\quad +(433 \pm 3) \sin 2\pi[\phi - (6 \pm 1) \times 10^{-3}] \end{aligned} \tag{3.2}$$

$$V_{2(m)} = (4 \pm 2) - (433 \pm 3) \sin 2\pi[\phi - (6 \pm 1) \times 10^{-3}] \quad (3.3)$$

where $V_{2(marsh)}$ is the radial velocity of the companion star in Marsh *et al.* (1994), $V_{2(m)}$ is the orbital phase corrected radial velocity of the companion star, and ϕ is the phase shift factor.

The difference in the sign of the equation is attributed to the different definition of the orbital phase zero. Marsh *et al.* (1994) had defined the orbital phase zero at the superior conjunction of the companion star. In this thesis, definition of the orbital phase zero follows the suit of McClintock & Remillard (1986), at the inferior conjunction. To rectify the expected phase lag of 180° or half of an orbital phase shown by Marsh *et al.* (1994), Equation 3.3 is the orbital phase corrected Equation 3.2.

The sine function fit of this analysis (hereafter sine-fit) yielded a companion radial velocity semi-amplitude, $K_2 = 431 \pm 8$ km s^{-1}, which is consistent with $K_{2(Marsh)} = 433 \pm 3$ km s^{-1} determined by Marsh *et al.* (1994). Marsh *et al.* (1994) derived a mass ratio of A0620-00, q, from their calculated mass function. Recalling the definition of a mass function, the mass ratio was rewritten using the semi-amplitudes of the radial velocities (Equation 3.5):

$$q = \frac{m_2}{m_1} \quad (3.4)$$

$$= \sqrt[3]{\frac{f(m_2)}{f(m_1)}}$$

$$= \frac{K_1}{K_2} \quad (3.5)$$

where m_1 and m_2 are the masses, $f(m_1)$ and $f(m_2)$ are the mass functions, and K_1, K_2 are the semi-amplitudes of the velocity fit of the compact and companion object, respectively.

The semi-amplitude of the radial velocity of the black hole in this analysis was estimated using Equation 3.6 and the mass ratio derived in Marsh *et al.* (1994), $q = 0.07 \pm 0.01$. Thus, obtained $K_1 = 29 \pm 4$ km s^{-1} , which is similar to

$K_{1(Marsh)} = 29 \pm 4$ km s^{-1} (Marsh *et al.*, 1994).

$$V_1 = -qV_2 \tag{3.6}$$

Analogously, the radial velocity function of the black hole can be derived by applying by Equation 3.6. The negative sign of V_1 is due to the black hole moving in the opposite direction of the companion star.

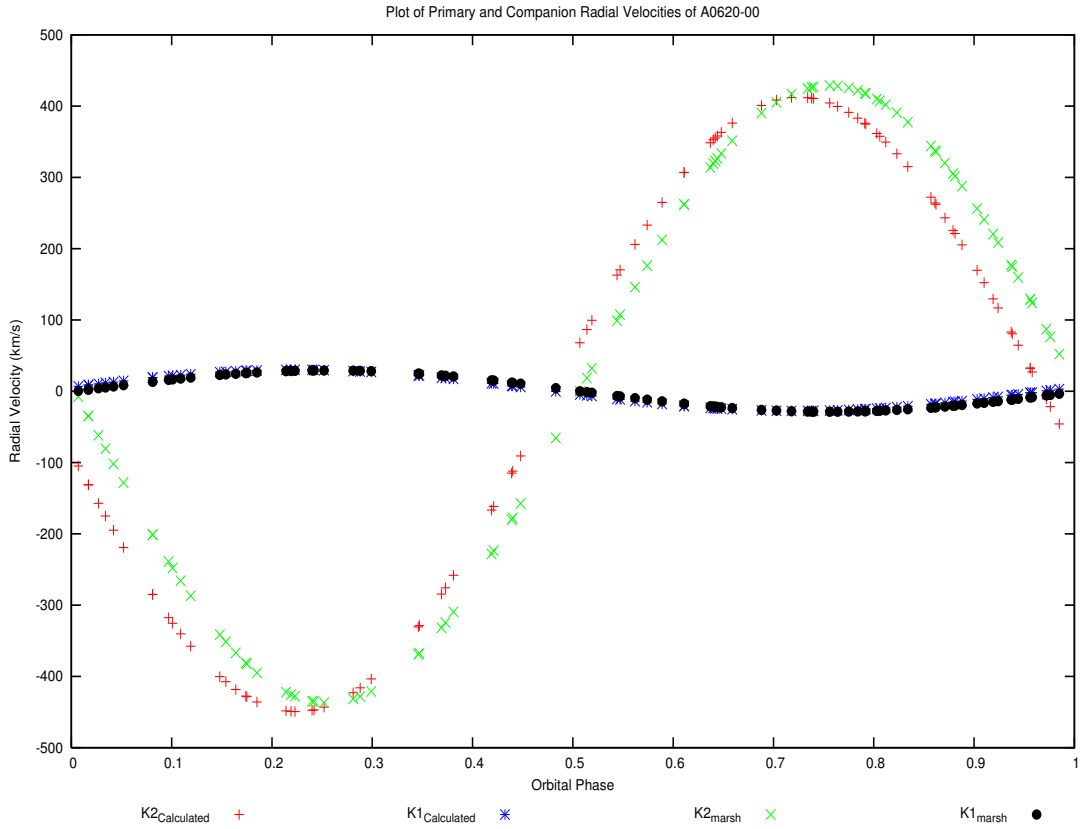

Figure 3.11: Comparison of the radial velocity fit function of the primary object and the companion object. The velocities are in the black hole reference frame. $K_{1(Measured)}$ and $K_{2(Measured)}$ are denoted by '$*$' (blue) and '$+$' (red) respectively. Subsequently, $K_{1(Marsh)}$ and $K_{2(Marsh)}$ are represented by '$\times$' (green) and '$\bullet$' (brown)

Figure 3.11 shows both the radial velocity functions of the compact object and companion object obtained by the different sine function fits. The fit by Marsh *et al.* (1994) appears to lag sine-fit by ~ 0.025 of an orbital cycle. This

is much smaller to the uncertainty asserted by Marsh *et al.* (1994), which was of the order 0.22-0.28, determined in Chapter 2. This could be a result of Marsh *et al.* (1994) overestimating the uncertainty of their measurement.

3.3.2 The Black Hole Reference Frame

Each spectrum of A0620-00 covers the wavelength range from 6250 Å to roughly 6855 Å, and was taken in the centre-of-mass reference frame, therefore it is necessary to correct for the orbital motion. The black hole was chosen as the frame of reference because the Hα line originates from the accretion disc surrounding it.

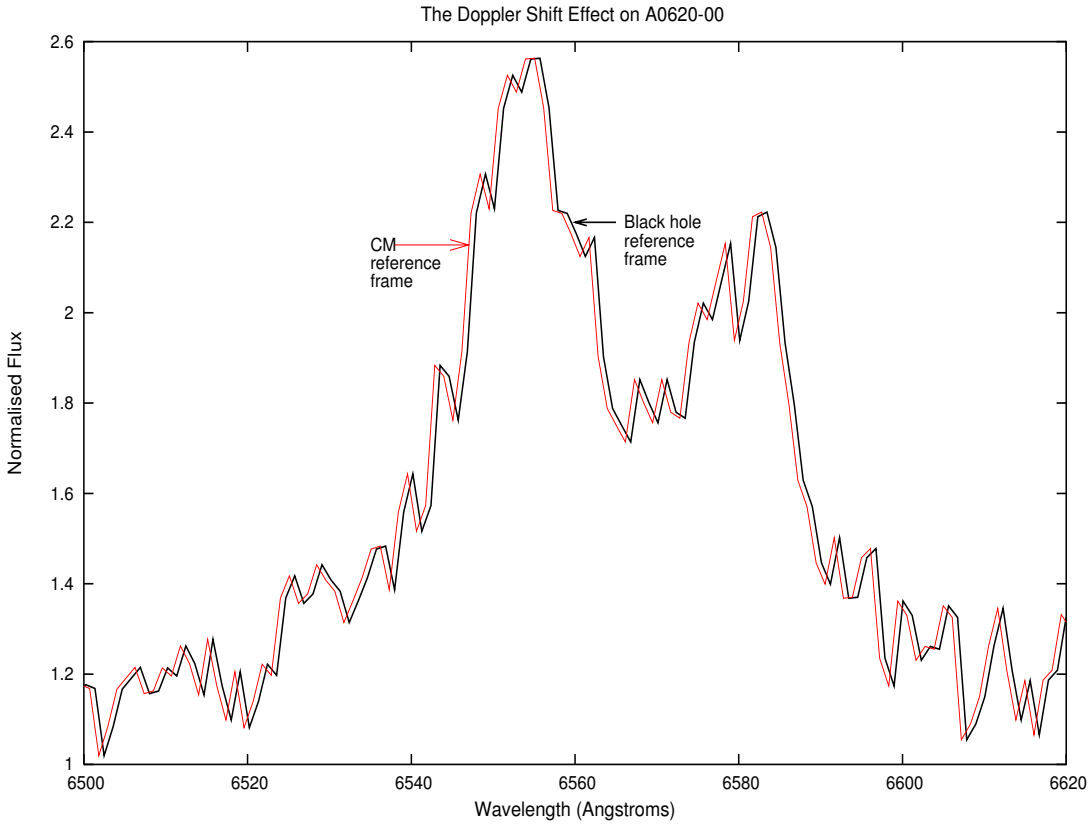

Figure 3.12: The Doppler shift effect on A0620-00 between the centre-of-mass and the black hole reference frames. This is a spectrum of the observation taken on JD +1902.97 (2000 December 24), in the 0.219 orbital phase. Its Doppler shift effect is estimated to be the strongest of all the observations.

The radial velocity of each spectrum is estimated from the radial velocity fit function of the black hole (V_1) at each orbital phase. The Doppler shift is then

calculated from the velocities for each spectrum (see Equation 1.1). Finally, the spectra were wavelength shifted to the reference frame of the black hole. The Doppler shift effect is found to be negligible. The maximum shift obtained from the effect of the radial velocity of the black hole is $\sim \pm 0.66$ Å. Figure 3.12 depicts the comparison of a A0620-00 spectrum in the observer frame and in the black hole reference frame. This spectrum is chosen for it shows the most significant Doppler shift effect in all of the observations.

3.4 The Normalised Spectra in the Black Hole Reference Frame

The spectra presented and applied in this analysis are hereafter normalised spectra in the black hole reference frame, unless stated otherwise.

All the spectra in Figure 3.13 to 3.22 are vertically evenly-spaced, and arranged in ascending JD for each orbital phase bin. The spectrum of the companion star is represented at the bottom of each figure, by the template spectrum, BS753. The template spectrum is Doppler shifted to include the companion star's orbital motion observed from the black hole.

The tic marks on the vertical axis indicate the normalised flux unit one for each spectrum. In each figure, the mean of the spectra for that orbital phase (hereafter referred to as orbital mean) and the respective template spectrum of the companion object are plotted below all the spectra. The depth of the absorption lines in the template spectra are not scaled to match the intensity of absorption lines in the A0620-00 spectra.

The spectra in Figures 3.13 to 3.22 are in their respective orbital phase bin. As expected, the normalised spectra have a more consistent continuum level. It can be seen from the spectra JD +1905.06 (2000 December 26) and JD +2653.15 (2003 January 13) in Figure 3.19, JD +1903.16 and JD +1905.08 (2000 December 26) in Figure 3.20, that the Hα emission line profile is more intense compared to the original unnormalised spectra (as shown in Figures C.7 and 3.1 respectively).

Some spectra do not have an obvious double peaked Hα line profile, such as the spectra JD +1903.20 and JD +1903.23 (2000 December 24), JD +2652.09 (2003 January 12), and JD +2653.05 (2003 January 13) in Figures 3.13 and 3.16.

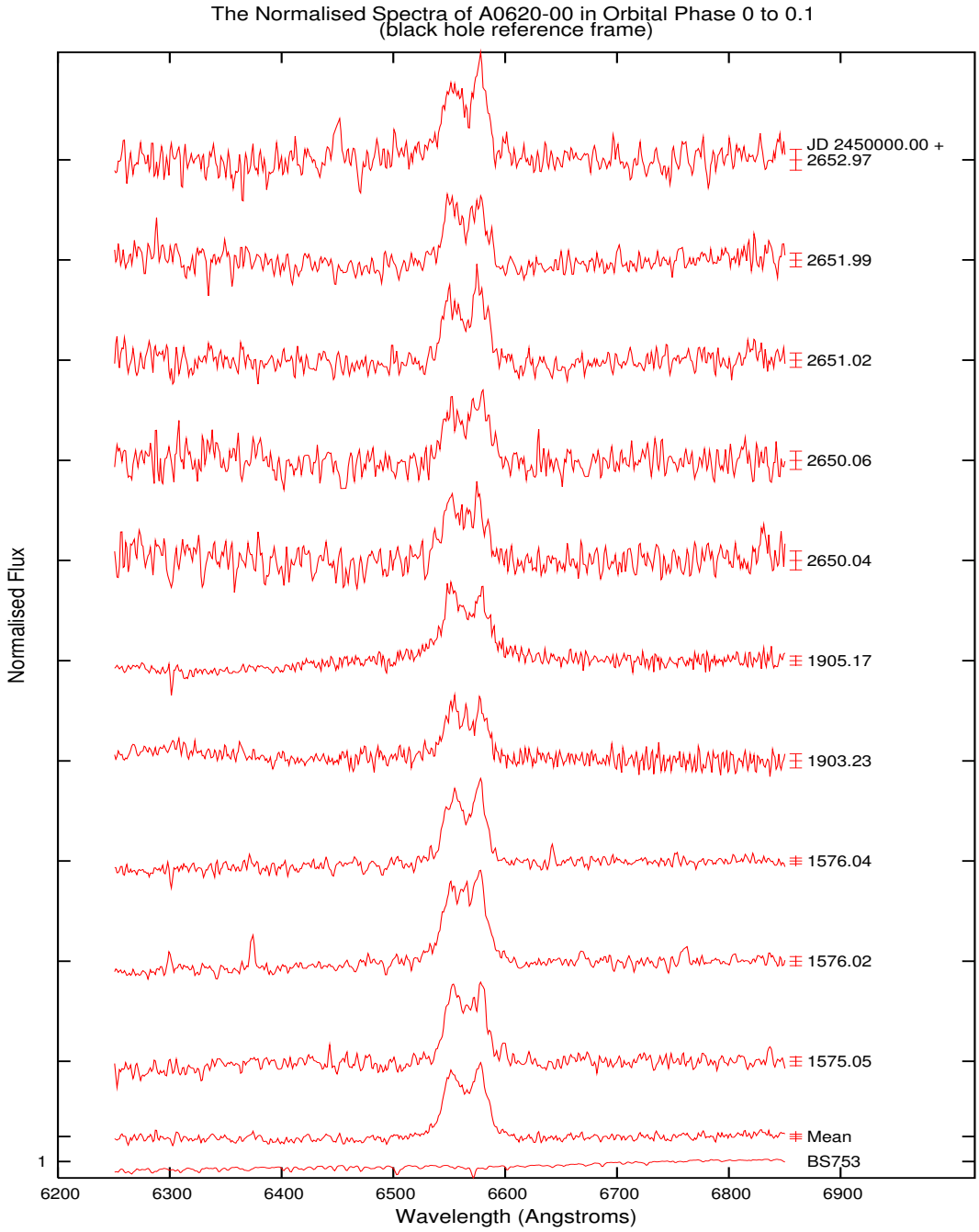

Figure 3.13: The normalised A0620-00 spectra in the orbital phase bin 0.0-0.1, in the black hole reference frame. Each spectrum is plotted with an error bar on the right. The double peaked emission line is sharp and very well defined for the orbital mean spectrum in the bin. The Hα profile of JD +1576.04, JD +2651.02, JD +1905.17, JD +2650.06, JD +2651.02, JD +2651.99 and JD +2652.97 are double peaked. The spectrum JD +2650.06 shows almost symmetrical double peaks, while in the spectra JD +2651.99 and JD +1905.17, the blue peak is higher and narrower. However, the spectra JD +1576.04, JD +2651.02 and JD +2652.97 reflect a stronger and narrower red peak. The region between the peaks in both spectra JD +1575.05 and JD +2650.04 is obscured by possibly noise or other spectral components.

It is also noted that the shape of both the Hα emission line and its wings varies within the same orbital phase bin. This is most evident in orbital phase bin 0.5-0.6 (Figure 3.18). The Hα profile started as a double peaked in 2000 (JD + 1572.00) became a "flat topped" dominated profile in 2003 (JD +2650.20), and returned to a double peaked profile in 2004 (JD +3032.98).

It is also apparent that in Figures 3.13-3.19 the width of the Hα line seemed to be wider in the late 2000 (JD +1903 to JD +1905) spectra. In addition, the wings of the latter's Hα line appeared to extend at a slower rate to the continuum than those found in early 2000 (JD +1572.95 to JD +1576.06). The variation in the Hα line widths from the spectra indicates that the line may have originated from a different region on the accretion disc for different spectra.

In the orbital phase bin 0.0-0.1, shown in Figure 3.13, the double peaked Hα emission line of the orbital mean is very well defined. The features of the spectra are described as follows and summarised in Table 3.2.

Table 3.2: Orbital phase bin 0.0-0.1.

JD +	**Double Peaked**			**Remarks**	**Blue Peak (Å)**	**Red Peak (Å)**	**Peaks Sepn (Å)**
	Symm	**Blue**	**Red**				
1575.05			√	possible 3rd peak	8.80	13.50	22.30±0.88
1576.02			√	3 peaks	8.60	12.00	20.60±1.11
1576.04			√		9.10	13.50	22.60±0.96
1903.23		√		3 peaks	9.20	15.10	24.30±0.86
1905.17		√			9.90	14.80	24.70±0.98
2650.04			√	possible 3rd peak	11.90	12.70	24.60±2.49
2650.06			√		12.00	13.30	25.30±3.08
2651.02			√		11.80	13.40	25.20±4.65
2651.99		√			11.00	12.70	23.70±9.61
2652.97			√		9.30	14.20	23.50±2.58
mean_0			√		10.20	13.50	23.70±1.13

Symm denotes Symmetrical Peaks
Peak Sepn refers to Peak separation
A tick in the Symm, Blue or Red column indicate if the peaks are symmetric or if one peak is more intense in the bluer or redder region
mean_0 denotes orbital mean spectrum of bin 0.0 to 0.1

It appears that the red peak of the orbital mean spectrum is more intense and

narrower than the blue peak. This characteristic is also reflected in the spectra of observations taken on JD +1576.04, JD +2651.02 and JD +2651.99.

Though spectra JD +1575.05, +1576.02, JD +1903.23 and JD +2650.04 are double peaked as well, there are apparent noise or other spectral components between the peaks. The spectra JD +1576.02 and JD +1903.23 appeared to be triple peaked due to the third central peak. These peaks are almost equally high and narrow.

Table 3.2 also lists the wavelength position of each peak, determined by fitting a Gaussian function to each peak. The peak position is expressed as a displacement from the rest wavelength of Hα, $\lambda_{H\alpha}\sim$ 6563 Å. The peak-to-peak separation (hereafter referred to as peak separation) is calculated for each spectrum with unambiguous blue and red peaks in the Hα line profile. For spectra with three peaks, the peak separation is measured between the Gaussian centred on the shortest wavelength and the Gaussian centred on the longest wavelength.

The red peak of the spectra in this orbital bin 0.0-0.1 is more displaced than the blue peak from the rest wavelength. The peak separation of the orbital mean spectrum is 23.7 Å. Spectrum JD +1576.02 has the smallest peak separation at 20.6 Å, and spectrum JD +2650.06 has the largest at 25.3 Å.

There are 9 spectra in the orbital phase bin 0.1-0.2 (see Figure 3.14). The double peaked profile of the orbital mean spectrum appears to be symmetrical. However, the spectra JD +2650.09, JD +2651.04 and JD +2652.03 have a stronger and narrower blue peak than red peak. In contrast, the stronger and narrower red peak is prevalent in spectra JD +1905.20, JD +1905.22 and JD +2651.04. Though the double peaks in spectra JD +1576.06 and JD +2652.01 appear to be quite symmetrical, JD +2652.01 has a smaller but noticeable "spike" between the blue and red peaks. Since the spectra JD +2652.99 does not have an obvious double peak feature, no measurements were made for the position of the peak. It is found that the red peak is generally more displaced from $\lambda_{H\alpha}$.

Table 3.3 summarises the profile description and lists the position of the peaks and their separation. It is found that the spectrum JD +1905.20 has the largest peak separation at 26.9 Å and the spectrum JD +1576.06 has the smallest separation at 21.3 Å. The peak separation of the orbital mean spectrum of the 0.1-0.2 bin is measured at 24.6 Å.

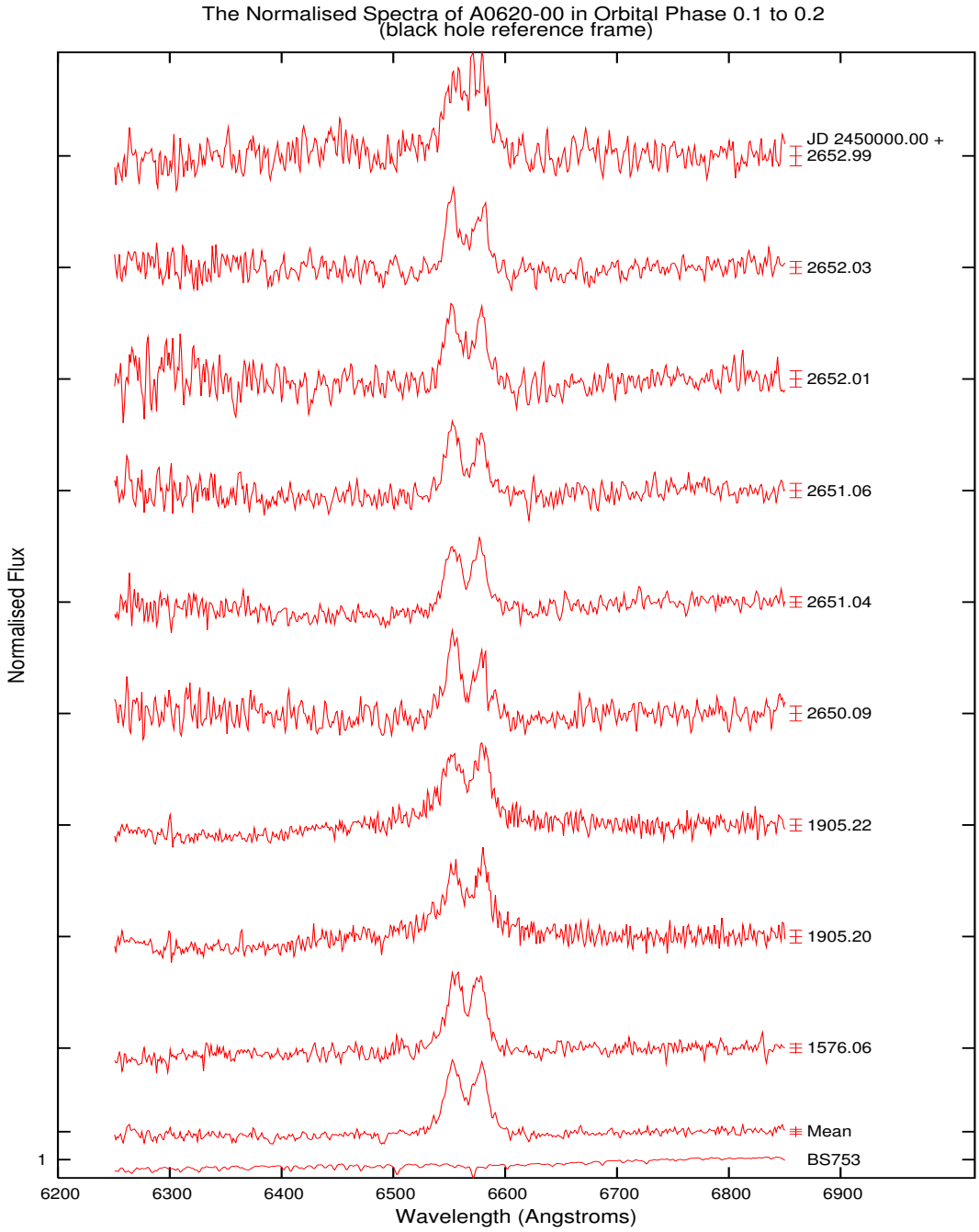

Figure 3.14: The normalised A0620-00 spectra in the orbital phase bin 0.1-0.2, in the black hole reference frame. Each spectrum is plotted with an error bar on the right. The double peaked profile of the orbital mean spectrum appears to be symmetrical, like the profiles of the spectra JD +1576.06 and JD +2652.01. However JD +2652.01 has a smaller but noticeable "spike" between the blue and red peaks. Though the spectra JD +2652.99 does not have an obvious double peak feature, its peaks approximate two peaks, with the red peak being stronger and narrower. The stronger and narrower red peak is prevalent in the spectra JD +1905.20, JD +1905.22 and JD +2651.04, while it is the case for the blue peak in the spectra JD +2650.09 and JD +2652.03.

Table 3.3: Orbital phase bin 0.1-0.2.

JD +	**Double Peaked**			**Remarks**	**Blue Peak (Å)**	**Red Peak (Å)**	**Peaks Sepn (Å)**
	Symm	**Blue**	**Red**				
1576.06		√			8.20	13.10	21.30±3.82
1905.20			√		10.40	16.50	26.90±0.95
1905.22			√		9.10	16.30	25.40±0.96
2650.09		√			9.80	14.70	24.50±14.9
2651.04			√		10.20	13.60	23.80±5.59
2651.06		√			10.40	14.40	24.80±5.91
2652.01		√		possible 3rd peak	10.70	14.70	25.40±10.9
2652.03		√			11.10	14.10	25.20±8.63
2652.99			√	not clearly double peaked	-	-	-
$mean_1$	√				10.00	14.00	24.60±2.11

Symm denotes Symmetrical Peaks
A tick in the Symm, Blue or Red column indicate if the peaks are symmetric or if one peak is more intense in the bluer or redder region
$mean_1$ denotes the orbital mean spectrum of bin 0.1 to 0.2

The orbital mean spectrum phase bin 0.2-0.3 in Figure 3.15 is dominated by characteristics of a stronger blue peak. The spectra JD +2650.13 and JD +2651.08 differ from the orbital mean, JD +2650.13 has almost symmetrical double peaks, and JD +2650.13 apparently has a small "spike" tending to the red peak. It is not obvious whether there is a double peaked emission line in the spectrum JD +2653.03. However, it is suggestive that it could be double peaked, with a stronger blue peak.

As ambiguous peaks are observed instead of the two expected peaks of the Hα line in spectrum JD +2653.03, its peak positions and separation were not measured. The largest peak separation (25.9 Å) is in the spectrum JD +2650.11, the smallest (23.1 Å) in JD +1902.99, and the separation of the peaks in the orbital mean spectrum of the 0.2-0.3 bin is measured at 24.5 Å. The measurements of the peak separation and profile description of the spectra are summarised in Table 3.4. The red peaks in this phase bin are more displaced from $\lambda_{H\alpha}$than the blue peaks.

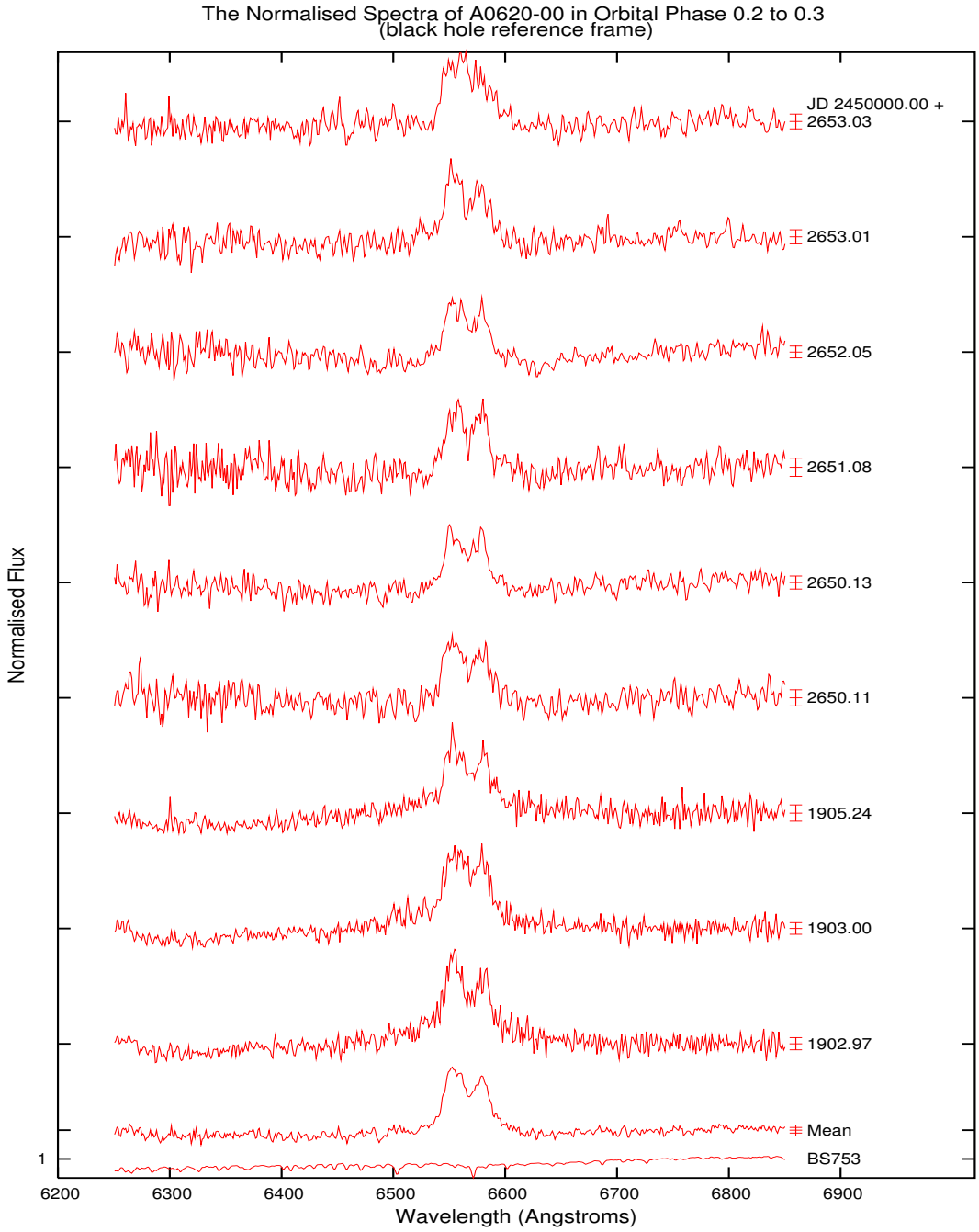

Figure 3.15: The normalised A0620-00 spectra in the orbital phase bin 0.2-0.3, in the black hole reference frame. Each spectrum is plotted with an error bar on the right. The orbital mean spectrum shows the dominating characteristics of an asymmetrical double peaked, with a stronger blue peak. The spectra JD +2650.13 and JD +2651.08 have almost symmetrical double peaks, but spectrum JD +2650.13 has a smaller "spike" tending to the red peak. It is not obvious whether the spectrum JD +2653.03 has a double peaked profile.

Table 3.4: Orbital phase bin 0.2-0.3.

JD +	**Double Peaked**			**Remarks**	**Blue Peak (Å)**	**Red Peak (Å)**	**Peaks Sepn (Å)**
	Symm	**Blue**	**Red**				
1902.97		√			9.20	16.70	25.9±0.87
1903.00		√			7.00	16.10	23.1±5.42
1905.24		√			9.10	16.50	25.6±0.94
2650.11		√			10.60	15.30	25.9±2.66
2650.13	√			small $3rd$ peak	10.00	13.80	23.8±2.34
2651.08	√				8.10	15.20	23.3±4.02
2652.05		√			8.30	16.00	24.3±8.66
2653.01		√			9.90	13.90	23.8±9.82
2653.03		√		ambiguous peaks	-	-	-
mean_2		√			9.00	15.40	24.5±1.45

Symm denotes Symmetrical Peaks
A tick in the Symm, Blue or Red column indicate if the peaks are symmetric or if one peak is more intense in the bluer or redder region
mean_2 denotes the orbital mean spectrum of bin 0.2 to 0.3

The orbital mean spectrum of the 0.3-0.4 bin does not have a prominent double peaked profile as shown in the previous phase bins. Nonetheless, the blue peak appeared to be stronger and broader than the red peak. The double peaked profile is obvious in the spectra JD +1904.95 and JD +2650.16. However, the region between the peaks of the orbital mean spectrum is obscured as shown in spectra JD +1903.02, JD +2652.09 and JD +2653.05. These spectra have an emission line with possibly other spectral components that gave rise to the almost "flat topped" profile.

Table 3.5 summaries the profile description of each spectrum and tabulates the peaks' properties. The peak separation of the orbital mean spectrum of the 0.3-0.4 bin is 23.4 Å, and the smallest and largest separation is 22.3 Å (JD +2652.09) and 24.9 Å (JD +1904.95), respectively. As in the previous orbital phase bins, the red peaks in this bin are displaced further from $\lambda_{H\alpha}$ than the blue peaks.

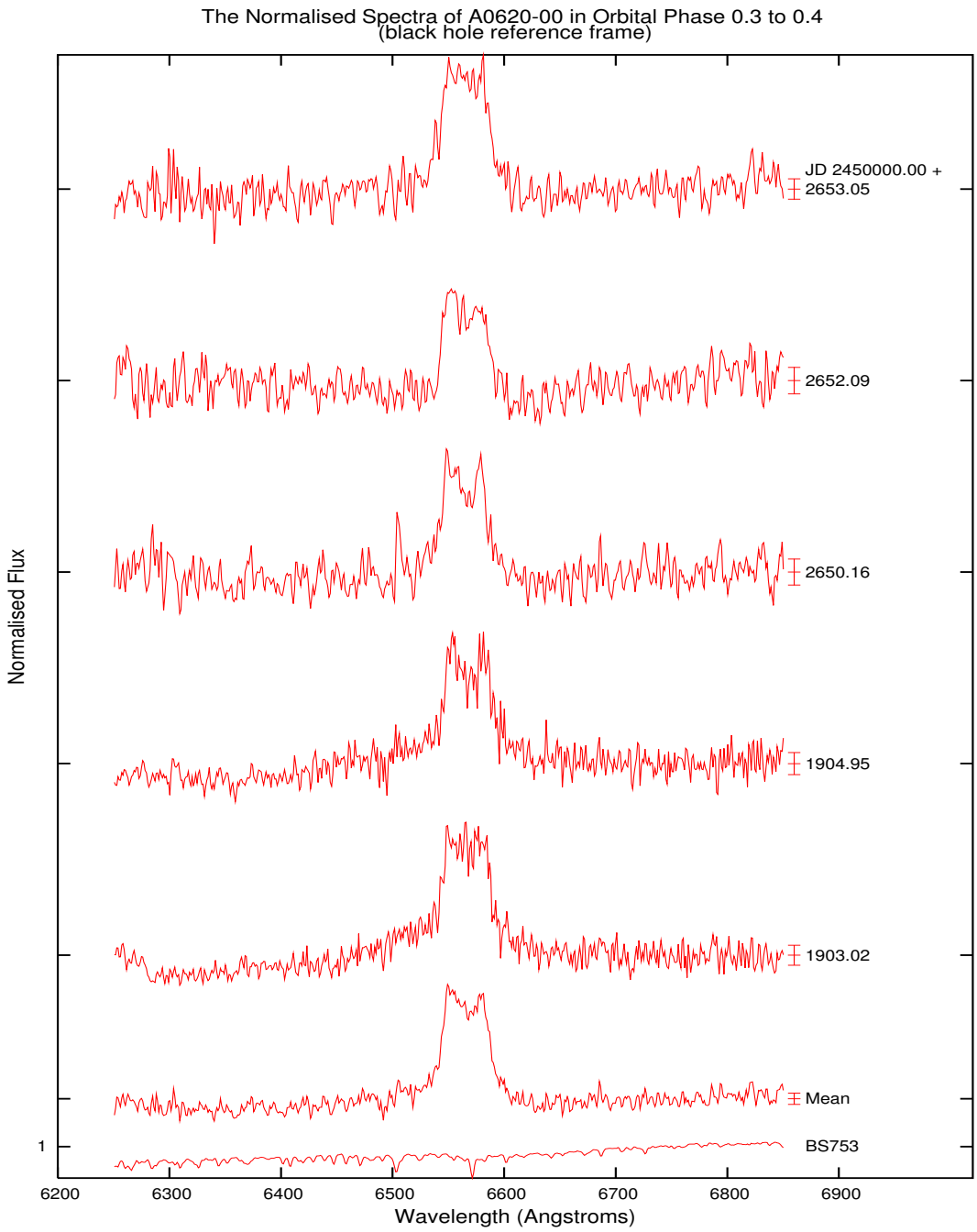

Figure 3.16: The normalised A0620-00 spectra in the orbital phase bin 0.3-0.4, in the black hole reference frame. Each spectrum is plotted with an error bar on the right. The profile of the orbital mean spectrum is dominated by features of spectra of the likes of JD +1903.02, JD +2652.09 and JD +2653.05. The double peaked profile is obvious in the spectra JD +1904.95 and +2650.16. However, there are spectra with emission line profiles that also consists of other possible spectral components which gave rise to a "flat topped" emission line profile.

Table 3.5: Orbital phase bin 0.3-0.4.

JD +	**Double Peaked**			**Remarks**	**Blue Peak (Å)**	**Red Peak (Å)**	**Peak Sepn (Å)**
	Symm	**Blue**	**Red**				
1903.02				"flat topped"	-	-	- ±5.25
1904.95	√			possible $3rd$ peak	8.60	16.30	24.9±0.92
2650.16		√			9.40	14.50	23.9±2.23
2652.09		√		possible $3rd$ peak	10.70	11.60	22.3±7.71
2653.05				"flat topped"	-	-	-
$mean_3$		√			9.10	14.30	23.4±0.48

Symm denotes Symmetrical Peaks
A tick in the Symm, Blue or Red column indicate if the peaks are symmetric or if one peak is more intense in the bluer or redder region
$mean_3$ denotes the orbital mean spectrum of bin 0.3 to 0.4

In the 0.4-0.5 orbital phase bin, most spectra have a stronger and broader red peak than blue, as reflected by the orbital mean spectrum. Possible presence of weaker spectral components between the expected positions of the double peaks in most of the spectra resulted in a "flat topped" emission line profile. The "flat topped" profile can be seen in spectrum JD +2653.08. The Hα line of JD +2652.11 is also not double peaked, and is shown to be weakening in the red region of the emission line.

The summary of each profile description for the spectra of the 0.4-0.5 orbital phase bin is shown in Table 3.6. It is observed from the table that the red peak of each spectrum is further displaced from the Hα rest wavelength, $\lambda_{H\alpha}$. The peak separation for the orbital mean spectrum of the 0.4-0.5 bin is 24.2 Å. The values of the largest and the smallest separation of this orbital phase bin measured at 25.2 Å (JD +1903.04) and 23.1 Å (JD +2653.10).

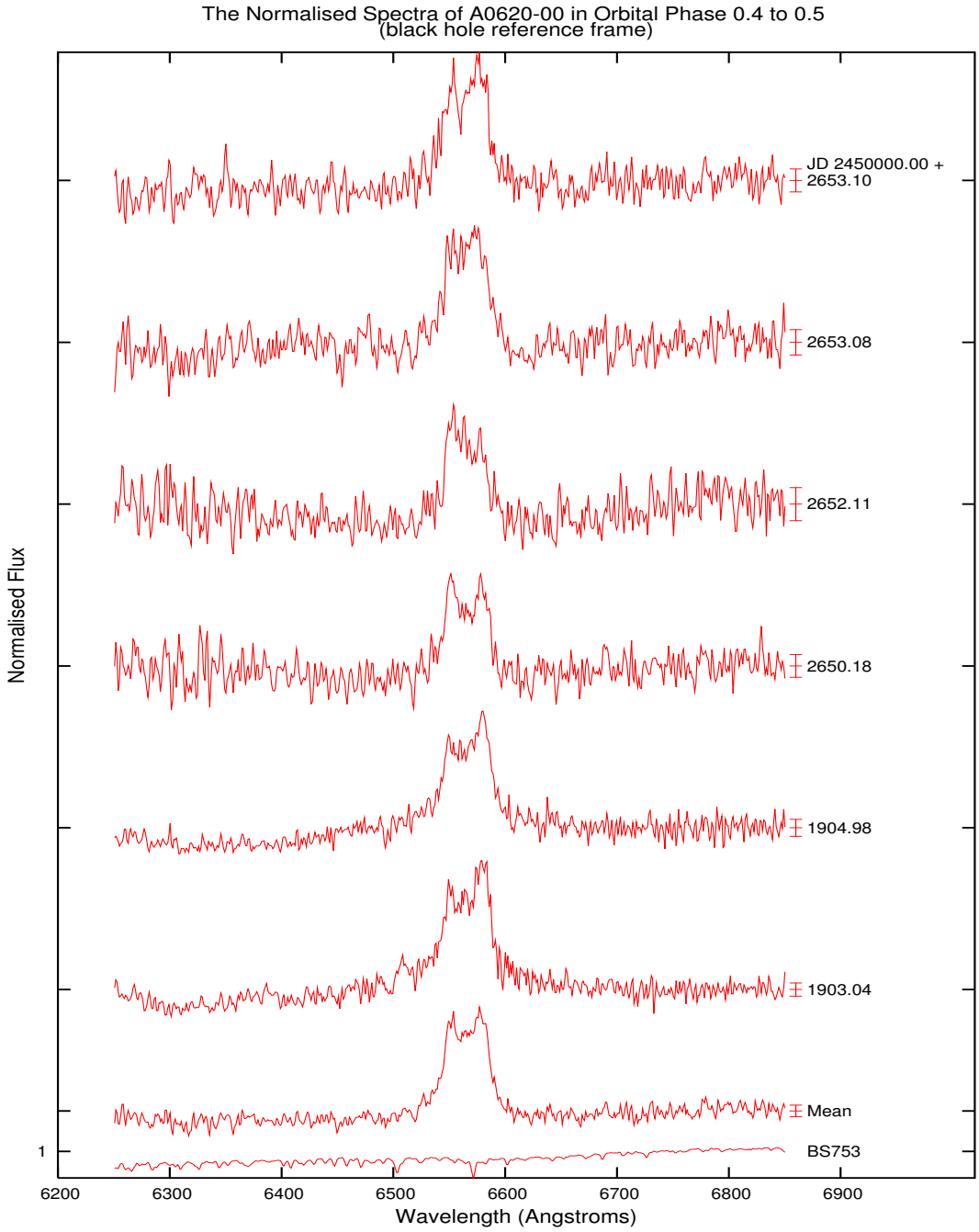

Figure 3.17: The normalised A0620-00 spectra in the orbital phase bin 0.4-0.5, in the black hole reference frame. Each spectrum is plotted with an error bar on the right. The region between the 2 peaks of the orbital mean spectrum is obscured by other weaker spectral components. These components are responsible for "flat topped" profile of the Hα line shown in the spectra JD +2653.08. The Hα feature of JD +2652.11 is also not double peaked, but is shown to be weakening in the red region of the emission line.

Table 3.6: Orbital phase bin 0.4-0.5.

JD +	**Double Peaked**			**Remarks**	**Blue Peak (Å)**	**Red Peak (Å)**	**Peak Sepn (Å)**
	Symm	**Blue**	**Red**				
1903.04			√	possible $3rd$ Gaussian	9.30	15.90	25.2±0.94
1904.98			√		8.30	15.70	24.0±0.85
2650.18	√				9.30	15.10	24.4±2.12
2652.11		√		appeared single peaked	-	-	-
2653.08			√	almost "flat topped"	-	-	-
2653.10			√		10.60	12.50	23.1±3.05
$mean_4$			√		9.40	14.80	24.2±0.98

Symm denotes Symmetrical Peaks
A tick in the Symm, Blue or Red column indicate if the peaks are symmetric or if one peak is more intense in the bluer or redder region
$mean_4$ denotes the orbital mean spectrum of bin 0.4 to 0.5

The orbital mean spectra of bin 0.5-0.6 is an asymmetric double peaked profile with a stronger blue peak. The spectra taken in 2003 in Figure 3.18 primarily consist either of a "flat topped" Hα line (shown in spectra JD +2651.17 and JD +2653.12), or an asymmetrical double peaked Hα line. Unlike the spectra JD +1572.97, JD +2652.15 and JD +3032.98, the asymmetric double peaked Hα profiles of JD +1572.95 and JD +2652.15 show noise or weaker spectral components in the region between the distinctive double peaks.

Table 3.7 summaries the profile descriptions and properties of the peaks. From the table, it is discerned that the red peak of each spectrum is generally more displaced from $\lambda_{H\alpha}$ than the blue peak. The position and separation of the peaks were not measured for spectra with the "flat topped" profile. The measured peak separation for the orbital mean spectrum of the 0.5-0.6 bin is 22.5 Å. The largest separation measured is 24.1 Å, from spectrum JD +2652.15, and the smallest separation is 21.4 Å from the spectrum JD +2651.19.

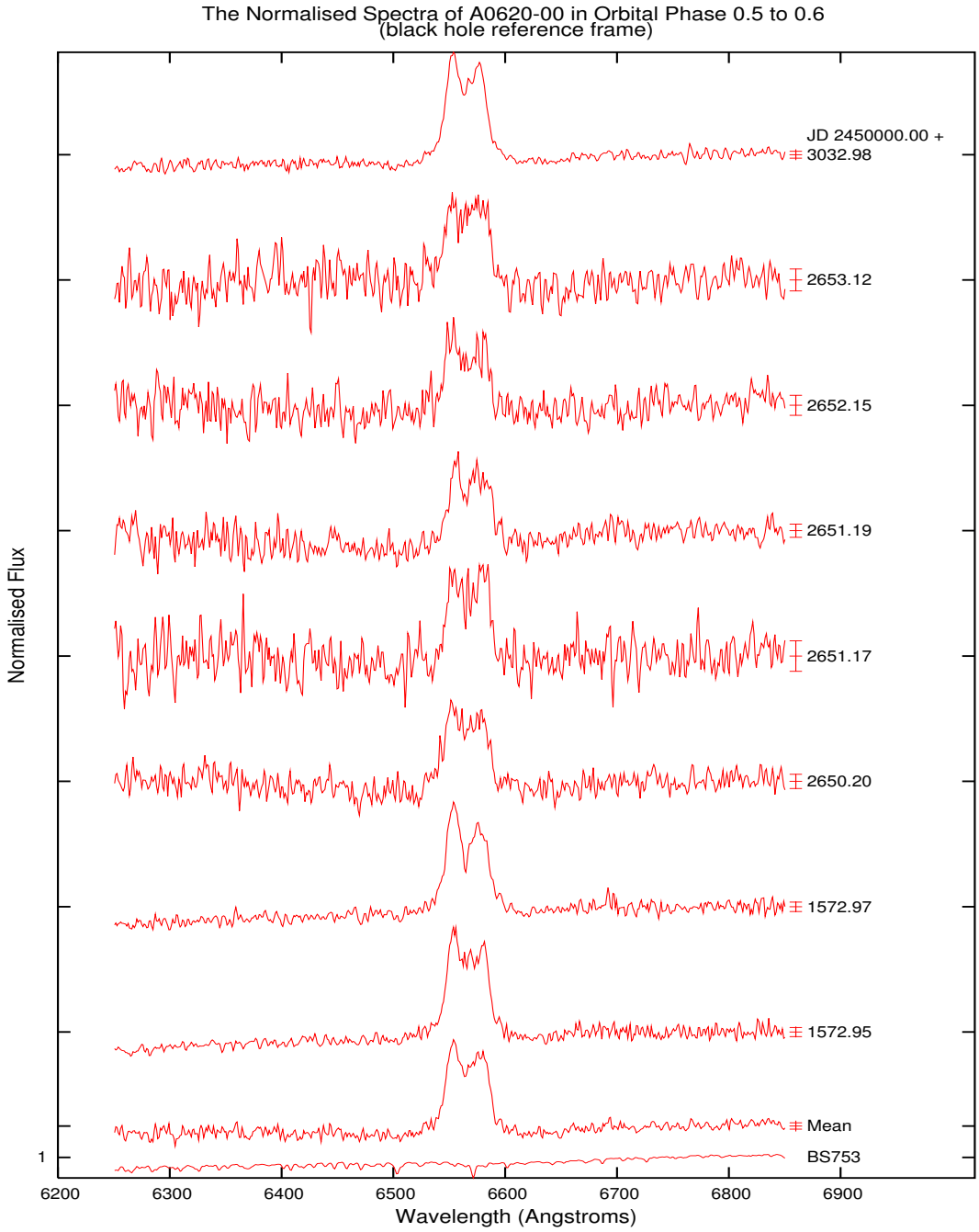

Figure 3.18: The normalised A0620-00 spectra in the orbital phase bin 0.5-0.6, in the black hole reference frame. Each spectrum is plotted with an error bar on the right. The orbital mean Hα line has an asymmetric double peaked profile which has a stronger blue peak. The spectra JD +2650.20, +2651.17 and +2653.12 have a "flat topped" Hα line. Unlike the asymmetric double peaked Hα of JD +1572.97, JD +2652.15 and JD +3032.98, the double peaked Hα profiles of JD +1572.95 and JD +2652.15 are obscured by noise or weaker spectral components between the distinctive double peaks.

Table 3.7: Orbital phase bin 0.5-0.6.

JD +	**Double Peaked**			**Remarks**	**Blue Peak (Å)**	**Red Peak (Å)**	**Peak Sepn (Å)**
	Symm	**Blue**	**Red**				
1572.95		√		possible $3rd$ peak	7.70	13.80	21.5±1.89
1572.97		√			8.80	14.00	22.8±1.64
2650.20		√			8.40	14.40	22.8±2.23
2651.17				almost "flat topped"	-	-	-
2651.19		√			7.20	14.20	21.4±15.22
2652.15		√			9.10	15.00	24.1±9.47
2653.12					9.00	13.20	22.2±2.61
3032.98		√		almost "flat topped"	-	-	-
mean_5		√			8.40	14.10	22.7±2.46

Symm denotes Symmetrical Peaks
A tick in the Symm, Blue or Red column indicate if the peaks are symmetric or if one peak is more intense in the bluer or redder region
mean_5 denotes orbital mean spectrum of bin 0.5 to 0.6

Moving on to Figure 3.19, which depicts the spectra in the orbital phase bin 0.6-0.7. The orbital mean spectrum is a well defined symmetrical double peaked Hα. All of the spectra have a distinctively double peaked Hα, except JD +2653.149, which has a 'flat-top' Hα. The double peaks in the spectra JD +1905.04, JD +2653.148, JD +2653.149, JD +3032.04 and JD +3033.00 appear to be almost symmetrical, while the rest of the spectra (JD +1572.99, JD +1573.96, JD +1905.06, JD +2651.21) are asymmetrical.

Table 3.8 summarises the description of the Hα line profile for the spectra in the orbital phase bin 0.6-0.7. The peak separation was not measured in spectrum JD +2653.149 due to the nearly 'flat-top' Hα emission line. The measured peak separation for this orbital mean spectrum is 23.5 Å. Spectrum JD + 1905.04 has the largest peak separation (25.5 Å) and spectrum JD +3033.00 (21.6 Å) has the smallest separation. The table also shows the red peaks of the spectra in this orbital phase bin to be more red-shifted than it is blue-shifted from its rest wavelength.

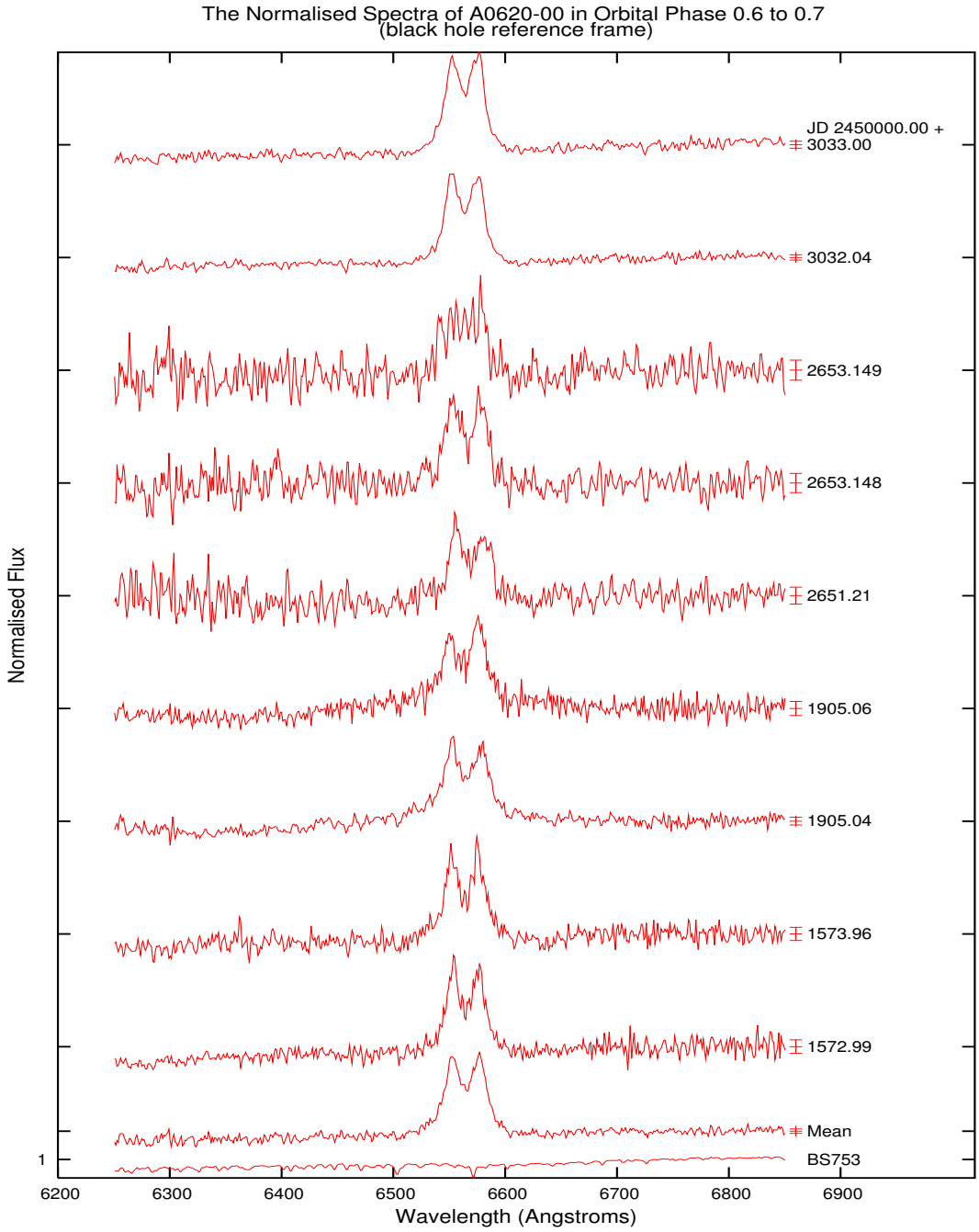

Figure 3.19: The normalised A0620-00 spectra in the orbital phase bin 0.6-0.7, in the black hole reference frame. Each spectrum is plotted with an error bar on the right. The orbital mean spectrum shows a well defined almost symmetrical double peaked Hα. The spectra JD +1905.04, JD +2651.94, JD +2653.148, JD +3032.04 and JD +3033.00 have an almost symmetrical double peaked Hα profile. The Hα profilea of spectra JD +1572.99, JD +1573.96, JD +1905.06, JD +2651.21 are asymmetric. The spectrum JD +2653.149 is quite noisy and appeared to be "flat topped" instead of the expected double peak profile.

Table 3.8: Orbital phase bin 0.6-0.7.

JD +	**Double Peaked**			**Remarks**	**Blue Peak (Å)**	**Red Peak (Å)**	**Peak Sepn (Å)**
	Symm	**Blue**	**Red**				
1572.99		√			8.90	13.50	22.4±1.95
1573.96			√		10.00	13.30	23.3±4.21
1905.04		√		almost symmetrical	9.90	15.60	25.5±0.98
1905.06			√		11.50	13.60	25.1±0.94
2651.21		√			6.20	17.50	23.7±4.62
2653.148			√		8.60	15.70	24.3±20.39
2653.149				"flat topped"	-	-	-
3032.04			√	almost symmetrical	9.70	12.40	22.1±2.32
3033.00			√	almost symmetrical	9.10	12.50	21.6±2.71
$mean_6$			√	almost symmetrical	9.20	14.30	23.5±1.48

Symm denotes Symmetrical Peaks
A tick in the Symm, Blue or Red column indicate if the peaks are symmetric or if one peak is more intense in the bluer or redder region
$mean_6$ denotes the orbital mean spectrum of bin 0.6 to 0.7

Next, in Figure 3.20, all the spectra in the 0.7-0.8 phase bin appeared to be double peaked. The orbital mean spectrum has a well defined double peaked Hα profile. The double peaks are fairly symmetrical for all spectra except for spectra JD +1903.16, JD +1905.08, JD +2653.19. These spectra have a wider red peak, and spectrum JD +1905.08 has an ambiguous weaker spectral components tending to the red peak of the Hα line.

Table 3.9 presents a summary of the Hα line profile of the spectra in phase bin 0.7-0.8, and the wavelength position of the blue and the red peaks and the distances between them. Unlike the spectra in the previous orbital phase bins, the red peaks are not generally red shifted more than the blue peaks are blue shifted from the rest wavelength. The peaks of the spectrum JD +1574.00 were shifted equally away from the rest wavelength, but the blue peaks of the spectra JD +1903.16, JD +1905.08, JD +2653.19, JD +3032.09 and JD +3033.06 are more blue shifted from $\lambda_{H\alpha}$ than the red peaks are red shifted.

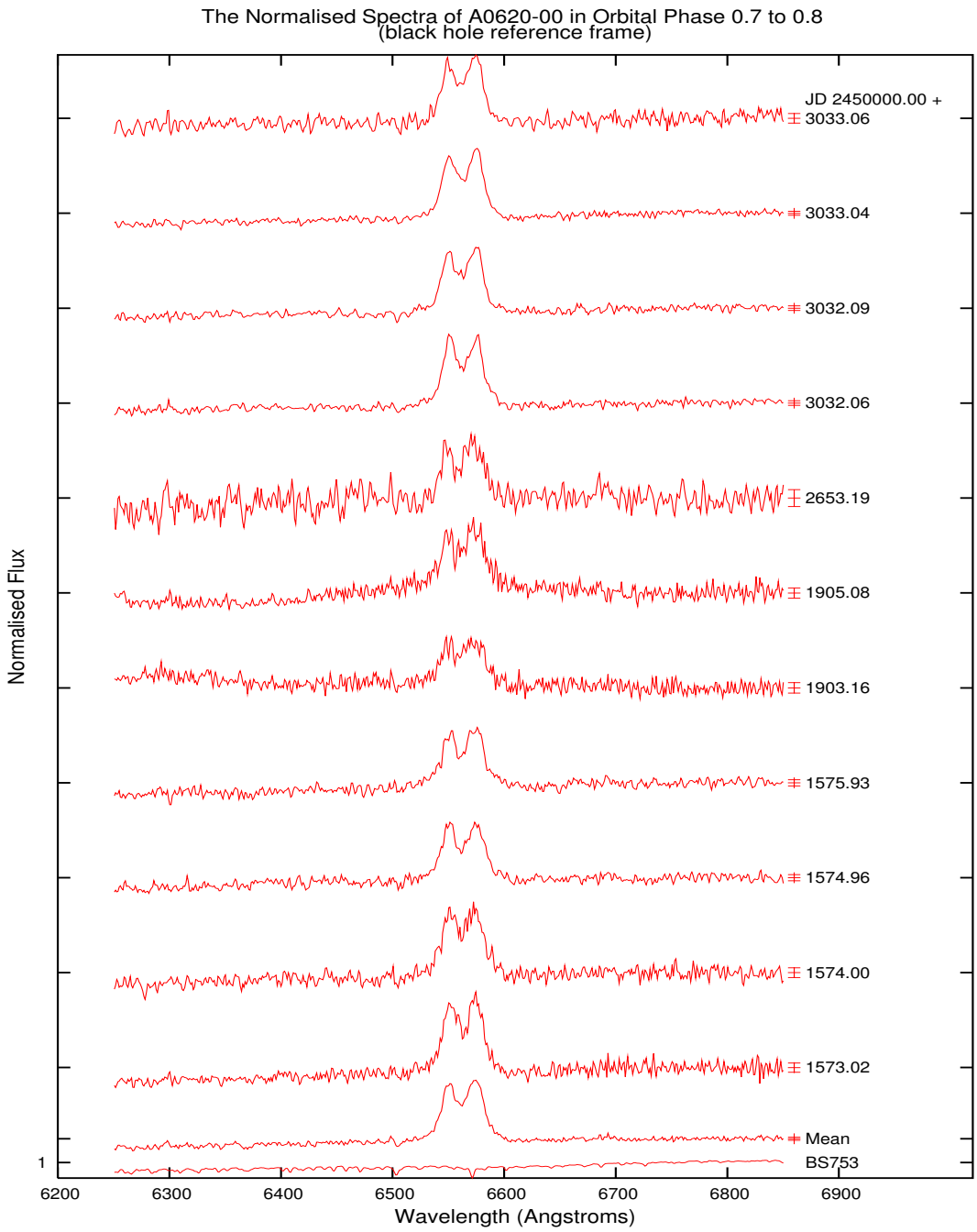

Figure 3.20: The normalised A0620-00 spectra in the orbital phase bin 0.7-0.8, in the black hole reference frame. Each spectrum is plotted with an error bar on the right. All the spectra appeared to be double peaked, which is the dominating profile of the spectra, as shown in the orbital mean spectrum. The double peaks are fairly symmetrical except in spectra JD +1903.16, JD +1905.08, JD +2653.19. These spectra have a wider red peak and other smaller spectral components between the blue and red peaks of Hα, shown in spectra JD +1905.08 ad JD +2653.19.

The orbital mean spectrum of the 0.7-0.8 bin has a peak separation of 23.1 Å, while the spectra JD +1574.96 and JD +1574.00 has the largest (24.1 Å) and smallest (22 Å) separation, respectively.

Table 3.9: Orbital phase bin 0.7-0.8.

JD +	**Double Peaked**			**Remarks**	**Blue Peak (Å)**	**Red Peak (Å)**	**Peak Sepn (Å)**
	Symm	**Blue**	**Red**				
1573.02			√		9.90	12.60	22.5±1.69
1574.00	√				11.00	11.00	22 ±3.77
1574.96	√				11.80	12.30	24.1±2.17
1575.93			√		11.30	11.60	22.9±2.56
1903.16			√		12.80	10.00	22.8±0.92
1905.08			√	possible $3rd$ peak	13.00	10.80	23.8±0.93
2653.19			√	possible $3rd$ peak	14.10	9.20	23.3±2.27
3032.06	√				10.70	11.90	22.6±2.64
3032.09			√		12.00	11.50	23.5±2.7
3033.04			√		10.70	13.10	23.8±2.06
3033.06			√		11.80	11.10	22.9±6.53
mean_7			√		11.70	11.40	23.1±1.23

Symm denotes Symmetrical Peaks
A tick in the Symm, Blue or Red column indicate if the peaks are symmetric or if one peak is more intense in the bluer or redder region
mean_7 denotes the orbital mean spectrum of bin 0.7 to 0.8

In the orbital phase bin 0.8-0.9 (see Figure 3.21), as illustrated by the orbital mean spectrum, the region between the blue and red peaks in the spectra is dominated by weaker spectral components that gave the Hα line a "flat topped" profile. The spectra JD +1573.06, JD + 1574.02, JD +1575.00, JD +1903.18, and JD +1905.11 show the overriding "flat topped" Hα attribute. The double peaked feature is present in JD +1573.04, JD +1574.98, JD +1575.00, JD +13032.11 and JD +3033.09.

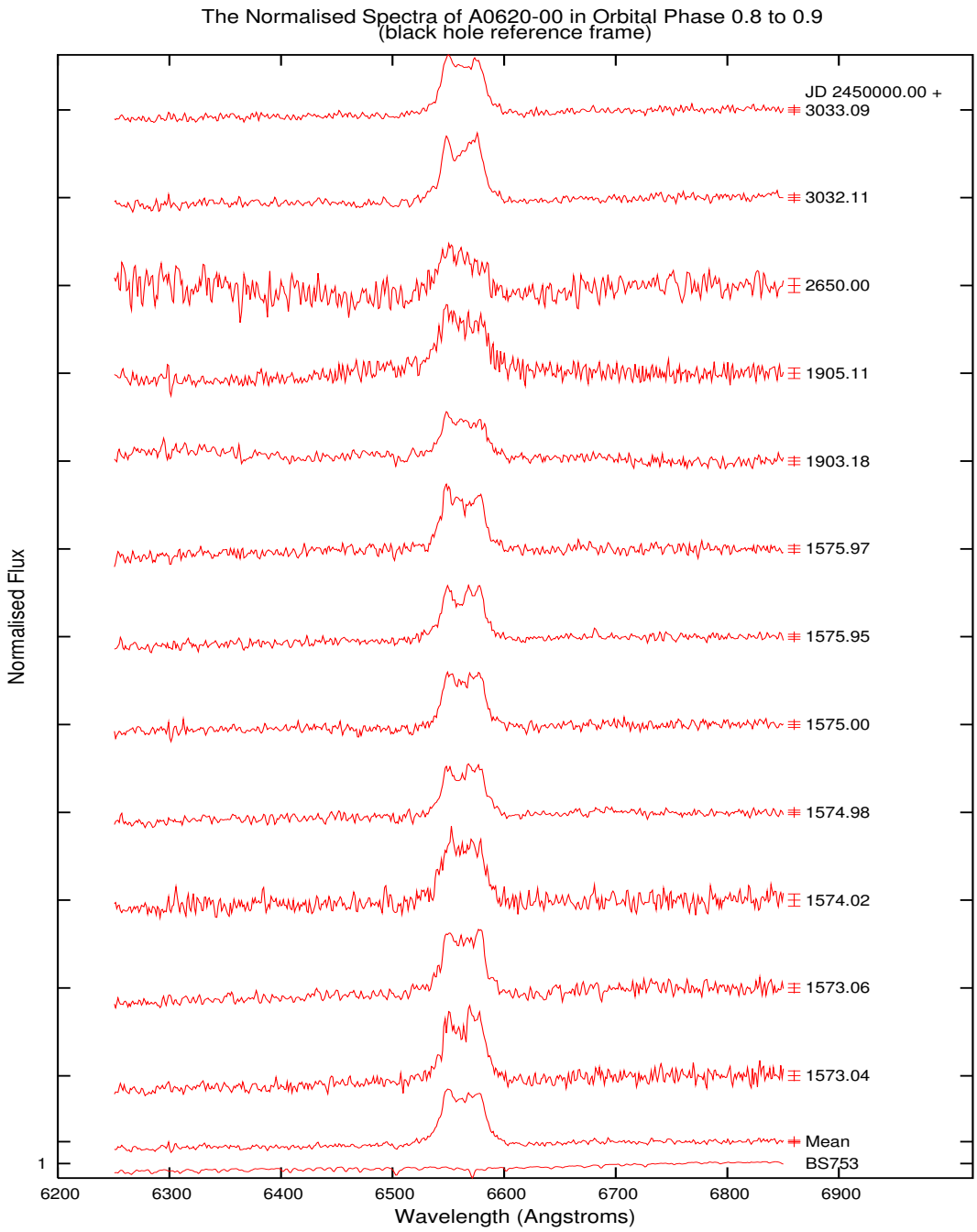

Figure 3.21: The normalised A0620-00 spectra in the orbital phase bin 0.8-0.9, in the black hole reference frame. Each spectrum is plotted with an error bar on the right. The region between the blue and red peaks of the Hα profile of the orbital mean spectrum spectrum is dominated by the "flat topped" profile of the spectra. The spectra JD +1573.06, JD +1574.02, JD +1575.00, JD +1903.18, JD +1905.11 have the overriding "flat topped" Hα attribute. The double peaked Hα is present in JD +1573.04, JD +1574.98, JD +1575.00, JD +3032.11 and JD +3033.09. However, the spectra JD +1574.98 and JD +1575.95 suggest presence of other spectral components superimposed onto the red peak.

Spectra JD 1573.04, JD +1574.98, JD +1575.00, JD +1575.95 and JD +3032.11 show an asymmetrical double peak profile, with a wider red peak. The stronger red peak of JD +3023.11 is a possible effect of another spectral component being very close to the red peak. The Hα profiles of JD +1574.98, JD +1575.00 and JD +1575.95 strongly suggest the presence of a third peak. These spectra appeared to have a wider red peak due to the presence of other weaker spectral components superimposed onto the red peak region of the Hα line.

Table 3.10: Orbital phase bin 0.8-0.9.

JD +	**Double Peaked**			**Remarks**	**Blue Peak (Å)**	**Red Peak (Å)**	**Peak Sepn (Å)**
	Symm	**Blue**	**Red**				
1573.04			√		12.00	10.00	22.0±1.69
1573.06				"flat topped"	-	-	-
1574.02				"flat topped"	-	-	-
1574.98			√	possible $3rd$ peak	13.10	9.10	22.2±1.01
1575.00			√	possible $3rd$ peak	11.90	10.30	22.2±0.91
1575.95			√	possible $3rd$ peak	13.20	9.50	22.7±1.04
1575.97		√			11.20	11.50	22.7±1.02
1903.18		√		almost "flat topped"	-	-	-
1905.11				"flat topped"	-	-	-
2650.00		√		appeared single peaked tending to the bluer region	-	-	-
3032.11			√		14.00	7.60	21.6±3.72
3033.09		√			11.60	9.60	21.2±2.64
mean_8		√		almost "flat topped"	12.30	9.80	22.0±0.43

Symm denotes Symmetrical Peaks
A tick in the Symm, Blue or Red column indicate if the peaks are symmetric or if one peak is more intense in the bluer or redder region
mean_8 denotes the orbital mean spectrum of bin 0.8 to 0.9

The blue peaks in the spectra in this orbital phase bin are generally shifted more from the rest wavelength than the red peak. The peak separation is calcu-

lated for every spectrum with a clear double peaked Hα line profile, which yielded 22.0 Å for the orbital mean spectrum of the 0.8-0.9 bin. The largest separation is 22.7 Å from the spectrum JD +1575.95 and JD +1575.97, and the smallest separation is 21.2 Å from the spectrum JD +3033.09 (see Table 3.10).

Lastly, the spectra in the orbital phase bin 0.9-1.0 in Figure 3.22 are examined and found to be dominated by a double peaked Hα, as shown by the orbital mean spectrum. The double peaked Hα is obvious in the spectra JD +1574.06, JD +1575.03, JD +1575.99, JD +1903.20, JD +2650.98, JD +2651.94 and JD +3033.11. However, there were also spectra with the "flat topped" Hα profile, such as the spectra JD +1905.15 and JD +3032.13. The peaks of the Hα profile of the spectra JD +2650.02, JD +2651.00 and +2651.96 are clouded by the presence of other weaker spectral components between the stronger blue and red peaks.

Table 3.11 is an overview of the Hα line profile description of each spectrum and the properties of its respective peaks. The red peaks of the spectra in the 0.9-1.0 orbital phase bin are more red shifted from $\lambda_{H\alpha}$ than the blue peaks are blue shifted. It is shown from Table 3.11 that the largest peak separation is 30 Å in the spectrum JD +1903.20. By examining the spectra taken on the same observing night, this spectrum is uniquely different, and needs to be examined closer to determine the cause of the broad Hα emission line. The smallest separation was determined from the spectrum JD +1574.06 (21.3Å). The orbital mean spectrum has a separation measuring 23.5 Å.

The measured values of the separation of the peaks of all the spectra were examined and compared. The mean of all the peak separations from all orbital phases is calculated to be 23.3 Å, and the associated standard deviation is 1.6 Å. The spectrum JD +1903.20 needs to be closely examined as its peak separation does not fall within the expected errors.

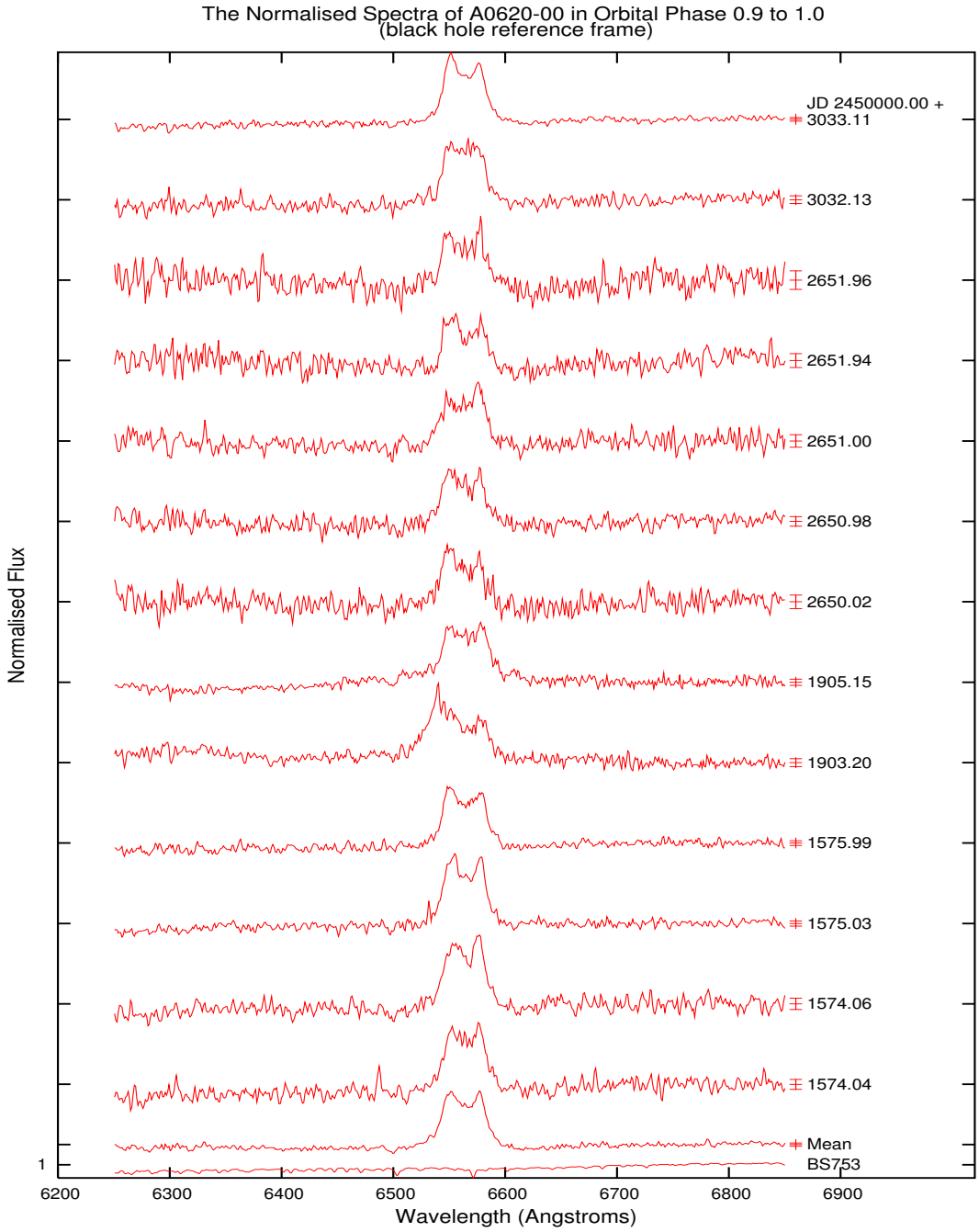

Figure 3.22: The normalised A0620-00 spectra in the orbital phase bin 0.9-1.0, in the black hole reference frame. Each spectrum is plotted with an error bar on the right. The double peaked Hα is the overriding profile of the spectra, as shown by the orbital mean spectrum. The profiles of the spectra JD +1574.06, JD +1575.03, JD +1575.99, JD +1903.20, JD +2650.98, JD +2651.94 and JD +3033.11 are double peaked. However, the spectra JD +1574.04, JD +1905.15 and JD +3032.13 have the "flat topped" Hα profile. In the spectra JD +2650.02, JD +2651.00 and JD +2651.96, the peaks are clouded by the presence of other smaller spectral components between the blue and red peaks.

Table 3.11: Orbital phase bin 0.9-1.0.

JD +	**Double Peaked**			**Remarks**	**Blue Peak (Å)**	**Red Peak (Å)**	**Peak Sepn (Å)**
	Symm	**Blue**	**Red**				
1574.04			√	noise or other components	9.10	12.30	21.4±8.76
1574.06			√		8.00	13.30	21.3±4.58
1575.03		√			8.80	13.80	22.6±3.43
1575.99		√		noise or other components	10.90	12.10	23.0±2.56
1903.20		√			13.40	16.60	30.0±0.94
1905.15				"flat topped"	-	-	-
2650.02		√		noise or other components	12.00	12.10	24.1±2.27
2650.98				broad blue peak	10.50	12.60	23.1±5.89
2651.00			√	noise or other components, almost "flat topped"	-	-	-
2651.94		√			10.20	13.80	24.0±11.8
2651.96			√	noise or other components	12.00	12.50	24.5±9.76
3032.13				"flat topped"	-	-	-
3033.11		√			10.40	11.60	22.0±2.76
$mean_9$	√			almost symmetric peaks	10.50	13.10	23.6±1.16

Symm denotes Symmetrical Peaks

A tick in the Symm, Blue or Red column indicate if the peaks are symmetric or if one peak is more intense in the bluer or redder region

$mean_9$ denotes the orbital mean spectrum of bin 0.9 to 1.0

Chapter 4

Results & Discussions

The procedures set in Chapter 3 were carried out using the derived radial velocity functions (in Section 3.3.1) to place the spectra of A0620-00 on a normalised scale in the black hole frame of reference. The results of the data analysis are presented and discussed here.

4.1 The Orbital Parameters Measured

The radial velocity fit function obtained by Marsh *et al.* (1994) defines the orbital phase zero at the inferior conjunction of the companion star, contrary to the definition used here. The velocity fit function derived in Marsh *et al.* (1994), in Equation 3.3 has been phase corrected.

The first term of the derived fit function, $V_2 = -(22 \pm 6)$ (Equation 3.1), is smaller than that of Equation 3.3, $V_{2(m)} = (4 \pm 2)$. This is because Marsh *et al.* (1994) had included the effect of the radial velocity of the template star (+23.4 km s^{-1}), which was excluded in this investigation.

The determined phase-shift factor, $\phi + (30 \pm 3) \times 10^{-3}$, leads that of Marsh *et al.* (1994), $\phi - (6 \pm 1) \times 10^{-3}$. This is could be due to the uncertainty from the extrapolation of the ephemeris, T_0 (spectroscopic) = HJD 2,446,082.7481 $\pm 0^d.0008$, (McClintock & Remillard, 1986), to the epochs of both studies. The calculated uncertainty for extrapolating T_0 to the epoch of the observations in this study is of the order 0.22-0.28, and 0.14 for that of (Marsh *et al.*, 1994). Moreover, the difference could also be the result of not considering the effects of Heliocentric correction. The maximum Heliocentric correction for the observations is roughly $\sim$ -0.006 day, which will affect the phase shift term by $\sim$ -0.019.

Table 4.1: Comparison of orbital parameters obtained in other literature

Literature	**Ephemeris** T_0	**M_2 Spectral Type**	**Radial Velocity Ampl (km s^{-1})**	$f(M)$ **($M_\odot$)**
McClintock & Remillard (1986)	HJD 2,446,082.7481	K5V	457 ± 8	3.18 ± 0.16
Johnston *et al.* (1989)	HJD 2,446,082.7481	K3V-K5V	462 ± 44	3.30 ± 0.95
McClintock & Remillard (1989)	-	K5V	442 ± 4	2.90 ± 0.08
Haswell & Shafter (1990)	HJD 2,446,082.7481	-	486 ± 10	3.82 ± 0.24
Johnston & Kulkarini (1990)	HJD 2,446,082.7481	K3V-K5V	453 ± 11	3.1 ± 0.2
Marsh *et al.* (1994)	HJD 2,446,082.7481	K3V	433 ± 3	2.7 ± 0.1
Shahbaz *et al.* (2004)	HJD 2,452,646.637	K3V-K4V	403 ± 5	2.19 ± 0.07
Findings of this thesis	HJD 2,446,082.7481	K3V	431 ± 8	2.66 ± 0.15

HJD denotes Heliocentric Julian Date

Radial Velocity refers to that of the companion star.

M_2 Spectral Type refers to the spectral type of the template spectrum used in cross-correlation.

The radial velocity fit function obtained by Marsh *et al.* (1994) defines the orbital phase zero at the inferior conjunction of the companion star, contrary to the definition used here. The velocity fit function derived in Marsh *et al.* (1994), in Equation 3.3 has been phase corrected.

However, when the radial velocity and orbital phase function obtained in this study is compared to that obtained in (Marsh *et al.*, 1994), a much smaller uncertainty ($\sim$0.025) was yielded. This suggests that (McClintock & Remillard, 1986) had overestimated the uncertainty in their measurement.

Moreover, the difference could also be the result of not considering the ef-

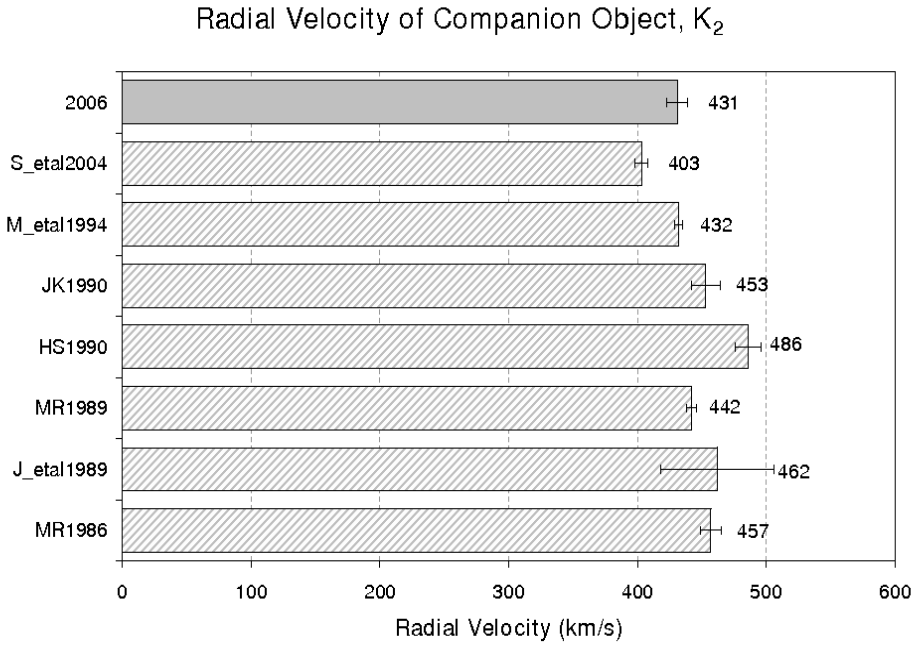

Figure 4.1: This is a graphical comparison of the calculated radial velocity of the companion star measured in this study (solid filled bar) to those from previous studies (patterned bars).

fects of Heliocentric correction. The maximum Heliocentric correction for the observations is roughly $\sim$ -0.006 day, which will affect the phase shift term by $\sim$ -0.019.

Table 4.1 lists the different values obtained for the radial velocity semi-amplitude, K_2, and mass function, $f(M)$, from different literature. Figure 4.1 compares the K_2 values and Figure 4.2 the mass function values. These values are obtained using the different methods and the different spectral classes for the companion star.

The radial velocities, K_2, yielded in Table 4.1 are in the range of $\sim$ 400 - 500km s^{-1}, the associated mass functions thus fall in the range of 2.1 - 4 M$_{\odot}$. However, the largest K_2 value obtained by Haswell & Shafter (1990), was inferred

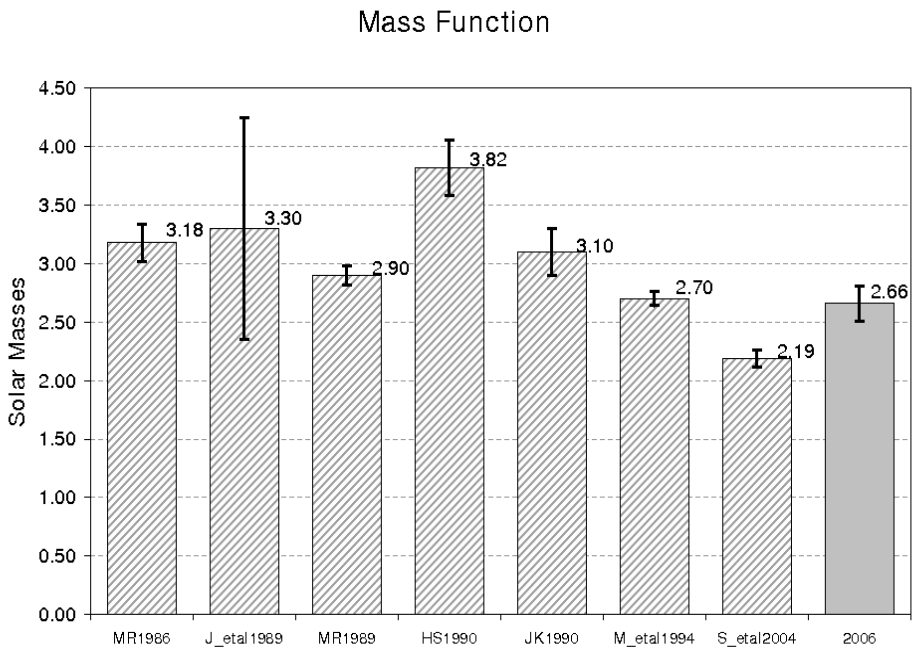

Figure 4.2: This is a graphical comparison of the calculated mass function of the compact object calculated in this study (solid filled bar) to those from previous studies (patterned bars).

from their derived mass function using Equation 1.3.

On the other hand, the lowest value of radial velocity was derived by Shahbaz *et al.* (2004) using a different ephemeris. They had attributed the small value to the incomplete coverage of the minimum in the velocity curve.

The parameters and methodology used to obtain K_2 and $f(M)$ in this study are similar to those of Johnston *et al.* (1989), Johnston & Kulkarini (1990), and Marsh *et al.* (1994). The derived K_2, and mass function are consistent with the latter findings. However, the lower limit of the mass function obtained in this analysis borders the maximum limit for a neutron star, therefore the claim for the compact object being a black hole is still to be defended.

Due to limited time and information, it was not determined if the data used in

this study will produce similar K_2 and $f(M)$ using methods similar to the other investigations listed here.

4.2 The Overall Mean Spectrum and the Orbital Mean Spectra

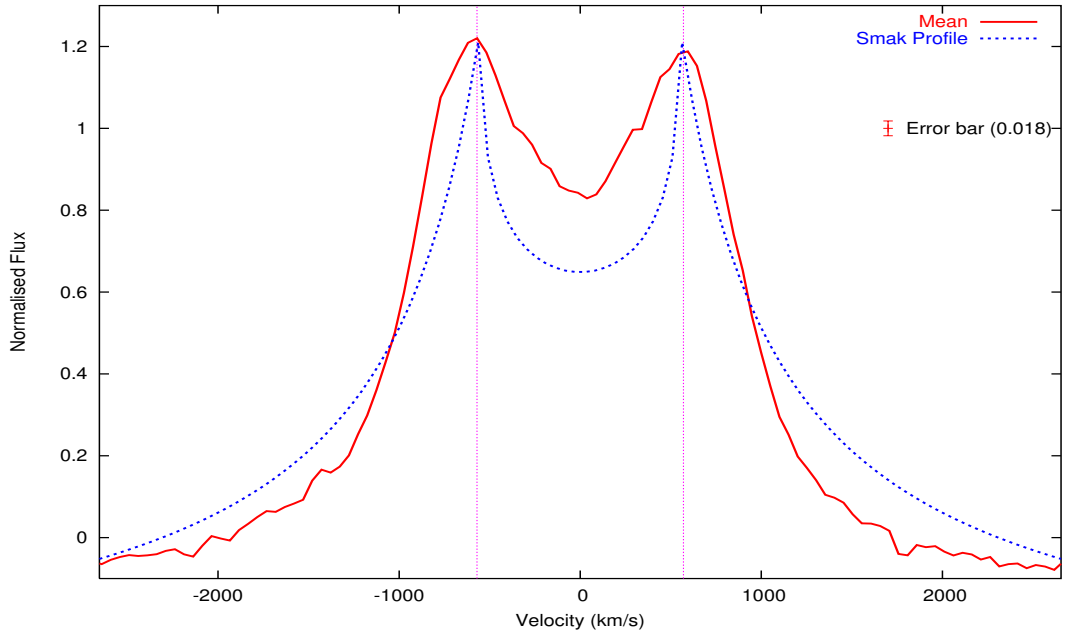

Figure 4.3: The overall mean spectrum (line) is compared to the symmetric double peaked Smak profile (short dashes). The error bar on the right describes the standard deviation of the overall mean spectrum, excluding the Hα line interval, 6520 - 6620 Å (see Equation 4.2). The two vertical dotted lines indicate the centre wavelengths of the blue and the red peak, determined by the best fit of the peaks using the Smak profile. The blue peak and its wing seemed to have stronger emission compared to the red peak and its wing.

The overall mean spectrum has an unambiguous double peaked Hα line. Compared to the symmetric Smak profile (dashes), in Figure 4.3, the peak at the shorter (blue) wavelength region of the double peaked line appears to be marginally more intense than that on the longer (red) wavelength region (~ 0.04). The height of the peaks are measured by fitting 3 Gaussian functions (see Figure 4.4) to the spectrum (shown in figure 4.5). Moreover, it is noted that the wing

on the shorter wavelength region is also broader than the wing on the longer wavelength region.

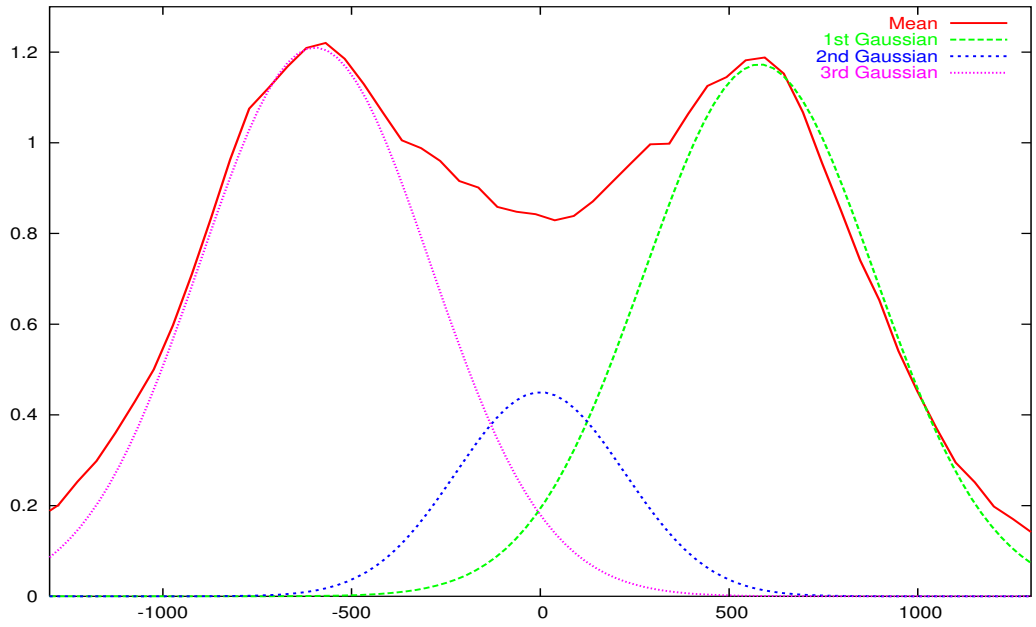

Figure 4.4: The above shows the 3 Gaussian functions used to fit the overall mean spectrum of the spectra. These Gaussian functions are the components of the function used to fit the overall mean spectrum.

The orbital period was divided into ten orbital phase bins, and a mean spectrum was derived for each bin, hereafter referred as the orbital mean. Figure 4.6 shows a plot of the orbital mean spectra obtained in each phase bin, together with the overall mean spectrum.

Though the overall mean spectrum shows a clear double peaked Hα line, some of the phase-resolved mean spectra show different line profiles. One example is the orbital mean spectrum of orbital phase bin 0.8-0.9, which shows no clear dip between the blue and red peaks (as shown on Figure 4.6). It can be seen from Figure 4.6 that the shape of the Hα line appears to change from phase bin to phase bin.

The orbital means of the phase bins 0.2-0.3 to 0.5-0.6 in Figure 4.6 show asymmetric peaks: this suggests the presence of other components within the double peaked profile. The asymmetry appears to shift from the blue peak and the red peak in the phase bins 0.2-0.3 to 0.5-0.6, and from the red peak back to the blue peak in the orbital phase bins 0.7-0.8 to 0.9-1.0.

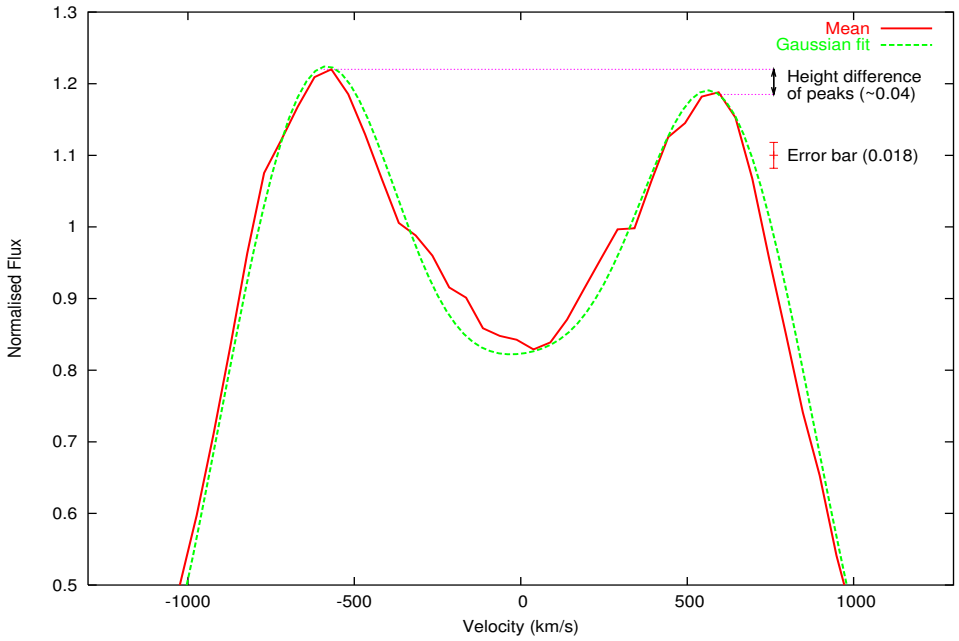

Figure 4.5: The peaks of the overall mean spectrum (line) is measured by fitting 3 Gaussian functions (short dashes) to the peaks. The error bar on the right describes the standard deviation of the overall mean spectrum, the arrow indicates the height difference between the two peaks.

Although Haswell & Shafter (1990) noted the presence of a third central peak of the Hα line in their investigation, the third peak is not strongly validated by the physical appearance of the spectra in Section 3.4. Furthermore, Haswell & Shafter (1990) found the the third central peak to be migrating from the blue peak to the red peak in orbital phases 0.3, 0.4, 0.5 and 0.6 (phase corrected to convention used in McClintock & Remillard (1986)). This displacement coincides with the migration of the asymmetry of the red and blue peaks mentioned above.

Haswell & Shafter (1990) suspected that the asymmetry and the third peak in their investigation could be the result of a possible hotspot on the surface of the disc. Both Shahbaz *et al.* (2004) and Marsh *et al.* (1994) computed Doppler images of A0620-00 for the Hα and the Hβ line, and showing conclusive results that there is a bright spot on the disc. The presence of a hotspot in this investigation is substantiated by the EW measurements in Section 4.5.

Shahbaz *et al.* (2004) and Marsh *et al.* (1994) had also calculated the corresponding theoretical gas stream path from the inner Lagrangian point, and the gas stream path defined by the derived mass ratio ($q = 0.067$) and measured

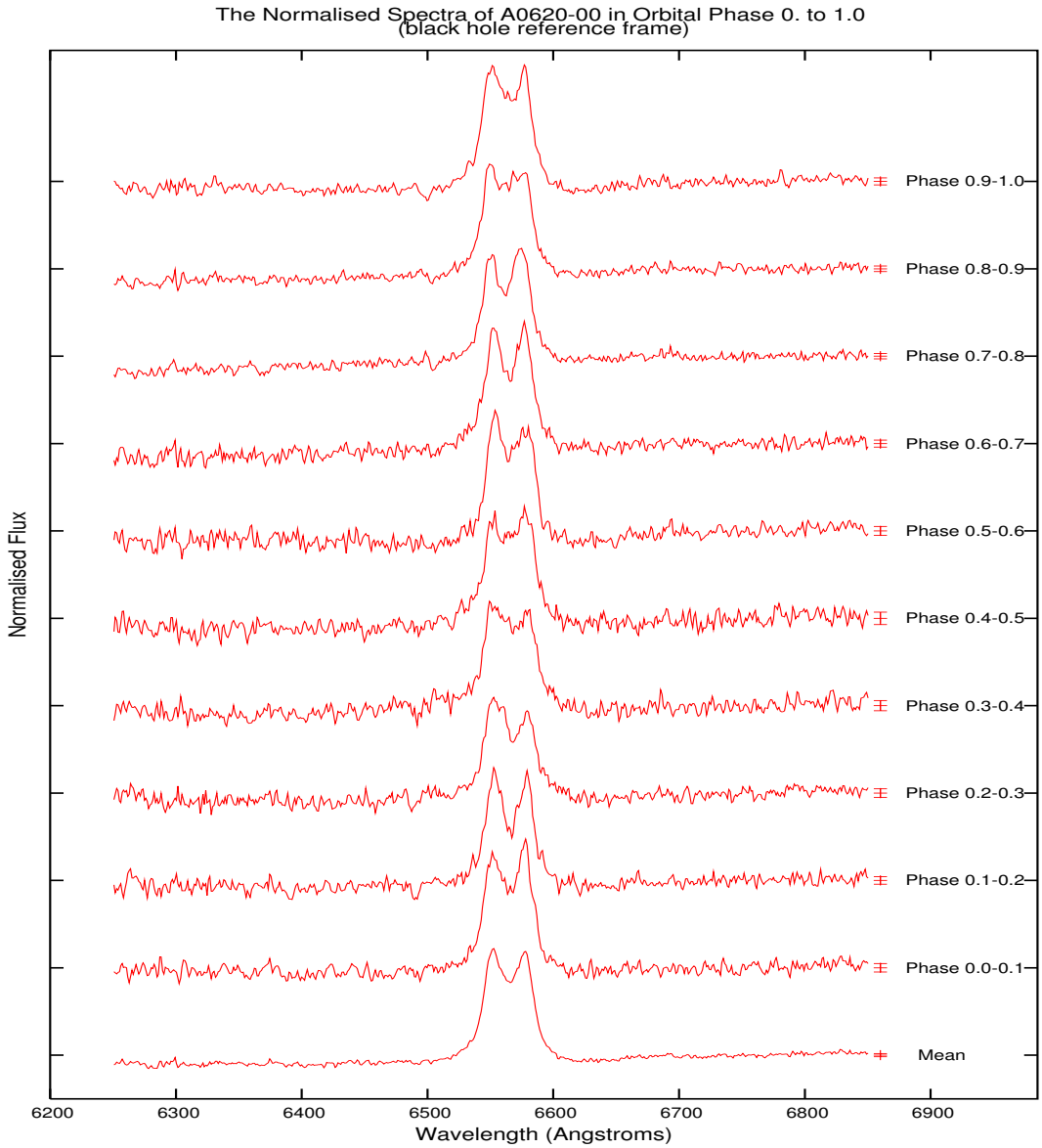

Figure 4.6: The mean spectrum of each orbital phase bin is plotted with the overall mean spectrum. Each tic mark on the vertical flux axis indicates the normalised flux unit of 1 of each spectrum. The error bar on the right of each spectrum describes the standard deviation of all the points of that spectrum, excluding the Hα line region, 6520 - 6620 Å (see Equation 4.2). It can be inferred from the orbital means of the phase bins 0.2-0.3 to 0.5-0.6 that there may be presences of other spectral components. The components are migrating from blue peak to red peak (in bins 0.2-0.3 to 0.5-0.6), and from red peak back to blue peak (in bins 0.7-0.8 to 0.9-1.0).

radial velocity (K_2). However, the hotspot in both investigations does not lie on either predicted paths of the gas stream, rather it lay between them.

Marsh *et al.* (1994) speculated that this is due to the effect of gas around the hotspot after it has passed through the shock at the edge of the disk. They also found that the extension of the emission from the hotspot region to high velocities corresponds to the emission at high velocities in the blue region of their data.

Hence, it is probable that the stronger blue emission in Marsh *et al.* (1994) and the marginally stronger blue wing of the overall mean spectra found in this thesis, are due to the latter effect.

4.3 The Spectra and the Overall Mean Spectrum

Each spectrum is compared to the overall mean spectrum. This comparison is quantified using the chi-squared test. The chi-squared test computes the difference between each point of the considered spectrum and the corresponding point in the overall mean spectrum. The weighted squared difference of each point are then summed as the chi-squared statistic, χ^2, expressed as Equation 4.1.

$$\chi^2 = \sum_i \frac{(m_i - s_i)^2}{(\sigma_m^2 + \sigma_s^2)} \tag{4.1}$$

where m_i is the flux in the ith wavelength bin of the mean spectrum, and s_i is that of an individual spectrum. σ_m^2 denotes the expected error or variance (see Equation 4.2) of the mean spectrum, and σ_s^2 the uncertainty of the spectrum. σ^2 defined as:

$$\sigma^2 = \sum_i^N \frac{(\tilde{s} - s_i)^2}{(N-1)} \tag{4.2}$$

where N is the number of wavelength bins, and $\tilde{s}$ is the mean of flux between 6680 Å and 6820 Å of the spectrum s.

To establish how each spectrum had changed with respect to the orbital mean spectrum, χ^2 is calculated for each spectrum for the Hα line region. The degrees of freedom (df) for each spectrum is 91. This is defined by the number of wavelength bins minus 1. The reduced $\chi^2(\frac{\chi^2}{df})$ of the spectra indicates that a majority of spectra are similar to the overall mean spectrum ($\frac{\chi^2}{df} \leq 5$). However, there are also some spectra which vary quite significantly from the overall mean spectrum ($\frac{\chi^2}{df} \gg 1$).

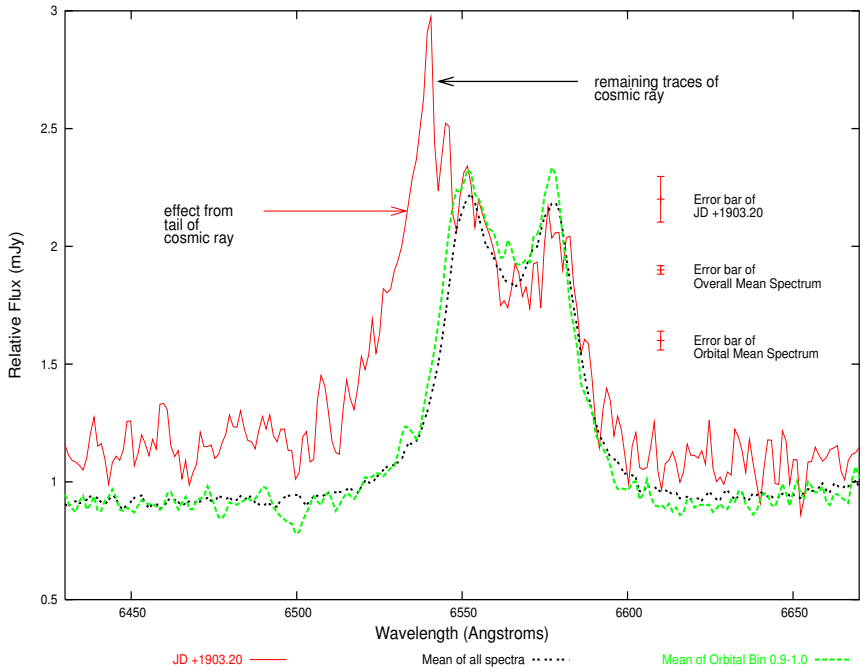

Figure 4.7: This is a close-up of the spectrum (line) taken on JD +1903.2, overlaid with the mean of its orbital phase bin (dashes), and the mean of all the spectra (double dots). This plot shows the wide blue wing of the spectrum. The inspection the raw image of the spectrum strongly suggests that the high intensity blue peak and its wide blue wing are due to the effects of the tail of the cosmic ray.

The spectrum JD +1903.20 has a large $\frac{\chi^2}{df}$ ($\sim$ 27), which suggests that the latter should be examined more carefully. It is possible that the large $\frac{\chi^2}{df}$ is an effect of a mini outburst or contamination by a cosmic ray. The raw image of the spectrum confirmed the suspicion that the shape of the blue peak of the spectrum (see Figure 4.7) is largely due to a cosmic ray. There is a bright cosmic ray with a tail that lies very close to the Hα line in the shorter wavelength region. Though much of the effect of the cosmic ray on the blue peak was masked by taking the average of the counts in the pixels around the image during the initial reduction

of the raw image, the effects from the tail might have been unaccounted for. Any cosmic tail effects combined with the rebinning of the counts could result in the wide blue wing.

Consequently, all results pertaining to the spectrum taken on JD +1903.20 are ignored in the analysis. As a result, the degrees of freedom (df) was reduced to 90, and values of the $\frac{\chi^2}{df}$ recalculated. The following plots have included the latter spectrum for comparison.

Figure 4.8 shows the χ^2 and $\frac{\chi^2}{df}$ of each observation, arranged chronologically, for the Hα line interval (6520 - 6620 Å). Each panel shows the χ^2 and $\frac{\chi^2}{df}$ of each observation from the same observing campaign, the spectra in each panel are further categorised according to the observing night. The subsequent bars of the same colour in each panel represent the χ^2 and $\frac{\chi^2}{df}$ of the succeeding spectrum of same observing night.

The lowest panel is composed of spectra from observations taken in early 2000, from 29 Jan to 1 Feb (JD +1572.94 to JD +1576.06), will hereafter be referred to as E2000a. The observations in late December 2000 (JD +1902.97 to JD +1905.24) were grouped into E2000b, shown in the second panel from the bottom. The third panel depicts the χ^2 and $\frac{\chi^2}{df}$ of observations taken in January 2003 (JD +2650.00 to JD +2653.19), E2003. Finally, the top panel illustrates the χ^2 and $\frac{\chi^2}{df}$ of the last group of observations, E2004, which were taken in January 2004 (JD +3032.04 to JD +3032.98).

The $7th$ spectrum in panel (b), JD +1903.20, with $\frac{\chi^2}{df} \sim 27$, is ignored. The $\frac{\chi^2}{df}$ of $15th$ spectrum (JD +1575.03) in panel (a) is significantly larger ($\frac{\chi^2}{df} \sim 13$) than all other spectra. On the other hand, the $\frac{\chi^2}{df}$ of the $8th$ spectrum in panel (b), JD +1903.22, is much smaller ($\frac{\chi^2}{df} \sim 1.25$).

Most of the spectra in Figure 4.8 have a $\frac{\chi^2}{df} \sim 1$. Besides the $\frac{\chi^2}{df}$ of spectrum JD +1903.20 ($7th$ spectrum of panel (b)), the $\frac{\chi^2}{df}$s of spectra JD +1575.03 (15th spectrum of panel (a)), JD +1903.04 ($4th$ spectrum of panel (b)), and JD +3033.11 ($11th$ spectrum of panel (d)) are much larger than 1. This indicates that these spectra are more significantly different from the overall mean spectrum. It is also apparent that the shape of some spectra does change within the same observing night.

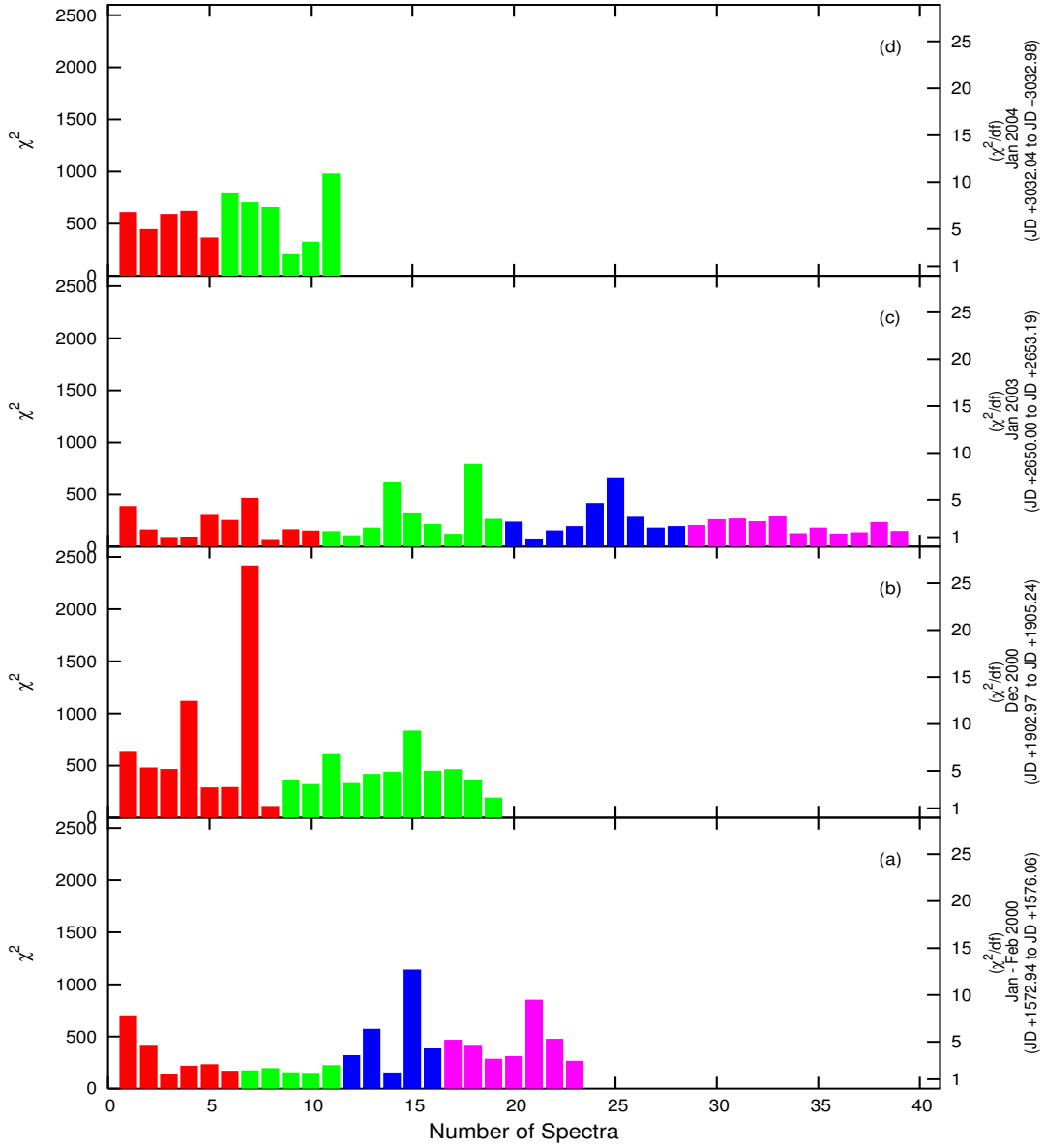

Figure 4.8: The χ^2 and $\frac{\chi^2}{df}$ values obtained by comparing the Hα line (6520 - 6620 Å) of each spectrum to that of the overall mean spectrum, plotted in chronological order. Each χ^2 and $\frac{\chi^2}{df}$ represents a measure of how each of the Hα line profile is different from that of the overall mean spectrum. The subsequent bars of the same colour in each panel represent the χ^2 and $\frac{\chi^2}{df}$ of the succeeding spectrum of same observing night. The right vertical axis shows the $\frac{\chi^2}{df}$ value of each spectrum. Most of the spectra have a $\frac{\chi^2}{df} \sim 1$. Besides the $\frac{\chi^2}{df}$ of spectrum JD +1903.20 ($7th$ spectrum of panel (b)), the $\frac{\chi^2}{df}$s of spectra JD +1575.03 (15th spectrum of panel (a)), JD +1903.04 ($4th$ spectrum of panel (b)), and JD +3033.11 ($11th$ spectrum of panel (d)) are much larger than 1. This indicates that these spectra are more significantly different from the overall mean spectrum.

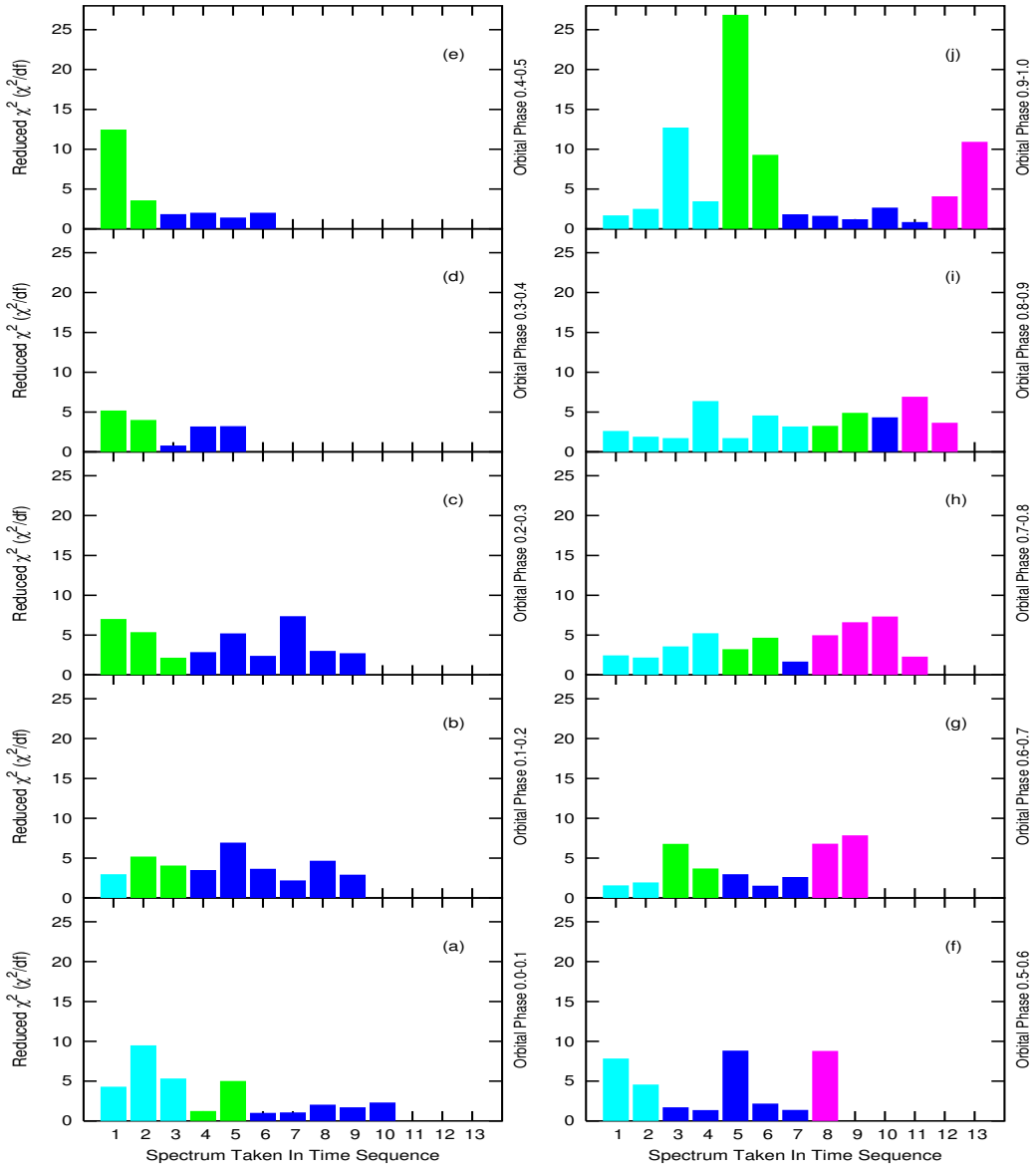

Figure 4.9: These are the same $\frac{\chi^2}{df}$ from Figure 4.8, in orbital phase order. Each panel represents an orbital phase bin, and each bar of the same colour identifies a spectrum of the same observing campaign. The adjacent bar of the same colour represents the $\frac{\chi^2}{df}$ of the subsequent spectrum in the phase bin in the same epoch. Some of the $\frac{\chi^2}{df}$ of spectra taken in the same observing campaign in each orbital phase are relatively consistent. For example, the spectra in E2003 in the phase bin 0.0-0.1, 0.4-0.5 and 0.9-1.0 etc. Similarly, the changes do not appear to have a phase dependent trend.

Though the $\frac{\chi^2}{df}$ of the spectra change with time, there does not appear to be any evidence of a time dependent trend in the change of the $\frac{\chi^2}{df}$ in Figure 4.8. The $\frac{\chi^2}{df}$ were replotted in Figure 4.9 in orbital phase order to look for an orbital phase dependent trend in the changes.

Each panel in Figure 4.9 represents an orbital phase bin, and each bar of the same colour identifies a spectrum of the same observing campaign. The adjacent bar of the same colour represents the $\frac{\chi^2}{df}$ of the subsequent spectrum in the phase bin in the same epoch.

Similarly, there is no obvious trend in the variation of the $\frac{\chi^2}{df}$ in Figure 4.9. Some of the $\frac{\chi^2}{df}$ of the spectra taken in the same observing campaign in each orbital phase are consistent with one another, as illustrated by the E2003 spectra in the phase bin 0.0-0.1, 0.4-0.5 and 0.9-1.0. However, the largest $\frac{\chi^2}{df}$ are found mostly in phase 0.9-1.0.

The changes in the spectra of the same orbital phase or same observing run are not uniform. Most of the large values of $\frac{\chi^2}{df}$ are noted to be in orbital phase 0.9-1.0, hence showing a phase dependent trend. Though the Hα line profile in each spectrum changes over time, there was no strong evidence of a time dependent trend in the variation of $\frac{\chi^2}{df}$.

4.4 The Spectra and their Orbital Mean Spectrum

The spectra were compared to their respective orbital mean spectrum in Section 4.3. Here, the difference between an individual spectrum and the orbital mean spectrum is quantified using the chi-squared test, mentioned in Section 4.3. The chi-square determined in this section are in the form of reduced chi-square, hereafter labelled as ${\chi^2}_{orb}$.

Each panel in Figure 4.10 represents an orbital phase bin, and each bar of the same colour identifies the ${\chi^2}_{orb}$ of a spectrum of the same observing campaign. The adjacent bar of the same colour is the ${\chi^2}_{orb}$ of the subsequent observation of the phase in the same epoch. As discussed in the Section 4.3, the ${\chi^2}_{orb}$ of JD +1903.20, the $5th$ spectrum of panel (j) in Figure 4.10, is ignored.

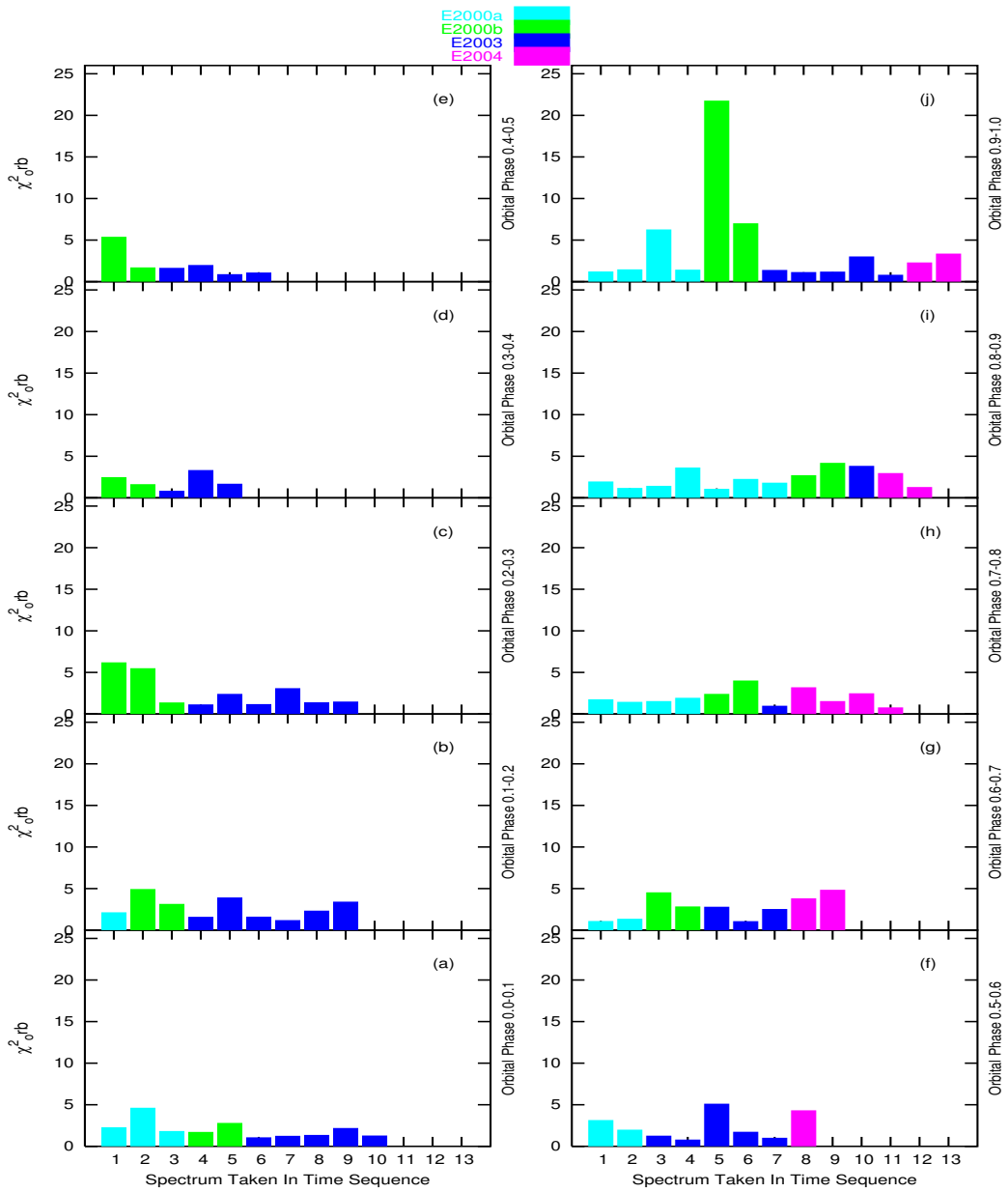

Figure 4.10: The $\chi^2{}_{orb}$ here is a comparison of the Hα line region of each spectrum to its respective orbital mean spectrum. Each panel represents an orbital phase bin, and each bar of the same colour identifies a spectrum of the same observing campaign. The adjacent bar of the same colour represents the $\chi^2{}_{orb}$ of the subsequent spectrum in the phase bin in the same epoch. The $\chi^2{}_{orb}$ of JD +1903.20 ($5th$ spectrum of panel (j)) is ignored. Most of the spectra seemed to different by almost the same $\chi^2{}_{orb}$ for all orbital phase bin, except some of the spectra from the campaign E2000b. The spectrum JD +1905.50 ($6th$ spectrum of panel (j)), has the highest $\chi^2{}_{orb}$ ($\sim$ 7). The other spectra from the same observing campaign with large $\chi^2{}_{orb}$s are JD +1902.97 ($1st$ spectrum of panel (c)), JD +1902.99 ($2nd$ spectrum of panel (c)), JD +1903.04 ($1st$ spectrum of panel (e)), and JD +1903.23 ($6th$ spectrum of panel (j)).

Most of the spectra differed by a similar ${\chi^2}_{orb}$ for all orbital phase bins, except some of the spectra from the campaign E2000b. The spectrum JD +1905.15 ($6th$ spectrum of panel (j)) in orbital phase bin 0.9-1.0 has the highest ${\chi^2}_{orb}$ (~ 7).

The other spectra from the E2000b observing campaign with large ${\chi^2}_{orb}$ are JD +1902.97 (${\chi^2}_{orb} \sim 6$) and JD +1902.99 (${\chi^2}_{orb} \sim 5.5$). These are the $1st$ and $2nd$ spectrum of panel (c), respectively, and are from the orbital phase bin 0.2-0.3. Other spectra such as spectrum JD +1575.03, $3rd$ spectrum of panel (j), of phase bin 0.9-1.0, and spectrum JD +1903.04, $1st$ spectrum of panel (e), of phase bin 0.4-0.5, also have a ${\chi^2}_{orb} \geq 5$.

Therefore, it is clear that within the same orbital phase, the Hα region of each spectrum can still be significantly different from its respective orbital mean spectrum. In addition, it is noted that the changes are not uniform for spectra of the same observing night, hence there is no indication of trend in the variation of the Hα line.

Most of the large $\frac{\chi^2}{df}$ and ${\chi^2}_{orb}$ resulted from the same spectra. Though each associated orbital mean spectrum resembles a corresponding spectrum more than the overall mean spectrum, some of the spectra still yield a ${\chi^2}_{orb}$ which is as large as the $\frac{\chi^2}{df}$. For instance, in panel (b) and (c) of both Figures 4.9 and 4.10, the $\frac{\chi^2}{df}$ and the ${\chi^2}_{orb}$ of the $2nd$ spectrum (JD +1902.97) of panel (b) (~ 5), and the $1st$ spectrum (JD +1903.02) of panel (c) (~ 6) are similar.

Just as it was shown in the comparison of the overall mean spectrum, there are no uniform changes for the spectra in the same orbital phase bin or same observing run. However, most of the spectra in the orbital phase 0.9-1.0 bin has a ${\chi^2}_{orb} \geq 5$, hence supporting a phase dependent trend in ${\chi^2}_{orb}$ variation. Though the Hα line profile in each spectrum changes over time, neither variations in the $\frac{\chi^2}{df}$ and the ${\chi^2}_{orb}$ values show evidence of a time dependent trend or an orbital phase dependent trend.

4.5 The Equivalent Width of Hα

The equivalent width (EW) of the Hα line of each spectrum is determined by fitting the spectrum with a function consisting of 3 Gaussians, and measuring the area under the Hα line profile.

There are spectra with small spectral components between the dip of the blue and red peaks. These components are approximated by one of the three Gaussian

function. The measured EWs are tabulated in Table 4.2.

The EW of each phase bin is plotted in Figures 4.11 and 4.12. Figure 4.11 is a plot of EW of spectra taken in E2000a, E2000b and E2003, and Figure 4.12 continues with E2003 and E20004. Separate plots were made for each observation in E2000b and E2003 to highlight the different EW obtained for the same orbital phase in different observing runs. Figures 4.11 and 4.12 also show overall mean of the EW of each orbital phase. Each panel is overlaid with an EW fit function ($EW(\mathring{A}) = 61.4 \pm 0.6) + (7.8 \pm 0.8)\ cos\ 4\pi\phi)$) extracted from Marsh *et al.* (1994).

The largest EWs in each observing run is in orbital phase bin 0.0-0.1, while the largest overall mean EW is in bin 0.9-1.0. These bins are very close to the superior conjunction of the companion. The height of the Hα line (with respect to the continuum) is higher at this conjunction than at the inferior conjunction. This is due to less flux from the companion star in the spectrum.

The smallest EWs in each observing run, and the smallest overall mean EW are found in orbital phase bin 0.2-0.3. This bin is very close to a quadrature phase, i.e. where the companion is positioned at the side of the compact object in the line-of-sight. At this position, the oblong shape of the companion star caused by the tidal distortion by the compact object is visible in the line-of-sight. As a result, the continuum flux is higher as there is more flux from the companion star, therefore it yields a smaller equivalent width. This indicates that the system is most luminous at orbital phase 0.2-0.3.

The companion star is also at quadrature in the orbital phase bin 0.7-0.8. However, the overall mean EW is in the orbital phase bin 0.7-0.8 is greater than that at the other quadrature (0.2-0.3). This reflects that the binary system is fainter at this quadrature (bin 0.7-0.8), thus suggests the presence of another spectral component, such as a hotspot, at phase bin 0.2-0.3 with a more luminous spectrum. Incidentally, the discovery of possible hotspot at this phase is consistent with the bright spot found at $\phi = 0.25$ (phase corrected) of the near-infrared observations by Froning & Robinson (2001). Alternatively, it is also probable that this luminosity behaviour is due an asymmetric accretion disc.

The companion star is at inferior conjunction in the orbital phase bin 0.5-0.6. The equivalent width at this phase certifies that the luminosity at this orbital phase is greater than that at superior conjunction (phase 0.0-0.1), which advocates a possible hotspot, visible in the line-of-sight on the accretion disc at this conjunction.

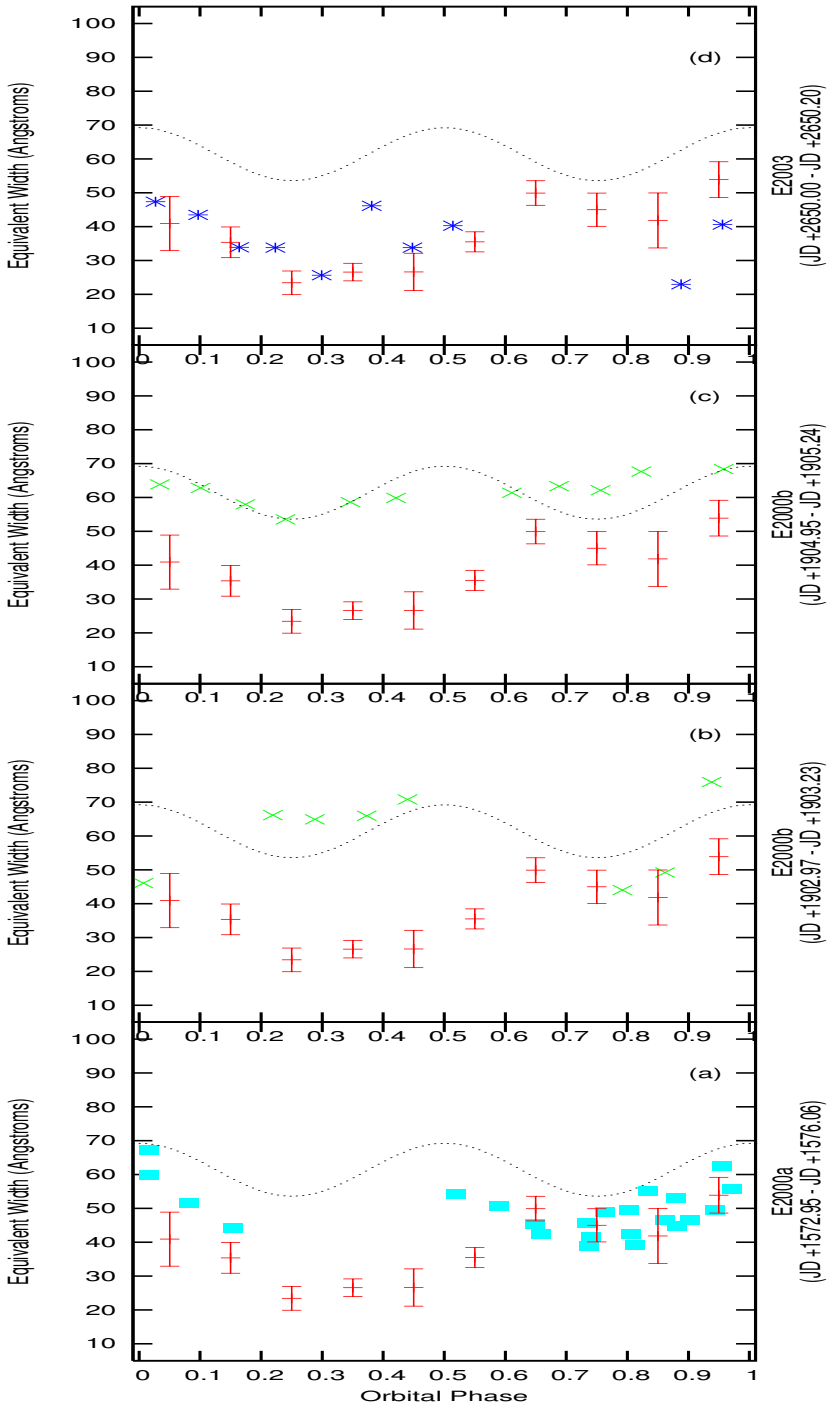

Figure 4.11: The equivalent width (EW) of each orbital phase bin plotted for all observations taken in E2000a, E2000b, and E2003. Separate plots were made for each observation in E2000b and E2003 to show the different EWs obtained for the same phases. The EWs from E2000a are represented by '■', E2000b by '×', and E2003 by '∗'. Each panel includes the the EW fit taken from Marsh *et al.* (1994) (dotted line), and the overall mean EW (error bars) in each orbital phase.

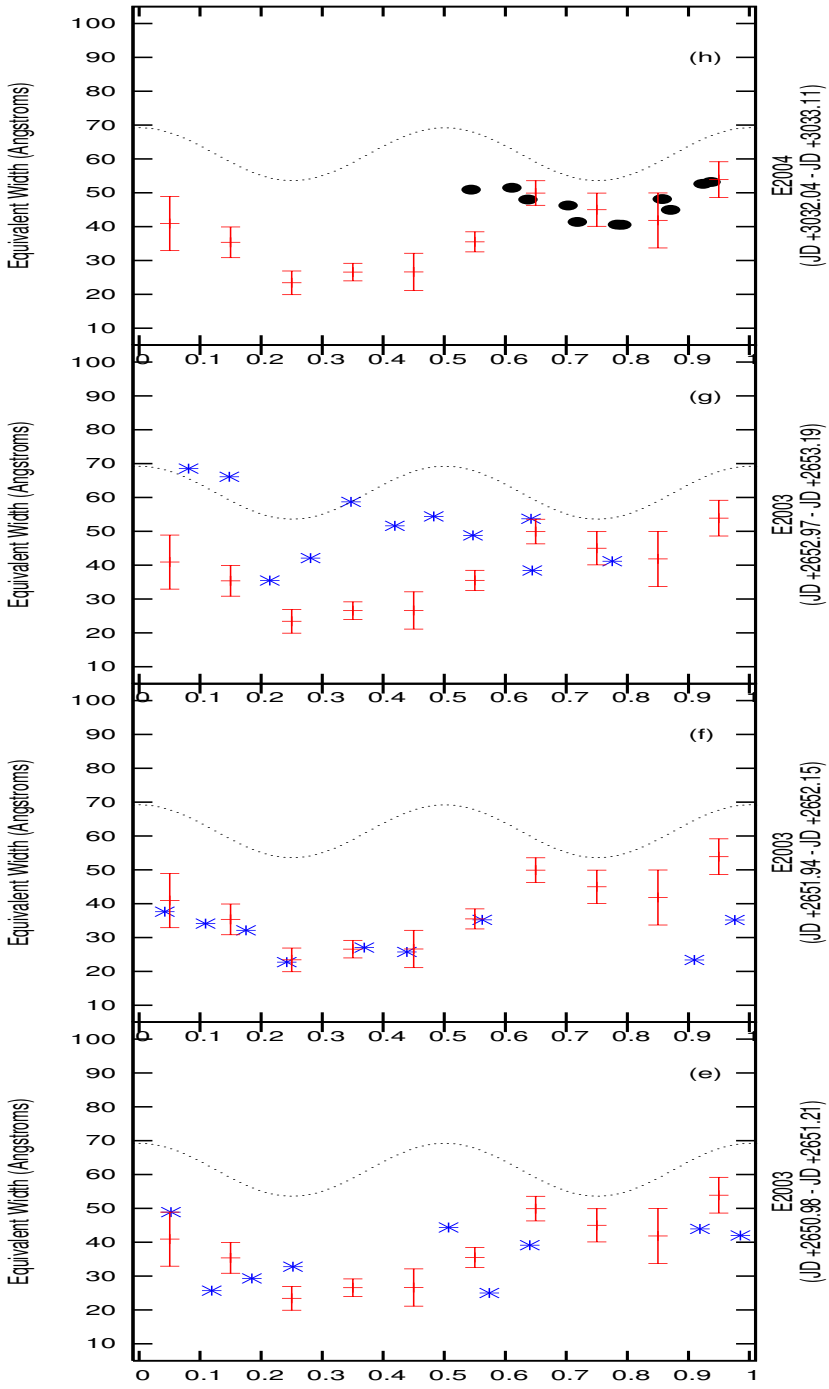

Figure 4.12: The equivalent width (EW) of each orbital phase bin plotted for all observations taken in E2003 (continued) and E2004. The EWs from E2003 are represented by '$*$', and E2004 by '$\bullet$'. Separate plots were made for each observation in E2003 to highlight the different EWs obtained for the same phases. Each panel includes the the EW fit taken from Marsh *et al.* (1994) (dotted line), and the overall mean EW (error bars) in each orbital phase

The overall mean EW data of each observing run in Figures 4.11 and 4.12 were compared with the EW fit derived by Marsh *et al.* (1994) (hereafter known as template EW fit).

The outline defined by the overall mean EW is different from the fit. A similar shape was expected as the same method was used in obtaining the radial velocity and mass function. In addition, the yield radial velocity and mass function obtained are very close to that of Marsh *et al.* (1994). It is suspected that such difference was due to the higher resolution of data used in this study.

Table 4.2: Equivalent widths of the Hα emission line.

JD +	**Orbital Phase**	**EW (Å)**	**JD +**	**Orbital Phase**	**EW (Å)**
Orbital Mean 0.0-0.1			Orbital Mean 0.5-0.6		
1575.05	0.017	59.80	1572.95	0.519	54.36
1576.02	0.017	67.16	1572.97	0.589	50.55
1576.04	0.081	51.69	2650.20	0.514	40.28
1903.23	0.007	46.08	2651.17	0.507	44.34
1905.17	0.034	63.85	2651.19	0.574	25.00
2650.04	0.027	47.36	2652.15	0.562	35.23
2650.06	0.097	43.48	2653.12	0.547	48.80
2651.02	0.052	48.91	3032.98	0.544	50.91
2651.99	0.042	37.66			
2652.97	0.081	68.51			
Orbital Mean 0.1-0.2			Orbital Mean 0.6-0.7		
1576.06	0.154	44.23	1572.99	0.659	42.39
1905.20	0.101	62.84	1573.96	0.648	45.32
1905.22	0.174	57.98	1905.04	0.611	61.41
2650.09	0.164	33.90	1905.06	0.688	63.32
2651.04	0.119	25.68	2651.21	0.64	39.11
2651.06	0.185	29.3	2653.148	0.642	53.69
2652.01	0.109	34.13	2653.149	0.644	38.41
2652.03	0.175	32.13	3032.04	0.637	47.99
2652.99	0.148	66.13	3033.00	0.611	51.48

EW refers to the Equivalent width

Continued on next page...

Table 4.2: continued

JD +	**Orbital Phase**	**EW (Å)**	**JD +**	**Orbital Phase**	**EW (Å)**
Orbital Mean 0.2-0.3			Orbital Mean 0.7-0.8		
1902.97	0.219	66.18	1573.02	0.734	45.61
1902.99	0.288	64.92	1574.00	0.764	48.83
1905.24	0.24	53.51	1574.96	0.74	41.59
2650.11	0.223	33.80	1575.93	0.738	38.93
2650.13	0.299	25.65	1903.16	0.792	44.04
2651.08	0.252	32.76	1905.08	0.756	62.14
2652.05	0.242	22.73	2653.19	0.775	41.14
2653.01	0.214	35.47	3032.06	0.703	46.27
2653.03	0.281	42.08	3032.09	0.791	40.56
			3033.04	0.718	41.40
			3033.06	0.784	40.60
Orbital Mean 0.3-0.4			Orbital Mean 0.8-0.9		
1903.02	0.373	65.98	1573.04	0.803	49.65
1904.95	0.346	58.61	1573.06	0.861	46.60
2650.16	0.381	46.16	1574.02	0.834	55.01
2652.09	0.369	27.05	1574.98	0.812	39.25
2653.05	0.347	58.70	1575.00	0.881	44.90
			1575.95	0.806	42.37
			1575.97	0.879	53.03
			1903.18	0.862	49.23
			1905.11	0.823	67.66
			2650.00	0.888	22.94
			3032.11	0.857	48.15
			3033.09	0.871	44.96
Orbital Mean 0.4-0.5			Orbital Mean 0.9-1.0		
1903.04	0.44	70.79	1574.04	0.903	46.60
1904.98	0.421	59.87	1574.06	0.972	55.69
2650.18	0.448	33.81	1575.03	0.956	62.44
2652.11	0.439	24.53	1575.99	0.944	49.45

EW refers to the Equivalent width

Continued on next page...

Table 4.2: continued

JD +	**Orbital Phase**	**EW (Å)**	**JD +**	**Orbital Phase**	**EW (Å)**
2653.08	0.419	51.64	1903.20	0.938	75.91
2653.10	0.483	54.38	1905.15	0.958	68.36
			2650.02	0.956	40.59
			2650.98	0.919	43.95
			2651.00	0.985	41.98
			2651.94	0.91	23.38
			2651.96	0.976	35.17
			3032.13	0.924	52.62
			3033.11	0.937	53.18

EW refers to the Equivalent width

The phase dependent variation in the EW is detected over the long timescale of 5 years, and the overall mean EW. The shallow incurvature of the EW-phase plot at orbital phase 0.4-0.5 and the two deeper (but of different depth) incurvatures at quadrature phases (orbital phase 0.2-0.3 and 0.7-0.8) suggest the presence of a hotspot on the accretion disc.

There is an apparent broad feature in Figure 4.13. If this feature is to be interpreted as a broad absorption trough, seen in some of the spectra. It hints at the presence of wind on the accretion disc. The latter is most evident in the E2003 spectra, and the EW of these spectra are also much lower than the values of the template EW fit.

Furthermore, the lower EW (or higher luminosity) of the spectra in E2003 could also be evidence of a higher than normal mass transfer rate. This increase in mass transfer could generate an outflow/wind on the accretion disc, hence the broad absorption trough.

If only the region of the blue peak of the H$\alpha$is considered, this feature resembles a P-Cyngni profile. Potentially, it is produced in a region on the accretion disc very close to the accreting object. However, symmetry of the shape of the red and blue peaks is preserved in some of these spectra, implying that this wind is not strong enough to significantly absorb and to perturb the symmetry of shape of the peaks of the Hα line.

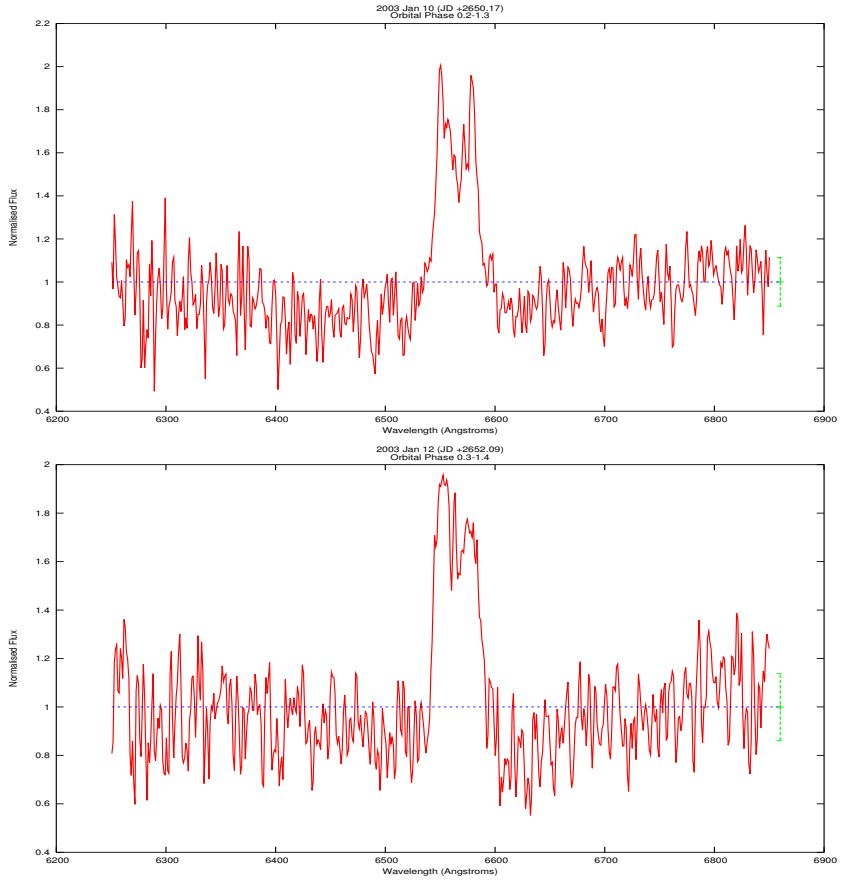

Figure 4.13: Examples of a narrow Hα emission line superimposed onto a broad feature. The top spectrum (JD +2650.13) is at the orbital phase 0.299, and the bottom spectrum (JD +2651.04) is at phase 0.369. The straight line is the normalised continuum. The Hα emission line occurs in a broad feature in both spectra.

However, the extension of the trough into region where the red peak of the Hα line, and the symmetry of the two peaks of the Hα line makes the feature an unlikely candidate for absorption. It is plausible that this feature is an intrinsic feature of the companion star that has not been studied, or is a result of a change in mass lost that is not understood.

The change in the asymmetry of the shape of the peaks seen in some of these the Hα line profile could, therefore, be mainly a result of the motion of a hotspot on the disc, and to some extent the absorption by wind on the accretion disc.

4.6 Emission Lines Shapes

Some of the spectra (see Figures 3.13 to 3.22) do not have a distinctive double peaked profile. Instead, some of these spectra have a flat-topped line profile, and there are few which seem to have a triple peaked profile.

There are two main possibilities which could have caused the flat-topped profile, namely the presence of other components such as a hotspot on the accretion disc or the effect of a wind in the accretion disc.

When the emitted line from the accretion disc passes through a region of wind, the peaks may be smeared out and the line profile may appear flat-topped, if the lines have substantial optical depth ($\tau \gtrsim 2$) (Murray & Chiang (1997), see Figure 4.14). Depending on the direction of the motion of the wind, the emitted line would be fainter for wind accelerating away from the observer and brighter for wind accelerating towards the observer.

The spectrum in panel (a) of Figure 4.14 is an example of a profile of the emitted line which propagated through a wind accelerating away from the observer. It is fainter than the overall mean spectrum.

Alternatively, the presence of other spectral components could also smear the double peaked, and produce a flat-topped profile. It is plausible that there are unknown components which are superimposed onto the Hα line. One of the possible components is a hotspot on the accretion disc, which when added onto the Hα component, will give raise the line profile see in Figure 4.14b.

Besides the profiles similar to those in Figure 4.14b, there are some double peaked profiles of the spectra which suggest the presence of a hot spot. For instance, for a hotspot moving on the accretion disc, away from the observer, it is expected to manifest in the red region of the double peaked line (see Figure 4.15b), thus making the peak more intense and wider than the other. For profiles that seem to be triple peaked, the central peak can be attributed to a possible hot spot component, as it moves from the red region towards the blue region or vice versa, for example, Figure 4.15a.

However the line profile of the overall mean of the spectra is clearly double peaked, thus suggesting that the effects from either or both the above-mentioned conditions are not dominant. The marginal asymmetry of the peaks in the overall mean does, however support the possibility that the stronger bluer region of the line is likely to be due to the hot spot component superimposed onto the Hα line

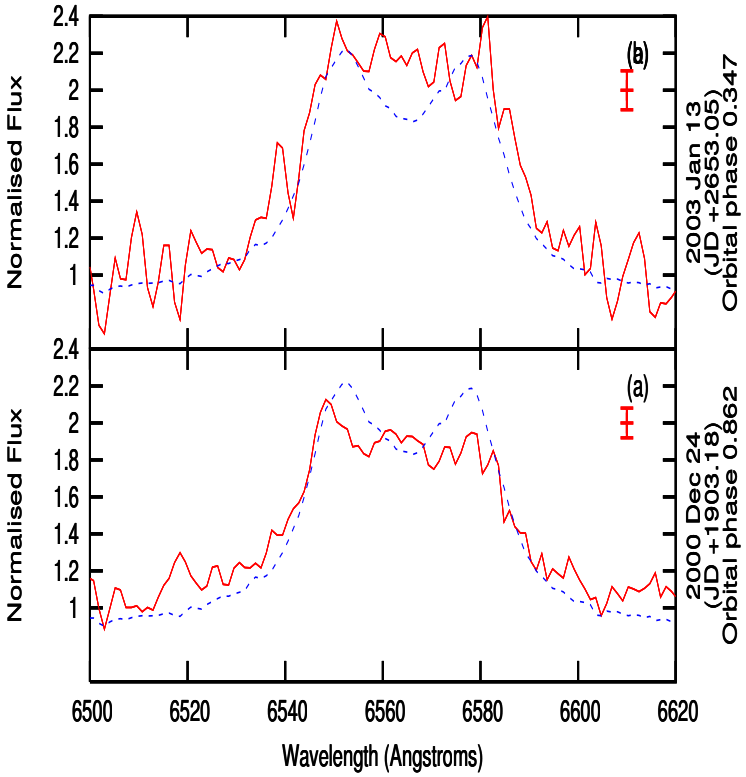

Figure 4.14: These are two examples of the flat-topped Hα line from the considered spectra (lines) are plotted over by the overall mean spectrum (short dashes). The error bar on the top right indicates the error of the considered spectrum. The flat-topped feature is usually found in the orbital phase bins 0.3-0.4 and 0.8-0.9. The spectrum in panel (a) is an example of how a line profile would look if the emitted line was passed through a wind accelerating away from the observer. It is fainter than the overall mean spectrum. Panel (b), on the other hand, shows a flat-topped profile which is likely due to the effect wind from the accretion propagating towards the observer. The intensity in (b) was not attenuated as shown in panel (a), but increased. Alternatively, this gain in brightness could be the presence of unknown components superimposed onto the Hα line.

and/or due to the wind in the accretion disc accelerating towards the observer.

There was another parameter measured in Chapter 3, it is the displacement of the peaks of the Doppler shift lines from the rest wavelength. The measurements of the Doppler shift lines in Section 3.4 show that the peak of the redshifted line (the red peak) is generally displaced further from the rest wavelength than the peak of the blue shifted line (the blue peak). However, exceptions were also noted

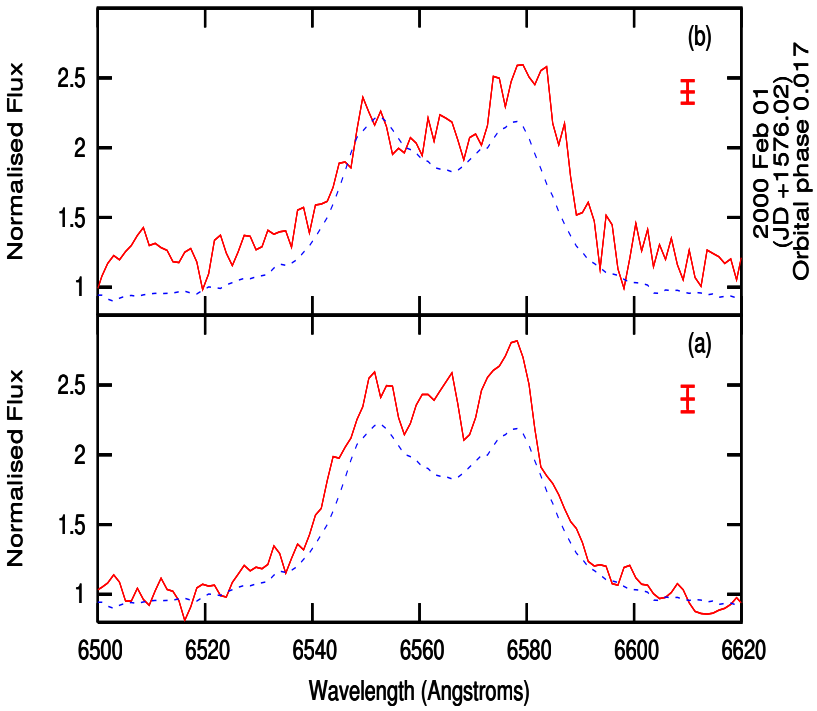

Figure 4.15: These are examples of the triple peaked Hα line from the spectra. The considered spectra (lines) are plotted over by the overall mean spectrum (short dashes). The error bar on the top right indicates the error of the considered spectrum. This third middle peak feature is usually found in the orbital phase bins 0.0-0.1 and 0.4-0.5.

in the orbital phase bins 0.7-0.8 and 0.8-0.9, where most of the blue peaks of the latter bins were either displaced equally or more than the red peaks.

When one of a Doppler shift emission line is displaced further than its counterpart, it indicates that the former line has a higher velocity. Hence it is plausible that it originated from a region closer to the central object. In this case, the difference in peaks displacement is likely to be due to an asymmetric disc. However, for an accretion disc with a probable hotspot, the difference in the displacement of the peaks will also be affected by the presence of the hotspot. The decrease of the red shifted peak's displacements and the increase of the blue peak's displacement in the orbital phase bin 0.7-0.8 and 0.8-0.9 could be due to the movement of the hotspot. The position of the hotspot at orbital phase bin 0.7-0.8 and 0.8-0.9

is significantly further from the central object than at other phase bins. The spectra in these two near quadrature orbital phase bins are generally fainter than those in the opposite quadrature.

4.7 Width of the Hα Line

The previous section has examined the changes in the shape of the Hα line. This section will focus on changes in the line width. The 10% level of the lower peak is chosen to ensure that the width of the line is measured at the lowest possible height from the continuum. The changes in the width indicate a change in the distance of the emitting region to the centre of the compact object (Smak, 1981).

Figure 4.16 describes how each line width is measured. A spectrum is first fitted by a 3 Gaussian function, and the width of the fitted function is taken at 10% of the lowest peak. The spectra of each observing run were first measured to serve as a check to ensure that the variation of the line widths are not due to random but strong fluctuations. The spectra in Figure 4.16 are plotted on the same vertical scale, each overlaid with its respective fitted function (dashes).

The width of the Hα line is plotted for each spectrum as a function of time in Figure 4.17. Each panel presents the widths of Hα lines from the same observing campaign, and each subsequent bar of the same colour represents the width of a succeeding observation taken on the same night.

The line widths of the spectra in panel (a), taken in 2000 between January and February, are found to be in the range from $\sim$ 55 - 85 Å, with a majority of the line width $\sim$ 60 Å. In contrast, the line widths of all of the spectra in panel (b), which were observed in 2000 December, were measured to be wider at $\sim$ 90 Å. The observation logs reflected non photometric observing conditions for the 2000 December observations, but the SNR for each spectrum was high. Thus, it is unlikely that the observing conditions could significantly affect line width. Therefore the change in the line width is most probably due to a change in the emitting region on the accretion disc. The wider wings of the Hα line indicate that the emission are of a higher velocity, as so originate from a region closer to the central accreting object.

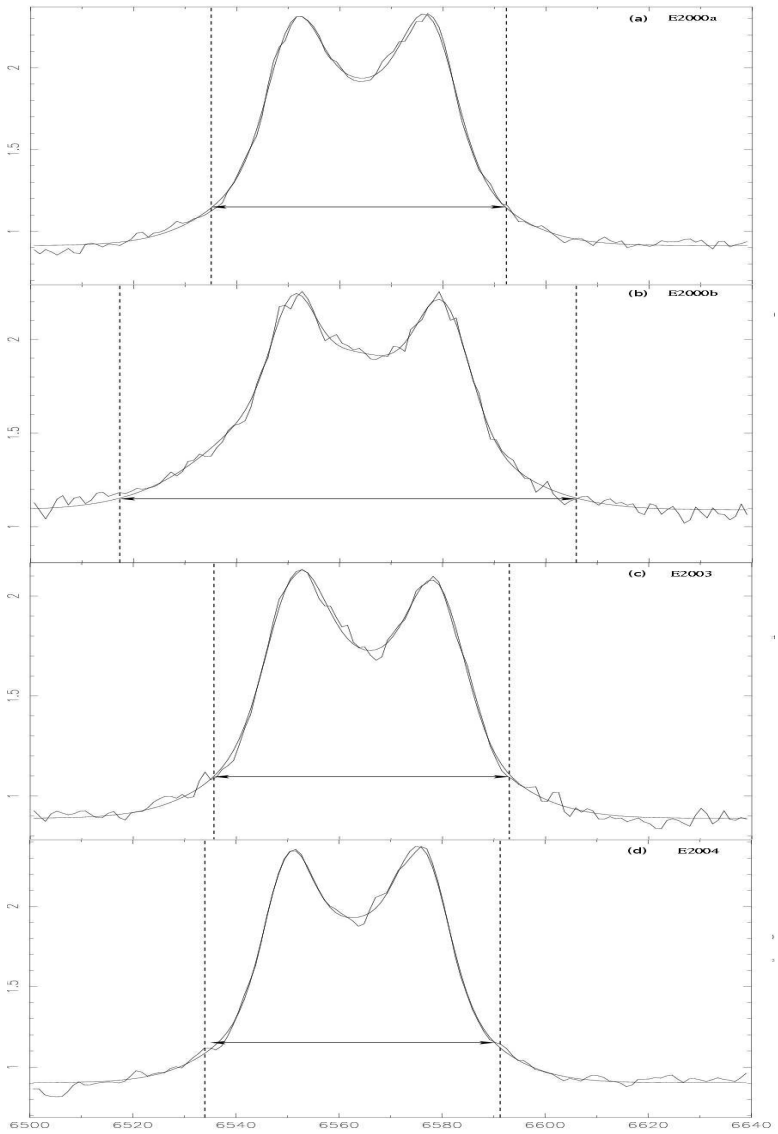

Figure 4.16: A comparison of the line widths of Hα of the mean spectrum the mean spectrum of each campaign. The individual mean spectrum (line) in each panel is plotted with a model of the Gaussians fit (dashes). The two vertical lines in each panel indicates the width of the Hα line, marked out by the horizontal double arrowed line at 10% of the lower peak. The panel (a),(b),(c) and (d) shows the average spectrum of the E2000a, E2000b, E2003 and E2004 campaign.

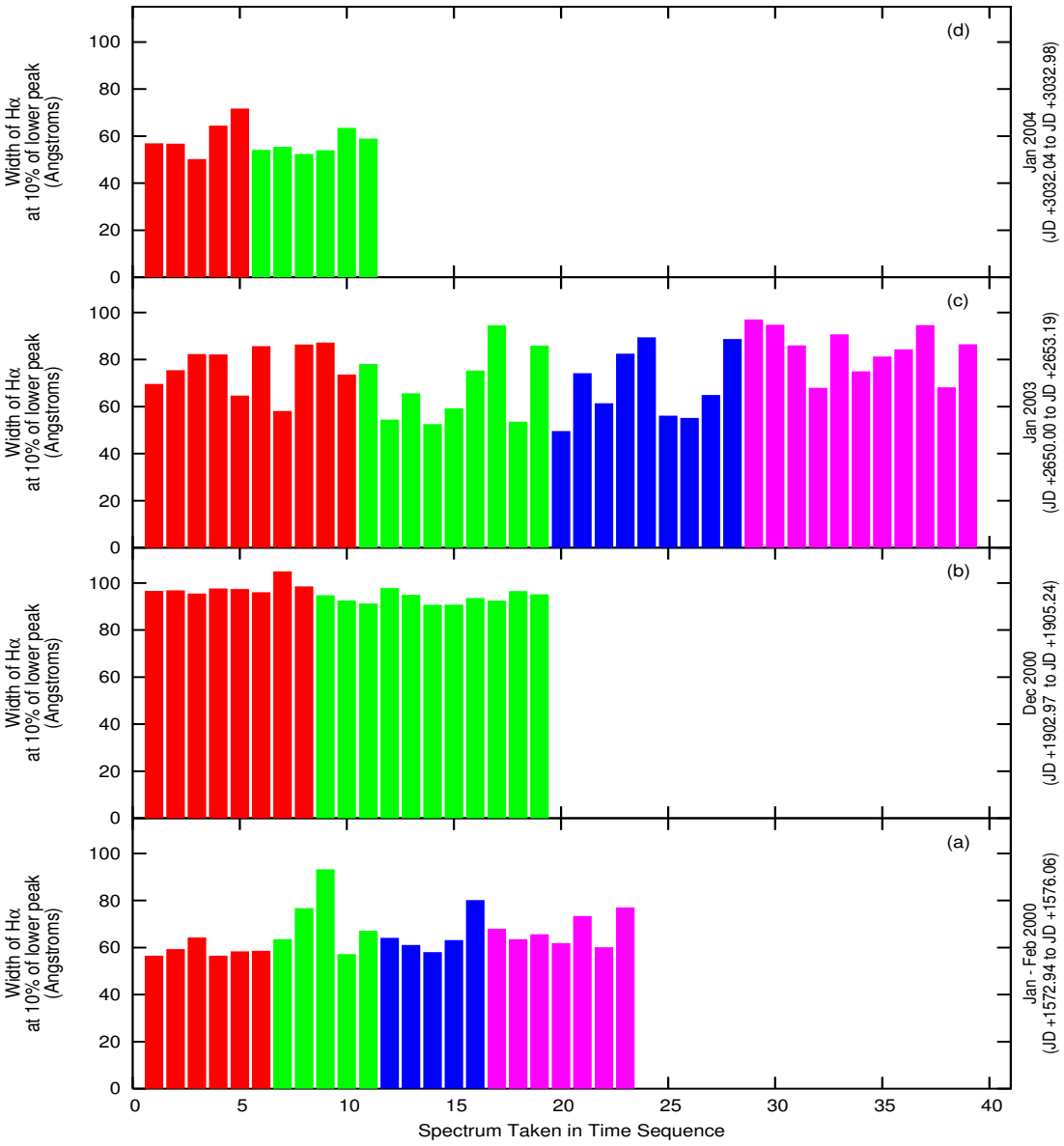

Figure 4.17: The line widths of Hα at 10% of the lower peak (chronological order). Each panel presents the widths of Hα lines from the same observing campaign, and each subsequent bar of the same colour represents the width of the next observation taken on the same night. The line widths of the spectra from E2000b are consistently wider than those of other campaigns. The 10-month observing gap between the observations in 2000 (between January and December) is comparable to the 12 months between 2003 and 2004. A change in the line width suggests a change in the emitting region on the accretion disc. A wider line width could be a result of the inner edge of the disc extending towards the central object. Hence, the emission of the E2000b spectra could have occurred in a region closer to the accreting object.

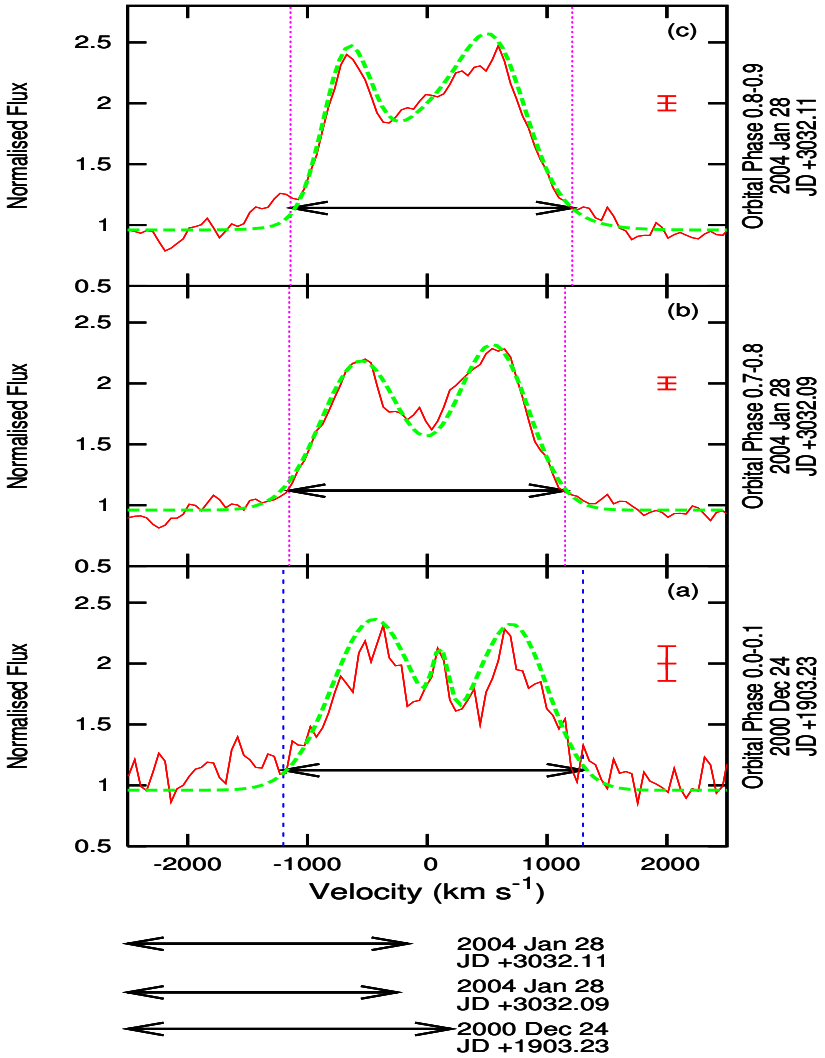

Figure 4.18: A comparison of the line widths of Hα. The individual spectrum (line) in each panel is plotted with its error and the fit using a 3 Gaussians function (dashes). The two vertical lines in each panel indicates the width of the Hα line, marked out by the horizontal double arrowed line at 10% of the lower peak. The lowest panel (a) shows the spectrum with the widest line width, taken on 2000 Dec 24 (JD +1903.23). The spectrum in panel (b) shows the spectrum with the narrowest line width, taken on JD 3032.09 (2004 Jan 28). The spectrum in panel (c) is taken on the same observing night JD 3032.11 (2004 Jan 28), however the line width is significant larger than the other spectra taken in the same observing run. The length of the arrows corresponding to the width of the spectra are compared below the plots.

The line widths of the spectra in the 2003 January observing campaign in panel (c) vary more from spectrum to spectrum for the same observing night than those of panels (a), (b) and (d). The E2003 line widths vary from $\sim$ 50 Å to $\sim$ 95 Å, with the average of the line widths at $\sim$ 60 Å.

The observing conditions of these spectra were photometric except for the observations done on the last day of this campaign (2003 Jan 13, JD +2652.97 to JD +2653.19). However, the general SNR for the spectra in this campaign is very low. Therefore the cause of the variability could to be due to the poor SNR of the spectra (see Appendix B).

The spectra taken in 2004 January in panel (d) measured an average line width of $\sim$ 60 Å, and are less variable compared to the line widths of the spectra in panel (c).

The changes in the line widths shown in Figure 4.17 are studied in Figure 4.18. The spectra are plotted on the same vertical scale, each overlaid with its respective Gaussian function fit (dashes).

The spectrum with the largest line width (2000 Dec 24, JD +1903.23) is plotted in the lowest panel (a). Panel (b) shows the spectrum with the smallest line width is taken on JD +3032.09 (2004 Jan 28). Although the spectrum in panel (c) is taken on the same observing night as JD +3032.11 (2004 Jan 28), its line width is much wider than that of the other spectra of the same observing run.

There has been no evidence of long-term variability of the width of the Hα line, since its outburst in 1975 (Whelan *et al.*, 1977). The $\sim$10-month observing gap between the observations in 2000 (between January and December) is comparable to the $\sim$12 month gap between 2003 and 2004, but the line widening effect was not present. This advocates that this spectral property is most probably a long timescale variability in the emission region of the disc, and is unique to the E2000b (2000 December) spectra.

With the exception of the spectra taken in E2003, the line widths in the observing campaigns E2000a and E2004 also seem to be changing. This suggests that there might also be a short timescale variability in the emission region on accretion disc.

The spectra taken on 2000 Jan 29 (JD +15727.94 to JD +1573.06), together with the first 4 spectra taken on 2004 Jan 28 (JD +3032.04 to JD +3032.11), and all but the $4th$ spectrum taken on 2004 Jan 29 (JD +3032.98 to JD +3033.11)

revealed that the variability in the line widths are intrinsic. These spectra were taken under photometric conditions, and they have high SNR.

Figure 4.19 examines the Hα line width to look for a trend in the change in terms of orbital phase. Each individual panel shows the line width as a function of time in an orbital phase bin. Each bar colour represents the line width of a spectrum from an observing campaign. A cyan bar is used for E2000a, a green bar for E2000b, a blue bar for E2003, and lastly a magenta bar for E2004.

The line widths of spectra from E2000a and E2004 in orbital phase bins 0.6-0.7 to 0.9-1.0 have less varying line widths, except for spectrum JD +1574.00, the $3rd$ spectrum in orbital phase bin 0.8-0.9. Despite that, there is little evidence from Figure 4.19 to indicate that the change of the line widths of the Hα line is orbital phase dependent.

4.8 Changes in the Shape of the Hα Line

It is established that the line profile of the Hα line changes with time and orbital phase, however it is unclear how the line profile changes with respect to the overall mean spectrum for each wavelength bin. In this section, each wavelength bin of each spectrum is compared to the overall mean spectrum. The flux difference between each wavelength bin of the individual spectrum and the overall mean spectrum is quantified by Δ (Equation 4.3). The plots of the Δs for each spectrum can be found in Appendix D.

$$\Delta(x) = \frac{(m(x) - s(x))^2}{(\sigma_m^2 + \sigma_s^2)} \tag{4.3}$$

where $\Delta(x)$ is the weighted squared difference of a spectrum and the mean spectrum at wavelength bin x, $m(x)$ is the value in the bin x of the mean spectrum and $s(x)$ is the value in the bin x of the spectrum under consideration. σ_m and σ_s are the expected errors or variances of the mean spectrum and the considered spectrum respectively (see Equation 4.2).

The χ^2 of each spectrum, in Sections 4.3 and 4.4, is the sum of all Δs. The $\frac{\chi^2}{df}$ indicates how similar the spectrum is to the overall mean spectrum. Thus $\Delta(x)$ provides a way to inspect the wavelength region responsible for the high $\frac{\chi^2}{df}$ value.

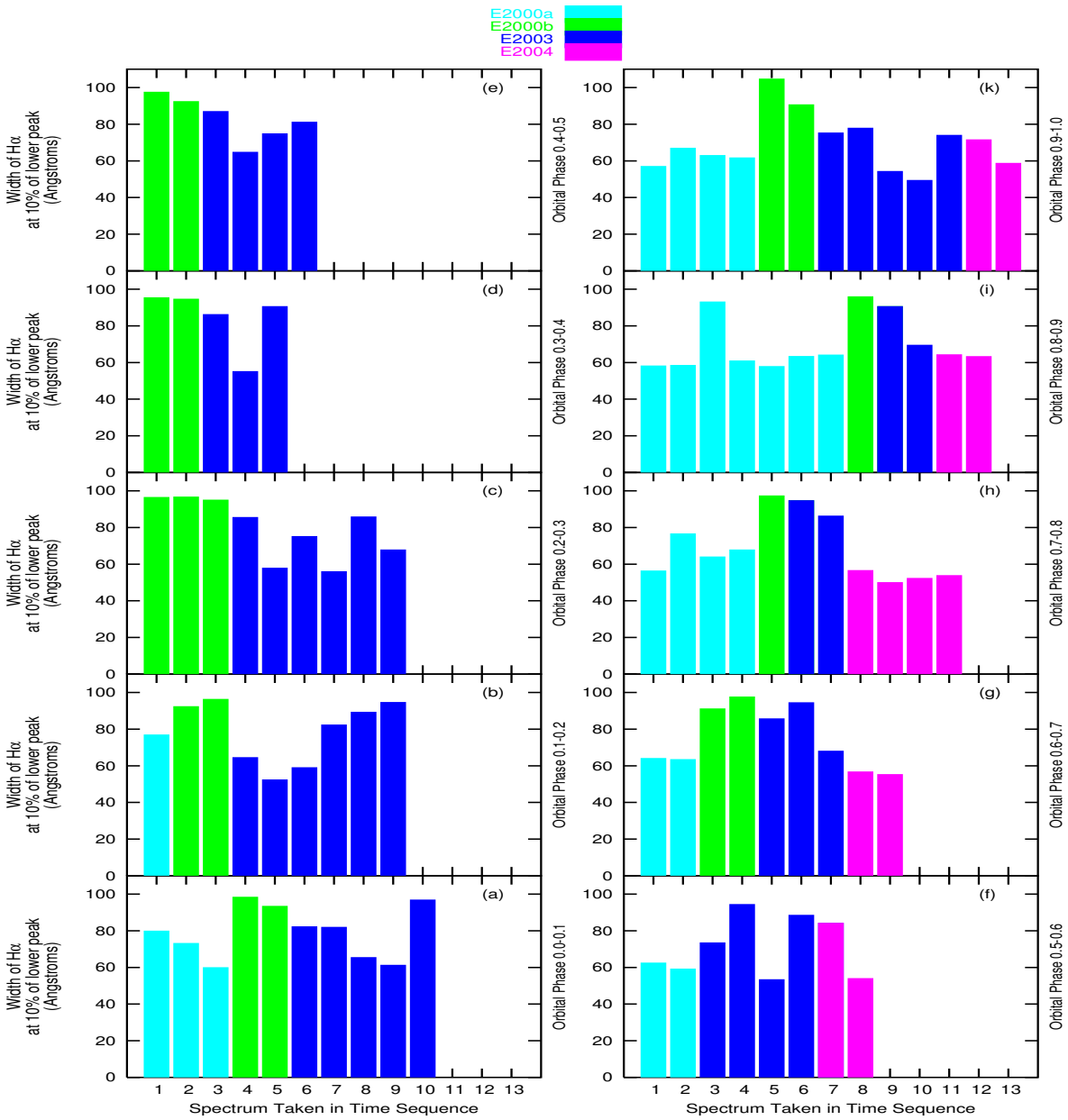

Figure 4.19: The line widths of Hα at 10% of the lower peak (orbital phase ordered). Each individual panel shows the line width as a function of time in an orbital phase bin. Each bar colour represents the line width of a spectrum from an observing campaign. A cyan bar is used for E2000a, a green bar for E2000b, a blue bar for E2003, and lastly a magenta bar for E2004. The changes in the width of Hα do not appear to be orbital phase dependent.

Figures 4.20 and 4.21 show the spectra with the highest and the lowest $\frac{\chi^2}{df}$. The spectrum taken on JD +1575.03 has the largest $\frac{\chi^2}{df}$, and the region responsible is shown in Figure 4.20. The figure shows the Δs in the Hα region overlaid with the overall mean spectrum (grey line) and the spectrum taken on JD +1575.03 (black line). Both the overall mean spectrum and the considered spectrum are plotted on the same arbitrary vertical axis, to illustrate the regions that correspond to the Δs.

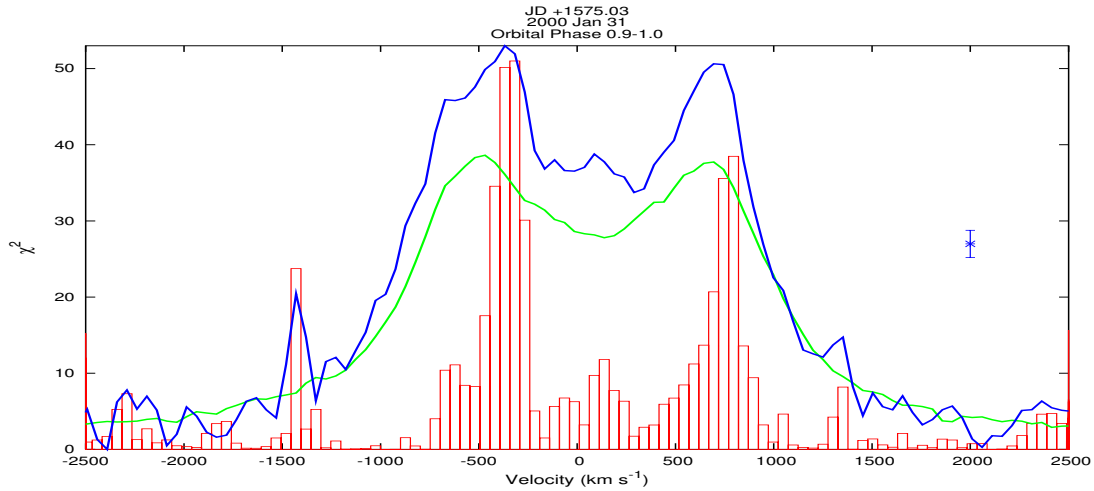

Figure 4.20: The largest $\frac{\chi^2}{df}$, and the region of the attributing Δs of spectrum JD +1575.03. The Δs are overlaid with the overall mean spectrum (grey line) and the spectrum JD +1575.03 (black line) and its the error bar. Both mean spectrum and the spectrum JD +1575.03 are plotted to an arbitrary vertical axis, to illustrate the regions that correspond to the Δ.

Figure 4.21 shows a spectrum with a very small $\frac{\chi^2}{df}$, it indicates that the considered spectrum is very similar in line profile to the overall mean spectrum. It is suggested in Figure 4.20 that most of the large $\frac{\chi^2}{df}$ values ($\frac{\chi^2}{df} \geq 5$) resulted from a change in the intensity of the line profile, and/or a change in the Hα line width, or from the flat-topped line profile, or a combination of these changes.

The largest $\frac{\chi^2}{df}$ is caused by a more intense and wider double peaked Hα line profile (see Figure 4.20). The difference in the intensity of the Hα line is found to be one of the major factors in getting a large $\frac{\chi^2}{df}$ value. Most of the large $\frac{\chi^2}{df}$ values are clearly due to a combination of the intensity and other factors such as the width of the Hα line (e.g. Figure 4.23), the flat-topped line profile (e.g. Figure 4.22) and a combination of all three factors (e.g. Figure 4.24). All details of

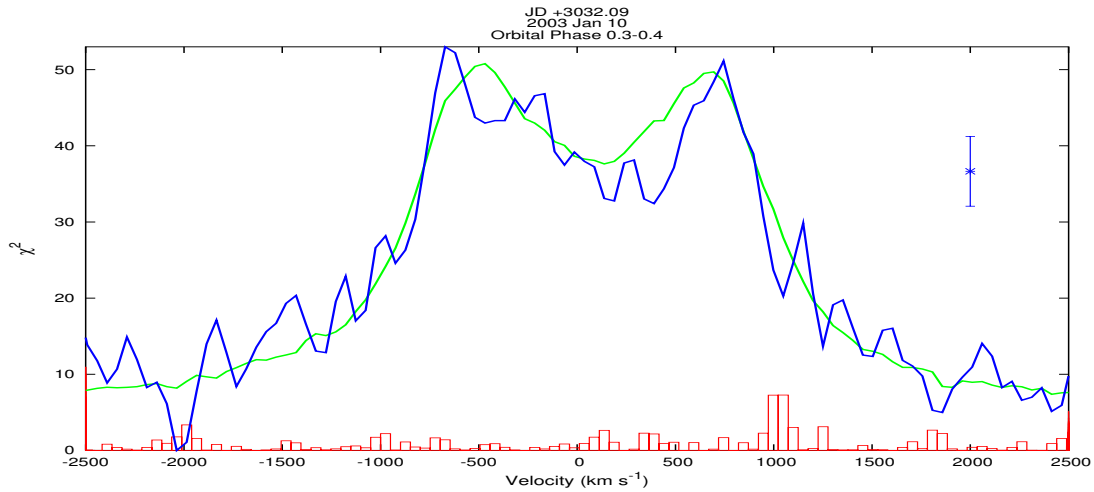

Figure 4.21: The smallest $\frac{\chi^2}{df}$, and the region of the attributing Δs of spectrum JD +3032.09. The Δs are overlaid with the overall mean spectrum (grey line) and the spectrum JD +3032.09 (black line) and its the error bar. Though the spectrum JD +1905.11 (black line) and the mean spectrum (grey line) are different, these difference are very small compared to the uncertainty or error of the mean spectrum, hence the small Δ.

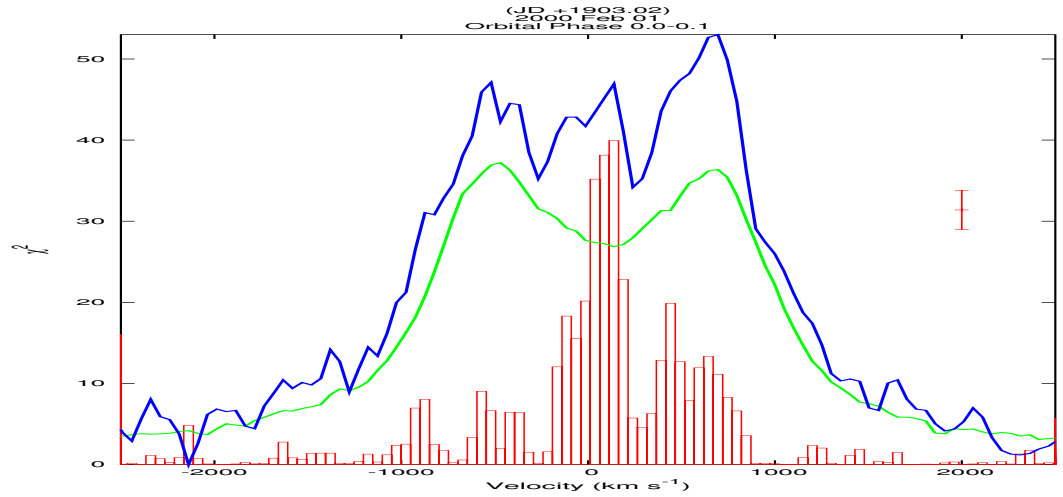

Figure 4.22: An example of the flat-topped profile affecting the $\frac{\chi^2}{df}$ value. The value of Δs are represented by the bars, and plotted over with the spectrum JD +1903.02 (2000 Feb 01) in black line, and the overall mean spectrum in grey line. The presence of the peak at about 0 km s^{-1}and the more intense red peak are most different from the mean, hence the resultant Δ.

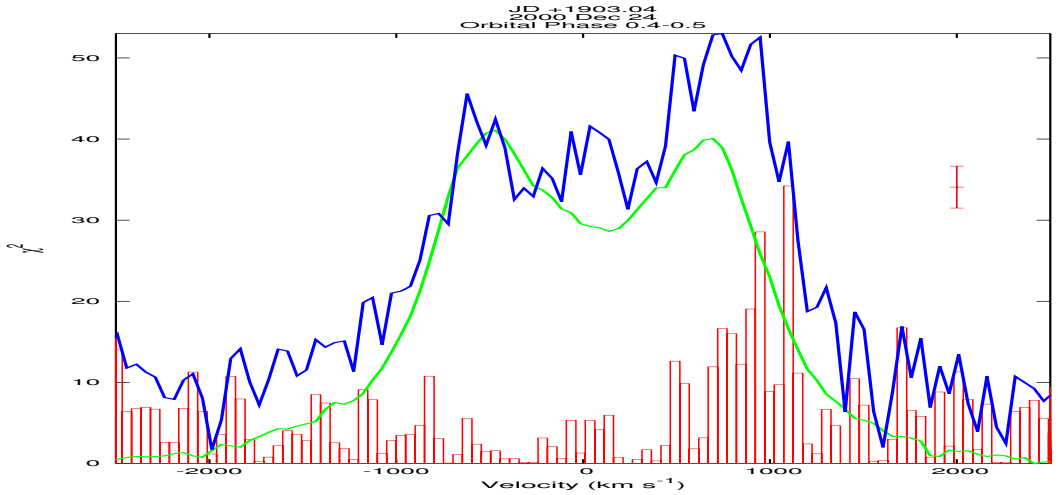

Figure 4.23: An example of the width of the Hα line profile affecting the $\frac{\chi^2}{df}$ value. The value of Δs are represented by the bars, and plotted over with the spectrum JD +1903.04 (2000 Dec 24) in black line, and the overall mean spectrum in grey line.

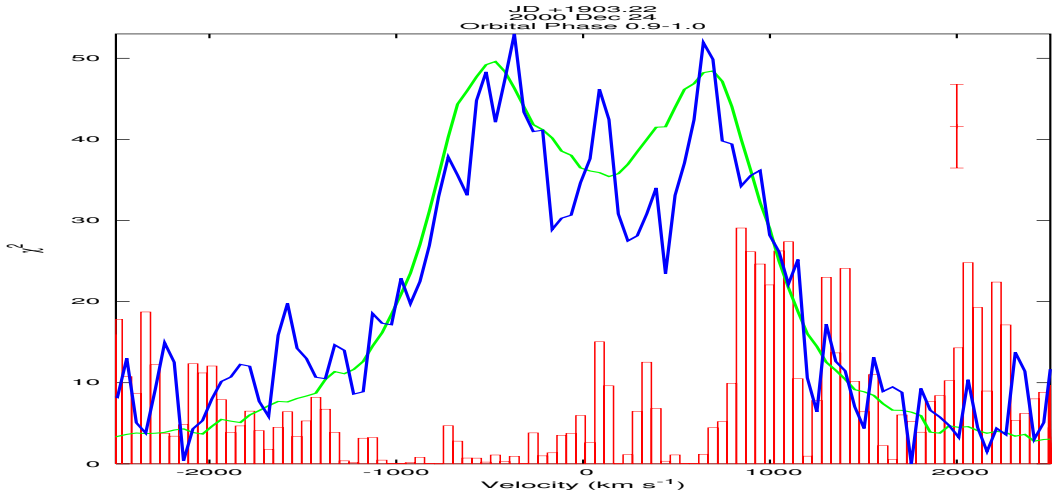

Figure 4.24: An example of the Hα line profile affecting the $\frac{\chi^2}{df}$ value. The value of Δs are represented by the bars, and plotted over with the spectrum JD +1903.22 (2000 Dec 24) in black line, and the overall mean spectrum in grey line.

the regions affecting the Hα line profile can be seen in Figures D.1 to D.10 in Appendix D.

4.9 Parameters That Change in Line Profile

The changes in the Hα line profile are measured by different parameters, namely, the equivalent width (EW), the $\frac{\chi^2}{df}$, and the line width. The causes of the high $\frac{\chi^2}{df}$ are examined in Section 4.8, and it is ascertained that there is a relationship between the $\frac{\chi^2}{df}$ values on the Hα line width, line intensity, and profile of the peaks. The line intensity is measured using the EW, and the profile is noted to change with the orbital phase.

There appears to be a linear dependence between the changes in each of these measured parameters and the orbital phase parameter. In order to determine which combination of these parameters contribute the most to the changes in the Hα line profile, the parameters were correlated and ranked using Principal Component Analysis (PCA) (Francis & Wills, 1999).

For example, to simplify the relationship of n set data where each set of data consist of m parameters. PCA identifies trends in the data by measuring how each element (each nth value) of a parameter varies from its respective mean. It then groups the element to a new parameter which is ranked according to the order of the differences. The first principal component, the first of the new parameters, accounts for most variability in the data, and the succeeding components account for the subsequent remaining variability.

Each principal component (PC) is a linear combination of the original parameters, and each element of the components indicates the weight of each of the input parameters, shown in Equation 4.4.

$$PC_i = a_{i1}x_1 + a_{i2}x_2 + ... + a_{in}x_n \tag{4.4}$$

where PC_i defines the ith principal component, a_{in} is the coefficient of parameter x_n of set 'a'. The coefficient is weighted such that the sum of the squares of a_{ij} is 1.

A sample of the parameters used for the analysis is listed in Table 4.3 and the full list is found in Appendix F. A total of 91 spectra, which excludes the spectrum JD +1903.20, were used for the PCA. The results of the analysis are tabulated in Table 4.4.

The PCA was then performed for different sets of data, each with 1 less

Table 4.3: Table of Parameters Used For PCA

Julian Date*	**Orbital Phase**	**EW (Å)**	$\frac{\chi^2}{df}$	**Line Width (Å)**	**..**
1572.95	0.519	54.36	7.83	56.51	..
1572.97	0.589	50.55	4.57	59.32	..
1572.99	0.659	42.39	1.58	64.26	..
...					

* not used in PCA, for identification purpose only

EW denotes Equivalent Width

parameter than the initial analysis which involves all the parameters. This was done to test the significance of a parameter's contribution to the variance (the derived eigenvalue). The line width parameter is the primary cause of the large variance of the data. However, the large variance is also affected to a lesser degree by the parameters EW and orbital phase. The orbital phase parameter has a much weaker correlation than the EW parameter. Comparing the results from the PCA results of the 4-parameters analysis and that of the 3 parameters, it is found that the largest variance of the spectra does not correlate with $\frac{\chi^2}{df}$. The values of the first eigenvalue and eigenvectors do not change significantly ($<$ 1%).

Table 4.4: Table of PCA results (4 parameters)

Principal Component	**PC1**	**PC2**	**PC3**	**PC4**
Eigenvalue	1.61	1.22	0.86	0.30
% of Total Variance	40.38	30.56	21.56	7.50
Parameters				
Orbital Phase	0.37	-0.41	-0.80	-0.22
EW (Å)	-0.63	-0.42	-0.25	0.62
$\frac{\chi^2}{df}$	-0.05	-0.78	0.48	-0.39
Line Width (Å)	-0.69	0.21	-0.25	-0.65

Although the next significant change in the feature of the data is dominated by $\frac{\chi^2}{df}$, the latter's contribution is affected by EW and the line width. The absence of either parameters reduces the significance of the $\frac{\chi^2}{df}$ parameter's contribution,

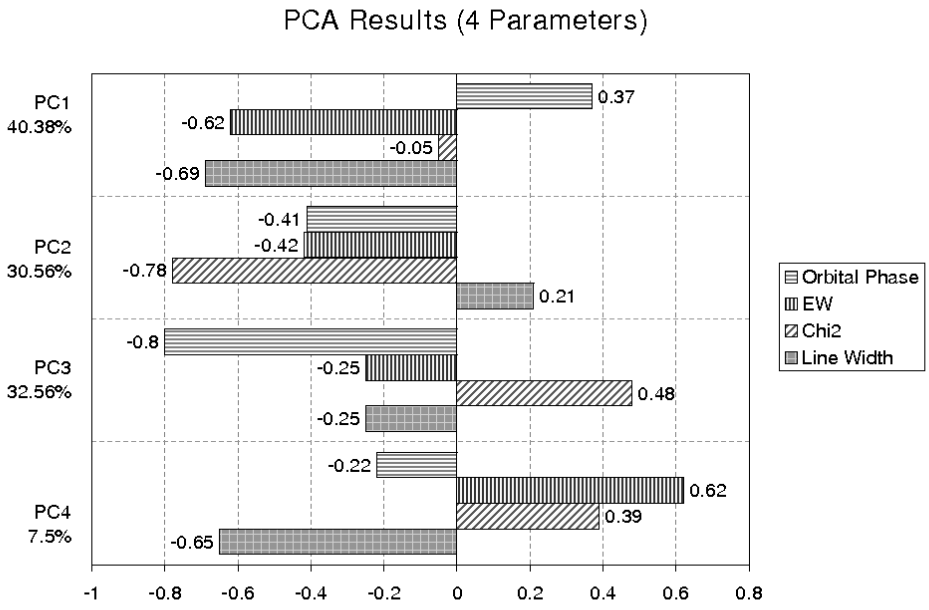

Figure 4.25: PCA Results yielded from 91 spectra consisting of 4 parameters. The first component PC1 accounts for more than 40% of the variance, dominated by the Line Width parameter.

but increases the significance of the orbital phase parameter. Hence the change in the line profile is largely correlated with the EW and the line width.

It is unclear if the peak separation of the double peaks are correlated with the overall changes of the spectra. To investigate, PCA was also performed on a another set of data with includes the peak separation measurement. As not all spectra have values for this parameter, the analysis only includes spectra which consist all 5 parameters, namely, the orbital phase, EW, $\frac{\chi^2}{df}$, line width, and peak separation. A total of 74 spectra (see Appendix F) were used as the unused spectra do not have a clear blue and red peak. The results of the analysis is found in Table 4.5.

The analysis show that both line width and peak separation play an important part in the defining the largest variance of the spectra. The line width parameter has a higher influence than the peak separation parameter. The correlation of

the parameters EW and orbital phase are weak with the major change in the feature of the spectra. As in the previous analysis, $\frac{\chi^2}{df}$ does not correlate with the largest variance of this set of data. The first eigenvalue and eigenvectors from the analysis of the all parameters and those of the analysis without the $\frac{\chi^2}{df}$ parameter do not differ more than 1%.

Table 4.5: Table of PCA results (5 parameters)

Principal Component	**PC1**	**PC2**	**PC3**	**PC4**	**PC5**
Eigenvalue	2.03	1.32	0.88	0.55	0.22
% of Total Variance	40.61	26.31	17.59	11.00	4.49
Parameters					
Orbital Phase	-0.47	0.13	-0.59	0.64	-0.06
EW (Å)	0.28	0.72	-0.32	-0.19	0.52
$\frac{\chi^2}{df}$	-0.16	0.63	0.63	0.30	-0.29
Line Width (Å)	0.61	0.14	-0.33	0.05	-0.70
Peak separation	0.55	-0.22	0.21	0.68	0.39

The second largest variance of the spectra is defined by the parameter EW, and is dependent on the presence of the peak separation and orbital phase parameters. However, in the absence of the latter parameters, $\frac{\chi^2}{df}$ becomes the major factor instead.

From the above analysis, it is found that the line width is the major contributor to the most significant overall variance of the spectra. The difference in the role played by other parameters is affected by the spectra involved in the analysis.

This is significant as the line width of the Hα line is indicative of the region where the emission occurs. The change in the emission region on the accretion disc is therefore the main cause of the changes in the line profile over the long timescale. The change in the emission region can be invoked by a change in the dynamics of the accretion disc. The inner edge of the disc could expanding towards or shrinking away from the compact object. A broader line width reflects an emission region which is closer to the accreting source. The change in line width, together with the change in the EW (see Section 4.5), suggest that the system, A0620-00, might have experienced a change in mass transfer rate and emission region.

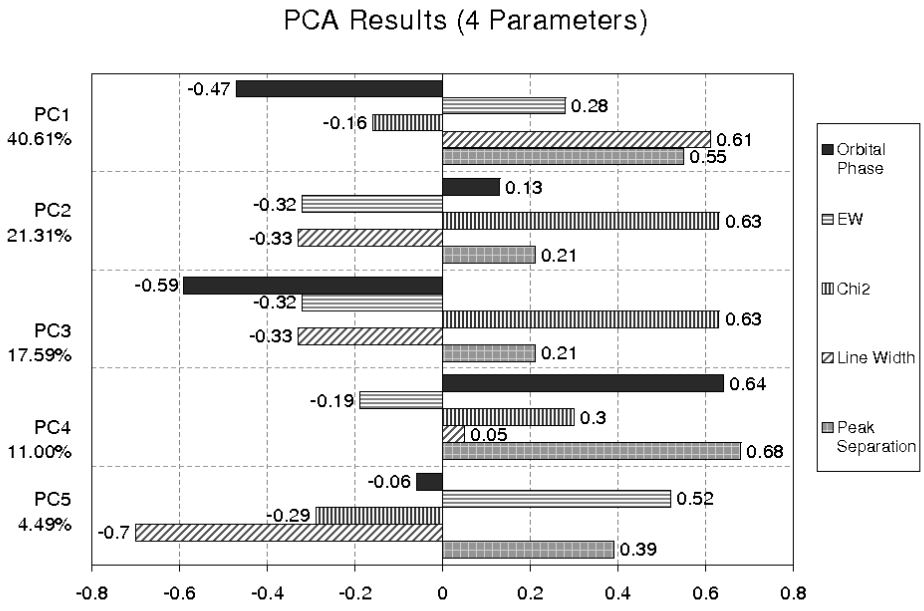

Figure 4.26: PCA Results yielded from 74 spectra consisting of 5 parameters. The first component PC1 accounts for more than 40% of the variance, dominated by the Line Width parameter.

Chapter 5

Summary & Conclusion

This thesis has examined the changes in the Hα line profile of the X-ray transient, A0620-00, over a span of 5 years to look for changes the shape, and width of the line profile.

A0620-00 is an X-ray transient which comprises of a stellar size black hole candidate, which is surrounded by a fully developed accretion disc (Haswell & Shafter, 1990), and a late-type main sequence star. It is the brightest optical source in quiescence among black hole candidates (Leibowitz *et al.*, 1998), and it has a long quiescence period ($\sim$ 60 years). Furthermore it has an orbital period of $\sim$ 0.323 days (McClintock & Remillard, 1986).

A total of 92 spectra collected over a span of 5 years, covering 2000 January, February and December, 2003 January, and 2004 January, were examined. The region of the spectrum in study consists of a double peaked Hα emission line, which is superimposed onto the continuum of the spectrum. The spectra used here were collected by Helen Johnson and Kinwah Wu, at the 2.3m ANU, and were reduced by Helen Johnson. The orbital phase of each spectrum was calculated by Helen Johnson using the ephemeris determined by McClintock & Remillard (1986).

Each spectrum was normalised to the continuum and corrected to the black hole reference frame. The normalised spectra were then cross correlated with a template spectrum of the companion star to obtain the radial velocity of the companion star. In this thesis, the spectrum of a K3 dwarf, BS 753, was used for the template spectrum. It was the same template spectrum used in Marsh *et al.* (1994). From the radial velocity of the companion star ($K_2 = 430.7 \pm 8.2$ km s^{-1}) obtained, the mass function, $f(M) = 2.66 \pm 0.15$ M$_\odot$ was derived.

Both the radial velocity (K_2) and mass function ($f(M)$) determined in this analysis are consistent with the values obtained in previous investigations. However, the mass function found here does not confirm A0620-00 to be a black hole. The lower limit of the mass function derived here, is below the maximum mass of a neutron star for the stiffest possible nuclear equation ($M_{ns} = 2.7$ M$_\odot$).

Subsequently, the spectra were grouped according to their orbital phase and examined. Each spectrum was compared to the orbital mean spectrum derived from the spectra in the same orbital phase bin. The orbital mean spectra of phase bins 0.2-0.3, 0.3-0.4, 0.4-0.5, 0.5-0.6 and 0.8-0.9 show an asymmetric double peaked Hα line.

In general, the line profile of each orbital mean was found to be changing over the orbital period. The primary suspect is the presence of smaller spectral components. There appears to be a component in the line causing the orbital phase related asymmetry. The asymmetry is noted to be migrating from the blue peak to the red peak at orbital phase 0.2-0.3 and 0.5-0.6 and from the red peak to the blue peak at orbital phase 0.7-0.8 and 0.9-1.0. The source of the component is suspected to be the presence of a hotspot on the accretion disk. In addition, the changes in the line profile also hint at the presence of wind on the disc.

The comparison of the peak separation of each double peaked Hα line in Section 3.4 found that the variation in the peak separation was found to be fairly uniform. The mean of the peak separation was calculated to be 23.45 Å with a standard deviation of 1.36 Å.

The equivalent width (EW) of the Hα line was measured by fitting a function with 3 Gaussians to the Hα line and measuring the area under the function. The 0.0-0.1 orbital phase, which corresponds to the superior conjunction of the companion star, where the largest overall mean EW is found. The smallest overall mean EW is found in the orbital phase 0.2-0.3, one of the quadrature phase.

At the inferior conjunction of the companion star (orbital phase 0.5-0.6), the overall mean EW reflects that the luminosity at this orbital phase is higher than that at superior conjunction (orbital phase 0.0-0.1). The EWs of spectra in each epoch and overall mean EW of the spectra at the two quadratures indicate that the orbital phase 0.7-0.8 have a generally larger EW than those at orbital phase 0.2-0.3.

The differences in the overall mean EW at both conjunctions and quadrature are significant, and advocates a probable presence of a hotspot which is visible in

the line-of-sight on the accretion disc at the orbital phase 0.2-0.3 to 0.7-0.8.

To get a better understanding of the changes in the Hα line profile, each of the normalised spectra was compared with their respective orbital mean spectrum and the overall mean spectrum. Most of the line profiles were found to differ from their respective orbital mean spectrum by a similar χ^2 for all orbital phase bins. The same is observed in comparing the line profiles of each spectrum with the overall mean spectrum.

The orbital phase dependent change in the shape of the line profile is suspected to be due to the presence of a hotspot. The line profiles also indicate that the spectra change with time, however, there was no strong evidence of a time dependent trend. To further quantify the change in the line profile, the width of the Hα line was measured.

The width of the Hα line is defined as the width of the line at the 10% height (from the continuum) of the lower peak. This height is chosen to ensure the width of the line is measured at the lowest possible height from the continuum.

The line widths are found to be changing with time. The spectra taken in 2000 Dec (E2000b) have a wider line width than the spectra of other observing campaigns. The wider line widths of these Hα line indicate that the emission originates from a region on the accretion disc closer to the accreting central object.

The varying line widths of the Hα line within the same observing night suggest that there is short term variability in the emission region of the accretion disk. This variability is reflected in almost all of the observation campaigns except those carried out in 2000 December (JD +1902 to JD +1904).

The low SNR in most of the spectra in E2003 render doubt if the short term line width variability in these spectra is intrinsic. Each mean spectrum of the observing campaigns was examined, and it was revealed that the change in line width was not due to observing conditions. It was most probably due to a change in the emission region on the accretion disc. The varying line widths in the observing campaigns E2000a and E2004 too, support a short term variability in the emission region on accretion disk.

The variability in the line width of the Hα line in the observing campaigns E2000a, E2003, and E2004 suggests that the emission region of the disc is changing with time. This also hints at a change size in the accretion disc, in which the inner edge of the accretion disc has expanded closer towards the compact object.

The spectra in E2000b suggest that A0620-00 may also have long term variability in the line widths, however, this suspicion could not be confirmed as the spectra were not collected under photometric conditions, and a lack of accessible data from previous observations for comparison.

The overall change in the spectra of A0620-00 is found to be due mainly to the changes in the line width. The orbital phase and EW play a smaller role in influencing the variance.

With consideration of the peak separation parameter, the line width remains the major contributor to the change of the spectra. The significance of the change in line width, together with the change in the EW (see Section 4.5), suggest that the system, A0620-00, might have experienced a change in mass transfer rate and emission region.

The Doppler shift lines of Hα are not equally displaced from the rest wavelength. The red shifted lines are generally more displaced than the blue shifted lines, except for spectra in the orbital phase bins 0.7-0.8 and 0.8-0.9. This observed effect suggests that the accretion disc may be asymmetrical. However, A0620-00 is suspected of having a hotspot on its accretion disk, therefore the shape of the disk cannot be ascertained at this stage.

The cause of the broad feature seen in some of the E2003 spectra cannot be attributed as it is unclear if it is a feature of the companion star or a feature brought about by some unknown mechanism.

The EWs of the spectra in E2003 are considerably smaller than that of other observing campaigns. The smaller EW is indicative of a higher luminosity, thus suggest that A0620-00 might have experienced a period of enhanced mass transfer. The relatively smaller EW measured suggests that the system might have undergone a mini outburst. These spectral effects, however faded off on 2003 January 13, when the measurements of the EW returned to the levels similar to other observing runs.

McClintock & Remillard (1986), Haswell (1992) and Leibowitz *et al.* (1998) had discovered that the mean brightness of A0620-00 is found to vary in its optical brightness (on a time scale of $\sim$ 200 days). However, the variation in brightness is considerably small ($\sim$ 0.3 mag, Leibowitz *et al.* (1998)), and could have been overlooked. Therefore, it is plausible that A0620-00 had undergone undetected several mini outbursts during its proposed period of quiescence.

In order for a system like A0620-00 to produce a double peaked Hα line

during quiescence, the accretion disc must be optically thin and hot. Suppose A0620-00 did undergo mini outbursts, the double peaked Hα line will be found superimposed on a broad absorption trough, as it was during its outburst in 1975 (Whelan *et al.*, 1977). The emission would be produced in the outer regions of an irradiated optically thick accretion disc (Wu *et al.*, 2001).

However, the amount of X-ray flux measured for A0620-00 in 1992 (McClintock *et al.*, 1995) and in 2000 (Garcia *et al.*, 2001) has been very low or undetectable ($\sim 10^{30}$ erg s^{-1}). Therefore the emission of the Hα line cannot be due to reprocessing of X-rays (Cherepashchuk, 2000). It is unlikely that A0620-00 underwent mini outbursts, so the Hα emission line is produce via a different mechanism. On the other hand, it is very probable that the lower EW indicate that A0620-00 experienced a period of enhanced mass transfer.

For an accretion disc with a lower accretion rate than its mass transfer rate, an increase in mass transfer will result in a gain in the density of the disc. As the mass density in the disc escalates, and surpasses its critical density, the accretion rate will rise to generate an increase in the optical luminosity. Hynes *et al.* (2003) established that similar optical flares observed in their investigation are associated with the accretion flow.

To summarise, the profile and intensity of the normalised flux of the Hα line in A0620-00 are confirmed to be varying. The double peaked Hα line is believed to be present in both during outburst and quiescence. The X-ray flux of A0620-00 since its outburst in 1975, was recently detected at $\sim 10^{30}$ erg s^{-1}. This period of quiescence suggests that the mechanisms that produce the Hα emission line for A0620-00 are different during quiescence and outburst. This is because the X-ray flux detected in quiescence would have been too weak to irradiate the disc to emit the Hα line. The asymmetry in the double peaked line profile and periodic variation of the EW support the presence of a hotspot, as well as a weak wind on the accretion disc. The widening of the line width of the spectra over time could be the result of an expanding of the inner edge of the accretion disc, resulting in emission region being much closer to the compact object. The decrease of the EW in E2003 indicates a possible increase in the mass accretion rate, hence a higher luminosity. However this increase in accretion rate is not enough to induce a mini outburst in the system, nor produce a strong wind in the disc. The diagnosis suggests that it is probable that the accretion disc is in a state of instability, where the inner edge is expanding and contracting.

Appendix A

Spectroscopic Observations of A0620-00

Table A.1: Spectral details of the A0620-00 Spectra

Date	**No.**	**Julian Time**	**Orbital Phase**	**Wavelength Range (Å)**	**No. of Bins**	**Bin Size (Å)**
00Jan29...	1	2451572.94882651	0.519	6250-6854.5	546	1.1092
	2	2451572.97167156	0.589			
	3	2451572.99411154	0.659			
	4	2451573.01833373	0.734			
	5	2451573.04063482	0.803			
	6	2451573.0593136	0.861			
00Jan30...	1	2451573.95974482	0.648	6250-6853.6	546	1.1074
	2	2451573.99724125	0.764			
	3	2451574.01958866	0.834			
	4	2451574.04188976	0.903			
	5	2451574.06422567	0.972			
00Jan31...	1	2451574.95831892	0.740	6250-6852.9	546	1.1062
	2	2451574.98183536	0.812			
	3	2451575.00398566	0.881			
	4	2451575.02817343	0.956			
	5	2451575.04798634	0.017			
00Feb01...	1	2451575.92678058	0.738	6250-6853.0	546	1.1064

Continued on next page...

Table A.1: (continued)

Date	**No.**	**Julian Time**	**Orbital Phase**	**Wavelength Range (Å)**	**No. of Bins**	**Bin Size (Å)**
	2	2451575.94866509	0.806			
	3	2451575.97226256	0.879			
	4	2451575.99347571	0.944			
	5	2451576.0170037	0.017			
	6	2451576.03771921	0.081			
	7	2451576.06129323	0.154			
00Dec24...	1	2451902.97238453	0.219	6250-6854.6	546	1.1093
	2	2451902.99474461	0.288			
	3	2451903.02231485	0.373			
	4	2451903.04405684	0.440			
	5	2451903.15764716	0.792			
	6	2451903.1801363	0.862			
	7	2451903.20490378	0.938			
	8	2451903.22705609	0.007			
00Dec26...	1	2451904.95178361	0.346	6250-6854.6	546	1.1093
	2	2451904.97572517	0.421			
	3	2451905.0371408	0.611			
	4	2451905.06200772	0.688			
	5	2451905.0842109	0.756			
	6	2451905.1055761	0.823			
	7	2451905.14919538	0.958			
	8	2451905.17390375	0.034			
	9	2451905.1953528	0.101			
	10	2451905.21919547	0.174			
	11	2451905.24053694	0.240			
03Jan10...	1	2452649.99730435	0.888	6250-6852.4	546	1.1054
	2	2452650.0193525	0.956			
	3	2452650.04227852	0.027			
	4	2452650.064881	0.097			
	5	2452650.08639621	0.164			

Continued on next page...

Table A.1: (continued)

Date	**No.**	**Julian Time**	**Orbital Phase**	**Wavelength Range (Å)**	**No. of Bins**	**Bin Size (Å)**
	6	2452650.10545593	0.223			
	7	2452650.13004916	0.299			
	8	2452650.15675635	0.381			
	9	2452650.17815342	0.448			
	10	2452650.19949225	0.514			
03Jan11...	1	2452650.97655811	0.919	6250-6852.4	546	1.1054
	2	2452650.99785961	0.985			
	3	2452651.01928731	0.052			
	4	2452651.04100382	0.119			
	5	2452651.06243215	0.185			
	6	2452651.08385237	0.252			
	7	2452651.16652	0.507			
	8	2452651.18794665	0.574			
	9	2452651.20937199	0.640			
03Jan12...	1	2452651.9424499	0.910	6250-6852.4	546	1.1054
	2	2452651.9638788	0.976			
	3	2452651.98530244	0.042			
	4	2452652.00672844	0.109			
	5	2452652.02815096	0.175			
	6	2452652.04970191	0.242			
	7	2452652.09090749	0.369			
	8	2452652.11337568	0.439			
	9	2452652.15322999	0.562			
03Jan13...	1	2452652.96675789	0.081	6250-6852.4	546	1.1054
	2	2452652.98850908	0.148			
	3	2452653.00993502	0.214			
	4	2452653.03135863	0.281			
	5	2452653.05278165	0.347			
	6	2452653.07598244	0.419			
	7	2452653.0966445	0.483			

Continued on next page...

Table A.1: (continued)

Date	**No.**	**Julian Time**	**Orbital Phase**	**Wavelength Range (Å)**	**No. of Bins**	**Bin Size (Å)**
	8	2452653.11747733	0.547			
	9	2452653.1481837	0.642			
	10	2452653.1487265	0.644			
	11	2452653.19105988	0.775			
04Jan28...	1	2453032.04209	0.637	6250-6851.8	546	1.1042
	2	2453032.06346	0.703			
	3	2453032.09180	0.791			
	4	2453032.11317	0.857			
	5	2453032.13465	0.924			
04Jan29...	1	2453032.98116	0.544	6250-6852.0	546	1.1046
	2	2453033.00258	0.611			
	3	2453033.03726	0.718			
	4	2453033.05870	0.784			
	5	2453033.08668	0.871			
	6	2453033.10810	0.937			

Appendix B

Observing Conditons of A0620-00

Table B.1: Observing conditions of the A0620-00 Spectra

Date	**No.**	**Julian Time**	**SNR**	**Cnts/pix**	**Observing Conditions**	**Seeing (″)**
00Jan29...	1	2451572.94882651	16.4	475	photo	1.4 - 2
	2	2451572.97167156	12.2	411		
	3	2451572.99411154	11.0	461		
	4	2451573.01833373	15.4	483		
	5	2451573.04063482	16.6	408		
	6	2451573.0593136	10.8	245		
00Jan30...	1	2451573.95974482	9.9	324	non	2+
	2	2451573.99724125	10.9	327	photo	
	3	2451574.01958866	8.4	278		
	4	2451574.04188976	7.1	252		
	5	2451574.06422567	5.6	263		
00Jan31...	1	2451574.95831892	16.9	359	non	2+
	2	2451574.98183536	17.9	431	photo	
	3	2451575.00398566	12.2	369		
	4	2451575.02817343	14.6	302		
	5	2451575.04798634	9.7	226		
00Feb01...	1	2451575.92678058	12.0	465	non	1.5

Cnt/pix refers to the number of counts per pixel

photo refers to photometric observing condition

Continued on next page...

Table B.1: (continued)

Date	**No.**	**Julian Time**	**SNR**	**Cnts/pix**	**Observing Conditions**	**Seeing (″)**
	2	2451575.94866509	21.6	448	photo	
	3	2451575.97226256	12.1	356		
	4	2451575.99347571	17.3	322		
	5	2451576.0170037	10.0	290		
	6	2451576.03771921	16.9	321		
	7	2451576.06129323	11.1	338		
00Dec24...	1	2451902.97238453	13.1	485	non	-
	2	2451902.99474461	13.2	486	photo	
	3	2451903.02231485	12.1	454		
	4	2451903.04405684	13.0	430		
	5	2451903.15764716	16.9	463		
	6	2451903.1801363	12.0	425		
	7	2451903.20490378	9.2	355		
	8	2451903.22705609	10.1	331		
00Dec26...	1	2451904.95178361	12.5	400	non	-
	2	2451904.97572517	22.3	418	photo	
	3	2451905.0371408	15.6	466		
	4	2451905.06200772	17.5	422		
	5	2451905.0842109	13.0	391		
	6	2451905.1055761	12.5	408		
	7	2451905.14919538	18.9	395		
	8	2451905.17390375	14.7	419		
	9	2451905.1953528	16.9	414		
	10	2451905.21919547	16.1	428		
	11	2451905.24053694	10.9	438		
03Jan10...	1	2452649.99730435	4.3	197	photo	1.5
	2	2452650.0193525	6.1	169		
	3	2452650.04227852	4.3	154		

Cnt/pix refers to the number of counts per pixel

photo refers to photometric observing condition

Continued on next page...

Table B.1: (continued)

Date	**No.**	**Julian Time**	**SNR**	**Cnts/pix**	**Observing Conditions**	**Seeing (″)**
	4	2452650.064881	4.4	147		
	5	2452650.08639621	6.0	157		
	6	2452650.10545593	5.3	135		
	7	2452650.13004916	7.7	206		
	8	2452650.15675635	6.7	175		
	9	2452650.17815342	5.5	133		
	10	2452650.19949225	7.1	180		
03Jan11...	1	2452650.97655811	6.0	190	photo	1.5
	2	2452650.99785961	7.1	184		
	3	2452651.01928731	7.5	137		
	4	2452651.04100382	5.9	220		
	5	2452651.06243215	6.7	176		
	6	2452651.08385237	5.0	116		
	7	2452651.16652	3.2	97		
	8	2452651.18794665	5.6	167		
	9	2452651.20937199	6.0	115		
03Jan12...	1	2452651.9424499	4.5	168	photo	poor
	2	2452651.9638788	4.7	131		
	3	2452651.98530244	7.1	152		
	4	2452652.00672844	5.7	123		
	5	2452652.02815096	4.9	159		
	6	2452652.04970191	8.4	177		
	7	2452652.09090749	5.8	159		
	8	2452652.11337568	3.7	119		
	9	2452652.15322999	3.9	124		
03Jan13...	1	2452652.96675789	4.8	133	non	1.3
	2	2452652.98850908	4.1	154	photo	
	3	2452653.00993502	9.1	228		

Cnt/pix refers to the number of counts per pixel

photo refers to photometric observing condition

Continued on next page...

Table B.1: (continued)

Date	**No.**	**Julian Time**	**SNR**	**Cnts/pix**	**Observing Conditions**	**Seeing (″)**
	4	2452653.03135863	5.7	202		
	5	2452653.05278165	8.7	215		
	6	2452653.07598244	5.0	163		
	7	2452653.0966445	5.5	169		
	8	2452653.11747733	5.4	145		
	9	2452653.1481837	4.9	117		
	10	2452653.1487265	4.8	111		
	11	2452653.19105988	4.4	114		
04Jan28...	1	2453032.04209	17.1	666	photo	<1
	2	2453032.06346	19.7	558		
	3	2453032.09180	18.7	599		
	4	2453032.11317	16.9	442		
	5	2453032.13465	7.9	207		
04Jan29...	1	2453032.98116	17.5	632	photo	1
	2	2453033.00258	25.4	660		
	3	2453033.03726	24.0	694		
	4	2453033.05870	8.3	284		
	5	2453033.08668	18.6	763		
	6	2453033.10810	18.5	651		

Cnt/pix refers to the number of counts per pixel

photo refers to photometric observing condition

Appendix C

The Original A0620-00 Spectra

The orbital phase of each spectrum was calculated by Helen Johnston, using the photometric ephemeris defined in McClintock & Remillard (1986). The Julian Date (JD) of the observations were converted to Heliocentric Julian Date (HJD). The photometric ephemeris is the HJD at the orbital phase zero, T_0 (photometric) = HJD 2,445,477.827 $\pm$ $0^d.005$ (see Table 1.1). The spectra were then grouped by their respective orbital phases from 0 to 1, in bin size of 0.1 of an orbital phase period.

The spectrum of the template star, BS753, is added to each figure for comparison of the absorption lines. The template spectrum was scaled down by a constant to match the flux of the A0620-00 spectra. The A0620-00 spectra and the template spectrum are evenly-spaced in flux and plotted in the observer reference frame (centre-of-mass reference frame for the A0620-00 spectra). Each mark on the vertical axis of the plots denotes the 1 flux unit mark for each spectrum. Each A0620-00 spectrum is identified by the JD of its observation. The spectra are plotted chronologically for each orbital phase bin. The JD reference of each spectrum e.g. JD 2453033.04, is abbreviated to the form JD +3033.04

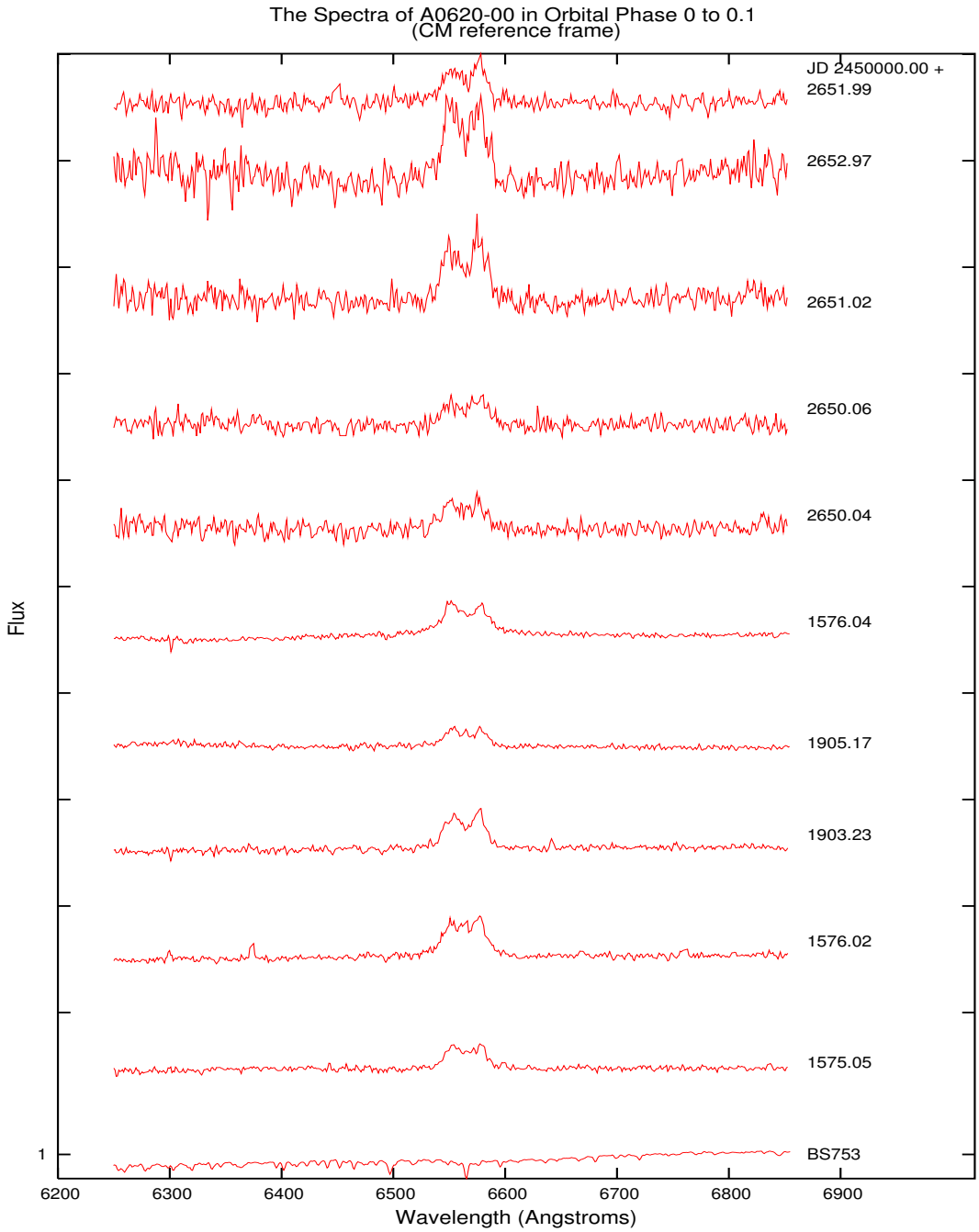

Figure C.1: The original A0620-00 spectra in the orbital phase bin 0.0-0.1, in the centre-of-mass reference frame.

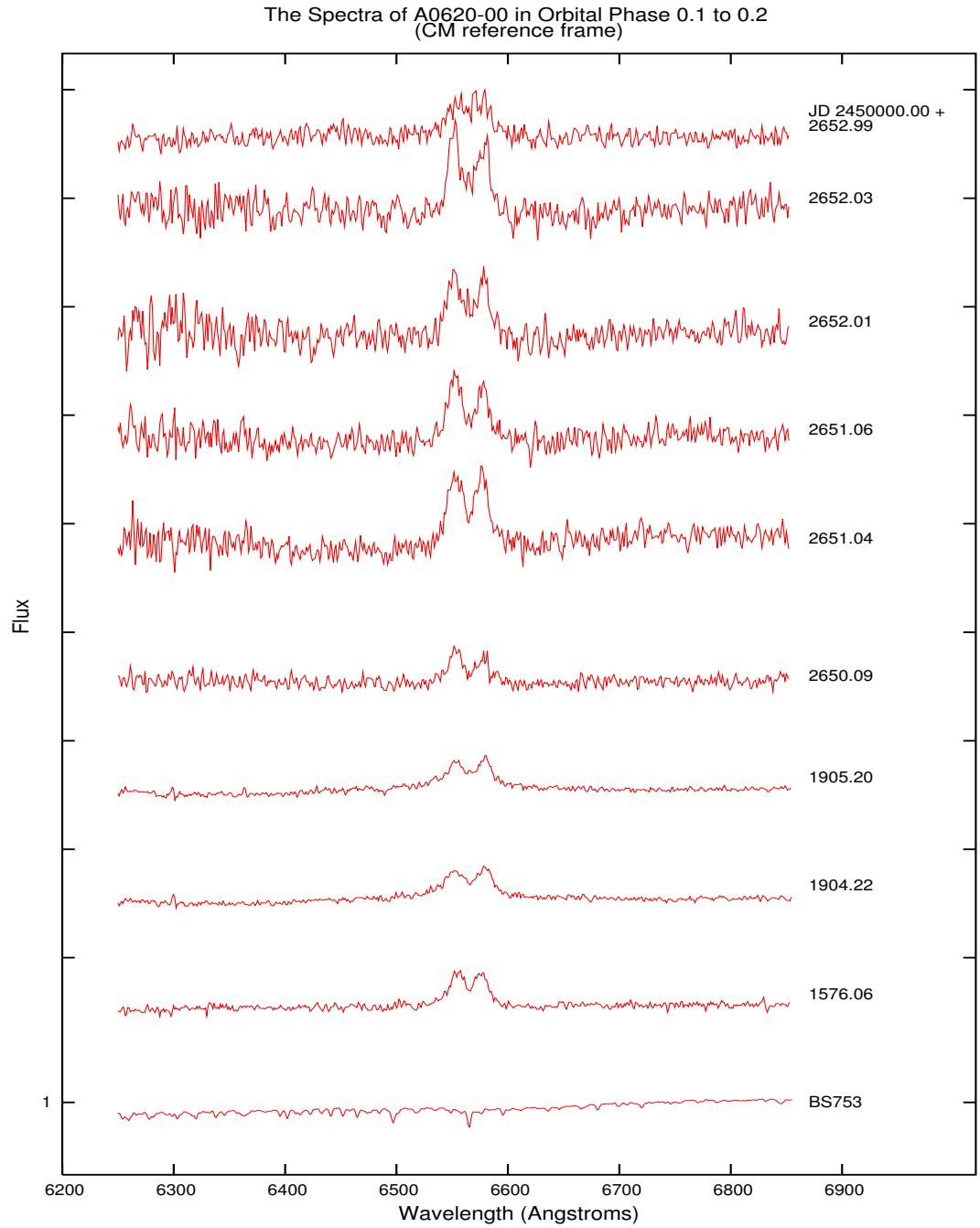

Figure C.2: The original A0620-00 spectra in the orbital phase bin 0.1-0.2, in the centre-of-mass reference frame.

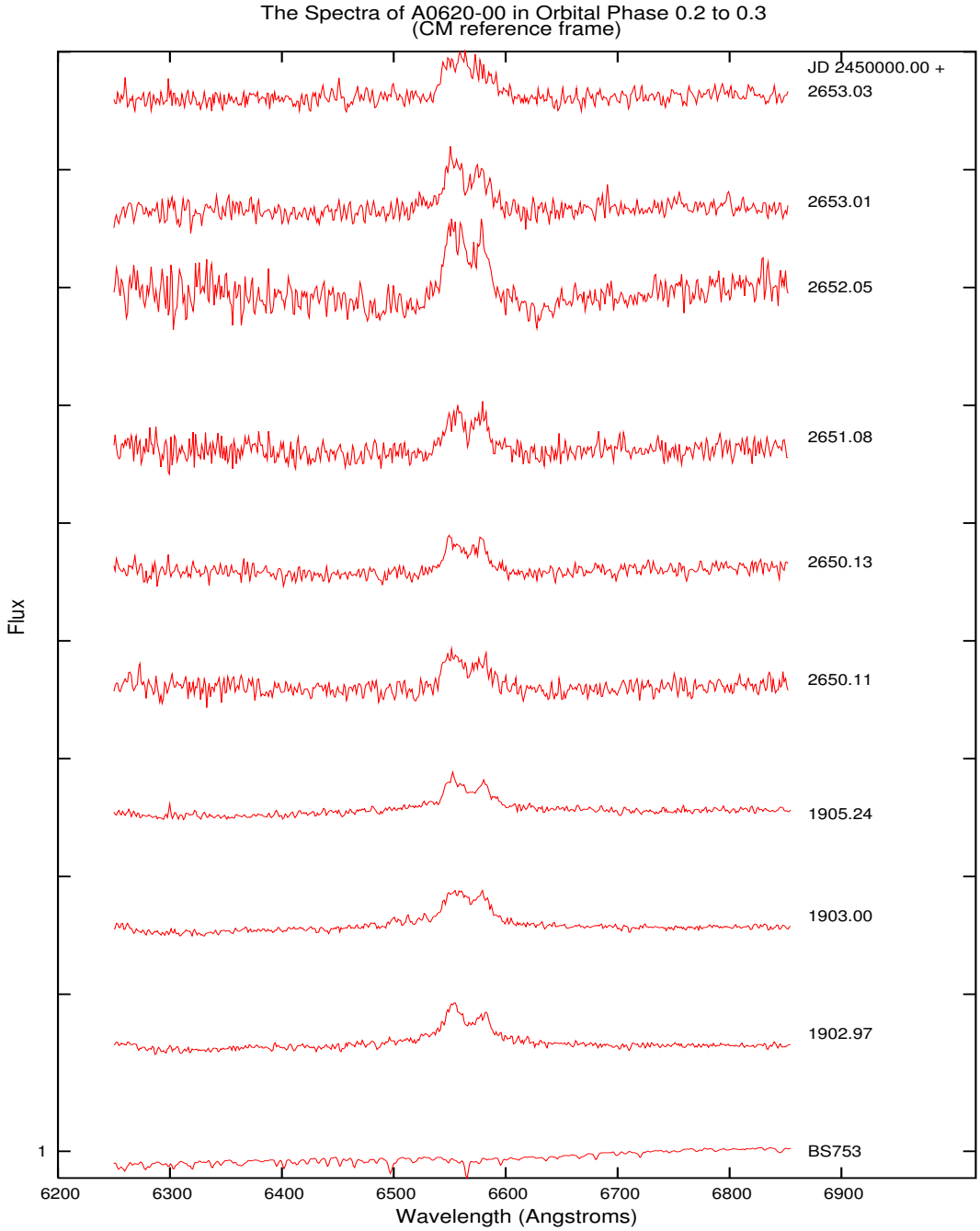

Figure C.3: The original A0620-00 spectra in the orbital phase bin 0.2-0.3, in the centre-of-mass reference frame. Note the differences in the continuum flux level of each spectra.

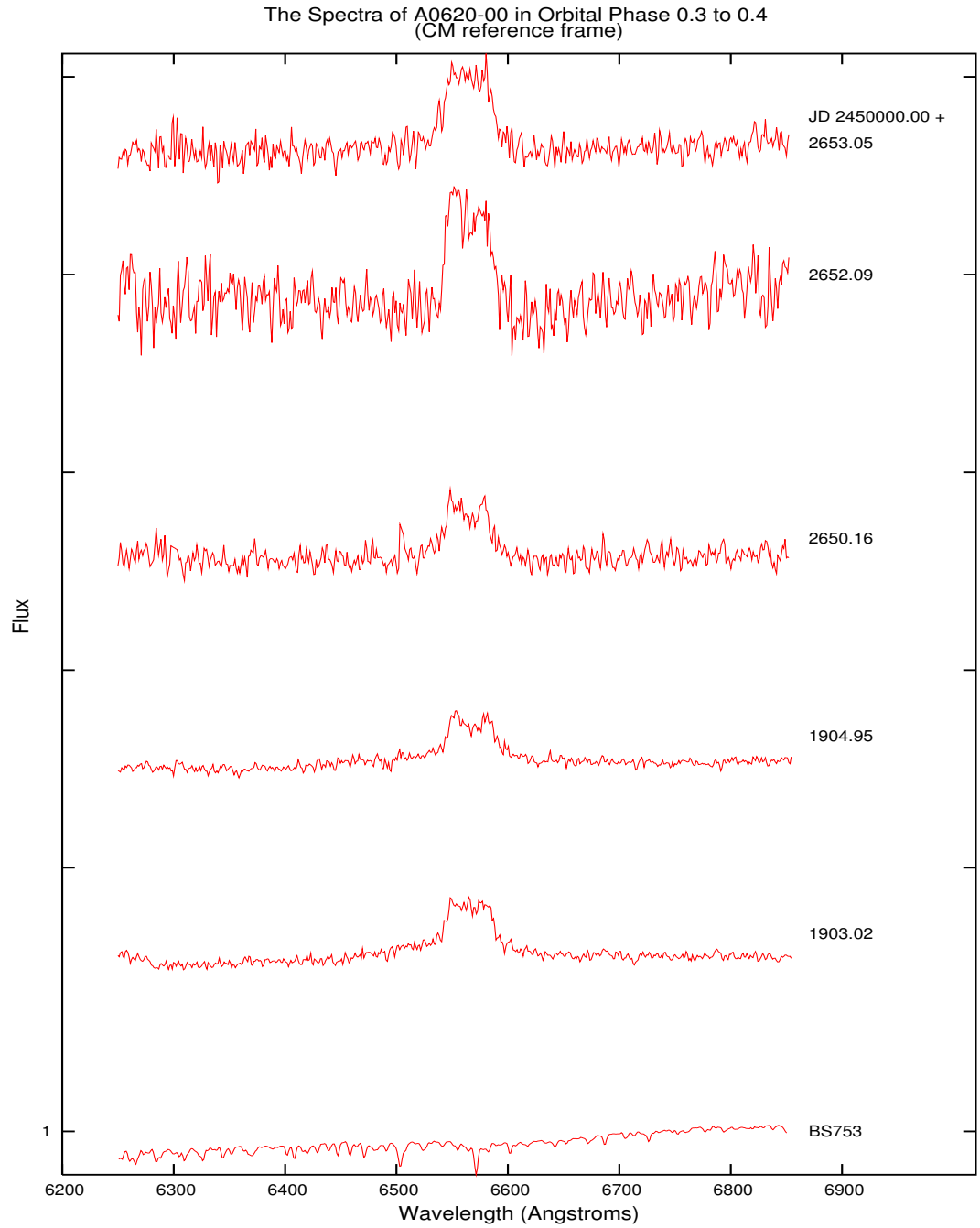

Figure C.4: The original A0620-00 spectra in the orbital phase bin 0.3-0.4, in the centre-of-mass reference frame.

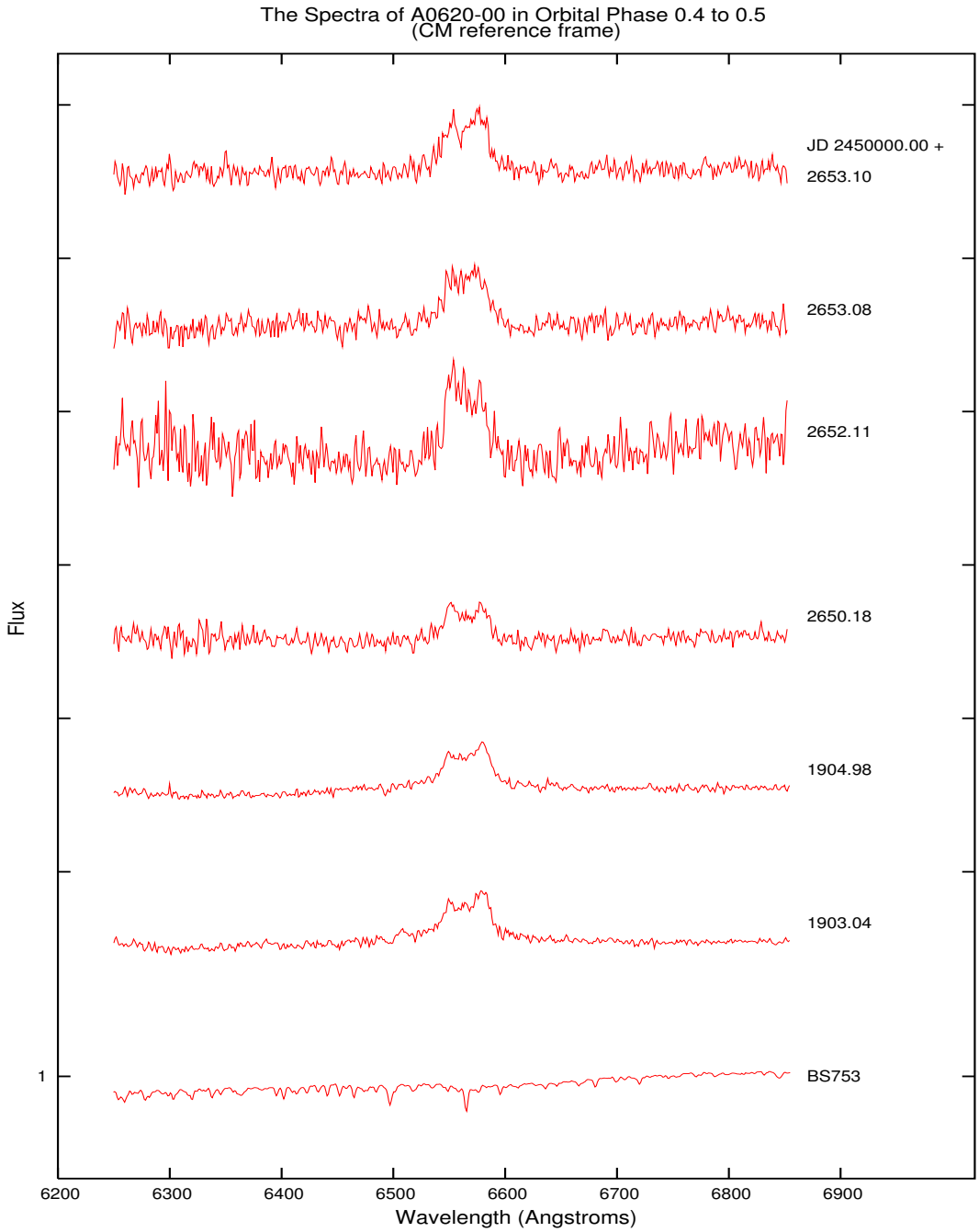

Figure C.5: The original A0620-00 spectra in the orbital phase bin 0.4-0.5, in the centre-of-mass reference frame.

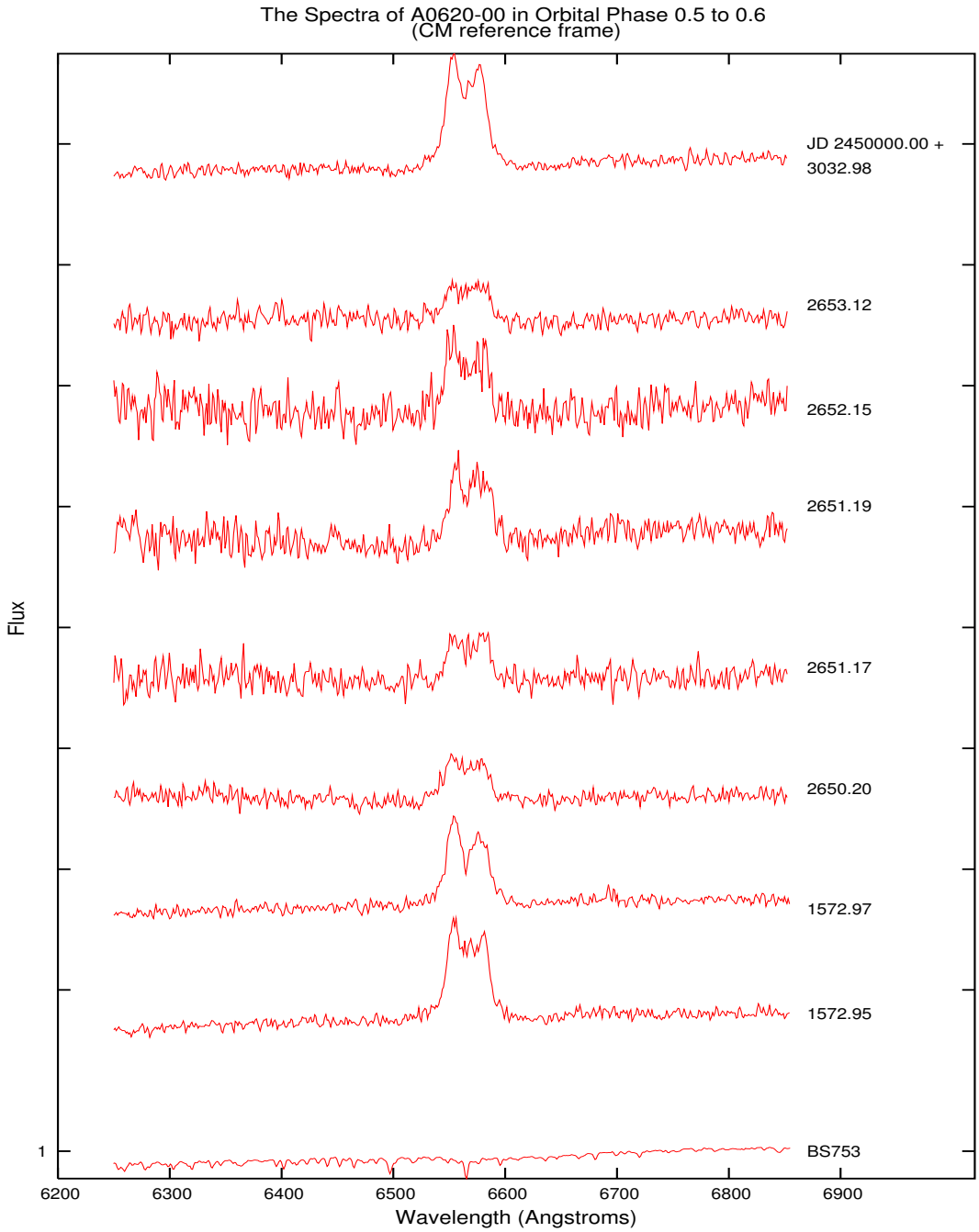

Figure C.6: The original A0620-00 spectra in the orbital phase bin 0.5-0.6, in the centre-of-mass reference frame.

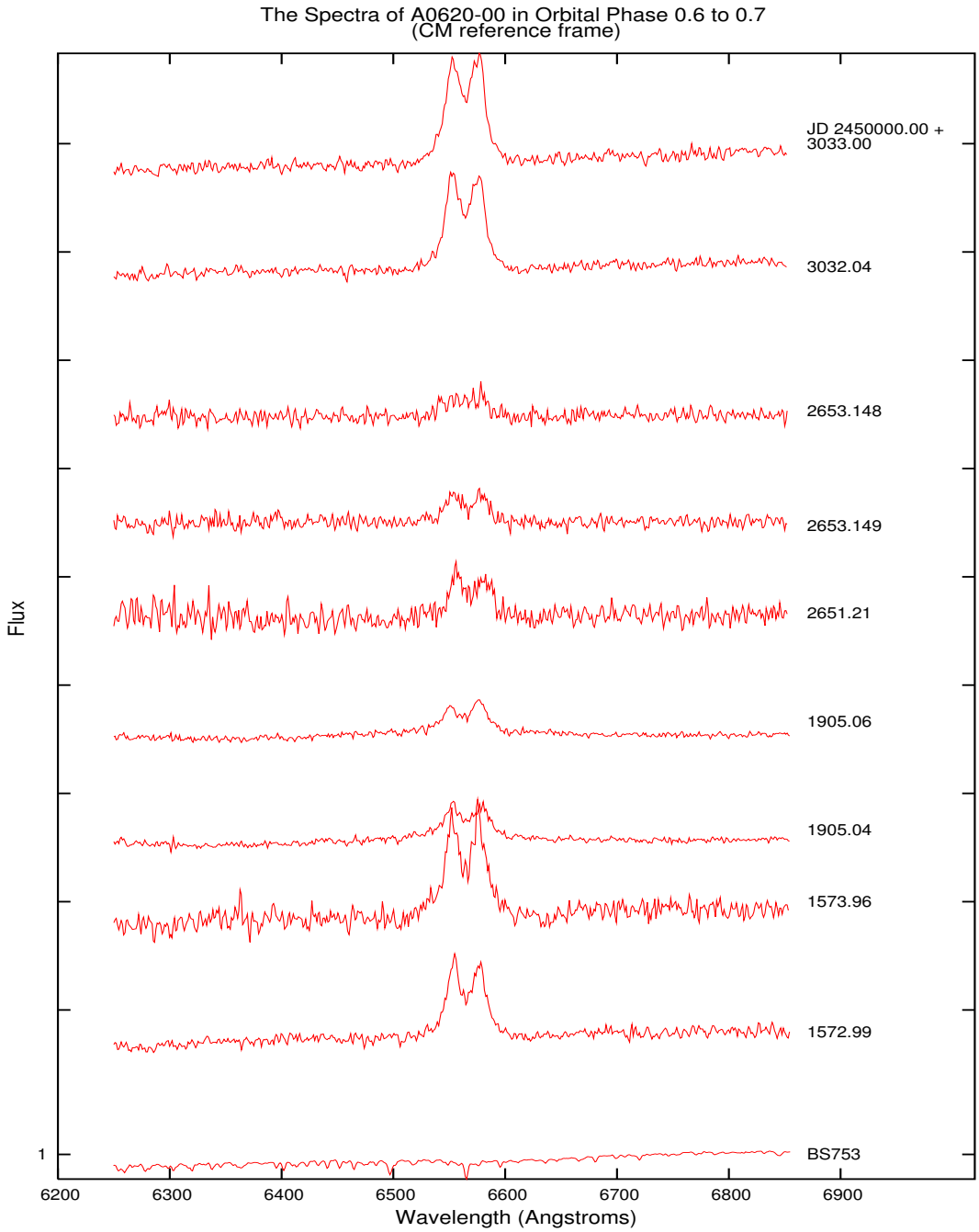

Figure C.7: The original A0620-00 spectra in the orbital phase bin 0.6-0.7, in the centre-of-mass reference frame. The intensity and shape of the Hα emission line vary from spectra to spectra.

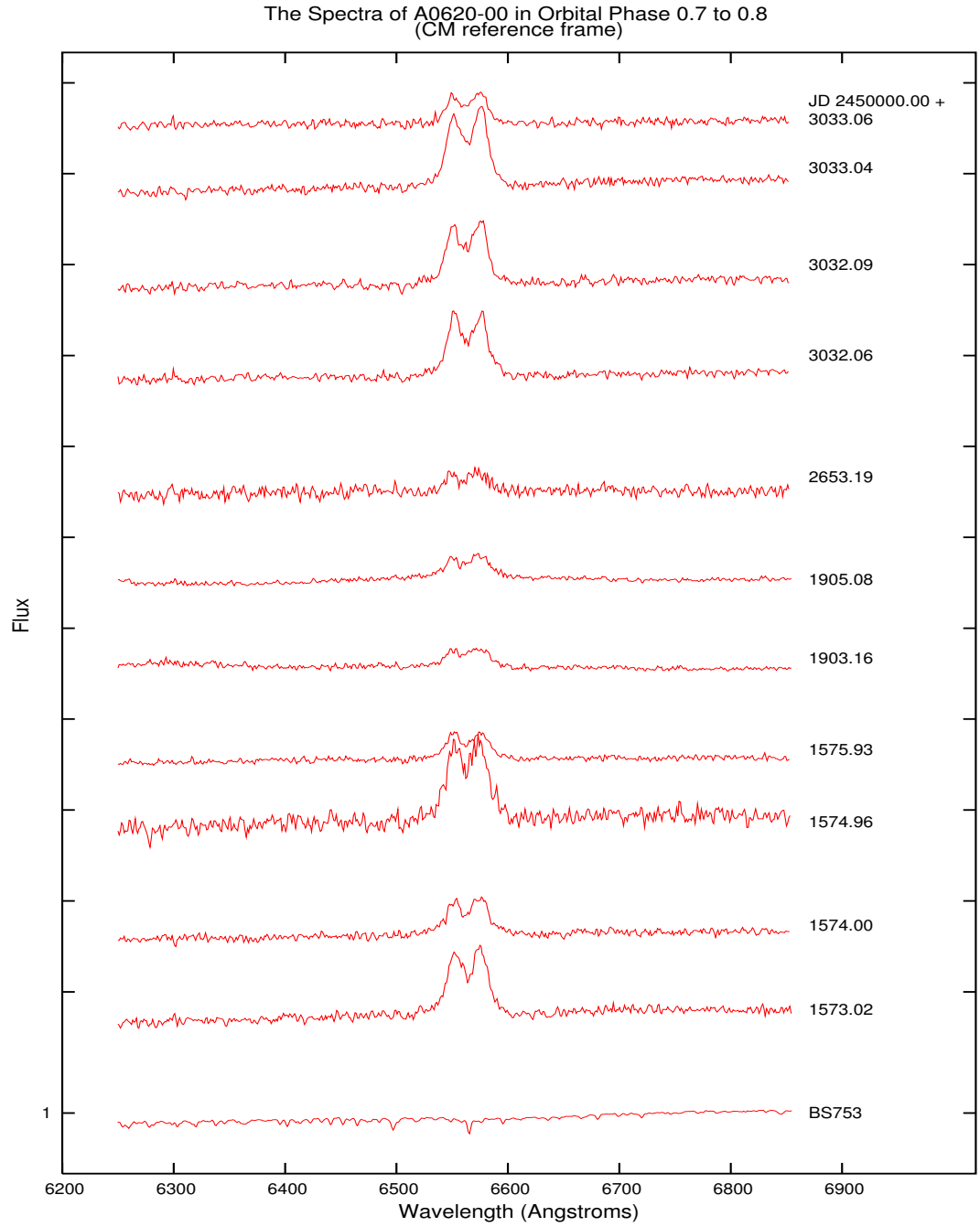

Figure C.8: The original A0620-00 spectra in the orbital phase bin 0.7-0.8, in the centre-of-mass reference frame. Note the differences in the continuum flux level, and the change in the intensity and shape of the Hα emission of each spectra. In particular, the profile of the Hα of the observation at JD +3033.04 is a stronger and well-defined double peaked emission line, compared to that of JD +1903.16.

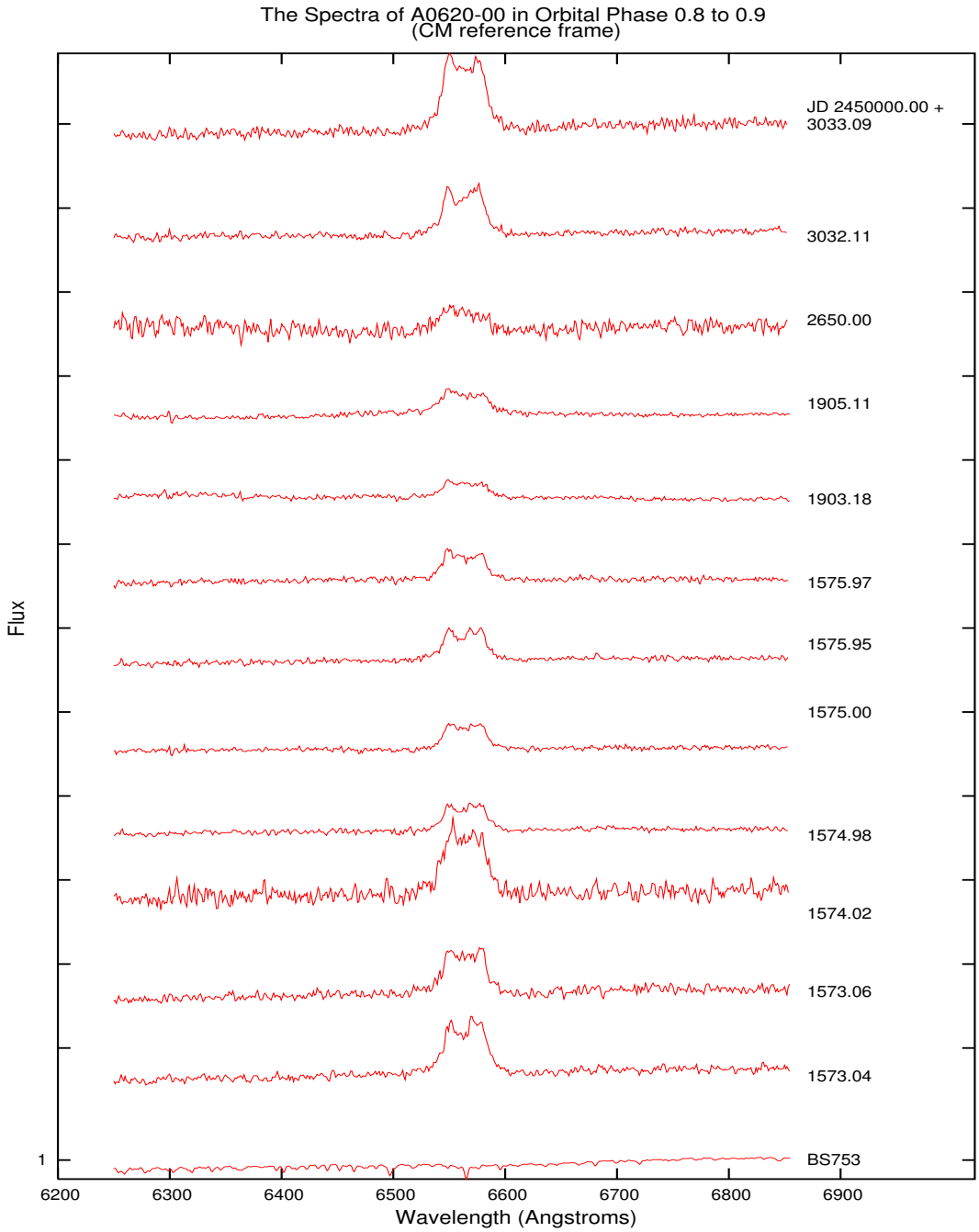

Figure C.9: The original A0620-00 spectra in the orbital phase bin 0.8-0.9, in the centre-of-mass reference frame. Note the differences in the continuum flux leveland the change in the intensity and shape of the Hα emission of each spectra.

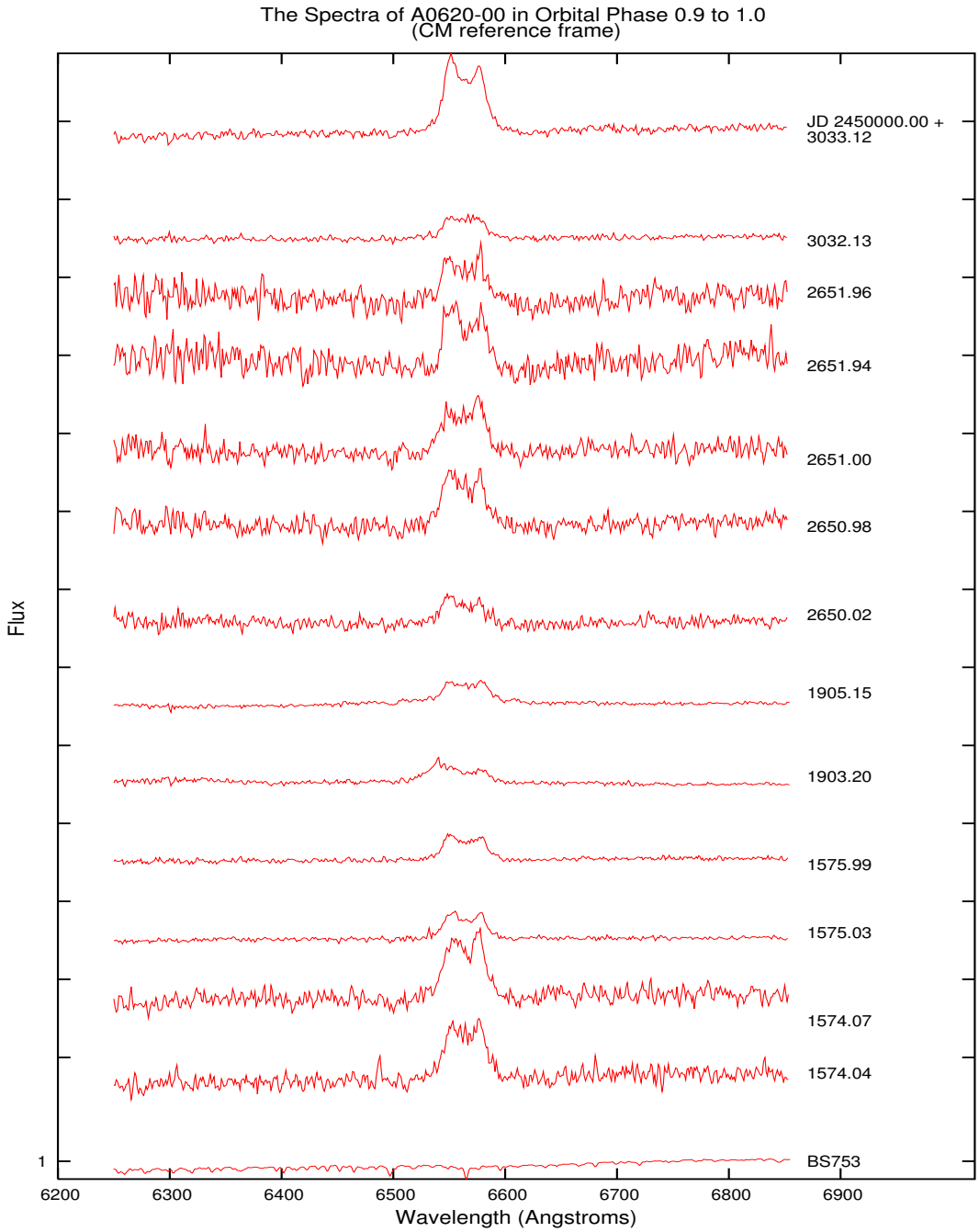

Figure C.10: The original A0620-00 spectra in the orbital phase bin 0.9-1.0, in the centre-of-mass reference frame. Note the differences in the continuum flux leveland the change in the intensity and shape of the Hα emission of each spectra.

Appendix D

The Overall Changes in the Line Profile

The following figures show how each spectrum varies from the overall mean spectrum. The difference between each spectrum and the mean spectrum is quantified by Δ in Equation 4.3.

There are 10 figures, which each figure shows the Δ calculated for each wavelength bin for each spectrum in the same orbital phase bin. The spectra in each figure are grouped in columns of observing campaigns.

Each panel shows the Δs overlaid with both the overall mean spectrum (dashes) and the respective spectrum (short dashes). The height of each red bar corresponds to the vertical axis on the left, it marks the value of each Δ. Both the mean spectrum and respective spectrum are plotted with respect to the same arbituary unmarked vertical axis.

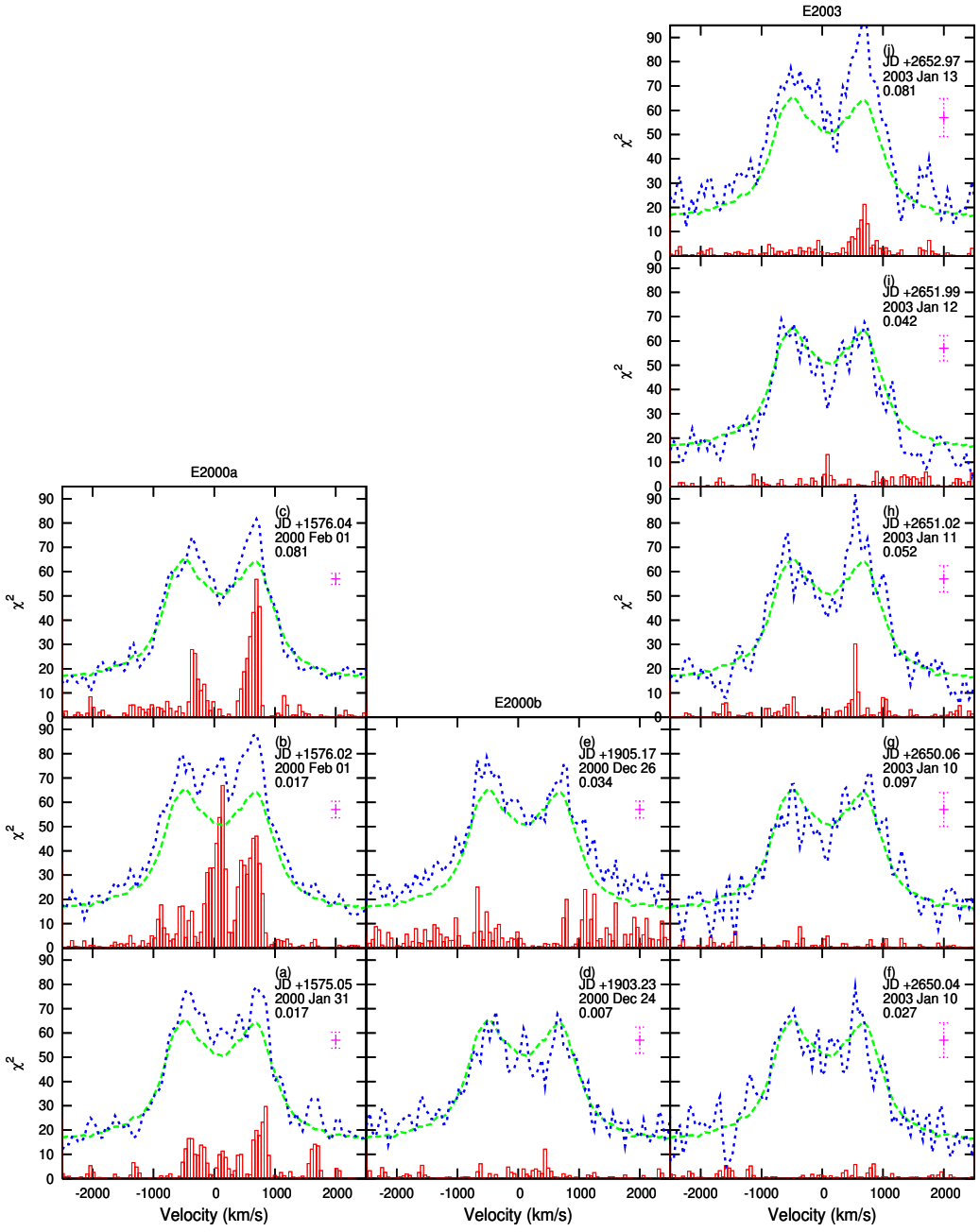

Figure D.1: The Δ of the flux in each wavelength bin of each spectrum (orbital phase 0-0.1). The Δs (bars) are plotted with both the overall mean spectrum (dashes) and the respective spectrum (short dashes) to illustrate the region the Δs correspond to.

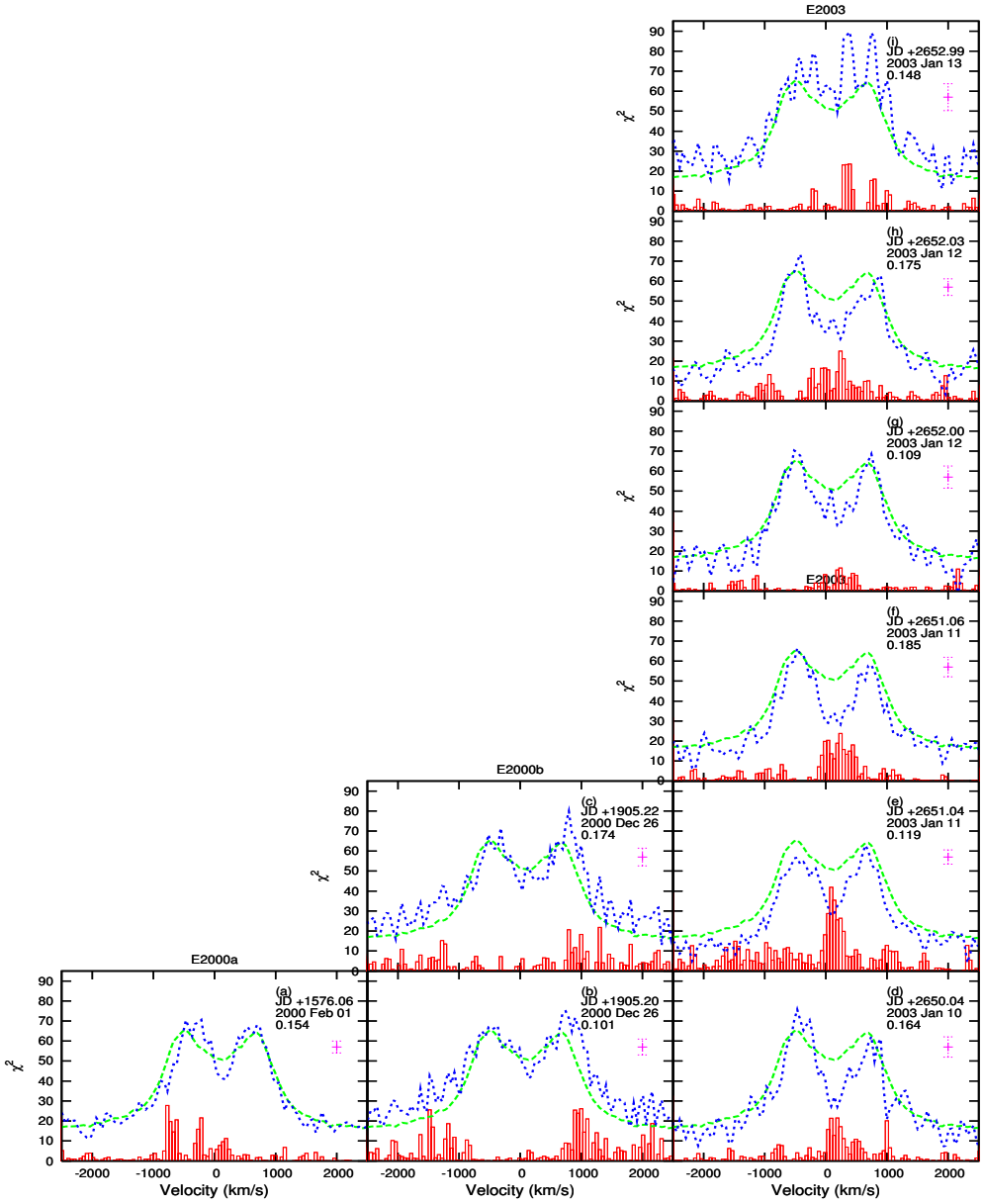

Figure D.2: The Δ of the flux in each wavelength bin of each spectrum (orbital phase 0.1-0.2). The Δs (bars) are plotted with both the overall mean spectrum (dashes) and the respective spectrum (short dashes) to illustrate the region the Δs correspond to.

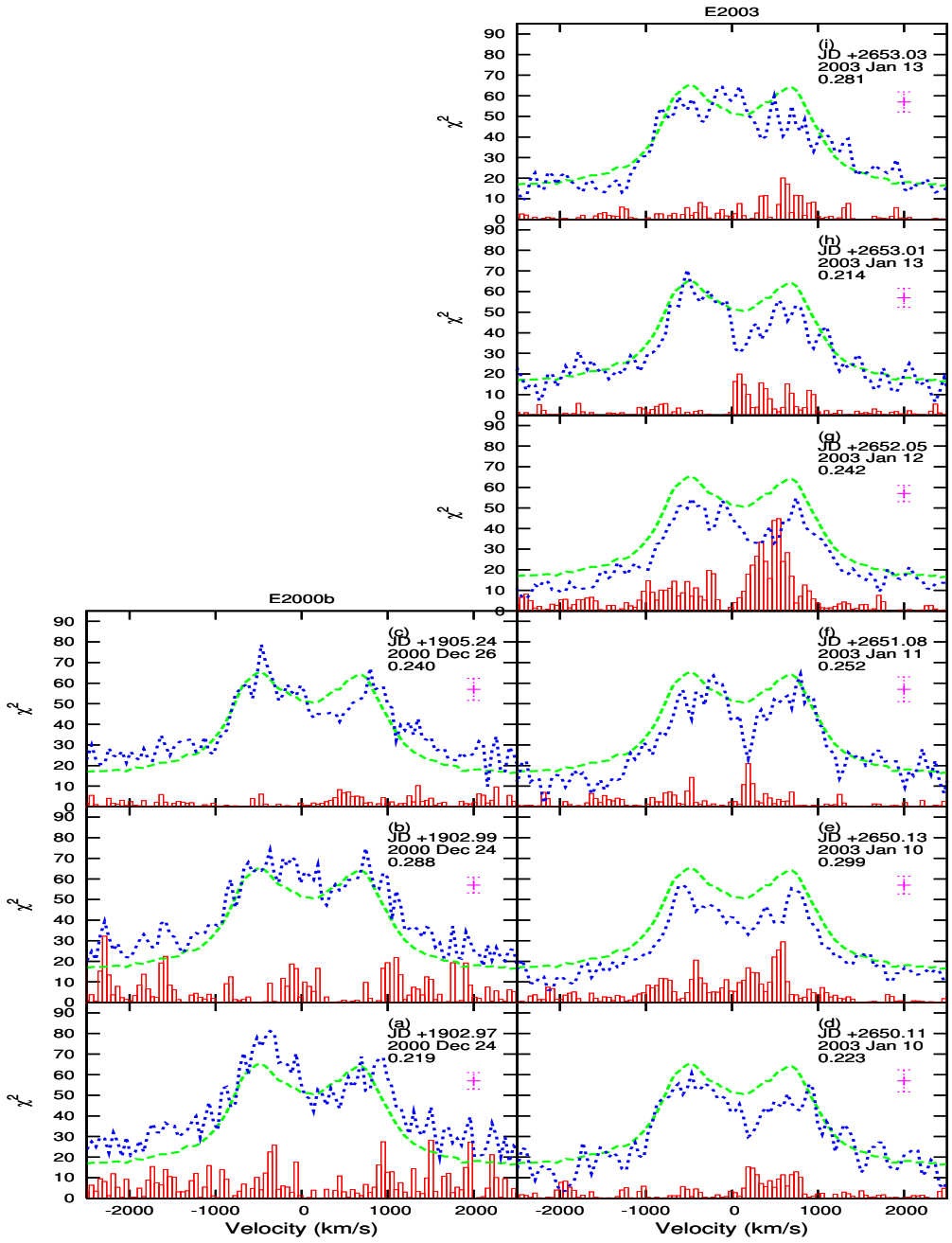

Figure D.3: The Δ of the flux in each wavelength bin of each spectrum (orbital phase 0.2-0.3). The Δs (bars) are plotted with both the overall mean spectrum (dashes) and the respective spectrum (short dashes) to illustrate the region the Δs correspond to.

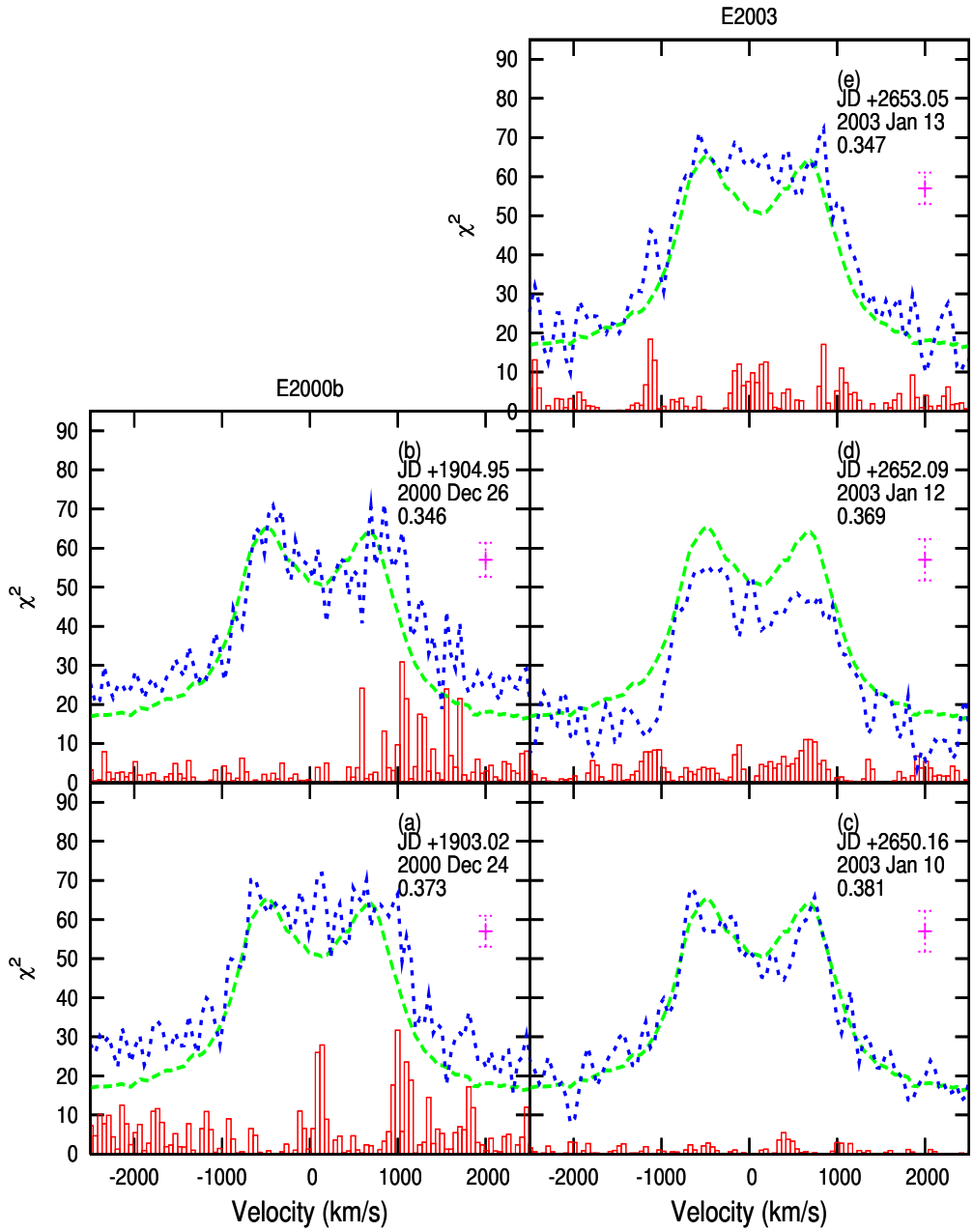

Figure D.4: The Δ of the flux in each wavelength bin of each spectrum (orbital phase 0.3-0.4). The Δs (bars) are plotted with both the overall mean spectrum (dashes) and the respective spectrum (short dashes) to illustrate the region the Δs correspond to.

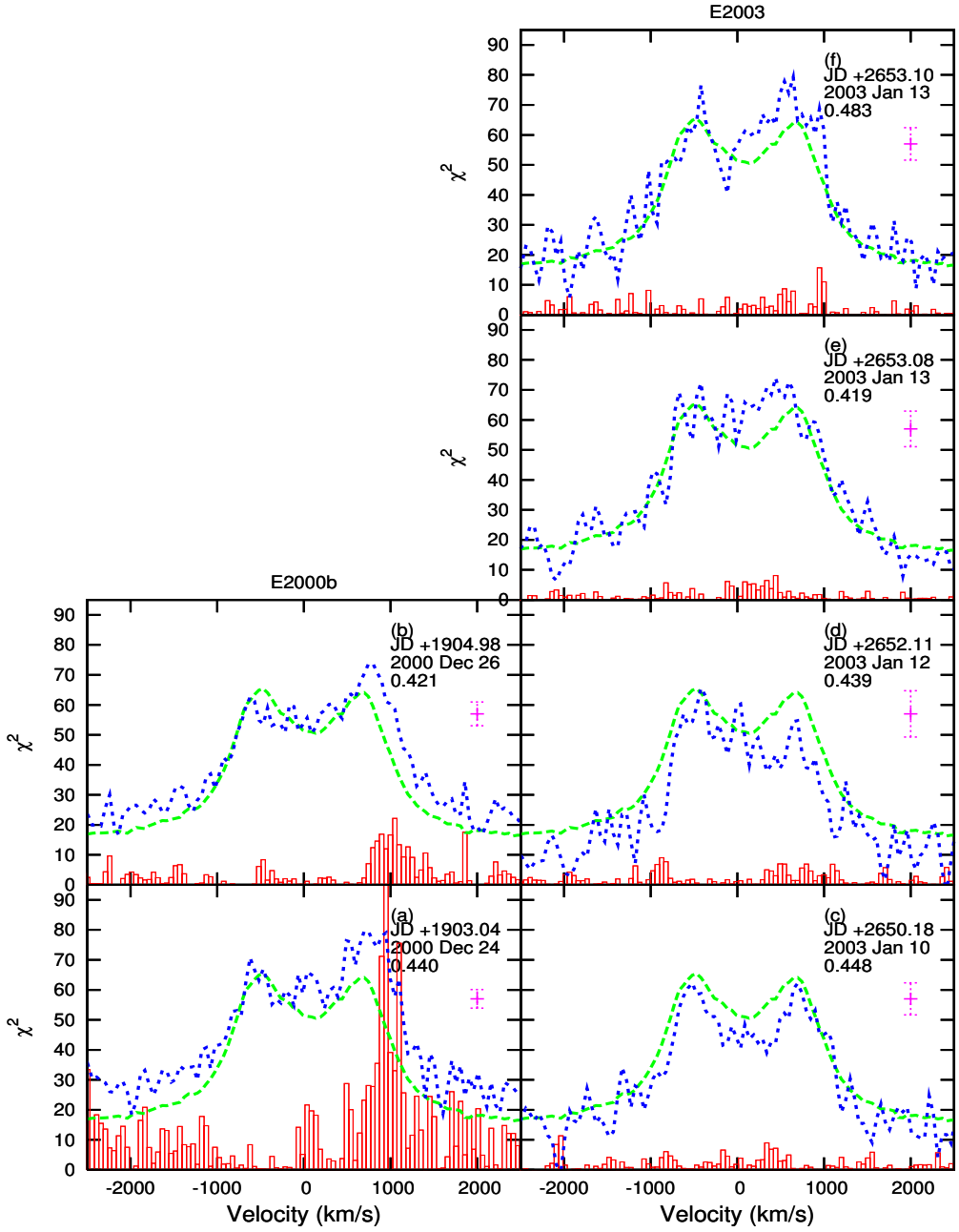

Figure D.5: The Δ of the flux in each wavelength bin of each spectrum (orbital phase 0.4-0.5). The Δs (bars) are plotted with both the overall mean spectrum (dashes) and the respective spectrum (short dashes) to illustrate the region the Δs correspond to.

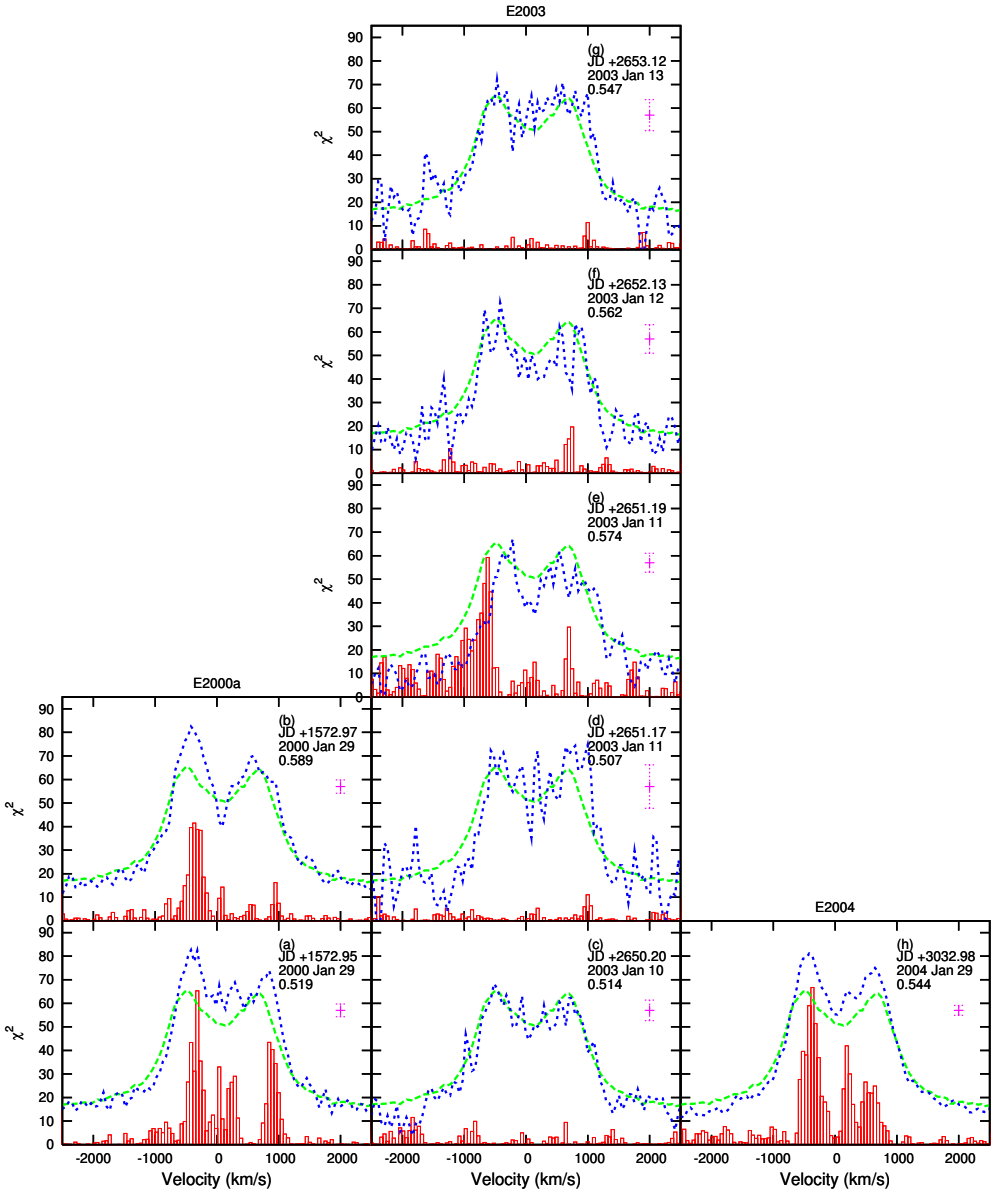

Figure D.6: The Δ of the flux in each wavelength bin of each spectrum (orbital phase 0.5-0.6). The Δs (bars) are plotted with both the overall mean spectrum (dashes) and the respective spectrum (short dashes) to illustrate the region the Δs correspond to.

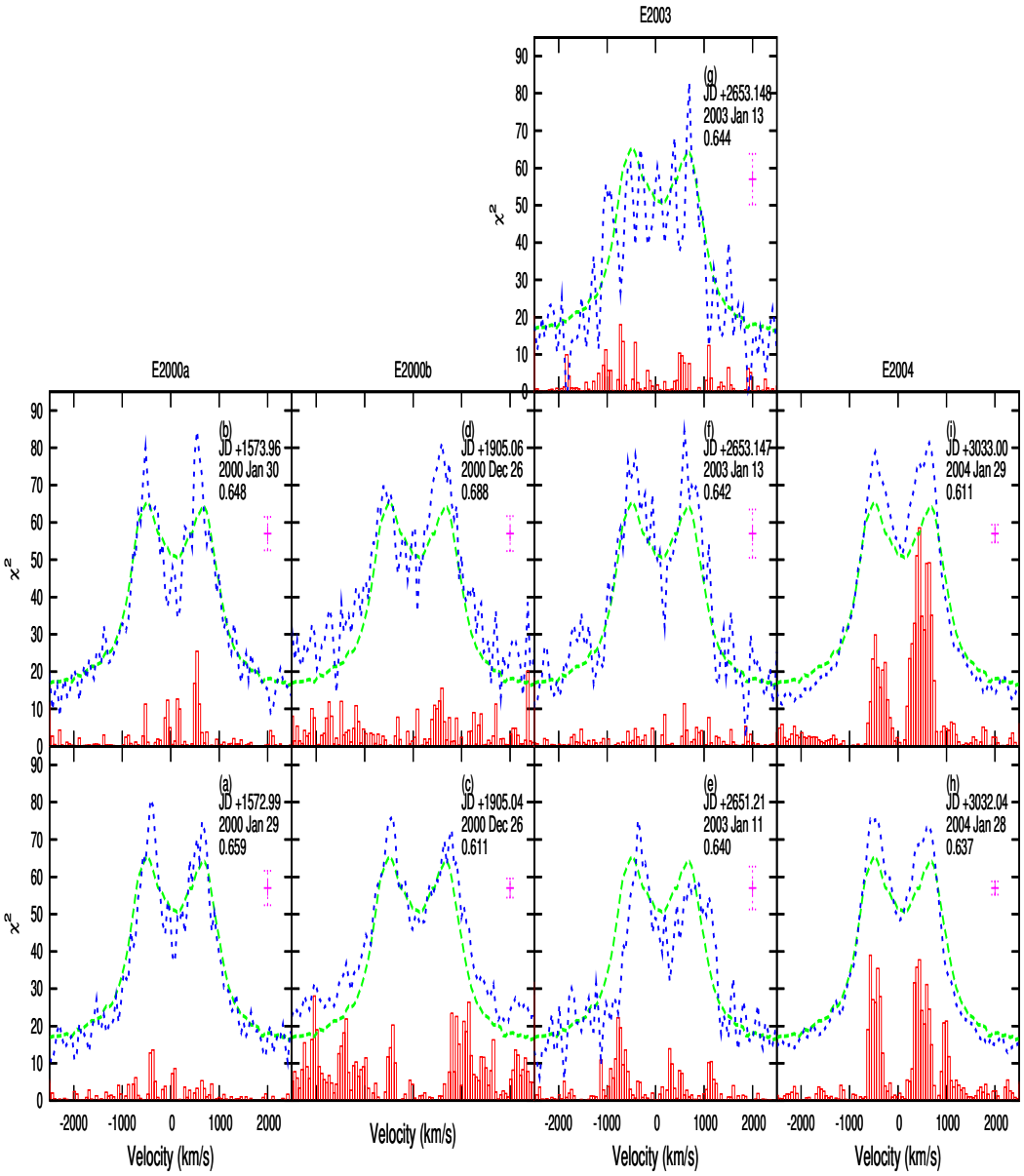

Figure D.7: The Δ of the flux in each wavelength bin of each spectrum (orbital phase 0.6-0.7). The Δs (bars) are plotted with both the overall mean spectrum (dashes) and the respective spectrum (short dashes) to illustrate the region the Δs correspond to.

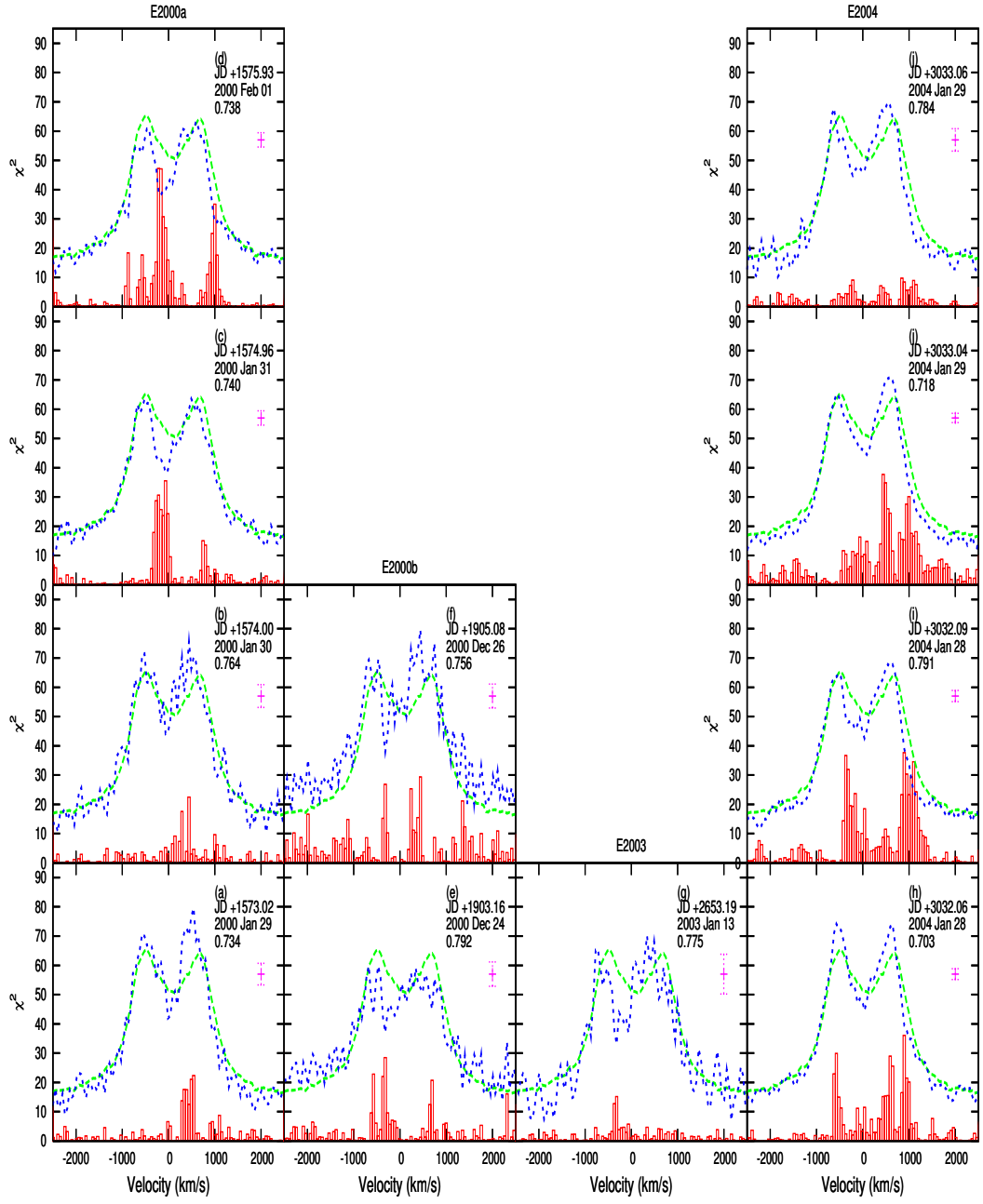

Figure D.8: The Δ of the flux in each wavelength bin of each spectrum (orbital phase 0.7-0.8). The Δs (bars) are plotted with both the overall mean spectrum (dashes) and the respective spectrum (short dashes) to illustrate the region the Δs correspond to.

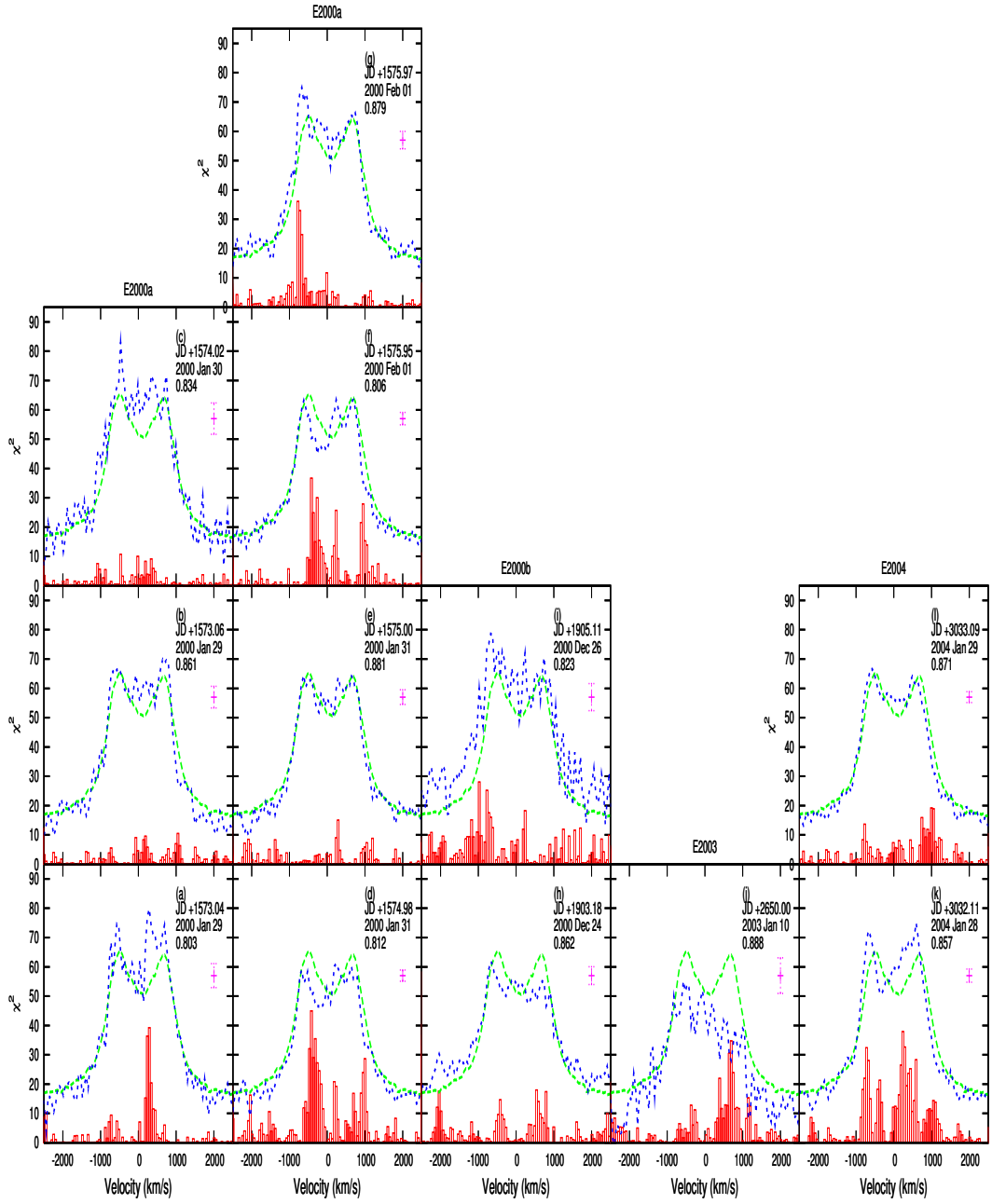

Figure D.9: The Δ of the flux in each wavelength bin of each spectrum (orbital phase 0.8-0.9). The Δs (bars) are plotted with both the overall mean spectrum (dashes) and the respective spectrum (short dashes) to illustrate the region the Δs correspond to.

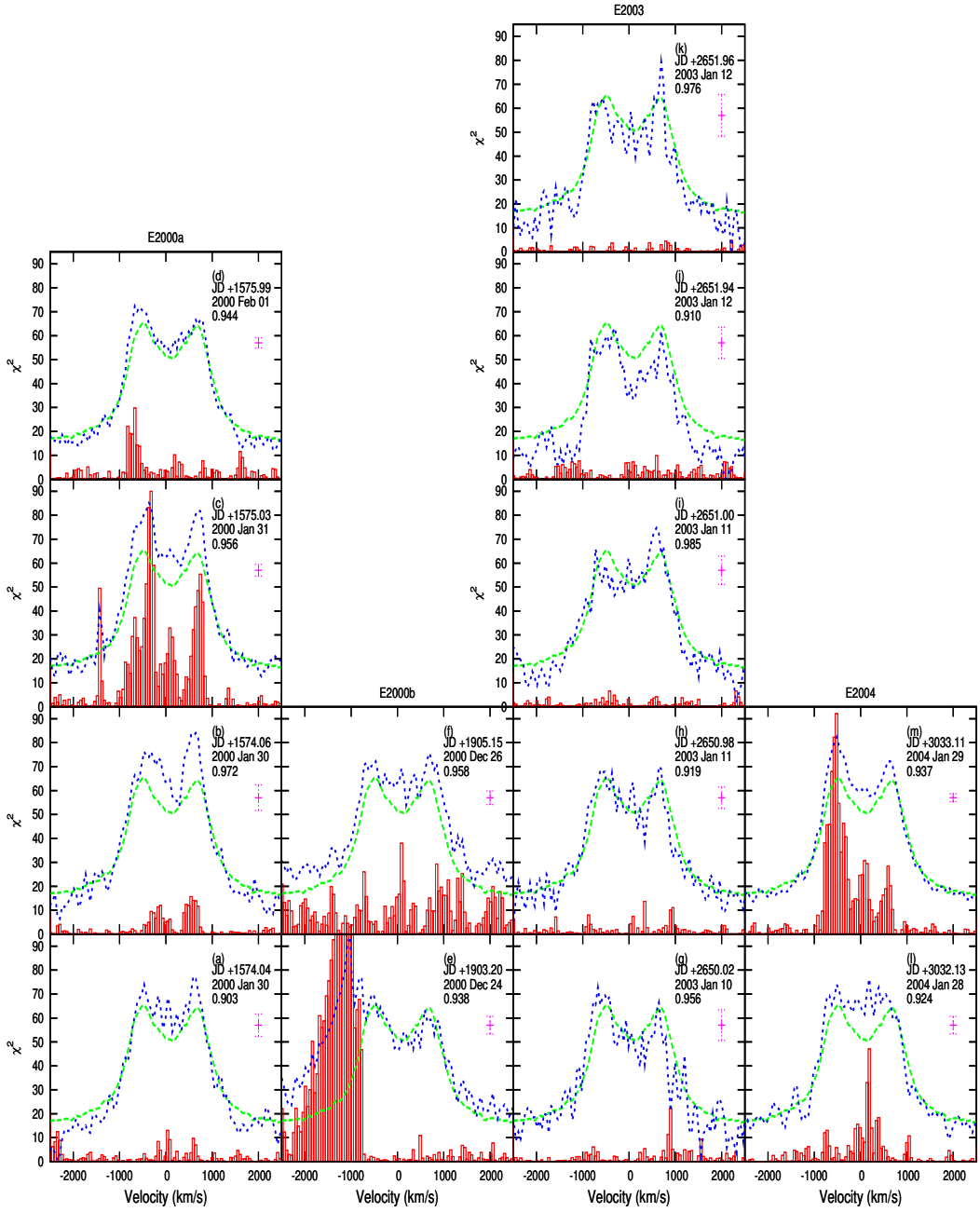

Figure D.10: The Δ of the flux in each wavelength bin of each spectrum (orbital phase 0.9-1.0). The Δs (bars) are plotted with both the overall mean spectrum (dashes) and the respective spectrum (short dashes) to illustrate the region the Δs correspond to.

Appendix E

The Orbital Phase Changes in the Line Profile

The following figures show how each spectrum varies from the orbital phase bin mean spectrum. The difference between each spectrum and the mean spectrum is quantified by Δ in Equation 4.3.

There are 10 figures, which each figure shows the Δ calculated for each wavelength bin for each spectrum in the same orbital phase bin. The spectra in each figure are grouped in columns of observing campaigns.

Each panel shows the Δs overlaid with both the orbital phase bin mean spectrum (dashes) and the respective spectrum (short dashes). The height of each bar corresponds to the vertical axis on the left, it marks the value of each Δ. Both the mean spectrum and respective spectrum are plotted with respect to the same arbituary unmarked vertical axis.

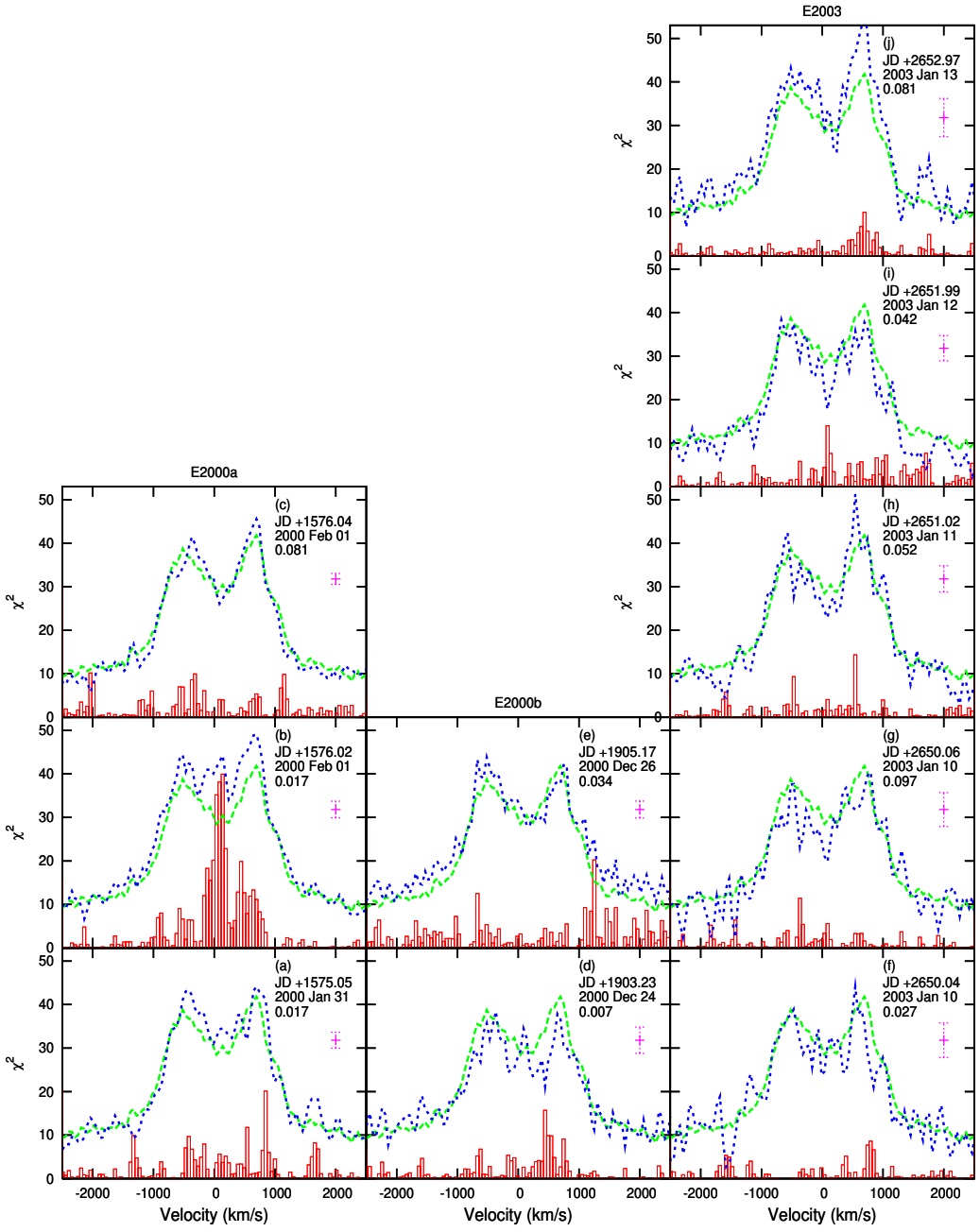

Figure E.1: The Δ of the flux in each wavelength bin of each spectrum (Orbital Phase 0-0.1). The Δs (bars) are plotted with both the orbital phase bin mean spectrum (dashes) and the respective spectrum (short dashes) to illustrate the region the Δs correspond to.

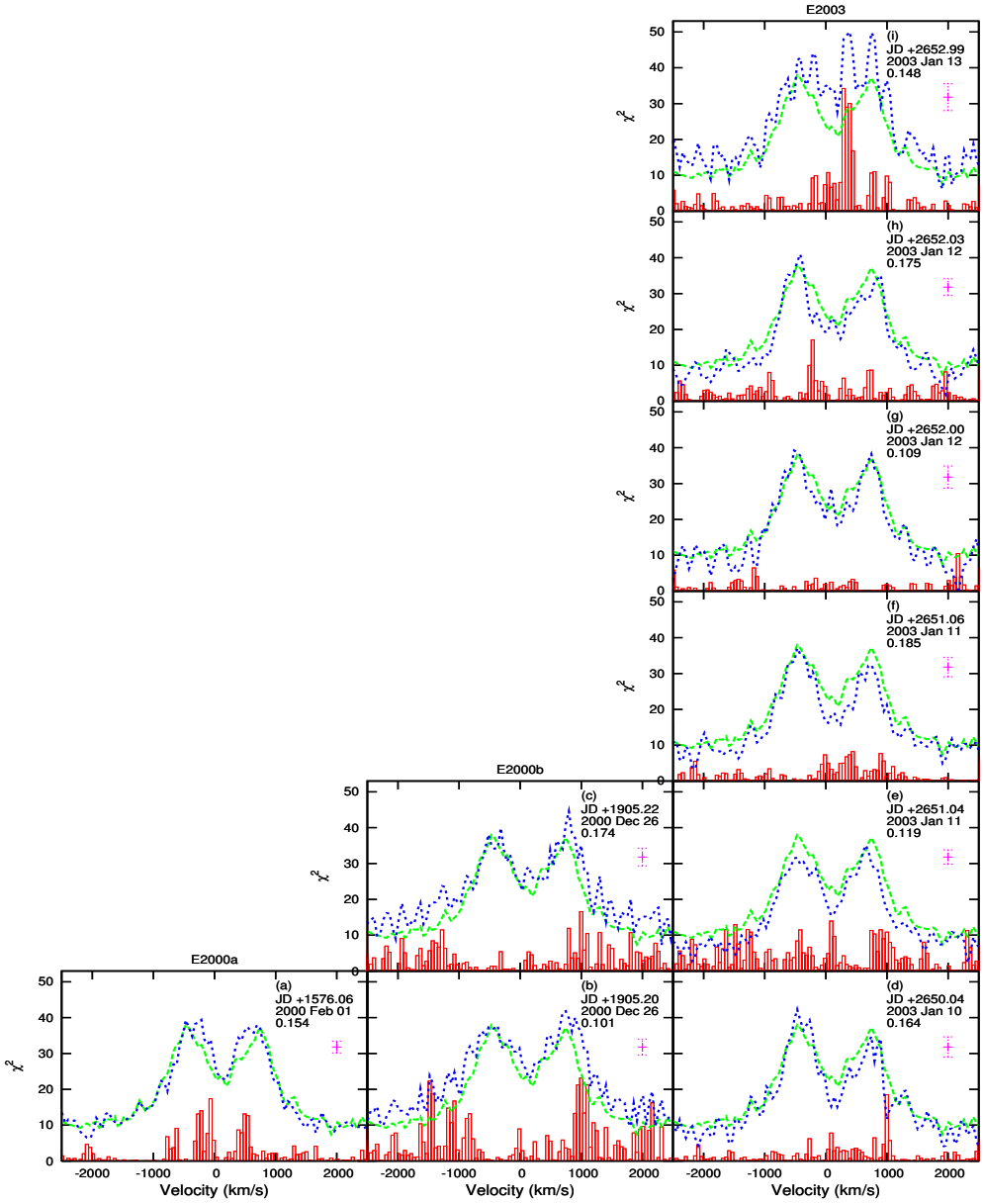

Figure E.2: The Δ of the flux in each wavelength bin of each spectrum (orbital phase 0.1-0.2). The Δs (bars) are plotted with both the orbital phase bin mean spectrum (dashes) and the respective spectrum (short dashes) to illustrate the region the Δs correspond to.

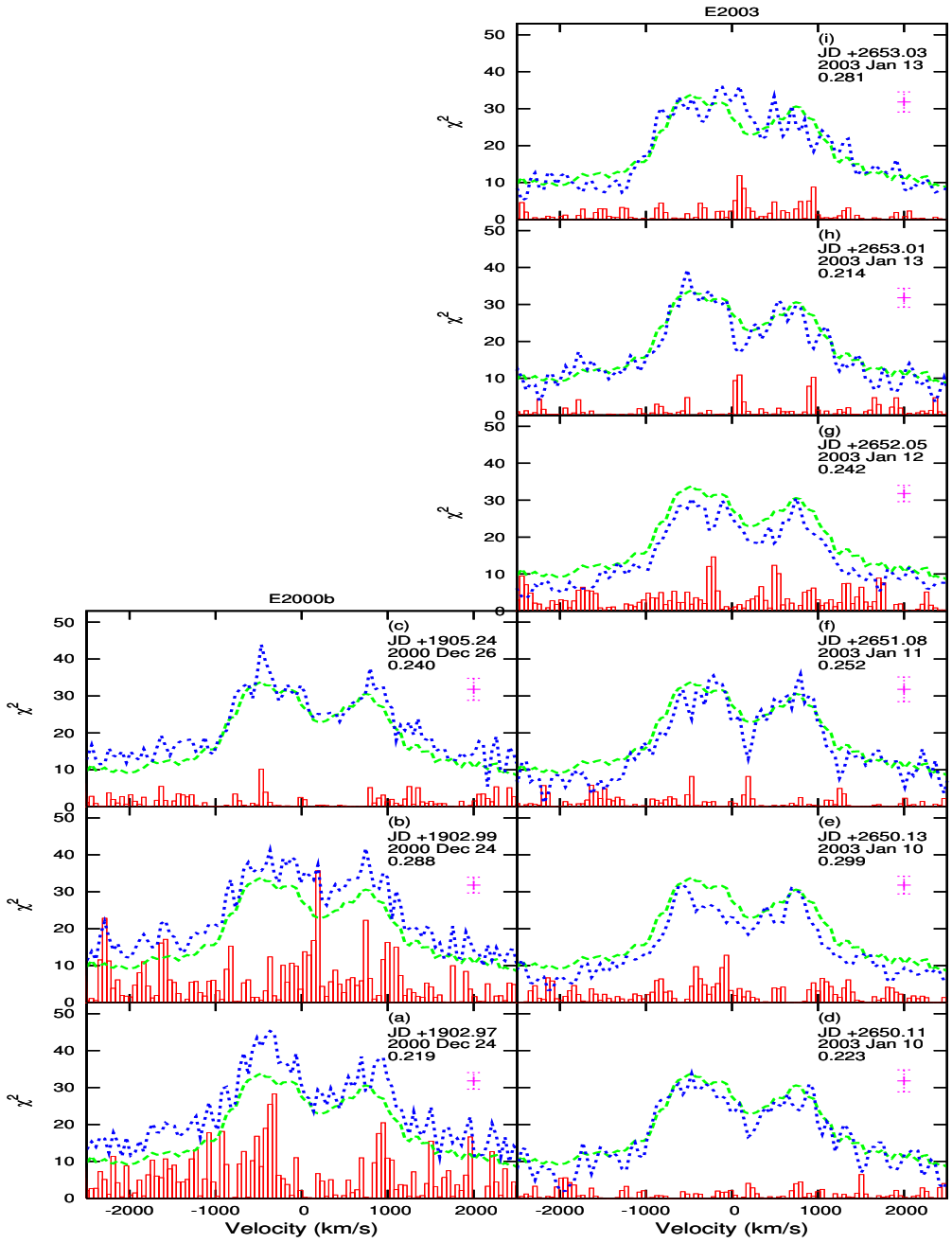

Figure E.3: The Δ of the flux in each wavelength bin of each spectrum (orbital phase 0.2-0.3). The Δs (bars) are plotted with both the orbital phase bin mean spectrum (dashes) and the respective spectrum (short dashes) to illustrate the region the Δs correspond to.

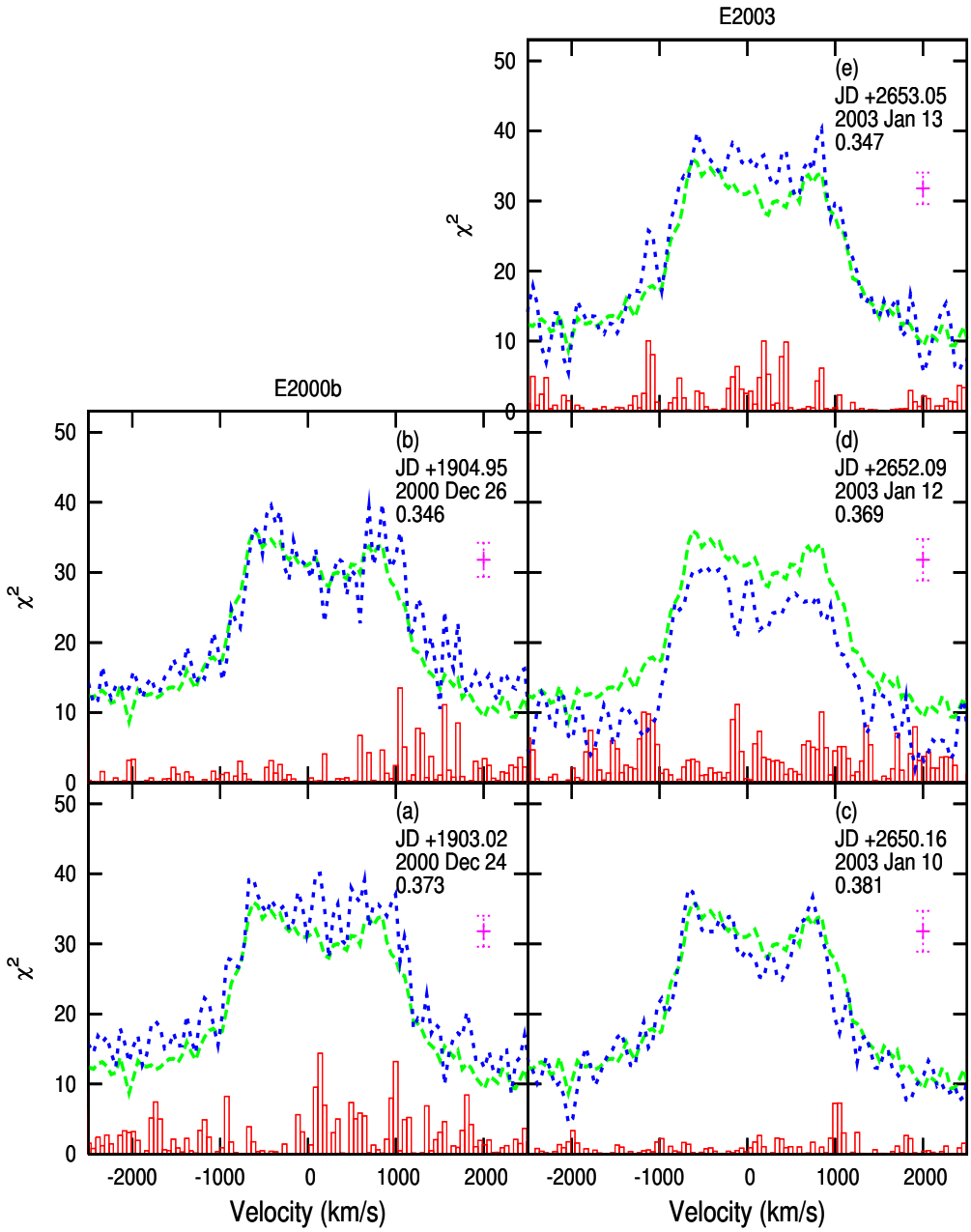

Figure E.4: The Δ of the flux in each wavelength bin of each spectrum (orbital phase 0.3-0.4). The Δs (bars) are plotted with both the orbital phase bin mean spectrum (dashes) and the respective spectrum (short dashes) to illustrate the region the Δs correspond to.

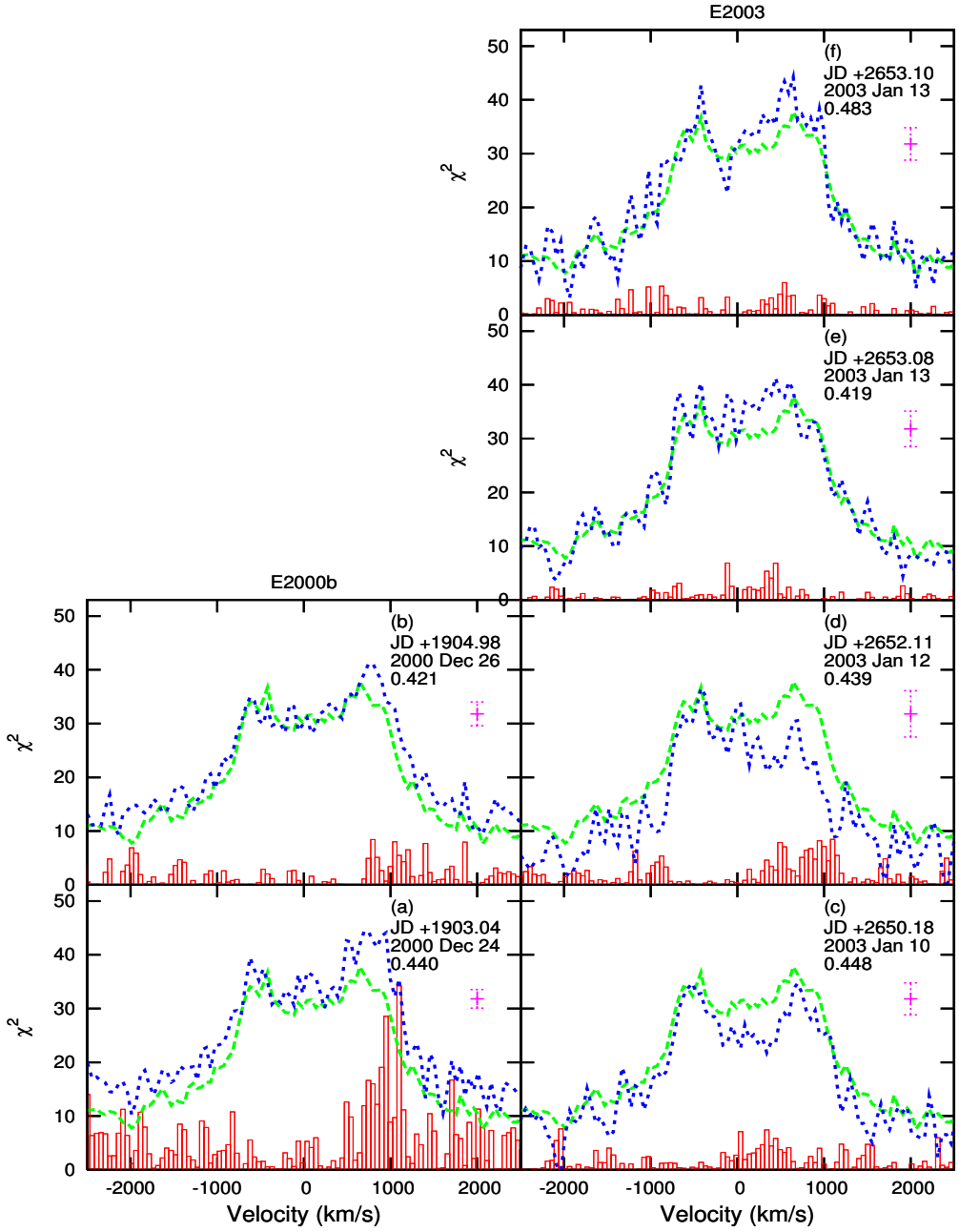

Figure E.5: The Δ of the flux in each wavelength bin of each spectrum (orbital phase 0.4-0.5). The Δs (bars) are plotted with both the orbital phase bin mean spectrum (dashes) and the respective spectrum (short dashes) to illustrate the region the Δs correspond to.

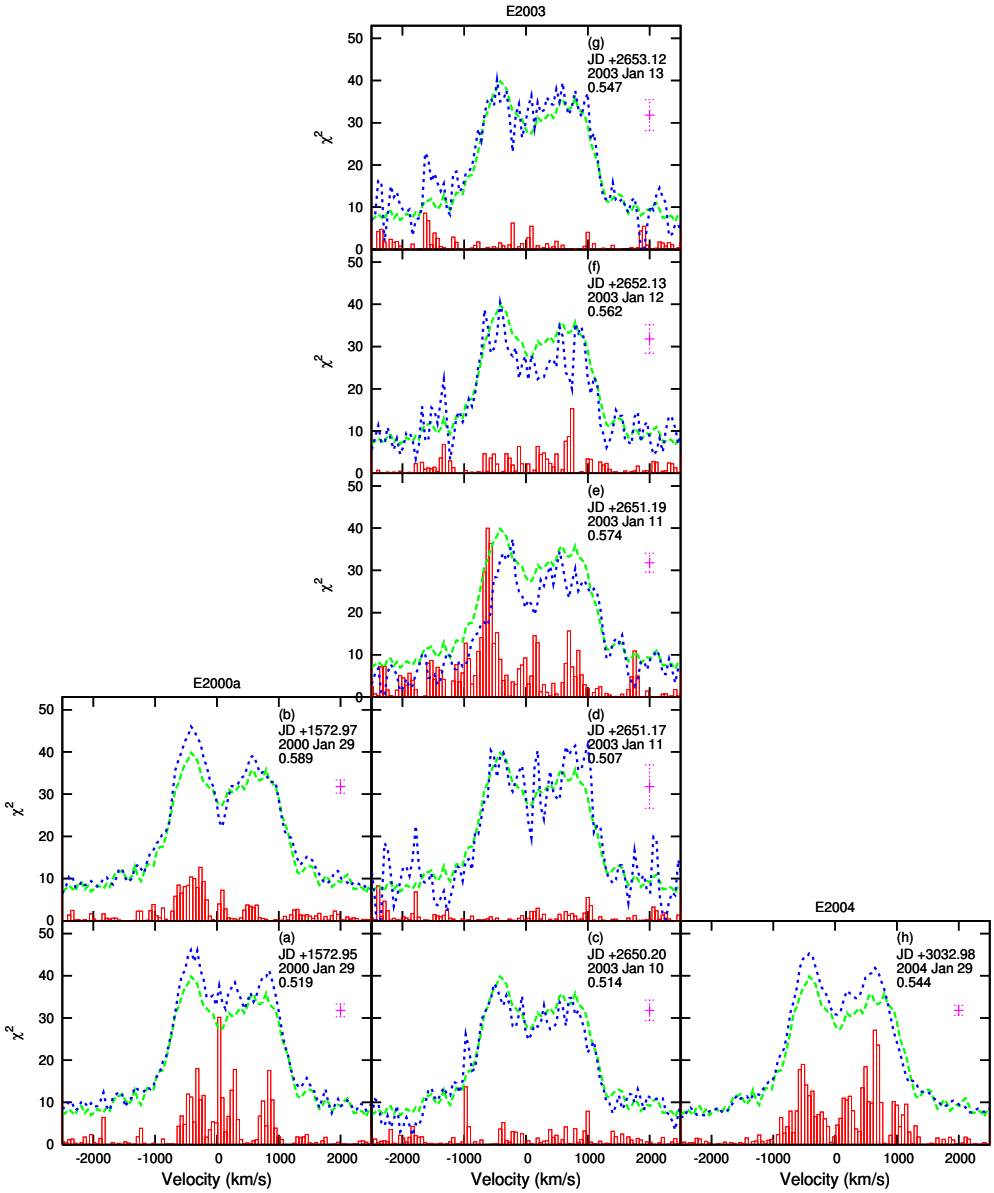

Figure E.6: The Δ of the flux in each wavelength bin of each spectrum (orbital phase 0.5-0.6). The Δs (bars) are plotted with both the orbital phase bin mean spectrum (dashes) and the respective spectrum (short dashes) to illustrate the region the Δs correspond to.

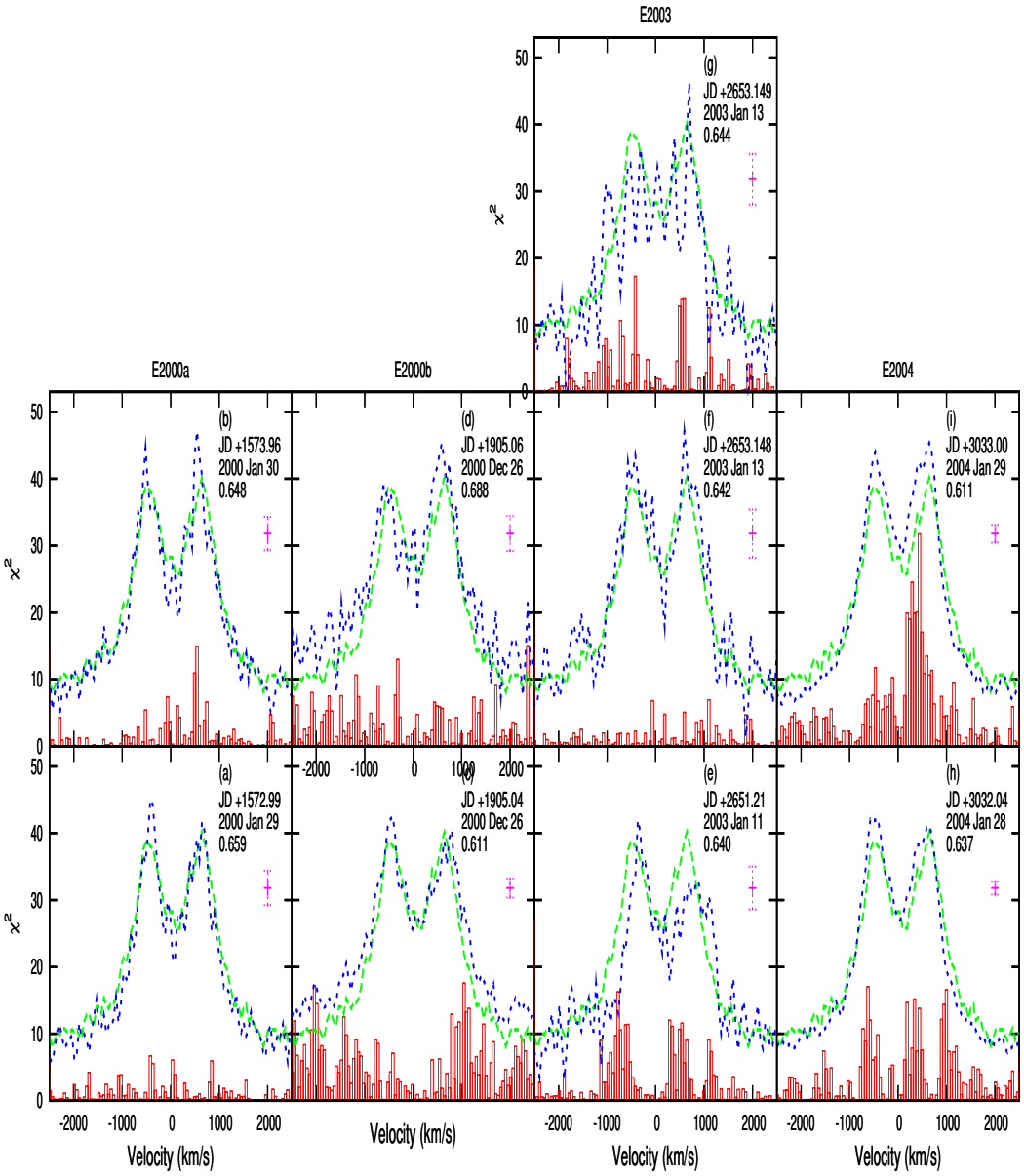

Figure E.7: The Δ of the flux in each wavelength bin of each spectrum (orbital phase 0.6-0.7). The Δs (bars) are plotted with both the orbital phase bin mean spectrum (dashes) and the respective spectrum (short dashes) to illustrate the region the Δs correspond to.

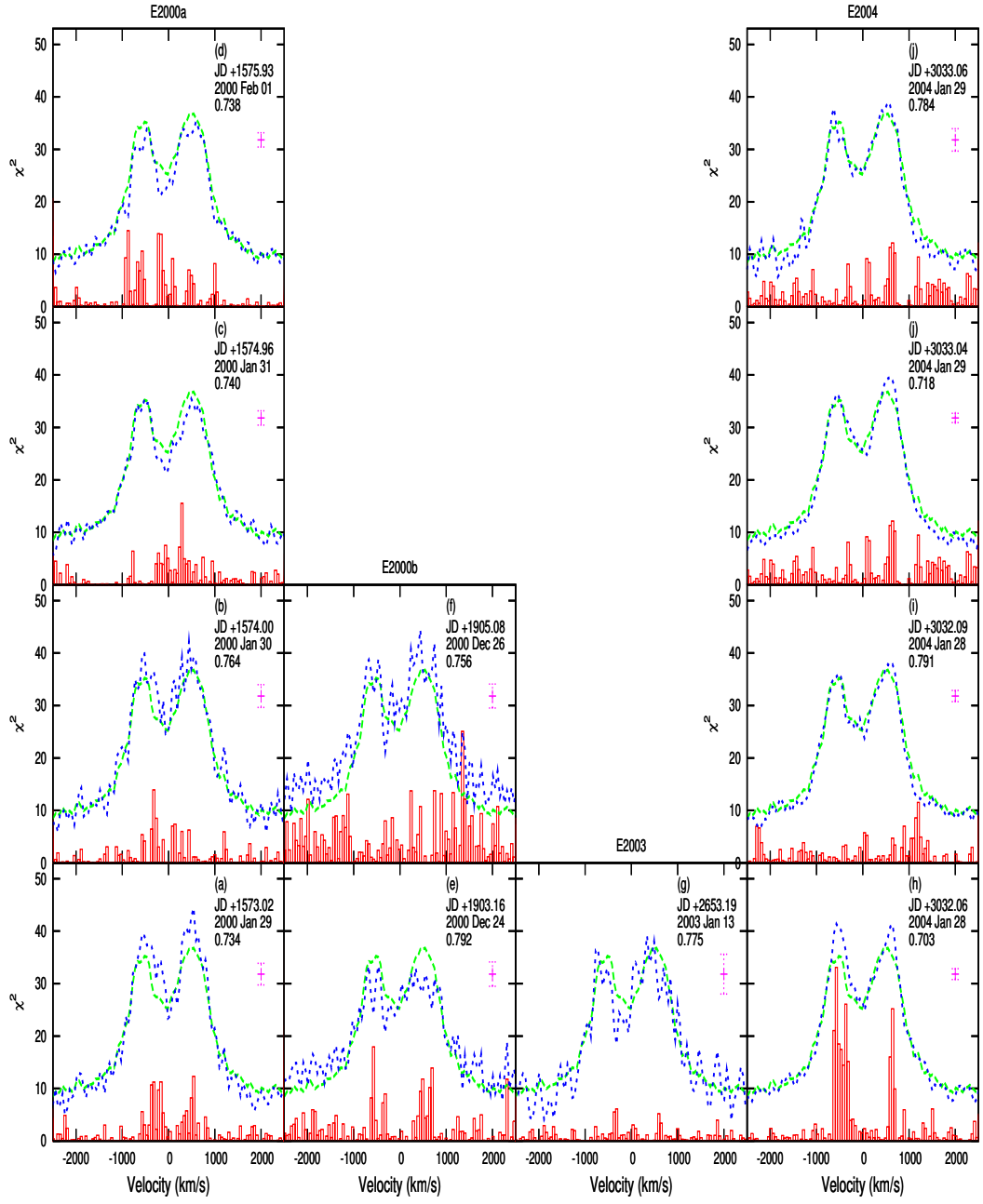

Figure E.8: The Δ of the flux in each wavelength bin of each spectrum (orbital phase 0.7-0.8). The Δs (bars) are plotted with both the orbital phase bin mean spectrum (dashes) and the respective spectrum (short dashes) to illustrate the region the Δs correspond to.

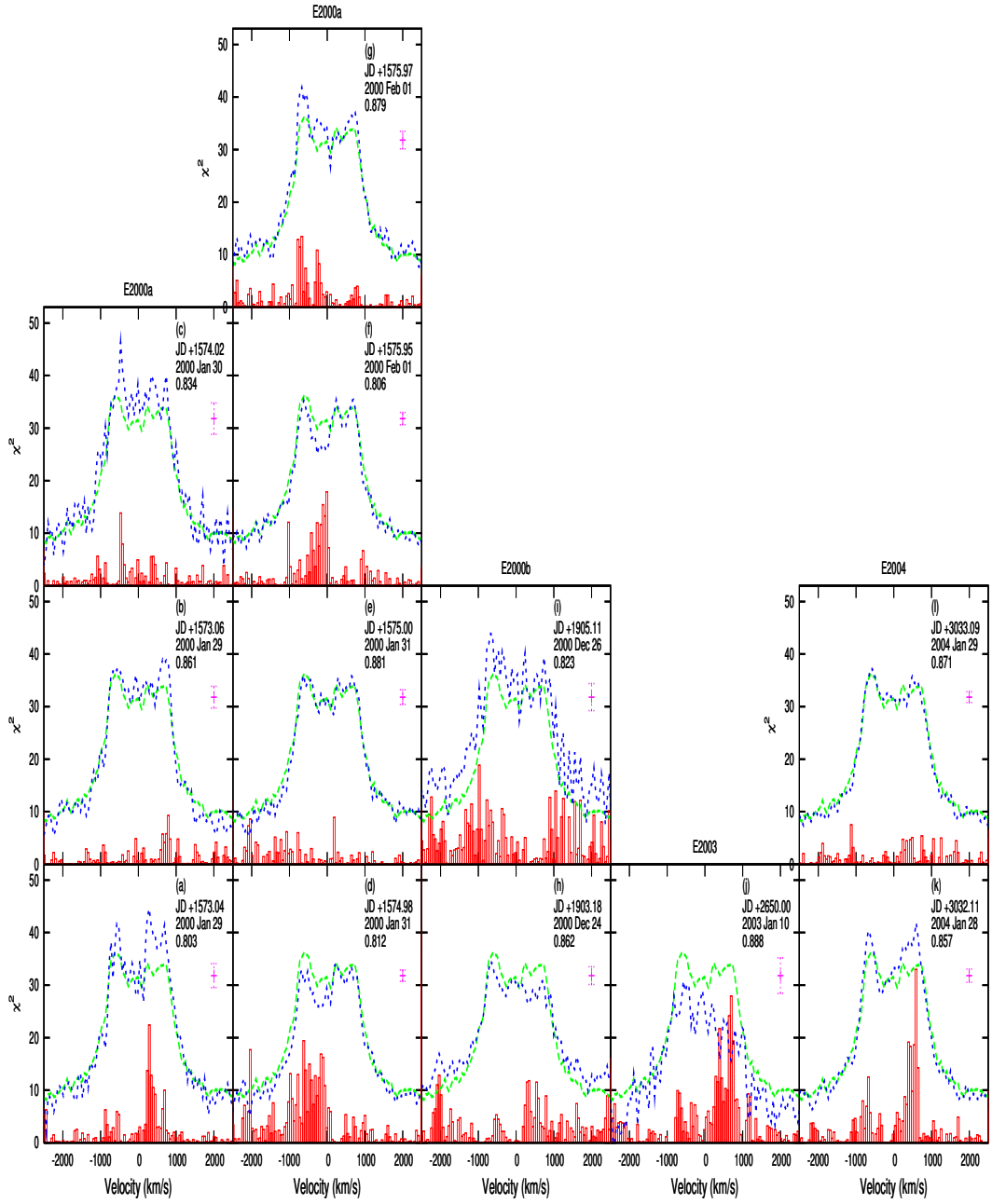

Figure E.9: The Δ of the flux in each wavelength bin of each spectrum (orbital phase 0.8-0.9). The Δs (bars) are plotted with both the orbital phase bin mean spectrum (dashes) and the respective spectrum (short dashes) to illustrate the region the Δs correspond to.

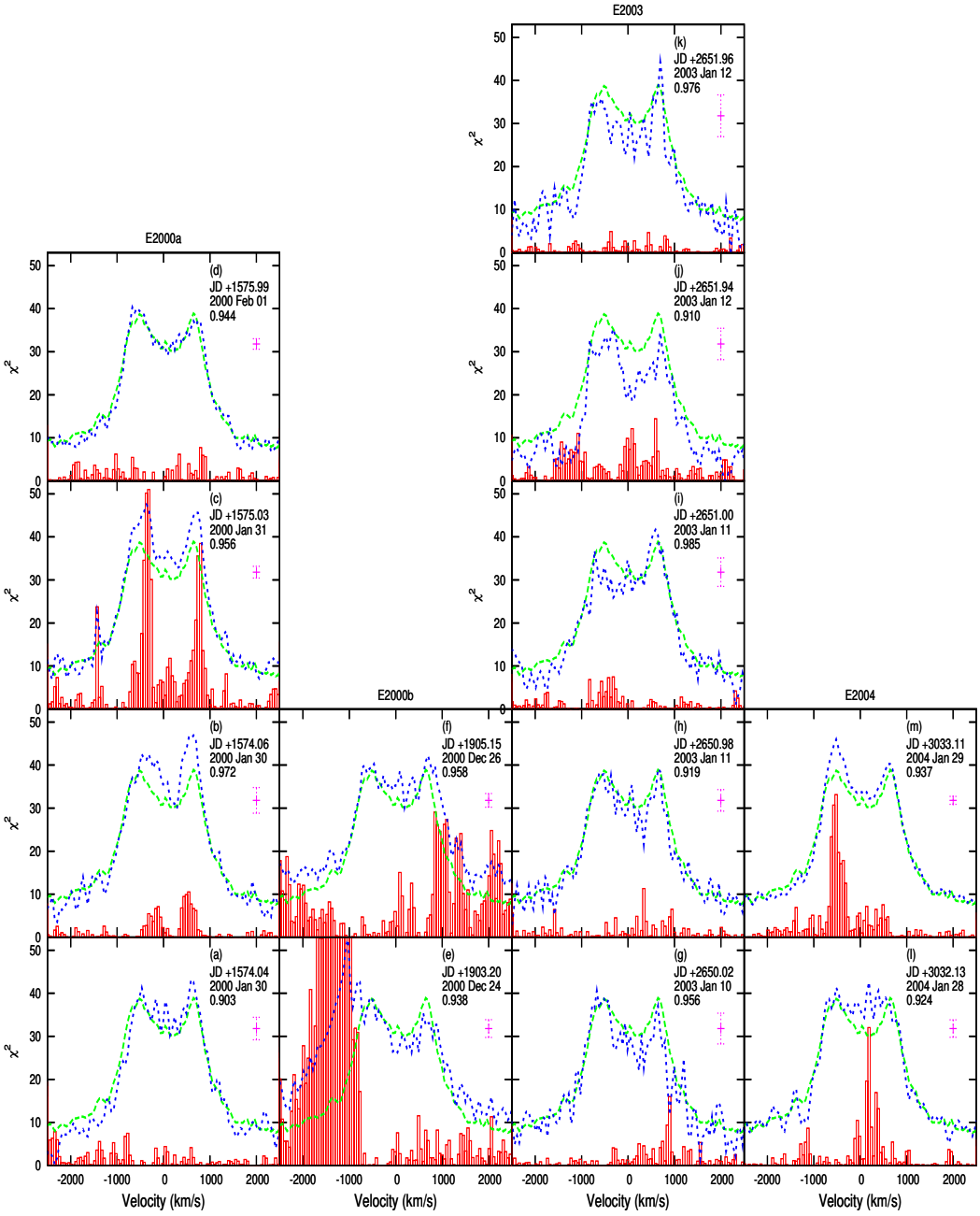

Figure E.10: The Δ of the flux in each wavelength bin of each spectrum (orbital phase 0.9-1.0). The Δs (bars) are plotted with both the orbital phase bin mean spectrum (dashes) and the respective spectrum (short dashes) to illustrate the region the Δs correspond to.

Appendix F

Table of Parameters Used For PCA

Table F.1: Table of Parameters Used For PCA

Julian Date*	**Orbital Phase**	**EW (Å)**	$\frac{\chi^2}{df}$	**Line Width (Å)**	**Peak Sep (Å)**
1572.95	0.519	54.36	7.83	56.51	21.5
1572.97	0.589	50.55	4.57	59.32	22.8
1572.99	0.659	42.39	1.58	64.26	22.4
1573.02	0.734	45.61	2.45	56.51	22.5
1573.04	0.803	49.65	2.62	58.37	22.0
1573.06	0.861	46.60	1.90	58.64	-
1573.96	0.648	45.32	1.94	63.61	23.3
1574.00	0.764	48.83	2.18	76.78	22.0
1574.02	0.834	55.01	1.74	93.30	-
1574.04	0.903	46.60	1.69	57.16	21.4
1574.06	0.972	55.69	2.51	67.12	21.3
1574.96	0.740	41.59	3.57	64.16	24.1

* not used in PCa, for identity purpose only

EW denotes Equivalent Width

Peak Sep denotes Peak separation, spectra without this value are not included in the PCA involving peak separation.

Continued on next page...

Table F.1: (continued)

Julian Date*	**Orbital Phase**	**EW (Å)**	$\frac{\chi^2}{df}$	**Line Width (Å)**	**Peak Sep (Å)**
1574.98	0.812	39.25	6.38	61.09	22.2
1575.00	0.881	44.90	1.72	58.03	22.2
1575.03	0.956	62.44	12.71	63.14	22.6
1575.05	0.017	59.80	4.29	80.15	22.3
1575.93	0.738	38.93	5.23	67.95	22.9
1575.95	0.806	42.37	4.58	63.57	22.7
1575.97	0.879	53.03	3.18	65.61	22.7
1575.99	0.944	49.45	3.46	61.89	23.0
1576.02	0.017	67.16	9.49	73.41	20.6
1576.04	0.081	51.69	5.32	60.10	22.6
1576.06	0.154	44.23	2.98	77.04	21.3
1902.97	0.219	66.18	7.02	96.62	25.9
1903.00	0.288	64.92	5.37	96.85	23.1
1903.02	0.373	65.98	5.2	95.55	-
1903.04	0.440	70.79	12.46	97.71	25.2
1903.16	0.792	44.04	3.24	97.47	22.8
1903.18	0.862	49.23	3.28	96.05	-
1903.20	spectrum not included				
1903.23	0.007	46.08	1.25	98.56	24.3
1904.95	0.346	58.61	4.01	94.82	24.9
1904.98	0.421	59.87	3.58	92.59	24.0
1905.04	0.611	61.41	6.79	91.30	25.5
1905.06	0.688	63.32	3.69	97.80	25.1
1905.08	0.756	62.14	4.67	94.92	23.8
1905.11	0.823	67.66	4.91	90.69	-

* not used in PCa, for identity purpose only

EW denotes Equivalent Width

Peak Sep denotes Peak separation, spectra without this value are not included in the PCA involving peak separation.

Continued on next page...

Table F.1: (continued)

Julian Date*	**Orbital Phase**	**EW (Å)**	$\frac{\chi^2}{df}$	**Line Width (Å)**	**Peak Sep (Å)**
1905.15	0.958	68.36	9.29	90.80	-
1905.17	0.034	63.85	5.02	93.56	24.7
1905.20	0.101	62.84	5.18	92.51	26.9
1905.22	0.174	57.98	4.06	96.53	25.4
1905.24	0.240	53.51	2.16	95.21	25.6
2650.00	0.888	22.94	4.33	69.66	-
2650.02	0.956	40.59	1.82	75.46	24.1
2650.04	0.027	47.36	1.02	82.37	24.6
2650.06	0.097	43.48	1.06	82.14	25.3
2650.09	0.164	33.90	3.50	64.71	24.5
2650.11	0.223	33.80	2.85	85.70	25.9
2650.13	0.299	25.65	5.20	58.11	23.8
2650.16	0.381	46.16	0.80	86.44	23.9
2650.18	0.448	33.81	1.84	87.17	24.4
2650.20	0.514	40.28	1.71	73.63	22.8
2650.98	0.919	43.95	1.64	78.13	23.1
2651.00	0.985	41.98	1.20	54.49	-
2651.02	0.052	48.91	2.04	65.64	25.2
2651.04	0.119	25.68	6.94	52.54	23.8
2651.06	0.185	29.30	3.66	59.24	24.8
2651.08	0.252	32.76	2.40	75.35	23.3
2651.17	0.507	44.34	1.37	94.55	-
2651.19	0.574	25.00	8.83	53.58	21.4
2651.21	0.640	39.12	2.98	85.90	23.7
2651.94	0.910	23.38	2.66	49.60	24.0

* not used in PCa, for identity purpose only

EW denotes Equivalent Width

Peak Sep denotes Peak separation, spectra without this value are not included in the PCA involving peak separation.

Continued on next page...

Table F.1: (continued)

Julian Date*	**Orbital Phase**	**EW (Å)**	$\frac{\chi^2}{df}$	**Line Width (Å)**	**Peak Sep (Å)**
2651.96	0.976	35.17	0.86	74.16	24.5
2651.99	0.042	37.66	1.72	61.39	23.7
2652.01	0.109	34.13	2.19	82.49	25.4
2652.03	0.175	32.13	4.66	89.44	25.2
2652.05	0.242	22.73	7.37	56.10	24.3
2652.09	0.369	27.05	3.19	55.15	22.3
2652.11	0.439	24.53	2.03	64.95	-
2652.15	0.562	35.23	2.18	88.73	24.1
2652.97	0.081	68.51	2.32	97.00	23.5
2652.99	0.148	66.13	2.92	94.78	-
2653.01	0.214	35.44	3.01	86.03	23.8
2653.03	0.281	42.08	2.71	67.94	-
2653.05	0.347	58.70	3.23	90.71	-
2653.08	0.419	51.64	1.42	75.00	-
2653.10	0.483	54.38	2.02	81.34	23.1
2653.12	0.547	48.80	1.39	84.31	22.2
2653.148	0.642	53.69	1.53	94.67	24.3
2653.149	0.644	38.41	2.63	68.23	-
2653.19	0.775	41.14	1.66	86.46	23.3
3032.04	0.637	47.99	6.80	56.94	22.1
3032.06	0.703	46.27	4.97	56.75	22.6
3032.09	0.791	40.56	6.60	50.23	23.5
3032.11	0.857	48.15	6.93	64.48	21.6
3032.13	0.924	52.62	4.09	71.75	-
3032.98	0.544	50.91	8.79	54.11	-

* not used in PCa, for identity purpose only

EW denotes Equivalent Width

Peak Sep denotes Peak separation, spectra without this value are not included in the PCA involving peak separation.

Continued on next page...

Table F.1: (continued)

Julian Date*	**Orbital Phase**	**EW (Å)**	$\frac{\chi^2}{df}$	**Line Width (Å)**	**Peak Sep (Å)**
3033.00	0.611	51.48	7.85	55.43	21.6
3033.04	0.718	41.40	7.34	52.37	23.8
3033.06	0.784	40.60	2.30	54.02	22.9
3033.09	0.871	44.96	3.65	63.46	21.2
3033.11	0.937	53.18	10.92	58.92	22.0

* not used in PCA, for identity purpose only

EW denotes Equivalent Width

Peak Sep denotes Peak separation, spectra without this value are not included in the PCA involving peak separation.

Appendix G

List of Acronyms

Abbreviation	Details
AAT	3.9 m Anglo-Australia Telescope
ANU	Australia National University
ASM	All Sky Monitor on board Ariel V, provides count rates in 3-6 keV energy band
ATT	Advanced Technology Telescope, also known as 2.3 m ANU.
Chandra	Chandra X-ray Observatory, which was launched on July 23, 1999. It is sensitive to energies of about 0.2 - 10 keV.
CCD	Charge coupled device
CM	centre-of-mass
DBS	Dual Beam Spectrograph
HJD	Heliocentric Julian Date
HMXB	High mass X-ray binaries
JD	Julian Date
LMXB	Low mass X-ray binaries
mks	units are in metres, Kilograms and seconds
PIMMS	Portable, Interactive Multi-Mission Simulator. It is a versatile simulation tool for X-ray astronomers. It is a Mission count-rate simulator for a specified input instrument.

Continued on next page...

Abbreviation	**Details**
ROSAT	Rontgensatellite is an X-ray observatory, which was launched on June 1, 1990. It is sensitive to 0.1 keV - 2 keV of the X-ray band and 0.04 keV - 0.2 keV of the extreme ultraviolet region.
RMC	Rotation Modulation Collimator, on board Ariel V. It conducts experiments aligned with the spin axis, sensitive to 0.3 - 30 keV energy band.
SSE	Sky Survey Experiment, also known as Sky Survey Instrument, on board Ariel V. It provides 8 channels of count rate in 2 - 18 keV energy band.
WebPIMMS	WWW interface to the command-line version of PIMMS.
XT	X-ray Transient

Bibliography

Borisov, Y.V., Derevyashkin, Y. & Deych, D. (1977). Photographic observations of A 0620-00 object. *Astronomicheskij Tsirkulyar*, 969, 7–+.

Cherepashchuk, A.M. (2000). X-ray Nova Binary Systems. *Space Science Reviews*, 93, 473–580.

Chevalier, C., Ilovaisky, S.A., Janot-Pacheco, E. & Mauder, H. (1980). UBV photometry of V616 MON /A0620-00/. *A&A*, 81, 368–370.

Duerbeck, H.W. & Walter, K. (1976). UBV photometry and an interpretation of Nova MON 1975. *A&A*, 48, 141–144.

Elvis, M., Page, C.G., Pounds, K.A., Ricketts, M.J. & Turner, M.J.L. (1975). Discovery of powerful transient X-ray source A0620-00 with Ariel V Sky Survey Experiment. *Nature*, 257, 656–+.

Francis, P.J. & Wills, B.J. (1999). Introduction to Principal Components Analysis. In *ASP Conf. Ser. 162: Quasars and Cosmology*, 363–+.

Frank, J., King, A. & Raine, D.J. (2002). *Accretion Power in Astrophysics: Third Edition*. Accretion Power in Astrophysics: Third Edition, by Juhan Frank, Andrew King, and Derek J. Raine. Cambridge University Press, 2002, 398 pp.

Froning, C.S. & Robinson, E.L. (2001). Near-Infrared Light Curves of the Black Hole Binary A0620-00. *AJ*, 121, 2212–2218.

Garcia, M.R., McClintock, J.E., Narayan, R., Callanan, P., Barret, D. & Murray, S.S. (2001). New Evidence for Black Hole Event Horizons from Chandra. *ApJ*, 553, L47–L50.

Gradshteyn, I.S. & Ryzhik, I.M. (1994). *Table of integrals, series and products*. New York: Academic Press, —c1994, 5th ed. completely reset, edited by Jeffrey, Alan.

Haswell, C.A. (1992). *The black hole candidate binary A0620-00*. Ph.D. thesis, Texas Univ., Austin.

Haswell, C.A. & Shafter, A.W. (1990). A detection of orbital radial velocity variations of the primary component in the black hole binary A0620 - 00 (= V616 Monocerotis). *ApJ*, 359, L47–L50.

Haswell, C.A., Robinson, E.L. & Horne, K.D. (1990). The Light Curve of A0620-00, the Black Hole Binary. In *Accretion-Powered Compact Binaries*, 11–+.

Horne, K. & Marsh, T.R. (1986). Emission line formation in accretion discs. *MNRAS*, 218, 761–773.

Hudec, R. (1977). Photographic Observations of the X-ray Nova Monocerotis 1975. *Bulletin of the Astronomical Institutes of Czechoslovakia*, 28, 374–+.

Hynes, R.I., Charles, P.A., Casares, J., Haswell, C.A., Zurita, C. & Shahbaz, T. (2003). Fast photometry of quiescent soft X-ray transients with the Acquisition Camera on Gemini-South. *MNRAS*, 340, 447–456.

Johnston, H. & Kulkarini, S. (1990). Optical Spectroscopy of A0620-00 and GS2023+338. In *Accretion-Powered Compact Binaries*, 17–+.

Johnston, H.M., Kulkarni, S.R. & Oke, J.B. (1989). The black hole A0620-00 and its accretion disk. *ApJ*, 345, 492–497.

Kaluzienski, L.J., Holt, S.S., Boldt, E.A. & Serlemitsos, P.J. (1977). All-Sky Monitor observations of the decay of A0620-00 /Nova Monocerotis 1975/. *ApJ*, 212, 203–210.

Kuulkers, E. (1998). A0620-00 revisited: a black-hole transient case-study. *New Astronomy Review*, 42, 1–22.

Lasota, J.P. (2001). The disc instability model of dwarf novae and low-mass X-ray binary transients. *New Astronomy Review*, 45, 449–508.

Leibowitz, E.M., Hemar, S. & Orio, M. (1998). Regularities in the long-term optical light curve of the black hole candidate binary A0620-00 (V616 Mon). *MNRAS*, 300, 463–468.

Lin, D.N.C. (1991). Accretion disks in interacting binary stars. In *ASP Conf. Ser. 20: Frontiers of Stellar Evolution*, 427–449.

Liutyi, V.M. (1976). U, B, V photometry of the object identified with the X-ray source A0620-00. *Soviet Astronomy Letters*, 2, 43–45.

Lloyd, C., Noble, R. & Penston, M.V. (1977). The light curve of V616 Mon=A 0620-00. *MNRAS*, 179, 675–681.

Locher, K. (1975). A0620-00. *IAU Circ.*, 2823, 1–+.

Lyutyi, V.M. (1976). Decline in brightness of V616 MON (A 0620-00). *Soviet Astronomy Letters*, 2, 156–157.

Marsh, T.R. & Horne, K. (1988). Images of accretion discs. II - Doppler tomography. *MNRAS*, 235, 269–286.

Marsh, T.R., Robinson, E.L. & Wood, J.H. (1994). Spectroscopy of A0620-00 - the Mass of the Black-Hole and an Image of its Accretion Disc. *MNRAS*, 266, 137.

Massey, P. (1997). *A User's Guide to CCD Reductions with IRAF*.

Massey, P., Valdes, F. & Barnes, J. (1992). *A User's Guide to Reducing Slit Spectra with IRAF,*.

McClintock, J. & Remillard, R. (1986). The Black Hole Binary A0620-00. *ApJ*, 308, 110.

McClintock, J.E. & Remillard, R.A. (1989). Further Observations of the Black Hole Binary A0620-00. *BAAS*, 21, 1206–+.

McClintock, J.E. & Remillard, R.A. (1990). The X-ray nova Centaurus X-4 - Comparisons with A0620 - 00. *ApJ*, 350, 386–394.

McClintock, J.E. & Remillard, R.A. (2000). HST/STIS UV Spectroscopy of Two Quiescent X-Ray Novae: A0620-00 and Centaurus X-4. *ApJ*, 531, 956–962.

McClintock, J.E., Horne, K. & Remillard, R.A. (1995). The DIM inner accretion disk of the quiescent black hole A0620-00. *ApJ*, 442, 358–365.

Murdin, P., Allen, D.A., Morton, D.C., Whelan, J.A.J. & Thomas, R.M. (1980). The K dwarfs associated with the X-ray transients A0620-00 and A1742-28. *MNRAS*, 192, 709–717.

Murray, N. & Chiang, J. (1997). Disk Winds and Disk Emission Lines. *ApJ*, 474, 91–+.

Oke, J.B. (1977). Further spectrophotometry of the transient X-ray source A0620-00. *ApJ*, 217, 181–185.

Oke, J.B. & Greenstein, J.L. (1977). Spectrophotometry of the transient X-ray source A0620-00. *ApJ*, 211, 872–880.

Robertson, B.S.C., Warren, P.R. & Bywater, R.A. (1976). Optical Photometry of the X-Ray Nova A0620-00. *Informational Bulletin on Variable Stars*, 1173, 1–+.

Rodgers, A.W., Conroy, P. & Bloxham, G. (1988). A dual-beam Nasmyth spectrograph. *PASP*, 100, 626–634.

Searle, L., Oke, J.B., Greenstein, J.L., Kirshner, R., French, H. & Locher, K. (1975). Nova Monocerotis 1975 (= A0620-00). *IAU Circ.*, 2840, 1–+.

Shahbaz, T., Naylor, T. & Charles, P.A. (1994). The Mass of the Black-Hole in A:0620-00. *MNRAS*, 268, 756–+.

Shahbaz, T., Hynes, R.I., Charles, P.A., Zurita, C., Casares, J., Haswell, C.A., Araujo-Betancor, S. & Powell, C. (2004). Optical spectroscopy of flares from the black hole X-ray transient A0620-00 in quiescence. *MNRAS*, 354, 31–42.

Smak, J. (1981). On the Emission Lines from Rotating Gaseous Disks. *Acta Astron.*, 31, 395.

Soria, R. (1999). *Accretion processes in Black Hole Binaries*. Ph.D. thesis, Australian National University.

Webbink, R. (1978). A Provisional Optical Light Curve of the X-ray Recurrent Nova V616 Mon = A0620-00, unpublished report.

Wheeler, J.C., Mineshige, S., Huang, M. & Kim, S.W. (1989). Accretion Disk Instabilities in A0620-00 and Related Systems. In *Accretion-Powered Compact Binaries*, 315.

Whelan, J.A.J., Allen, D.A., Danziger, I.J., Fosbury, R.A.E., Murdin, P.G., Penston, M.V., Peterson, B.A., Wampler, E.J., Webster, B.L. & Ward, M.J. (1977). Spectroscopic observations of the X-ray nova A0620-00. *MNRAS*, 180, 657–673.

Wilson, R.E. (1953). General Catalogue of Stellar Radial Velocities. *Carnegie Institute Washington D.C. Publication.*

Wu, C.C., Aalders, J.W.G., van Duinen, R.J., Kester, D. & Wesselius, P.R. (1976). A study of the transient X-ray source A 0620-00. *A&A*, 50, 445–449.

Wu, K., Soria, R., Hunstead, R.W. & Johnston, H.M. (2001). Optical spectroscopy of GX 339-4 during the high-soft and low-hard states - II. Line ionization and emission region. *MNRAS*, 320, 177–192.